

Response Modelling of Bitumen, Bituminous Mastic and Mortar

M.F. WOLDEKIDAN

Modelleren van het Responsgedrag van Bitumen, Bitumineuze Mastiek en Mortel

Proefschrift

ter verkrijging van de graad van doctor
aan de Technische Universiteit Delft,
op gezag van de Rector Magnificus prof.ir.K.C.A.M. Luyben,
voorzitter van het College voor Promoties,
in het openbaar te verdedigen op dinsdag 13 december 2011 om 10:00 uur

door

Milliyon Fekade WOLDEKIDAN

civiel ingenieur
geboren te Showa, Ethiopië

Dit proefschrift is goedgekeurd door de promotor:

Prof. dr. ir. A.A.A. Molenaar

Copromotor

Dr. ir. M. Hurman

Samenstelling promotiecommissie:

Rector Magnificus,	voorzitter
Prof. dr. ir. A.A.A. Molenaar,	Technische Universiteit Delft, promotor
Dr. ir. M. Hurman,	Technische Universiteit Delft, copromotor
Prof. dr. H. di Benedetto,	Ecole Nationale Des Travaux Publics De Le'Etat
Prof. G.D. Airey, BSc., MSc., PhD.,	University of Nottingham
Prof. dr. ir. J.G. Rots,	Technische Universiteit Delft
Prof. dr. ir. K. van Breugel,	Technische Universiteit Delft
Dr. L.T. Mo,	Wuhan University of Technology
Prof. ir. A.Q.C. van der Horst,	Technische Universiteit Delft, reserve lid

Published and distributed by:

M.F. Woldekidan

E-mail: M.F.Woldekidan@tudelft.nl; milliyon@gmail.com

Section of Road and Railway Engineering
Faculty of Civil Engineering and Geosciences
Delft University of Technology
P.O.Box 5048
2600 GA Delft
The Netherlands

ISBN 978-90-8570-762-2

Printing: Wohrmann Print Service, Zutphen (The Netherlands)

© 2011 Milliyon Fekade Woldekidan

All rights reserved. No part of the material protected by this copyright notice may be reproduced or utilized in any form or by any means, electronic or mechanical, including photocopying, recording or by any information storage and retrieval system, without written consent from the publisher.

I dedicate this dissertation to my parents.

Acknowledgements

The research presented in this dissertation was conducted at and funded by the Road and Railway Engineering section of the Faculty of Civil Engineering and Geosciences at the Delft University of Technology (TUD). The author would like to thank the section for the financial support.

I have greatly benefited from the support of a number of people. First of all I would like to thank Prof. dr. ir. A.A.A. Molenaar both for giving me the opportunity to pursue my PhD at the TUD and for his overall guidance and critical review of the research output at various stages. His ideas, constructive criticism and suggestions, from the very beginning to the completion of the research, were invaluable. His follow-up on the writing phase and careful review of the final manuscript are also highly appreciated.

I owe a bottomless debt of thanks to my daily supervisor, Assoc.Prof.dr.ir. M. Huurman. The knowledge I acquired from him while working on the LOT project as well as on this project was immense. His dedicated supervision and detail-level involvement have played a central role in the completion of this work. I consider myself very fortunate for being able to work with him.

I acknowledge with profound gratitude and sincerity the contribution of ir. A.C. Pronk. I have incorporated a range of excellent comments from him on the final manuscript. I have also greatly benefitted from his ideas and suggestions on the modelling work. Especially, the numerical formulations for the parabolic dashpot elements would not have been possible without the eye-opening introduction that he gave me on the topic of fractional derivatives.

An enormous amount of gratitude is also due to the staff of Road and Railway Engineering. First, my sincere gratitude goes to Assoc. Prof. ir. Martin van de Ven for his help and support whenever needed. His help and contribution in the literature review phase was very valuable. I am also grateful to Jan Moraal, Jan-Willem Bientjes, Marco Poot, and Jacqueline Barnhoorn. They all have, in various ways, provided valuable help and support. The support from Ing. W. Verwaal in performing CT scans on mixtures, for part of the work that is not included in this dissertation, is greatly appreciated. Words of thanks are also extended to my PhD colleagues; Yue, Minglian, Mairer, Pungky, Sadegh, Diederik, Ning, Dongxing, Xin, Nico, Gang, Marija, Mohamad, Jian and Wim van den Bergh for making my stay at the TU very pleasant. Especial thanks goes to Yue, Gang, Diederik and Jian for the help they provided, one way or another, in carrying out the experimental work.

Other past and present staff members that I have had the pleasure to work with or alongside are Oscar, Radjan, Abdol Miradi, Sonja van de Bos, Mo and Dirk Doedens. I especially would like to thank the LOT team; Mo, Radjan and Jan Moraal with whom I had spent very exciting period working as a team on the LOT project. They were all excellent team players.

I would like to thank my Ethiopian friends; Solomon Seyoum, Solomon Zegeye, Anteneh, Alemgena, Eyassu, Girum and Kassahun who made my stay in the Netherlands even more enjoyable.

Finally, my special gratitude goes to my wife, Mahilet Yilma, for her love, understanding and unwavering belief she has in me. Her support and encouragement, even when she was overwhelmingly busy on her study, had been nothing short of fantastic. I wish also to thank my family, especially my parents, for their endless love and support. My parents have thought me the importance of education and hard work, and as such have left an indelible mark on my career. This dissertation is dedicated to them.

Summary

This research focuses on testing and modelling the viscoelastic response of bituminous binders. The main goal is to find an appropriate response model for bituminous binders. The desired model should allow implementation into numerical environments such as ABAQUS. On the basis of such numerical environment, Delft University of Technology (TU) is developing mechanistic asphalt mixture design tools. These tools are based on Meso scale mechanics. For Porous Asphalt (PA) performance, such a tool is readily available in ABAQUS. Implementation of an accurate viscoelastic response model for bituminous mortar will improve the tool's capability in explaining PA performance at various temperatures and it is therefore a primary goal of this research. In addition the response model is also thought to be of equal importance for other meso mechanics tools for asphalt concrete mixtures that will be developed in the near future.

To realise the main objective of the study, first an extensive Dynamic Shear Rheometer (DSR) testing program was carried out on bituminous binder, mastic and mortar. The program was carried out to get a better understanding of the response behaviour of binders for various loading conditions. For the pure binder and mastic testing, a cone and plate setup was developed. For the mortar testing, a specially designed mortar column setup was utilized. The frequency and time domain response of the binders was first analysed in the linear viscoelastic range. Hereafter the frequency domain response of the binders beyond the linear range response was investigated. The results showed that binders exhibit nonlinear behaviour at higher levels of shear stress. At relatively high temperatures, in the range of 30°C and above, mortar and mastic show nonlinear behaviour at shear stresses as low as 10 kPa. At low temperatures of 0°C and below, high shear stresses in the range of 1 MPa were observed to cause nonlinear behaviour.

The second part of the study covers extensive modelling work. After a literature survey, two response models were first selected as a basis for further research; i.e. the Huet-Sayegh (HS) and the Burgers' model. These models were then utilised to describe the frequency domain response data. It was observed that the Burgers' model requires a number of Kelvin-Voigt elements to accurately describe experimental data. The HS model on the other hand presented an accurate description of response data. However, the HS model lacks the capability of explaining viscous deformation. For this reason the HS model was extended by adding a linear dashpot in series. The modified Huet-Sayegh (MHS) and the generalized Burgers' model were then used to describe the frequency domain response of various materials. Results have shown that the

MHS description of the response data excels that of the generalized Burgers' model.

For time domain use in numerical environments, incremental formulations of the response models were obtained. The formulations were coded and the numerical outputs were then validated by performing various simulations. The formulations were used to simulate time domain response tests. In this process parameter determination was first performed on the basis of frequency domain data. The parameters were then used to simulate time domain creep and relaxation tests. The simulation results showed that the frequency domain master curve data provided accurate material information for simulating the time domain response. The result further underlines the fact that binder's behaviour is intrinsic, and as such their behaviour in frequency and time domain is related. It is this intrinsic behaviour of the binders that was described by the generalized Burgers' and the MHS models.

Hereafter the models were finally implemented into ABAQUS, and they are made available for use in the meso mechanics PA design tool. The results from the PA design tool showed that both models lead to comparable results. The pros and cons of the models for practical application were evaluated. For relatively small numerical models, the MHS model is suggested because of its simplicity in the number of model parameters and its high accuracy in describing material response. However, for computationally intensive numerical models, the use of the generalized Burgers' model is suggested because of its high computational efficiency in numerical environments.

Finally, the nonlinear response of binders was analyzed using Schapery's nonlinear theory. Numerical formulation of the theory that incorporates the generalized Burgers' model was adopted. The formulation was coded into a User Subroutine Material code (UMAT) for use in ABAQUS. In the UMAT code an iterative scheme for obtaining correct stress state was incorporated at the material level. Results from the code were verified by performing various simulations. Application of the Schapery's nonlinear theory in the PA design tool showed that the effects of nonlinear behaviour are negligible at temperatures of 10°C and below. However, at 20°C and above, distinct and significant differences between linear and nonlinear simulations are observed. From the results it is concluded that common binders may be modelled as being linear viscoelastic for temperatures of 10°C and below. At 20°C and above nonlinear response becomes significant and, it needs to be considered in meso mechanistic computations.

Samenvatting

Dit onderzoek concentreert zich op het meten en modelleren van de visco-elastische respons van bitumineuze bindmiddelen. Het doel is de ontwikkeling van een bruikbaar respons model voor bitumineuze bindmiddelen. Dit model moet geschikt zijn voor implementatie in numerieke analyse systemen als ABAQUS. Op basis van dergelijke numerieke systemen ontwikkelt de Technische Universiteit Delft (TUD) een mechanistisch mengselontwerp instrument op meso schaal. Voor het ontwerp van Zeer Open Asfalt Beton, ZOAB, is zo'n instrument beschikbaar in ABAQUS. Implementatie van een nauwkeurig visco-elastisch respons model voor mastiek zal de mogelijkheden voor het verklaren van ZOAB-gedrag bij verschillende temperaturen vergroten en is daarom een tweede hoofddoel van dit onderzoek. Bovendien is de verwachting dat een nauwkeurig visco-elastisch respons model voor bindmiddelen ook van belang is voor andere mechanistische mengselontwerp methodieken op meso schaal die in de toekomst zullen worden ontwikkeld.

Om het hoofddoel te bereiken is begonnen met een uitgebreid onderzoeksprogramma op bitumineuze bindmiddelen met de Dynamic Shear Rheometer (DSR). Het doel van dit programma was om beter inzicht te krijgen in het respons gedrag van bindmiddelen bij verschillende lastcondities. Voor het testen van puur bitumen en mortel is een *Cone & Plate* geometrie ontwikkeld. Voor het testen van mastiek is gebruik gemaakt van speciaal ontworpen proefstukjes in de vorm van mastiekkolommetjes. Eerst is de lineaire visco-elastische respons van bindmiddelen in het frequentie- en tijdsdomein geanalyseerd. Daarna is, in het frequentiedomein, de respons buiten de lineair elastische range onderzocht. De resultaten maakten duidelijk dat bindmiddelen niet lineair gedrag vertonen bij hogere schuifspanningniveaus. Bij relatief hoge temperaturen, 30°C en daarboven, vertonen mastiek en mortel niet lineair gedrag bij lage spanningen van 10 kPa. Bij lage temperaturen van 0°C en lager, zijn schuifspanningen in de orde van 1 MPa nodig om niet lineair gedrag te veroorzaken.

Het tweede deel van de studie behelst omvangrijk modelleringwerk. Na een literatuurstudie zijn twee responsmodellen geselecteerd voor verder gebruik in deze studie, het Huet-Sayegh (HS) en het Burgers' model. Beide modellen zijn eerst gebruikt om frequentiedomein data te beschrijven. Gebleken is dat het gegeneraliseerde Burgers' model meerdere Kelvin-Voigt elementen moet bevatten om de laboratorium data nauwkeurig te beschrijven. Het HS model laat een nauwkeurige beschrijving van laboratorium data zien. Maar helaas kan het HS de ontwikkeling van viskeuze vervorming niet beschrijven. Hierom is het HS model uitgebreid met een lineaire viskeuze demper in serie. Het aangepaste Huet-Sayegh model (MHS) en het gegeneraliseerde Burgers'

model zijn hierna gebruikt om de frequentiedomein data van diverse materialen te beschrijven. De resultaten tonen dat het MHS model de data beter beschrijft dan het gegeneraliseerd Burgers' model.

Voor numerieke simulaties in het tijdsdomein zijn de responsmodellen incrementeel geformuleerd. De incrementele formulering in het tijdsdomein is gevalideerd met verschillende numerieke simulaties. Hierna zijn diverse tijddomein respons tests gesimuleerd. Hierbij zijn tijdsdomein kruip en relaxatie tests gesimuleerd op basis van responsparameters die bepaald zijn uit frequentiedomein data. De resultaten van dit werk geven aan dat frequentiedomein *master curve* data een nauwkeurig inzicht geven in het tijdsdomein respons gedrag. De resultaten onderstrepen het feit dat bindmiddelen een intrinsiek gedrag kennen en dat hun gedrag in frequentie- en tijdsdomein dus gerelateerd is. Het intrinsieke gedrag van bindmiddelen wordt beschreven door zowel het gegeneraliseerde Burgers' model en het MHS model.

Hierna zijn de modellen geïmplementeerd in ABAQUS en gebruikt in een mechanistisch ZOAB ontwerp instrument op meso schaal. De resultaten van het ontwerpinstrument tonen dat de modellen vergelijkbare resultaten geven. De voor- en nadelen van de modellen voor praktisch gebruik zijn bekeken. Voor relatief kleine numerieke modellen wordt het MHS geadviseerd omdat dit model met een beperkt aantal parameters een zeer nauwkeurige beschrijving van het respons gedrag geeft. Voor modellen die meer rekenkracht vragen wordt het gegeneraliseerde Burgers' model geadviseerd omdat dit model rekenkundig zeer efficiënt is.

Als laatste is het niet lineaire respons gedrag van bindmidden geanalyseerd met behulp van Schapery's theorie. Bij de numerieke formulering van deze theorie is gebruik gemaakt van het gegeneraliseerde Burgers' model. Op basis van de formulering is een *User Subroutine Material* code (UMAT) voor gebruik in ABAQUS geschreven. De UMAT code bevat een iteratie proces voor het verkrijgen van de juiste spanningssituatie. De UMAT code is met diverse simulaties geverifieerd. Toepassing van het niet lineaire gegeneraliseerde Burgers' model in het ZOAB ontwerp instrument toont dat de effecten van niet lineair gedrag verwaarloosbaar zijn bij temperaturen van 10°C en lager. Bij temperaturen van 20°C en hoger worden duidelijk verschillen tussen lineaire en niet lineaire simulaties gevonden. De resultaten geven aan dat reguliere bindmiddelen lineair visco-elastisch gemodelleerd kunnen worden bij temperaturen van 10°C en lager. Bij 20°C en hoger wordt de niet-lineaire respons van belang in mechanistische mengselontwerp methodieken op meso schaal.

TABLE OF CONTENTS

1	INTRODUCTION.....	1
1.1	CAUSES OF TOP-LAYER DISTRESSES.....	2
1.1.1	<i>Ravelling</i>	2
1.1.2	<i>Rutting</i>	4
1.1.3	<i>Surface Cracking</i>	5
1.2	DESIGN METHODS.....	5
1.2.1	<i>Design Methods for Pavements</i>	5
1.2.2	<i>Approaches for Addressing Top-Layer Distresses</i>	6
1.3	OBJECTIVES AND SCOPE OF THE RESEARCH.....	8
1.4	ORGANIZATION OF THE DISSERTATION.....	10
	REFERENCES.....	11
2	LITERATURE REVIEW.....	13
2.1	MESO MECHANICS DEFINITION.....	13
2.2	MESO MECHANICS APPROACH.....	14
2.2.1	<i>Early Developments in AC Modelling</i>	15
2.2.2	<i>Recent Developments in AC Modelling</i>	17
2.2.3	<i>Summary on Meso Mechanical Models</i>	21
2.3	MODELLING TIME DEPENDENT MATERIAL BEHAVIOUR.....	21
2.3.1	<i>Introduction</i>	21
2.3.2	<i>Modelling Linear Viscoelastic Materials</i>	22
2.3.3	<i>Modelling Nonlinear Viscoelastic Materials</i>	46
2.4	SUMMARY.....	51
2.4.1	<i>Meso Mechanics</i>	51
2.4.2	<i>Response Models</i>	51
	REFERENCES.....	52
3	RESEARCH METHODOLOGY.....	55
3.1	RESEARCH APPROACH.....	56
3.1.1	<i>Setting the Demands</i>	56
3.1.2	<i>Selected Response Models</i>	57
3.1.3	<i>Schapery's Nonlinear Theory</i>	59
3.2	METHODOLOGY.....	59
3.2.1	<i>Experimental Work</i>	60
3.2.2	<i>Modelling Work</i>	61
	REFERENCES.....	63
4	MATERIALS, EXPERIMENTS AND RESULTS.....	65
4.1	MATERIALS.....	65
4.1.1	<i>Bitumen</i>	65
4.1.2	<i>Mastic</i>	66

4.1.3	<i>Mortar</i>	66
4.2	EXPERIMENTAL SETUPS AND DESCRIPTIONS	67
4.2.1	<i>Setting the Framework</i>	67
4.2.2	<i>The Dynamic Shear Rheometer</i>	68
4.3	EXPERIMENTS AND RESULTS	83
4.3.1	<i>Experimental Plan</i>	83
4.3.2	<i>Bitumen and Mastic Response at Low Stress Levels</i>	84
4.3.3	<i>Bitumen and Mastic Response at High Stress Levels</i>	90
4.3.4	<i>Mortar Response at Low Stress Levels</i>	111
4.3.5	<i>Mortar Response at High Stress Levels</i>	115
4.4	CONCLUSIONS	123
4.4.1	<i>Experimental Setups</i>	123
4.4.2	<i>Test Results</i>	124
4.4.3	<i>Implications</i>	125
	REFERENCES	125
5	MODELLING LINEAR VISCOELASTIC RESPONSE OF BINDERS	127
5.1	RESPONSE OF BITUMINOUS MATERIALS	127
5.2	THE HUET-SAYEGH (HS) MODEL	128
5.2.1	<i>The Model Behaviour in Frequency Domain</i>	128
5.2.2	<i>Viscous Response Element</i>	130
5.3	A MODIFIED HS MODEL (MHS)	130
5.3.1	<i>The Model in Frequency Domain</i>	131
5.3.2	<i>The Model in Time Domain</i>	138
5.3.3	<i>Frequency vs. Time Domain Response</i>	145
5.4	THE BURGERS' MODEL	154
5.4.1	<i>The Model in Frequency Domain</i>	155
5.4.2	<i>The Model in Time Domain</i>	164
5.4.3	<i>Frequency vs. Time Domain Response</i>	168
5.5	SUMMARY OF FINDINGS	172
5.5.1	<i>The MHS model</i>	172
5.5.2	<i>The Generalized Burgers' Model</i>	172
5.5.3	<i>Frequency and Time Domain Responses</i>	173
5.5.4	<i>Choice of Models</i>	174
	REFERENCES	175
6	MODELLING NONLINEAR VISCOELASTIC RESPONSE OF BINDERS	177
6.1	SCHAPERY'S NONLINEAR THEORY	177
6.2	METHODS OF PARAMETER DETERMINATION	178
6.2.1	<i>Parameters From Frequency Domain Response Data</i>	181
6.3	MODEL PARAMETERS FOR THE BINDERS	182
6.3.1	<i>Results and Discussions</i>	187
6.4	NUMERICAL FORMULATION	190

6.4.1	<i>One Dimensional Formulation</i>	190
6.5	SUMMARY OF FINDINGS	193
	REFERENCES.....	194
7	IMPLEMENTATION INTO ABAQUS.....	195
7.1	CONSTITUTIVE LAW IN 3D	195
7.1.1	<i>General</i>	195
7.1.2	<i>Shear and Volumetric Deformation Characteristics of Asphaltic Materials</i> 197	
7.2	MHS MODEL IN 3D.....	197
7.2.1	<i>FE Implementation</i>	200
7.2.2	<i>Requirement for the UMAT</i>	200
7.2.3	<i>UMAT Verification Runs</i>	201
7.2.4	<i>Application in Meso Mechanistic PA Design Tool</i>	205
7.3	GENERALIZED BURGERS' MODEL IN 3D	211
7.3.1	<i>Requirement for the UMAT</i>	212
7.3.2	<i>UMAT Verification Runs</i>	213
7.3.3	<i>Application in Meso Mechanistic PA Design Tool</i>	213
7.4	NONLINEAR VISCOELASTIC MODEL IN 3D	217
7.4.1	<i>Schapery Theory in 3D</i>	217
7.4.2	<i>UMAT Runs</i>	220
7.4.3	<i>Effect of Nonlinearity on Data Interpretation Techniques</i>	223
7.4.4	<i>Nonlinear Simulations with the PA Design Tool</i>	225
7.5	SUMMARY OF FINDINGS AND REMARKS	231
7.5.1	<i>The MHS Model</i>	231
7.5.2	<i>The Generalized Burgers' Model</i>	231
7.5.3	<i>The Schapery Nonlinear Theory</i>	231
	REFERENCES.....	232
8	CONCLUSIONS AND RECOMMENDATIONS.....	233
8.1	GENERAL CONCLUSIONS AND RECOMMENDATIONS.....	233
8.1.1	<i>General Conclusions</i>	233
8.1.2	<i>General Recommendations</i>	235
8.2	SPECIFIC CONCLUSIONS AND RECOMMENDATIONS.....	235
8.2.1	<i>Related to Experimental Work</i>	235
8.2.2	<i>Related to Modelling Linear Viscoelastic Response of Binders</i>	236
8.2.3	<i>Related to Modelling Nonlinear Viscoelastic Response of Binders</i>	236
8.2.4	<i>Related to FE Implementation</i>	237
	APPENDIXES.....	239

USED ACRONYMS/ABBREVIATIONS

ABAQUS	A finite element package
AC	Asphalt Concrete
AR200ex	A Dynamic Shear Rheometer
CA	Christensen-Anderson model
CP	Cone and Plate setup
CT scan	Computer Tomography scan
DAC	Dense Asphalt Concrete
DBN	Di Benedetto-Neifar model
DEM	Discrete Element Modelling
DER	Dissipated Energy Ratio
DSR	Dynamic Shear Rheometer
FE	Finite Element modelling
ETC	Environmental Test Chamber
FORTRAN	A programming language
GUI	Graphic User Interface
HS	Huet-Sayegh model
LOT	Life time Optimization Tool for porous asphalt concrete
LVE	Linear Viscoelastic
Mastic	Mix of bitumen and filler
MATLAB	A programming language for scientific and engineering
MDEM	Micro-fabric Discrete Element Modelling
MHS	Modified Huet-Sayegh model
Mortar	Bitumen+sand fraction+ filler
PA	Porous Asphalt concrete
Pen	Penetration test/value
PFC3D	Particle Flow Code, A discrete element programme
PP	Parallel Plate setup
RAW	Dutch standard specification for the civil engineering sector
TUD	Delft University of Technology
UMAT	User Material Subroutine
UV	Ultraviolet light
ViscoRoute	Multilayer pavement design program
VEROAD	Multilayer pavement design program
WLF	William-Landel-Ferry model
2S2P1D	2 Spring-2 Parabolic dashpot and 1 Linear dashpot model
2D	Two dimensional
3D	Three dimensional

1

Introduction

Roads play a vital role in promoting the social and economic wellbeing of a society. Transport of goods, people and services from one place to the other within reasonable cost and time is made possible with the availability of good roads. To ensure a good level of service for road users, it is important that road conditions are kept to a certain acceptable standard.

The ability of roads or pavements to deliver the required level of service is governed by the pavement service life. The pavement service life is determined in relation to its performance with respect to various distress types. The most common distress types observed in flexible pavements include, but are not limited to, permanent deformation, longitudinal unevenness, cracking, disintegration and wear. Figure 1-1 presents examples for the aforementioned distress types.



Figure 1-1 Rutting, disintegration and cracking in pavements [13, 16, 17]

Distresses have a significant effect on the pavement's ability to meet its functional and structural requirements. The functional requirements of a pavement include traffic safety, riding comfort and noise reduction. Whereas structural requirements involve bearing capacity, surface cracking, longitudinal and transversal evenness, roughness and texture [14]. On Dutch motorways, the most common types of distress that necessitate maintenance intervention are related to damage of the top layer. Disintegration (ravelling) is by far the most predominant type of distress observed in motorways. To a lesser extent, rutting, and cracking are also observed [4].

The challenge to road managers is, therefore, to keep the road networks to an acceptable standard such that the functional and structural requirements are met. Doing so requires regular pavement maintenance. On today's densely trafficked motorways however, frequent maintenance activity is not desired as it disrupts traffic flow, reduces network availability and causes undesired traffic congestion on road networks. To strike a balance between road quality and network availability; cost-effective, long-life and low-maintenance pavements are sought. This in turn demands application of innovative materials for pavements, and necessitates the use of improved pavement design methods. Relevant performance models should also be introduced to predict the required type and amount of maintenance needed to keep the pavements in an optimal condition.

1.1 Causes of Top-Layer Distresses

Generally pavement distresses are caused by deterioration of the pavement quality due to traffic and disintegration of the road building materials due to climatic conditions. Experience has shown that, due to a myriad of factors involved, finding the specific cause of a pavement distress is quite complex. Therefore, the main causes and influencing factors for selected top-layer distresses that are of prime importance in Dutch motorways are discussed hereafter.

1.1.1 Ravelling

Application of a Porous Asphalt (PA) layer as a wearing course on primary road networks in the Netherlands is mandatory for environmental reasons. In the majority of cases ravelling is by far the decisive factor for PA maintenance. Ravelling is the loss of stone from the road surface and is the result of individual surface stones losing their bond to the rest of the pavement surface. This loss of bond may occur in two modes; i.e. cohesive failure, where failure occurs within the bituminous mortar material, and adhesive failure, where failure occurs in the form of detachment at the stone-mortar interfacial zones (Figure 1-2). Ravelling can also occur as a result of aggregate crushing. However, this mode of failure is rarely observed and hence often considered not detrimental for the service life of PA.

To understand the mechanisms leading to ravelling, it is important that all the factors affecting the cohesive and adhesive performance characteristics of the materials are known. The main factors affecting the adhesive and cohesive performance characteristics of the materials in PA are the traffic loading, the environmental loading, mixture composition and the physiochemistry of the asphalt mixture.

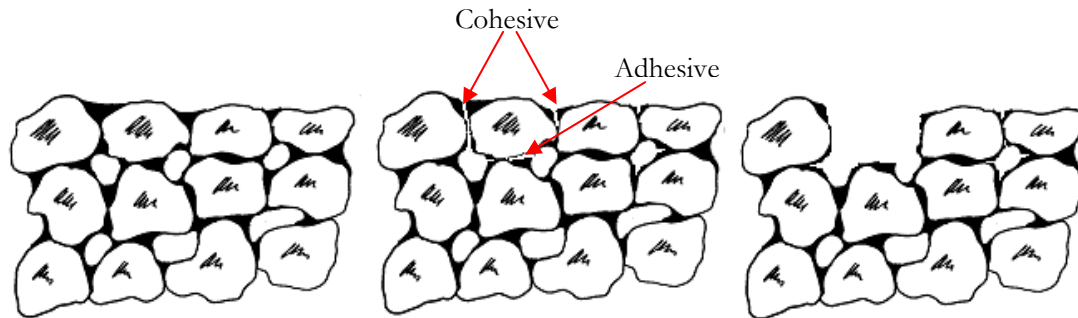


Figure 1-2 Schematic illustration of cohesive and adhesive failures [13]

Due to traffic loading, the pavement surface is subjected to signals of complex combinations of normal, shear and tangential contact-stress [3]. The traffic loading, combined with the presence of a high percentage of aggregates in PA layers (geometry effects), results in a wide range of stress signals in both the bituminous mortar and stone-mortar adhesive zones. Locally, in the mixture high stresses may develop; these stresses are potential causes for initiation of damage that ultimately leads to ravelling failure. Meso scale research on surface seals and PA layers have shown the development of a wide range of stresses in stone-to-stone contact areas within the bituminous mortar domain [7, 9, 19].

Due to the open structure of PA, the effect of the environmental loading is also severe. The high percentage of voids in the mixture allows oxygen, water and salt to penetrate easily into the surface layer resulting in deterioration of the cohesive and adhesive properties of the materials. The open structure of the material also makes it more vulnerable to ultra violet light and temperature changes. Combined, these climatic effects cause a change in material performance, i.e. aging. Research on the aging properties of asphalt materials showed the drastic effect of aging such that just within two years of service the binder in the PA mixture could behave brittle even for temperatures just above 0°C [5].

In addition to the mechanical and environmental loading, the chemical and physical characteristics of the aggregates, i.e. the texture, shape, angularity, size and mineralogical composition, influence the ravelling resistance of PA mixtures [18].

1.1.2 Rutting

The causes of rutting in Asphalt Concrete (AC) layers are well established nowadays. Rutting is caused by a combination of densification (volumetric change of the material), viscous flow and shear deformation, the later being the dominant behaviour causing permanent deformation [15]. Similar to ravelling; the rutting resistance of a mixture is a function of the mixture composition, material characteristics and loading conditions.

Literature has shown that linear elastic and linear viscoelastic representation of bituminous materials are not accurate enough for predicting permanent deformation characteristics of AC layers [11, 15]. It has also been shown that the load transfer mechanism within the mixtures is highly influenced by the mixture composition. The assumption that AC mixtures are homogeneous should, therefore, be improved to take the heterogeneous nature of the mixture into account [15].

Unlike the traditional assumption where the contact stress under a wheel is assumed to be uniform, literatures have shown the presence of a highly non-uniform contact stress distribution in the vertical, lateral and longitudinal direction [3]. Figure 1-3 illustrates the variation of the contact stress distribution under a wheel for the vertical, lateral and longitudinal directions. This non-uniform nature of the contact stress distribution needs to be considered for a proper analysis of top-layer distresses.

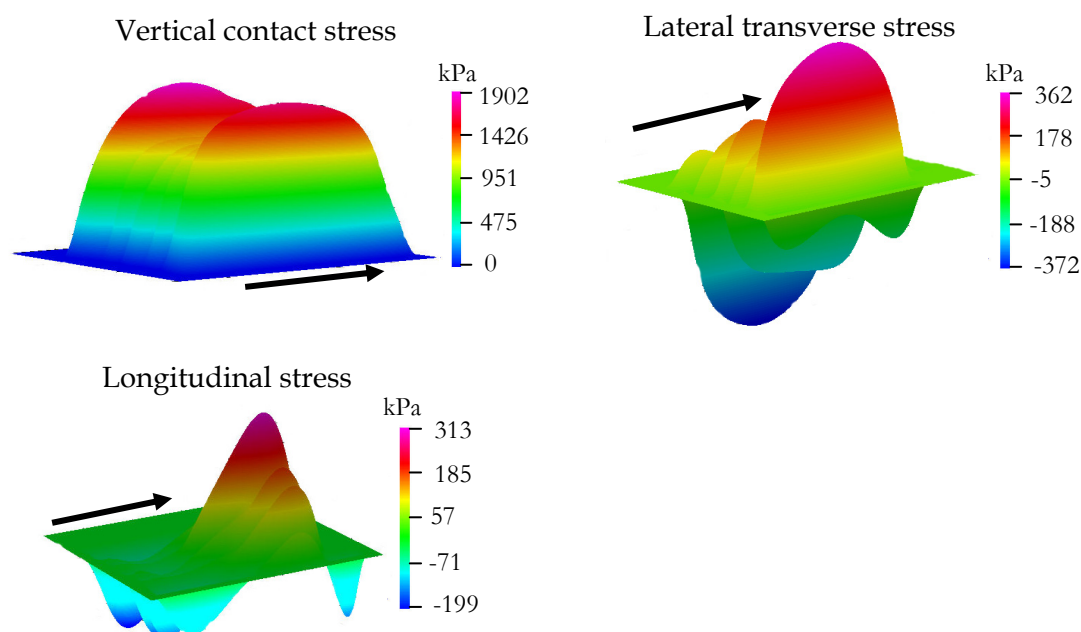


Figure 1-3 Contact stress distribution for a free-rolling truck tyre with 25 kN tyre load and 500 kPa tyre pressure, arrows indicate direction of travel [3]

1.1.3 Surface Cracking

Surface cracking in pavements occurs because of various reasons. It might be associated with traffic loading or with temperature fluctuations, i.e. thermal effects. At low temperatures the brittle behaviour of the binder due to aging in combination with traffic loading accelerates the development of surface cracking.

It is also possible that cracks initiated at the bottom of the asphalt layer propagate to the surface. However, these types of cracks are associated with structural performance of the pavement layers and are in a different category.

One of the major causes for traffic-related surface cracks is associated with the contact stress distribution. As illustrated in Figure 1-3, high lateral shear stresses are developed at the edge of the wheel. These stresses are the principal factor in causing surface cracking. In order to capture the crack initiation phenomenon, prediction of surface initiated cracks need to incorporate the non-uniform nature of the load distribution [20]. Other than the loading, the material behaviour in resisting crack initiation and propagation, and the geometrical (boundary) effects, such as narrow pavements that cause channelling of the traffic loads, determine the development of surface cracks in the pavement.

1.2 Design Methods

1.2.1 Design Methods for Pavements

Classical pavement design procedures involve both empirical and mechanistic methods. Methods used for mixture design are empirically based. For the structural pavement design, mechanistic methods, such as multi layer linear elastic programs, are widely used. Mixture design generally involves determination of the optimum binder content for a specific aggregate gradation. Depending on the mixture type, the mixture is then required to fulfil certain requirements; void content, Marshall stability and flow criteria. Recently, as of January 2008, the newly introduced CE marking rules as applied in the Netherlands set a stricter criterion to be met for asphalt mixtures. In this marking system the mixture properties such as fatigue performance, creep and stiffness have to meet certain standard.

Multi layer programs are basically used to design the pavement thickness based on structural responses, stresses and strains, which occur at the bottom of the pavement structure. In this process, these stress and strain values are matched with laboratory based performance criteria (such as fatigue and permanent deformation characteristics). The differences between the laboratory and field performances are adjusted with empirical correction factors that take into account effects of healing and lateral wander. For a given set of materials, the optimum design with respect to economy and performance is sought by

continuously changing the thickness of the layers till the pavement structural performance matches the specified performance criteria.

1.2.2 Approaches for Addressing Top-Layer Distresses

The approaches that need to be used for addressing top-layer distresses are fundamentally different from other approaches that are used for addressing structural problems. Structural design problems, like fatigue cracking, can be addressed with the classical pavement design methods. However, distresses observed at the top surface are not emanating from problems associated with thickness design. Surface distresses are more of a material design problem than a structural problem.

For example, at a meso scale, the ravelling performance of a PA layer is directly related to the performance of the constituent materials, i.e. stones, bituminous mortar and adhesive zones, to sustain the stresses and strains developed as a result of external loading. Under the effect of mechanical and environmental loading, failure in the constituent materials result in detachment of the aggregates particles. Ravelling can therefore be viewed as a mixture design problem. Similarly for rutting in AC layers, the rutting resistance of a mixture is highly influenced by the load transfer mechanism, which in turn is a function of the volumetric composition of the materials, i.e. aggregates and bituminous mortar. In addition the deformation characteristic of the constituent materials is also of prime importance.

The above discussion underlines the need for a mechanistic design approach that allows evaluation of component material performance at a localized level so as to predict localized distress at the pavement surface. With the three important components in focus, i.e. loading, material behaviour and geometry, the meso mechanics approach offers an ideal environment for addressing mixture design problems. In this regard, early attempts on application of meso mechanics models for evaluating the performance of road surfacing seals were made in early 2003 and promising results were obtained (see Figure 1-4). In recent developments, a meso mechanics based PA mixture performance design tool developed at Delft University of Technology has also delivered outstanding results in predicting mixture performance in terms of ravelling [6].

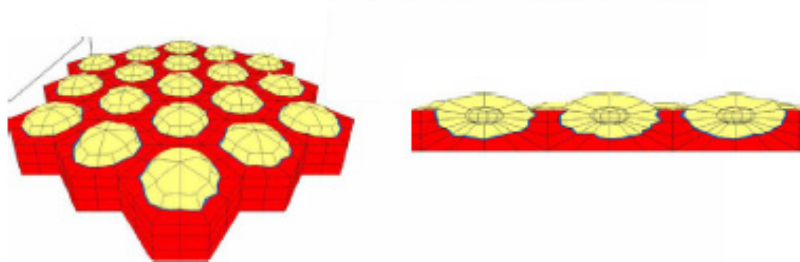


Figure 1-4 Prototype seal behaviour model, left: model overview, right: partial cross section [8]

1.2.2.1 Meso Mechanics for AC Mixture Design

Meso mechanics basically relies on the fundamental properties of the component materials that make up the AC mixture composite to predict the bulk behaviour of the mixture. This approach intrinsically allows a more realistic examination of the meso structural material response behaviour, such as stresses and strains in the component materials. It can therefore provide a powerful tool for optimizing the mixture design on the basis of given performance criteria. It has also the potential to eliminate costly tests to characterize asphalt concrete mixtures for the design and control purposes. This implies meso mechanics modelling has a tremendous potential benefits for AC mixture design.

To exploit the full merits of meso mechanistic approach a reasonable and accurate representation of the geometry, loading and material behaviour needs to be used. Other possible factors influencing the different pavement distress types, discussed qualitatively in the previous sections, can then be taken into account implicitly through their effect on these three major factors. Figure 1-5 illustrates how the various factors can implicitly be taken into account under the umbrella of a meso mechanics framework.

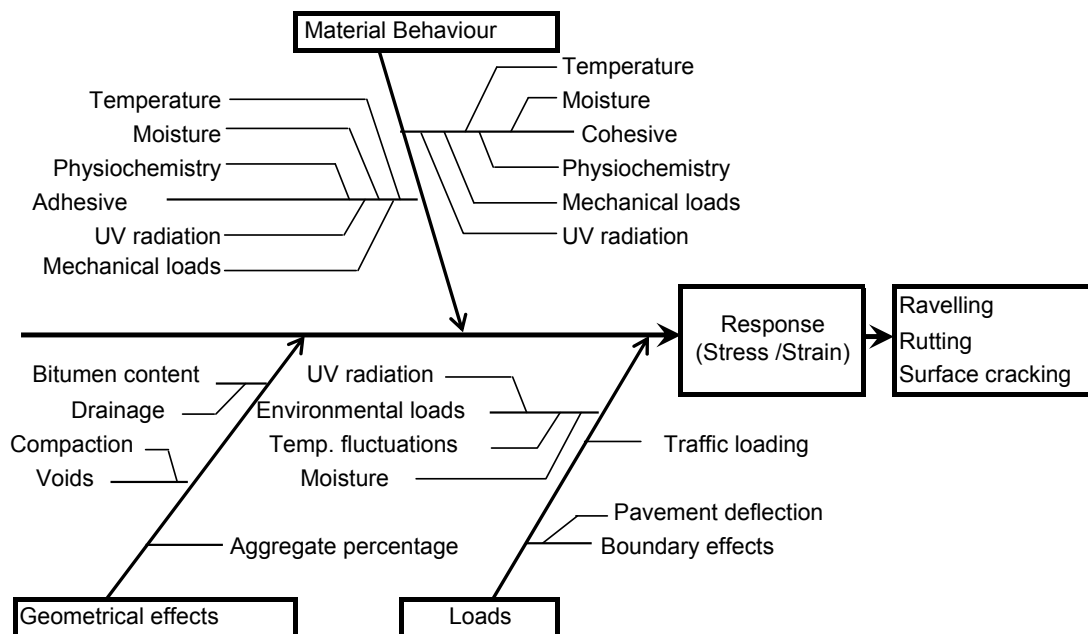


Figure 1-5 Cause and effect diagram for top-layer distresses (meso mechanics framework)

1.2.2.2 Material Response

In meso mechanics applications, it has been shown that fairly accurate representation of the meso structure can be obtained from the asphalt mixture geometry. For this purpose, X-ray computed tomography (CT scans) can be utilized. Accurate representation of the contact stress distribution under a wheel

is also available [3]. For material modelling, due to their simplicity, available linear elastic and viscoelastic models are often used. However, from literature it has, for example, been shown that linear viscoelastic assumption is not always good enough to predict pavement distresses. In this regard, an extensive finite element simulation that was made to investigate the rutting resistance of AC mixtures has shown that linear viscoelastic approximation underestimates the rutting development in AC mixtures [15]. For proper prediction, nonlinear viscoelastic and elasto-visco-plastic models were suggested. Investigation on bituminous binder's response also showed the existence of nonlinear behaviour [1, 2]. During development of the PA design tool, it has also been found that the mortar bridge in the stone-stone contact area in a PA mixture is subjected to complex states of stresses, which are varying both in time and space [10]. Relevant response models used for such computation need to be capable in describing the material response for a wide range of loading conditions, i.e. loading frequency and load levels.

The above discussion underlies the importance of appropriate material response models for better prediction results. It emphasizes the material modelling as the weakest link that hinder full utilization of the merits that meso mechanics methods have to offer. The main goal of this research focuses on bridging this gap. The primary goal is to provide a mortar response model that can be adopted in the current PA design tool. However, it is anticipated that the meso mechanical tools developed at the section of Road and Railway Engineering of the Delft University of Technology will be broadened in the near future. Focus will be on rutting, and fatigue cracking. This broadening demands for a highly accurate mortar response model. The results from this research can therefore be of equal importance for the meso mechanics tools that will be developed in the near future.

1.3 Objectives and Scope of the Research

The main goal of this research is to provide an appropriate material response model for use in the PA design tool [6]. This design tool is developed in the commercially available finite element program environment, ABAQUS. The tool is used to predict the life expectancy of PA. Basically, it translates the PA surface load, the mixture geometry and the response behaviour of the mortar into signals of stress and strain at various locations within the PA mixture. The stress and strain signals obtained in the mortar and adhesive zones at various locations within the mixture can then be translated into a lifetime expectancy using relevant damage models [12]. A short description of the PA design tool is attached in Appendix E.

At the current state the design tool utilizes a linear viscoelastic material model with Prony series representation for modelling the mortar behaviour. However, finite element simulations have shown that the stress signals resulting from moving tyre loads create complex 3D stress and strain signals, which differ

significantly from location to location, within the PA mixture. These results have various implications with regard to the response model for the mortar. It implies that the response model needs to incorporate the effects of the various states of stress to which the material is subjected. In other words the response model should reflect the material behaviour at various locations of the mixture as a function of local loading conditions, which may in turn differ both in magnitude and rate. The built-in material model in ABAQUS does not capture these response phenomena.

The above discussions emphasize the need to incorporate a relevant response model into the material library of ABAQUS. Hence this PhD research focuses on modelling bituminous mortar response. The research has two main parts; the first part involves a laboratory investigation of the response behaviour of selected materials. The second part involves numerical modelling and implementation work. For the laboratory work, test set-ups that were developed for mortar response testing during the development of the PA design tool project are used. A major part of the response investigation work is conducted in a stress controlled environment. The mortar response behaviour for various stress levels, frequencies and temperatures has been investigated. For the numerical modelling work, a couple of candidate response models from literature were selected. The selection was based on the models performance against a list of prescribed demands. For nonlinear material behaviour modelling, a suitable nonlinear theory has been selected. The selected response models are numerically implemented into the Abaqus environment through User Material Subroutines (UMAT). The material modelling work is integrated in the framework of the PA design tool as shown in bold arrows in Figure 1-6.

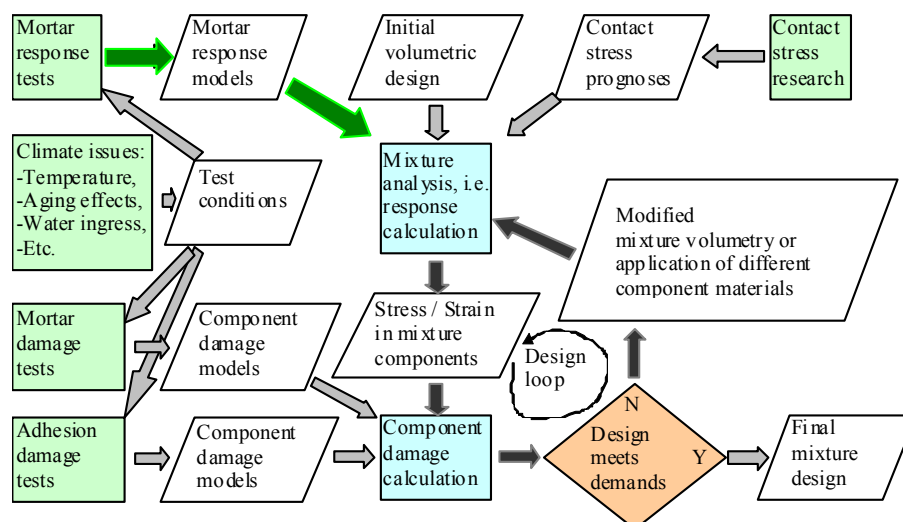


Figure 1-6 Research framework used for the PA design tool [6]

Once the material models were incorporated in the framework of the PA design tool, simulations were made to evaluate the effects of the response models on

the computed stresses and strains. Effects of the nonlinear material behaviour on the results obtained from the PA design tool were also evaluated.

1.4 Organization of the Dissertation

This thesis consists of eight chapters. Chapter 1 gives the general introduction on top-layer distresses in general and the raveling problem in particular. It outlines meso mechanics as a way forward to understand mixture related problems and defines the specific objective and scope of this research within a meso mechanics framework. It also states the importance of the geometry, material behaviour and loading in a meso mechanics problem and outlines the material modelling component as the main research topic.

Chapter 2, which is divided in two main parts, presents a literature review. The first part of the chapter presents recent and past developments in meso mechanics modelling approaches for asphalt concrete mixtures. The second part presents a review on the linear and nonlinear modelling approaches for material response with time dependent behaviour.

In Chapter 3, the research methodology is presented.

Details of the experimental work are presented in Chapter 4. Results of laboratory tests and interpretation techniques are also discussed.

In Chapter 5 the one dimensional constitutive modelling of linear viscoelastic materials is discussed. Methods of model parameter determination from laboratory results are presented. Pros and cons of the selected response models are discussed. Various numerical simulations that are performed to relate the time and frequency domain response of the materials are presented.

In Chapter 6, modelling of nonlinear viscoelastic materials is covered. Descriptions and numerical implementation techniques for the selected nonlinear theory are presented. Determination of nonlinear model parameters for binders is explained.

Chapter 7 presents the generalization of the one dimensional numerical formulations for the various models into 3D form. This is performed both for the linear and nonlinear viscoelastic models. The numerical formulations are incorporated into ABAQUS through User Material Subroutines (UMAT). Numerical outputs of the codes are thoroughly checked by performing various routine calculations. Application of the response models to the meso mechanistic PA design tool is presented. Using the 2D PA design tool, effects of nonlinear behaviour on the computed stresses and strains are evaluated.

Chapter 8 presents conclusions and recommendations.

References

- [1]. Airey, G., Rahimzadeh, B., and Collop, A., *Viscoelastic linearity limits for bituminous materials*. Materials and Structures, 2003. **36**(10): p. 643-647.
- [2]. Airey, G.D., Rahimzadeh, B., and Collop, A.C., *Linear Rheological Behavior of Bituminous Paving Materials*. Journal of Materials in Civil Engineering, 2004. **16**(3): p. 212-220.
- [3]. De Beer, M., Fisher, C., and Jooste, F.J. *Determination of Pneumatic/Pavement Interface Contact Stresses Under Moving Loads and Some Effects on Pavement with Thin Asphalt Surfacing Layers*. in *Proceedings of the Eighth International Conference Structural Design of Asphalt Pavements*. 1997. USA.
- [4]. Doorduyn, J. and Vos, L.A., *ZOAB; hoe lang gaat het mee(in Dutch)*. 1997, DWV: Delft.
- [5]. Hagos, E.T., *The Effect of Aging on Binder Properties of Porous Asphalt Concrete*. 2008, Delft.
- [6]. Huurman, M., *Lifetime Optimisation Tool, LOT, Main Report*. 2008: Delft.
- [7]. Huurman, M., Milne, T.I., and Van de Ven, M.F.C., *Development of a structural FEM for road surfacing seals*, in *ICCES*. 2003: Corfu, Greece.
- [8]. Huurman, M., Scarpas, T., Kasbergen, C., and T, M. *Development of a structural FEM for Road Surfacing Seals*. in *International Conference on Computational & Experimental Engineering & Sciences (ICCES' 03)*. 2003. Greece.
- [9]. Huurman, M., Mo, L., Woldekidan, M.F., Khedoe, R.N., and Moraal, J., *Overview of the LOT meso mechanical research into porous asphalt raveling*. Advanced Testing and Characterisation of Bituminous Materials, Vols 1 and 2, 2009: p. 507-518.
- [10]. Huurman, M., Mo, L., Woldekidan, M.F., Khedoe, R.N., and Moraal, J. *Overview of the LOT meso mechanical research into porous asphalt raveling*. in *Proceedings of the 7th Int. RILEM Symposium Advanced Testing and Characterization of Bituminous Materials*. 2009. Rhodes, Greece.
- [11]. Long, F.M., *Permanent Deformation of Asphalt Concrete Pavements; Development of nonlinear visco-elastic model for mix design and analysis*, in *Ninth International Conference on Asphalt Pavements*. 2002. p. 1:6-4.
- [12]. Mo, L., *Damage Development In The Adhesive Zone and Mortar of Porous Asphalt Concrete*. 2010, Delft.
- [13]. Molenaar, A.A.A., *Structural Pavement Design: Design of Flexible pavements*. 2007, Delft.
- [14]. Molenaar, J.M.M., *Performance related characterization of the mechanical behavior of asphalt mixtures*. 2004, Delft University of Technology: Delft.
- [15]. Muraya, P.M., *Permanent Deformation of Asphalt Mixtures*. 2007, Delft University of Technology: Delft.
- [16]. Pavement-Interactive.org. Available from: <http://pavementinteractive.org>.
- [17]. Rijkswaterstaat. Available from: <http://www.rijkswaterstaat.nl>.
- [18]. van Lent, D., Molenaar, A., and van de Ven, M.F.C., *The effect of specimen preparation techniques on the surface characteristics of aggregate*, in *TRB 2009, 88th Annual Meeting*. 2009: Washington DC, USA.
- [19]. Woldekidan, M.F., *Performance study of C-Fix in PAC using a 2D finite element model*. 2006, Delft University of Technology.

- [20]. Wu, H., Mahoney, J.P., Turkiyyah, L.M., Pierce, J., Uhlmeyer, J., and Mulvaney, R., *Non-uniform tire pressure effects on surface initiated cracks with EverFlex: a three dimensional FEA tool for flexible pavements*, in *9th International Conference on Asphalt Pavements*. 2002. p. 1:8-2.

2

Literature Review

In this chapter the results of a literature survey on topics that are relevant to the research project are presented. Since this project is one branch of a meso mechanics project for PA design, the first half of the literature review presents past and recent developments in meso mechanics studies. Special attention is given to meso mechanics applications in the field of asphalt concrete studies. The section that follows presents the fundamentals of time dependent material modelling. This is particularly important for modelling the bituminous mortar behaviour, which is the specific objective of this research.

2.1 Meso Mechanics Definition

Asphalt concrete is a composite material. For engineering analyses different idealizations are used to model its response behaviour. For example, in designing pavement layers using multilayer analysis programs the asphalt concrete layer is assumed to be an infinite, isotropic and homogeneous layer. This scale is referred as a macro scale.

For material characterization in the laboratory, asphalt concrete mixtures at bulk scale are used. Similar to the assumptions at the macro scale, laboratory performance of the asphalt concrete mixtures is approached based on a homogeneous mixture behaviour assumption.

In a meso scale analysis, the heterogeneous nature of the asphalt mixture is taken into account. At this scale, the constituent materials that make up the asphalt mixture, i.e. the binders and stones, are assigned different material properties. The interactions of these constituent materials dictate the bulk-scale response behaviour.

The micro scale goes one step further. It analyzes the heterogeneous nature of the constituent materials. Pictorial illustrations of the various scales, as used in this dissertation, are presented in Figure 2-1.

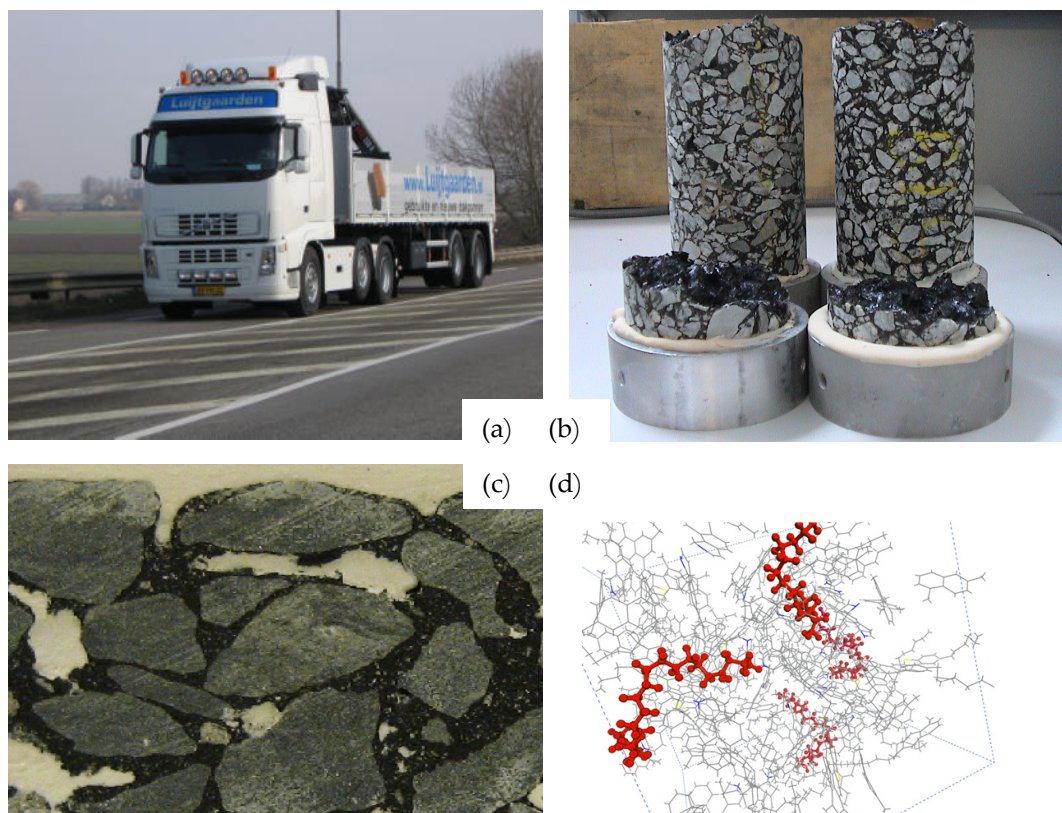


Figure 2-1 Asphalt concrete viewed at different scales (a) Macro scale, (b) Bulk scale, (c) Meso scale and (d) Micro scale

The PA design tool which was developed by Huurman et al. [20, 23] acts at the meso scale. It is, therefore, called a meso mechanics tool. This research also lies under the same category. Therefore, Meso mechanics in this research refers to the approach that is used to predict composite material properties based on the characteristics of the component materials. In literature, the same approach is sometimes referred as micromechanics. In this study, to avoid ambiguous use of terminologies, the term meso mechanics has consistently been used for studies that deal with the study of heterogeneous materials.

2.2 Meso Mechanics Approach

Meso mechanics is a mechanical analysis of composite or heterogeneous materials based on the properties of the individual constituents that make up the composite. One important goal of meso mechanics consists of predicting the response of a composite material without testing it in the laboratory. This contributes in reducing the number of expensive laboratory tests required to characterize a given composite material. The second important use of meso

mechanics is for analysis of localized effects. This includes evaluating local stresses and strains in the different constituent materials for a given loading at a macro scale. This is crucial to understand damage initiation and propagation in the materials that ultimately determine the performance characteristics of the materials.

Meso mechanics generally utilizes both Finite Element Methods (FEM) and Discrete Element Methods (DEM). While FEM is a continuum approach which is advantageous for describing quantitatively stress and strain distribution in asphalt mixtures, DEM is discrete in nature and is suitable for analyzing particulate systems by modelling the translational and rotational behaviour of individual particles according to Newton's second law. The latter has the ability to model complex and continuously changing contact geometries, which makes it very appropriate to model unbound granular materials [5, 46]. On the other hand, FEM is better suited for applications in material performance models. In such models, the ability of the materials to sustain repeated loads is predicted. For example, for determining the fatigue performance characteristics of bituminous mortar, the stresses and strains developed in the bituminous mortar are required. FEM approaches directly provide these parameters, and DEM do not.

2.2.1 Early Developments in AC Modelling

In the past two decades, the use of meso mechanics to predict the properties of asphalt mixtures has become increasingly popular. In the early 1990s, Rothenburg et al. [41] used a DEM approach to model the AC mixture response and understand the effect of aggregate interaction on the mixture response behaviour. In their model simple polygonal shapes were used to model the aggregate particles (Figure 2-2). Contact laws were defined for the interaction areas. Mechanical models comprising of springs and dashpots were utilized. The results pointed out the effect of the granular-materials interaction on the observed nonlinear trends in mechanical response of AC mixtures.

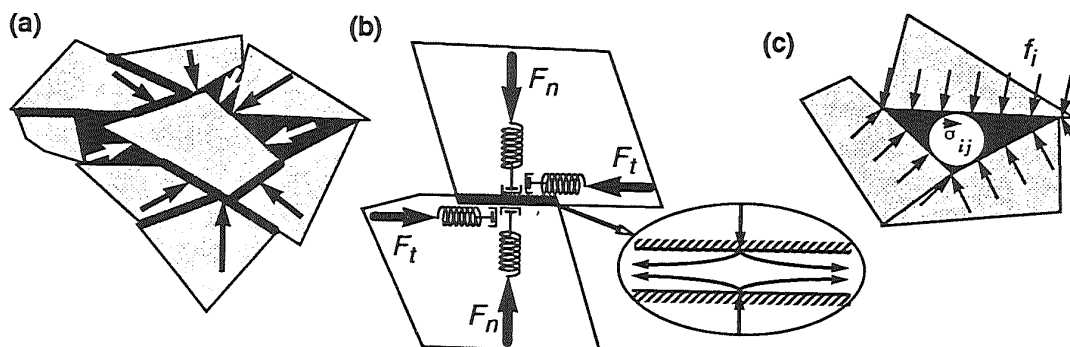


Figure 2-2 Forces Acting on Aggregate and Binder: (a) Forces Acting on Particles (b) Aggregate-Aggregate Interaction (c) Aggregate-Binder Interaction [41]

In a similar approach a more advanced three dimensional simulation of AC mixture response using DEM was made by Chang and Meegoda [8]. As shown

in Figure 2-3, their model contains cylindrical particles of different size connected by binder-aggregate and aggregate-aggregate contact points. To simulate viscoelastic behaviour of the bituminous binder, the contact was assigned viscoelastic behaviour. Kelvin-Voigt, Burgers' and Maxwell models were employed. This work showed that the AC mixture response was better captured when DEM is utilized.

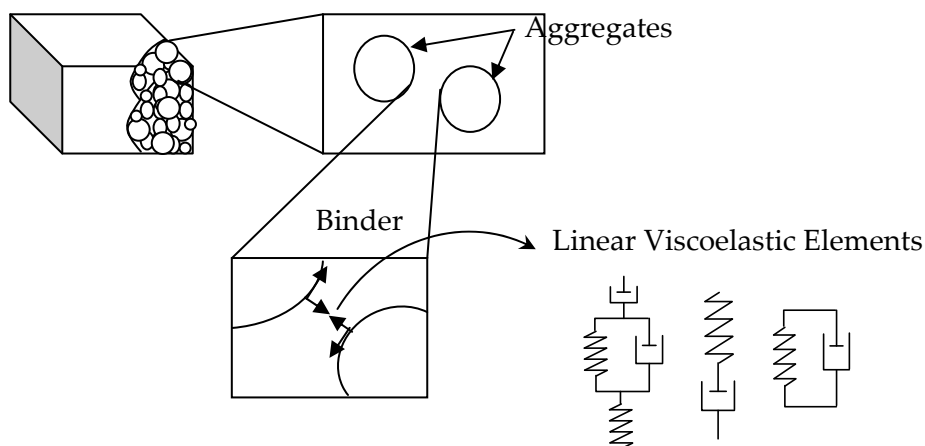


Figure 2-3 Three-Dimensional Simulation of AC Mixture using DEM [34]

FE investigation on the influence of the meso structural properties on the macro behaviour of pavement response was investigated by Sepehr et al. [44]. A multi layer pavement structure with an elastic and homogeneous sub-grade, sub-base and base layer properties was utilized. The top layer, AC, was modelled as a composite. The meso scale geometry of the AC layer was modelled by assigning different stiffness properties to the model elements. Air voids were simulated by assigning some elements low stiffness values. Various simulations were made, and the deflection of the pavement was studied. It was observed that increasing the air voids from 1% to 5% resulted in 1.2% increase in pavement surface deflection computed at the surface layer. It was also shown that reducing the binder stiffness from 1000 MPa to 250 MPa resulted in 2.25% increase in the deflection. Their analysis provided useful insights about the influence of the meso structural properties on the macroscopic behaviour of the pavement.

Bahia et al. [6, 29] used meso mechanics to analyze the behaviour of AC mixtures. At meso scale, the aggregate particles were idealized with a round geometry. Material properties were all assumed to be elastic. The study evaluated the range of strain magnitudes that occur in the binder domain for known strain levels applied at the mixture scale. From the simulation, a 1% strain applied at the mixture level resulted in strain magnitudes of up to 46% in the binder domain. This study highlighted the existence of high strain magnitudes at a meso scale within the AC mixture.

Huurman et al. [21] used meso mechanics to get insight into the performance characteristics of a surfacing seal (see Figure 2-4). Their model was used to obtain the structural response of the surface seal as a function of the applied load (mechanical and temperature), the structural geometry (grain size and shape, binder film thickness, embedment to the base) and the applied materials (properties of the binder and the base). The binder property was modelled with a visco-elasto-plastic model. Stone particles and the base layer were modelled linear elastically. Interface layers were introduced to model the adhesive characteristics. The applied loads included lateral, vertical and transversal loads. The results showed some interesting damage initiation phenomena in the materials. The study underlined the importance of meso mechanics for analyzing the performance of the seal layer in relation to stripping, permanent deformation and fatigue.

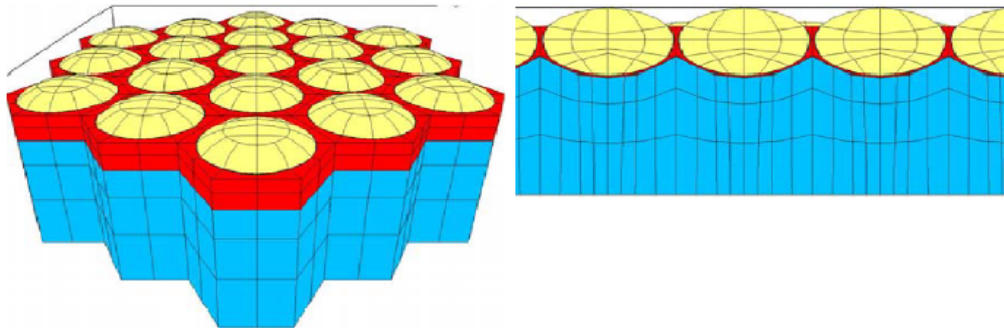


Figure 2-4 Surface seal models, Left: model overview, Right: partial cross section [21]

2.2.2 Recent Developments in AC Modelling

With the advancement in computational capacity of computers, meso mechanics application for asphalt concrete has seen a significant development in the last decade. Because of this reason a large amount of literature is available in this field. In this section a brief review of selected literature relevant to AC modelling is presented

Unlike the early stage developments in meso mechanics where meso scale geometry of the component materials were idealized, imaging technology now allows researchers to capture the meso scale geometry more accurately. Kose et al. [29] utilized this technology to capture the meso scale structure of AC mixtures. The study investigated the strain distribution within AC mixtures. With good representation of the meso scale geometry, they utilized finite element analysis to analyze the strain distribution within AC mixtures. Their work showed that the binder strain in the asphalt mixture could reach up to 250 times more than that suggested by the macroscopic strain of the mixture composite. Their study highlighted the importance of micro-mechanics and FE

analysis in providing information on the stress and strain distribution within the mixture structure.

In a similar category, Papagiannakis et al. [37, 49] studied the effect of meso scale image processing on predicted mixture behaviour. Their FE model used to simulate the dynamic response of AC mixtures showed promising results. Abbas et al. [1, 2] have also demonstrated application of imaging technologies to capture AC concrete mixture geometry. Based on uni-axial dynamic test results, their model predictions resulted in over prediction of dynamic modulus for mixtures with pen grade binder, and under prediction for mixtures made with modified binders.

Buttlar and You [7] simulated the behaviour of AC mixture in the indirect tension test using a Micro-fabric Discrete Element Modelling (MDEM). In this approach the various material phases, aggregates and mastics, were modelled as clusters of very small, discrete elements. Aggregates and mastics were modelled as being elastic. The results emphasized the importance of aggregate interaction in accurately simulating the stiffness of AC mixtures.

Wang et al. [47] utilized meso mechanics models to investigate top-down cracking in AC wearing courses. Their model prediction showed the possibility of top-down cracking to initiate at some distance down from the top surface. Similarly Sadd et al. [42] used meso mechanical model to investigate crack evolution under monotonic loading in the indirect tension test. In their FE model the asphalt meso structure was incorporated by replacing the aggregate-binder system with an equivalent finite element network that represents the load-carrying behaviour between aggregates in the material. Their results compared reasonably well with experimental data. Kim and Buttlar [28] also simulated crack initiation and propagation in AC using a disk-shaped compact tension test. The results demonstrated that fracture tests can be accurately modelled using DEM (see Figure 2-5).

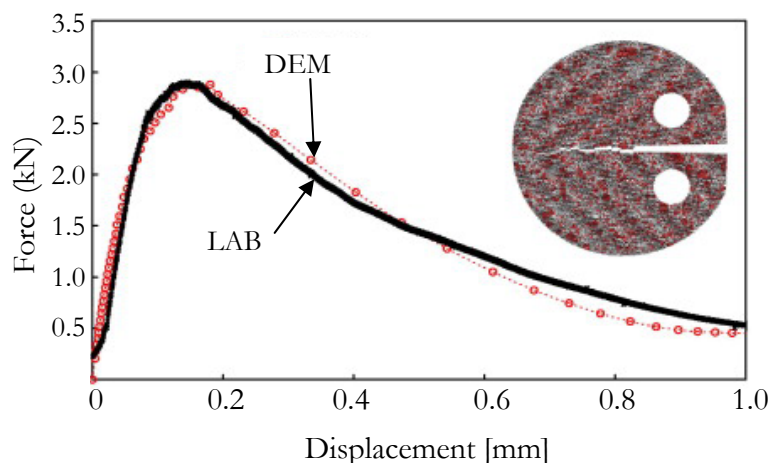


Figure 2-5 Cracking: comparison between numerical and experimental results [28]

Collop et al. [11] investigated the use of DEM to simulate the behaviour of a highly idealized bituminous mixture in a uni-axial compressive creep test. The mixture comprises 6,000 ideal single-sized spherical particles packed randomly. Normal and shear contact stiffness between the particles were defined. For this purpose a simple visco-elasto-plastic model was used. For the analysis, a DEM package called PFC3D was utilized. The simulation results revealed that with DEM it is possible to predict initial elastic, visco-elastic and visco-plastic behaviour of the bulk bituminous mixture.

Dai et al. [12-14] used meso mechanics to predict uni-axial creep test data. In the model, aggregates were modelled as rigid bodies. The binder was modelled as a linear viscoelastic material. In the image processing, each irregular shaped aggregate in the mixture is represented by an equivalent ellipse using a computer algorithm (Figure 2-6). Comparison of the simulated creep stiffness of the mixture with measured data revealed that the relative error between the model prediction and test data were about 11.7%. They concluded that the proposed micro-mechanical finite element model is applicable to predict the global viscoelastic behaviour of asphalt mixtures. In their latest works, Dai and You [13] improved the aggregate geometry which resulted in an improved prediction. Comparison of DEM and FEM simulation results were comparable. Similar works using DEM were also reported by Buttlar and You [12].

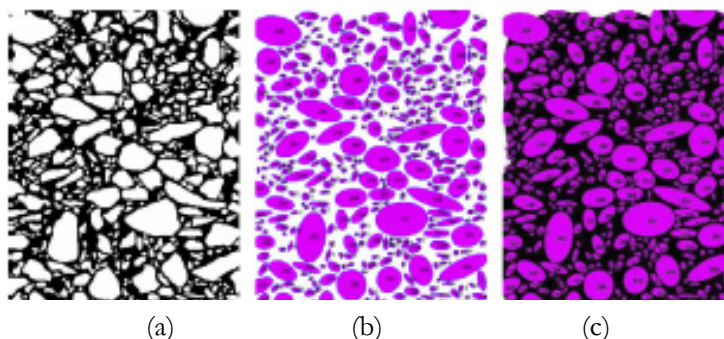


Figure 2-6 Uni-axial compression model [13]; (a) smooth surface of asphalt specimen, (b) elliptical fitted aggregates, (c) image model with aggregate and mastic

Kringos et al. [30] developed a micro-mechanical finite element model to simulate combined mechanical and moisture induced damage in asphalt concrete mixtures. The model assigns a hyper elastic material property to the stones and an elasto-visco-plastic material behaviour for the mastic that couples moisture and mechanical effects together. The model requires the absorption characteristics as well as the diffusion and the dispersion coefficients of the materials. It comprises an interface layer representing the stone-mastic adhesive zone. The model results have shown important mechanisms of moisture infiltration to asphalt concrete mixtures.

Huurman et al. [20, 22, 26, 35] used meso mechanics approach for evaluating the ravelling performance of PA layers. The work is an extension of the performance model developed earlier for surface seal layers [24]. The model translates a moving wheel load into stress and strain signals in the bituminous mortar and interface zones. In the development of the idealized 2D and 3D models, the aggregate geometry was simplified with a uniform grain size diameter (Figure 2-7). Equivalent aggregate sizes were determined based on the volumetric proportion of the asphalt mixture. In addition to the idealized models, the real shape of the aggregates was also modelled by using scan-images of PA mixtures. The model takes into account the clear distinction between the different phases, i.e. mortar, aggregate, interfacial zone and air voids. The wheel loading used in the simulation were rigorously derived from 3D contact stress distributions under a wheel. Illustration on the contact stress distribution under a wheel was shown in Chapter 1 (see Figure 1-3).

The models considered the aggregates as rigid bodies. The bituminous mortar was considered as viscoelastic material. Elastic normal and shear stiffness parameters were defined for the interface layer. By simulating a moving truck load, stresses and strains obtained in the cohesive and adhesive zone were translated into life time predictions. For this purpose, relevant damage models developed specifically for the cohesive and adhesive zone in the PA mixture were used. The results obtained from the simulation for various kinds of PA mixtures were validated with full scale tests. The performance ranking of the PA mixtures were consistent with the results obtained from the tests. The model application to a case study, where causes of a severe winter damage to a stretch of Dutch motorway with a PA surface layer was investigated, was also found to be in good agreement with actual observations.

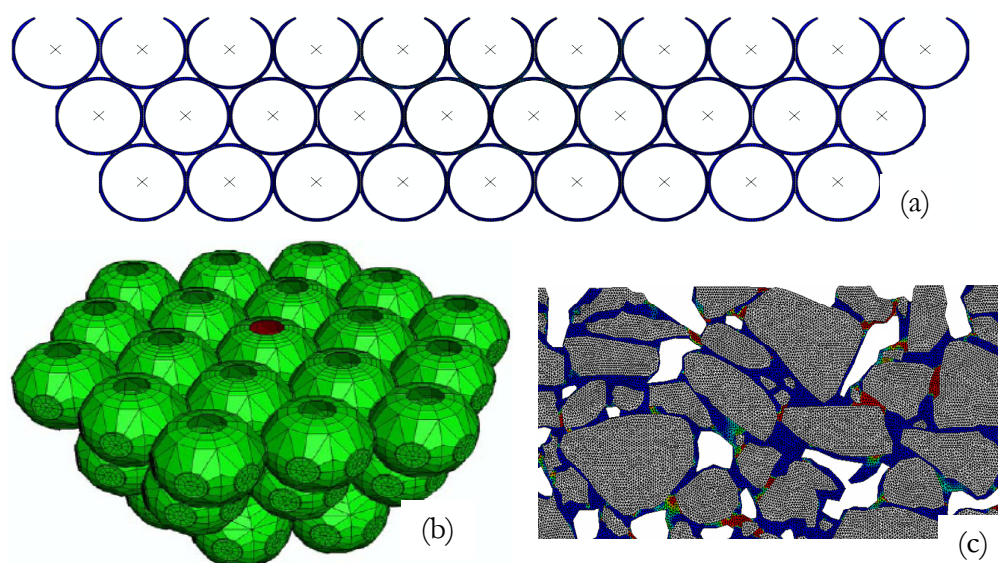


Figure 2-7 PA models: (a) idealised 2D (b) idealised 3D (c) 2D real [20, 25]

2.2.3 Summary on Meso Mechanical Models

Meso mechanical models directly consider the characteristics of the meso structure geometry, such as aggregate size, and nature, such as contact evolution, interlocking, and localization in modelling AC mixtures. They also explicitly provide information on the influence of changes in the meso structure on material response when the material undergoes deformation. This approach is valuable in relating meso structure properties to macroscopic response and thus is very powerful to understand constituent material contribution to a phenomenon observed at macro scale. The method consumes tremendous computing time; however, with the increasing computation power of computers the method is becoming more widely used.

2.2.3.1 FEM and DEM Approaches for AC Mixtures

Literature has shown that both FEM and DEM are used for modelling AC mixtures. For selected cases researchers have reported results obtained using both approaches are comparable [13]. In general, FEM, being a continuum approach, has a better ability to quantitatively describe the stress and strain distribution within an asphalt mixture than DEM. On the other hand, DEM has a great advantage to model large displacements, where existing contacts are lost and new ones are created during the deformation process. This phenomenon is quite common in granular materials. Because of this reason DEM is a preferred choice over FEM when modelling granular materials [5, 46].

2.2.3.2 Application to PA Mixture Design

The power of meso mechanics to provide insight on localized effects in different phases of composite materials makes the approach best suited to understand the ravelling failure phenomenon in PA. From the works of Huurman et al. [20, 22, 26, 35], very promising results were obtained using meso mechanics for PA performance modelling. To utilize the merits of this approach to the fullest, it is essential that correct material models for the constituents are used. Based on the first findings, it is likely that the binder in a PA mixture exhibits nonlinear properties due to the high stress and strain values. The different stress and strain signals obtained in the binder also indicated the presence of various loading rates in the material. These findings underlined the need to utilize appropriate response models that can describe the response of the binder for a wide range of loading magnitudes and rates in the meso mechanistic PA design tool.

2.3 Modelling Time Dependent Material Behaviour

2.3.1 Introduction

Analysis of mechanical problems using continuum mechanics follows certain physical laws. Mathematical expressions of the laws are required to analyze the

stresses and strains within a physical object having prescribed boundary conditions. The three most important formulas in continuum mechanics theory include the kinematic equation, equilibrium equation and constitutive equation. The kinematic equation relates displacements and deformations to strain within the body. The equilibrium equation deals with the force balance within the body. The constitutive relation defines the stress-strain relationship within the body. Irrespective of the material type, linear or nonlinear viscoelastic, the kinematic and equilibrium laws are common for all materials. The intrinsic mechanical response behaviour of a material is only reflected in the constitutive relation. As a result, theories in modelling the response of materials often refer to the stress-strain constitutive relation.

Bituminous materials exhibit a time dependent mechanical behaviour. In other words, they exhibit both viscous and elastic characteristics when undergoing deformation. The time dependent behaviour of bituminous materials is manifested through creep and relaxation. These phenomena are common to all time dependent materials. While the term creep represents an increasing deformation with time under a constant load, relaxation is the decrease in stress with time under a constant deformation. The time dependent behaviour implies the current stress within a material is influenced not only by the current strain but the complete strain history. Likewise the current strain is also influenced by the complete stress history. Because of this property, such materials in general are said to have a memory. Constitutive modelling of time dependent materials thus incorporates the time history effect in the stress-strain relationship.

Much work has been done on characterizing and modelling of time dependent materials in general. This section covers a literature survey on testing and modelling techniques applicable for time dependent materials in general and bituminous materials in particular. The first part begins with linear viscoelasticity and covers the fundamental approaches in modelling and laboratory testing methods. The most common rheological models used in modelling are also covered. Then reviews of the most widely used nonlinear theories are given. Suitability of the available viscoelastic models for the PA design tool is evaluated.

2.3.2 Modelling Linear Viscoelastic Materials

2.3.2.1 Linear Viscoelasticity

When a linear elastic material is loaded it results in an instantaneous deformation which increases linearly with a linear increasing load. The deformation remains as long as the load is maintained, and it recovers back to its original position once the load is removed. Since the applied stress for an elastic material is directly proportional to the resulting strain, obeying Hooke's law, the material is said to be linear elastic; otherwise it is called nonlinear.

On the other hand, when a constant applied stress to a material results in a continuous and constant rate of strain the material is referred as viscous. When the load is removed the deformation remains permanent. Thus if the applied stress and the resulting strain rate obeys Newton's viscosity law, $\sigma = \eta \dot{\epsilon}$, the viscous material is called linear; otherwise it is called nonlinear.

A viscoelastic material possesses characteristics of both elastic and viscous materials and, as such, exhibits time dependent strain behaviour, which is commonly referred to as creep. When a constant stress, σ_0 , is applied on a viscoelastic material, an instantaneous strain response, ϵ_0 , is observed. It is then followed by a continuously increasing strain. At the beginning, the strain rate follows a decreasing trend. If the load is kept constant for a longer duration, a linearly increasing strain with time is observed. When the load is removed, a delayed recovery follows an instant elastic recovery (see Figure 2-8). The unrecoverable deformation is called viscous deformation.

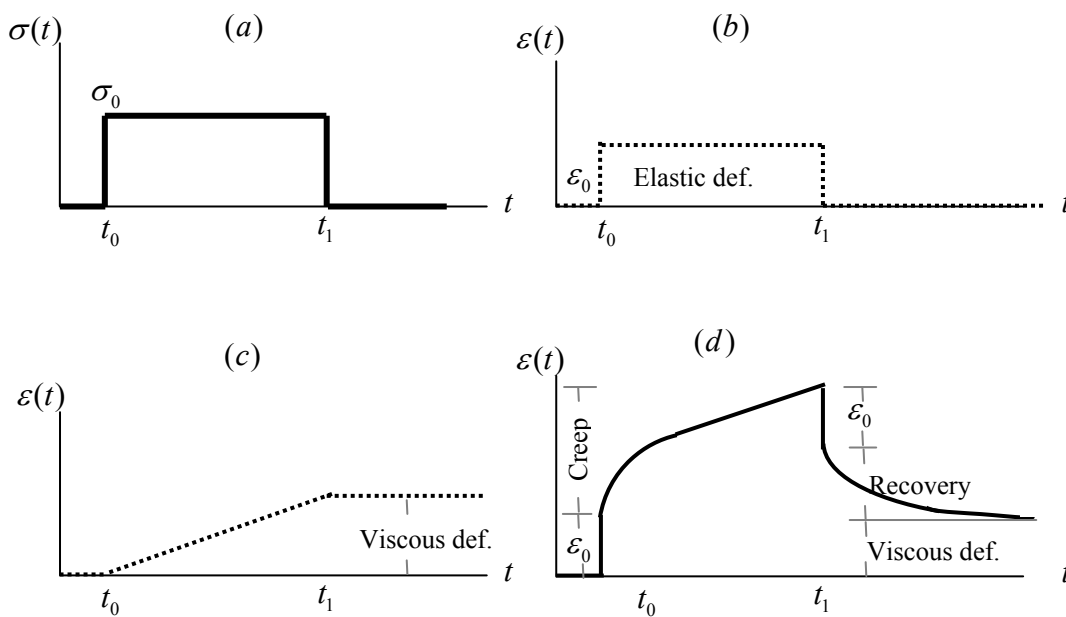


Figure 2-8 Material response to a step load: (b) Elastic, (c) Viscous, (d) Viscoelastic

When the applied loads are very small, bituminous materials are usually assumed to behave linear viscoelastic. If the time effects are taken out, the stress-strain relation of the materials is therefore linear. If the material is linear viscoelastic, doubling the applied load will result in doubling the response of the material. The response of the material for various loadings has also an additive effect. This implies that the overall response of the material is a result of the various loads acting together, and equals the summation of the response of the various loads acting independently on the material. This property follows from the well known superposition principle, which is assumed to be valid for most linear elastic and linear viscoelastic materials. However, if the applied

loads are large, as in the case within the binder domain of an asphalt mixture [6], bituminous materials exhibit a nonlinear behaviour. The approach for modelling nonlinear viscoelastic materials is therefore different. Fundamental approaches for modelling non linear viscoelastic behaviour are treated separately at the end of this chapter.

2.3.2.2 Constitutive Relations for Viscoelastic Materials

Constitutive relations define the stress-strain relationship of the material. Due to the time dependent nature of the relaxation modulus and creep compliance, the stress-strain relationship of a viscoelastic materials is also time dependent. Two forms of constitutive modelling are common for viscoelastic materials. The first is called hereditary form, where the stress-strain relationship is expressed in the form of hereditary integrals. The second form, known as differential form, expresses the stress-strain relationship with differential operators of polynomial orders.

a) Hereditary Integral Form

The basic approach used for modelling viscoelastic materials is similar with that of elastic materials. In analogy with constitutive relations for elastic materials, the stress in a viscoelastic material for a constant strain $\Delta\epsilon_0$ applied at time t_0 can be given as:

$$\sigma(t) = E(t - t_0)\Delta\epsilon_0 \quad 2-1$$

where

$\sigma(t)$ = time dependent stress

$E(t - t_0)$ = relaxation modulus

$\Delta\epsilon_0$ = strain step applied at time t_0

If various strain steps are applied at various times, load application time t_i corresponding to strain step $\Delta\epsilon_i$, then the stress response at any time t can be obtained as the sum of the individual responses.

$$\sigma(t) = \sum_{i=1}^n E(t - t_i)\Delta\epsilon_i \quad 2-2$$

Since any arbitrary stress-time curve can be approximated by the sum of a series of step functions which correspond to a series of step-like increments in load, Equation 2-2 can be generalized to a stress-strain relation in the form of hereditary integral as:

$$\sigma(t) = \int_0^t E(t - \tau)\dot{\epsilon}d\tau \quad 2-3$$

where:

$\sigma(t)$ = stress as a function of time

$E(t - \tau)$ = relaxation modulus

$\dot{\varepsilon}$ = strain rate at time τ

τ = time integration (hereditary) variable

Equation 2-3 is the fundamental constitutive relation for linear viscoelastic theory. It is referred as the hereditary integral or the memory function. The time integration variable, τ , in the hereditary integral represents the importance of the strain history for the stress at the current value. Following the same approach, an equivalent relationship for obtaining the strain, given an arbitrary stress signal, exists. Representing the deformation per unit stress, called creep compliance of the material as $D(t - \tau)$, where τ denotes time history variable, the corresponding relationship is given as:

$$\varepsilon(t) = \int_0^t D(t - \tau) \dot{\sigma} d\tau \quad 2-4$$

The two hereditary integrals given in Equation 2-3 and Equation 2-4 are defining the stress-strain relationship for a viscoelastic material, and are fundamentals for linear viscoelastic theory. For numerical applications, the creep and relaxation functions in the hereditary integrals are commonly represented with various mechanical models. In ABAQUS the Prony representation, discussed in Section 2.3.2.6, is used.

b) Differential Form

The other alternative for describing linear viscoelasticity is the use of differential form for the constitutive relation. This form is widely used by researchers in the past mainly because of its connection with the common rheological models, which comprise spring-dashpot elements of various order [45]. The general form for the differential constitutive relation is given as:

$$(p_0 + p_1 \frac{\partial}{\partial t} + p_2 \frac{\partial^2}{\partial t^2} + \dots p_n \frac{\partial^n}{\partial t^n}) \sigma(t) = (q_0 + q_1 \frac{\partial}{\partial t} + q_2 \frac{\partial^2}{\partial t^2} + \dots q_n \frac{\partial^n}{\partial t^n}) \varepsilon(t) \quad 2-5$$

$$P(D)\sigma(t) = Q(D)\varepsilon(t)$$

where:

$\sigma(t)$ = the stress as a function of time

$\varepsilon(t)$ = the strain as a function of time

$P(D)$ = polynomials in D such that $D^n = p_n \frac{\partial^n}{\partial t^n}$

$$Q(D) = \text{polynomials in } D \text{ such that } D^n = q_n \frac{\partial^n}{\partial t^n}$$
$$p_n, q_n = \text{material constants}$$

Constitutive relationships obtained using any combination of linear spring-dashpot elements can be expressed by the general differential formulation shown in Equation 2-5. Unlike the hereditary integrals, which involve time history variable τ , the differential form involves only the current values of stress and strain plus their time derivatives. This form is suitable for numerical applications and, therefore, widely used for solving engineering problems involving viscoelastic materials. By properly choosing the number of terms required in the differential series, the viscoelastic behaviour of a specific material can be well represented [15-17].

In these constitutive relations, the material behaviour parameters need to be determined before performing numerical calculations. The material behaviour, expressed as creep and relaxation functions, is usually determined from laboratory experiments. These functions are the fingerprints of the material. The experimental methods used to obtain these viscoelastic material functions are discussed in the following section.

2.3.2.3 Experimental Methods

a) Time Domain Tests

Relaxation and creep tests are the two most commonly used experimental methods to investigate the time dependent behaviour of viscoelastic materials. A creep test is characterized by an increasing deformation with time under a constant stress. In a relaxation test, a constant strain is applied resulting in a decreasing stress with time. Figure 2-9 gives an illustration of creep and relaxation test results for viscoelastic materials.

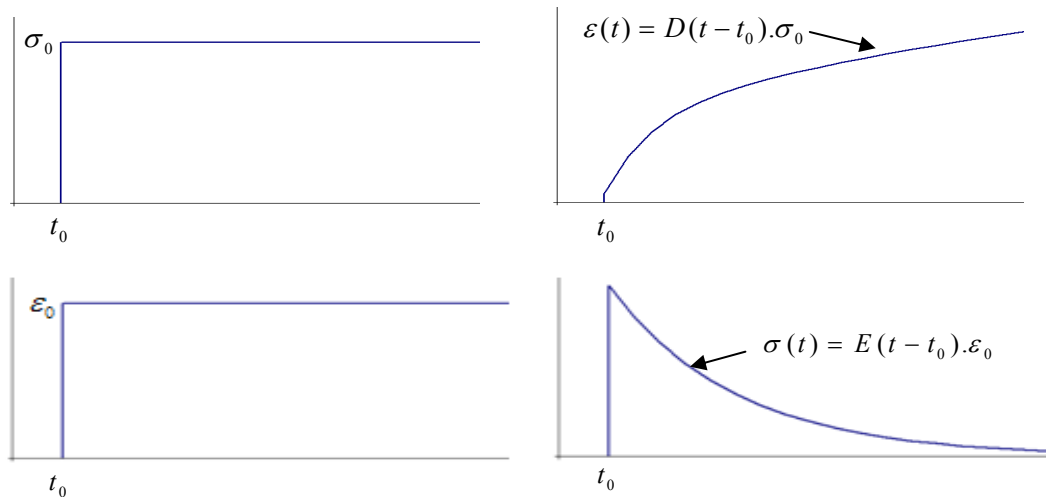


Figure 2-9 Creep phenomenon (top), Relaxation phenomenon (bottom)

These tests are suitable particularly for investigating the viscoelastic properties of materials for loading times larger than 1 second. For short loading times, which correspond to high frequency loadings, these tests cannot provide complete material information. This is mainly because it takes a finite time in practice, typically in the order of 0.1 to 1 second, to apply a constant stress or constant strain to the material [27]. Accurate material information for short time scales, in the order of a fraction of seconds can, therefore, not be obtained from time domain tests. Because of this reason, material information for short loading times is indirectly obtained from dynamic tests. In a dynamic test, material information is obtained as a function of loading frequency. This information can then be converted into time domain data using Laplace or Fourier transformations [15-17]. For conducting dynamic tests on bituminous binders, a Dynamic Shear Rheometer (DSR) is commonly used. The test principles, the frequency-time domain conversion methods are discussed in the following sections.

b) Frequency Domain Tests

As discussed in the previous section, dynamic tests are required to obtain the material response at very short loading times. The common approach is to apply a periodically varying strain or stress signal with a fixed frequency. By analysing the applied and the resulting periodic signals, intrinsic material information can be extracted.

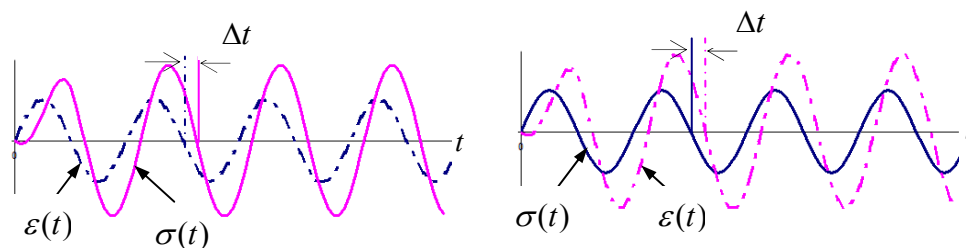


Figure 2-10 Input and output signal for dynamic test: strain control (left) and stress control (right)

Since bituminous materials are viscoelastic, there is a phase lag between the applied and the response signal in a dynamic test. In Figure 2-10 this phase lag is denoted by Δt . For a sinusoidal varying strain input with an amplitude ϵ_0 and frequency ω , the resulting response signal is also sinusoidal in shape with a phase lag, δ . In mathematical form it is expressed as:

$$\epsilon(t) = \epsilon_0 \sin(\omega t) \text{ and } \sigma(t) = \sigma_0 \sin(\omega t + \delta) \tag{2-6}$$

Using the basic theory of viscoelasticity (hereditary integral formulation) the stress in a viscoelastic material for a sinusoidal strain signal can be obtained. For a sinusoidal strain input the resulting formulation for the stress is

$$\sigma(t) = \epsilon_0 \left[\omega \int_0^{\infty} E(s) \sin(\omega s) ds \right] \sin(\omega t) + \epsilon_0 \left[\omega \int_0^{\infty} E(s) \cos(\omega s) ds \right] \cos(\omega t) \tag{2-7}$$

where:

$s = t - \tau$ where τ is history variable

$E(s)$ = relaxation function

In Equation 2-7 the expressions placed in bracket are functions of frequency only. The first term is in phase with the applied sinusoidal strain while the second term with the cosine expression is 90 degree out of phase. The expressions in the two brackets are the components of the dynamic modulus of the material. Equation 2-7 is expressed in terms of loss and storage modulus components as [16, 17, 27]

$$\sigma(t) = \epsilon_0 [E'] \sin(\omega t) + \epsilon_0 [E''] \cos(\omega t) \tag{2-8}$$

where:

E' = storage modulus

E'' = loss modulus

By comparing Equation 2-6 and Equation 2-8, the fundamental relations for analyzing dynamic analysis data that relate available experimental data, σ_0 , ε_0 and δ , to the material property, E' and E'' are obtained. After some mathematical manipulations, the relations given in Equation 2-9 summarize these fundamental relations for analyzing dynamic test data [27].

$$E'(\omega) = \frac{\sigma_0}{\varepsilon_0} \cos \delta, \quad \text{and}, \quad E''(\omega) = \frac{\sigma_0}{\varepsilon_0} \sin \delta$$

$$\tan \delta = \frac{E''(\omega)}{E'(\omega)} \quad 2-9$$

$$|E^*(\omega)| = \sqrt{(E''(\omega))^2 + (E'(\omega))^2}$$

where:

E' = storage modulus

E'' = loss modulus

δ = phase angle

$|E^*|$ = magnitude of the complex modulus

2.3.2.4 Interrelation between Viscoelastic Functions

With a steady state periodic excitation, the response of a material for short loading times (high frequency) can be obtained from frequency domain tests. To obtain the corresponding time domain material function, the frequency domain material function needs to be converted.

a) Time and Frequency Domain Relationships

The method used to convert the frequency domain material functions to time domain material functions involves Fourier or Laplace transformation. The principle is valid for the material functions in different modes being shear, extension and bulk modulus functions of a material. An illustration is given below for interrelation between the time and frequency domain material functions of the extension modulus [16, 17, 27]. The same principle can also be used for material functions describing the shear and volumetric deformation characteristics of the material.

$$E'(\omega) = \omega \int_0^{\infty} E(t) \sin(\omega t) dt = \omega F_s [E(t)]$$

2-10

$$E''(\omega) = \omega \int_0^{\infty} E(t) \cos(\omega t) dt = \omega F_c [E(t)]$$

$$E^*(\omega) = i\omega \mathcal{L}[E(t)]_{s=i\omega}$$

where:

$E(t)$ = extension modulus(relaxation modulus)

$E'(\omega)$ = loss modulus

$E''(\omega)$ = storage modulus

F_s = one sided sine Fourier transform

F_c = one sided cosine Fourier transform

$\mathcal{L}[E(t)]$ = Laplace transform of the relaxation function

i = the complex notation

b) Interrelation between Creep and Relaxation Functions

In addition to the time and frequency domain relationship of a given material function, there also exist relationships between the different material functions. Since material properties are intrinsic, different material functions obtained under different test conditions are interrelated to each other. This relation is particularly useful in cases where the response of a material under a certain excitation condition can be inaccessible to direct experimentation but may be obtained from measurements under other realizable conditions. Such relations are of importance in modelling because if the relaxation function, $E(t)$, of a material is known then the creep modulus, $D(t)$, can be calculated and vice versa. These relations are widely used in viscoelastic material modelling. Equation 2-11 presents a relationship between the relaxation modulus and creep compliance of a material [16, 17].

$$\int_0^t E(t-\tau)D(\tau)d\tau = \int_0^t E(\tau)D(t-\tau)d\tau = t \rightarrow E(s)D(s) = \frac{1}{s^2} \quad 2-11$$

where:

$E(s)$ = Laplace transform of the relaxation function

$D(s)$ = Laplace transform of the creep function

s = Laplace transform variable

The form shown in Equation 2-11 is also valid for material functions obtained from volumetric and shear loading conditions.

2.3.2.5 Thermo Viscoelasticity

In addition to the loading time, there are other effects which affect the behaviour of viscoelastic materials such as temperature and load levels. In relation to the load level, most engineering materials are assumed to behave

linear for small loads. If the loads become higher, the material may exhibit nonlinear behaviour. The nonlinear behaviour of materials is treated separately at the end of this chapter.

For viscoelastic materials, the effect of temperature on the material property is also significant. In the following section the modelling approach that is commonly used to incorporate the temperature effect on the material response is presented.

The Memory Function Approach

The memory function approach is based on Boltzmann superposition principle and is the most widely used formulation in viscoelastic material modelling. In this approach, the material remembers its past explicitly; its current response is affected by events which happened in the past [27]. In essence this approach is similar to the fundamental viscoelastic theory discussed in the previous sections.

$$\sigma(t, T, \varepsilon^r) = \int_0^t E(t-\tau, T) \frac{d\varepsilon(\tau)}{d\tau} d\tau \quad 2-12$$

In this approach the effect of temperature is incorporated in the material function and the hereditary integral formulation is used to obtain the stress in the material. The past strain history is taken care of using the hereditary integral.

Modelling Temperature Effects

In the memory function approach, the modulus function is dependent on temperature and time. Researchers have investigated the effect of temperature on the modulus and creep function. Their observation revealed that the material function plots at various temperatures showed a similar shape. A shift of the plots along the time axis results in one master curve. This principle is called time-temperature superposition principle and is widely used to model temperature effects on viscoelastic material properties [10, 16].

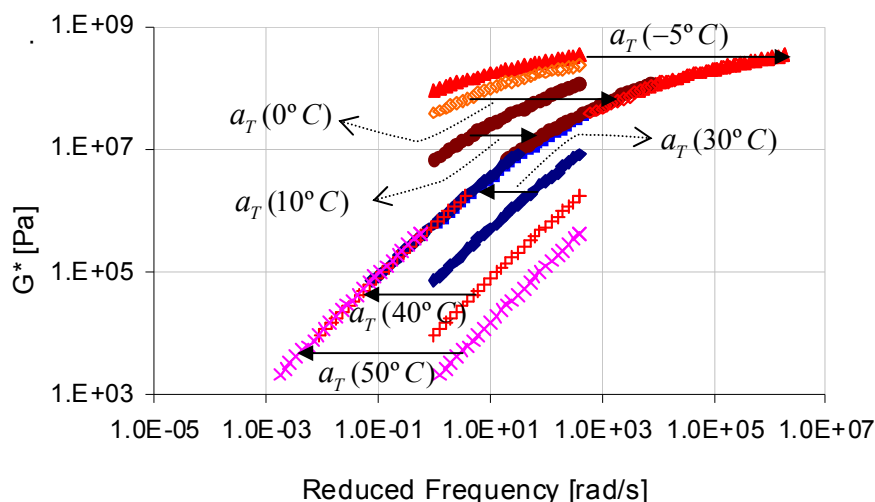


Figure 2-11 Example of dynamic shear modulus data shifted along the frequency axis for 40-60 pen grade bitumen

Figure 2-11 illustrates graphically the principle of time-temperature superposition applied in frequency domain. The principle states that the material function at temperature T and time t can be obtained from the material function plot at reference temperature T_{ref} evaluated at a reduced time t_{red} . Mathematically this principle can be written as:

$$E(t, T) = E(t_{red}, T_{ref}), \quad t_{red} = t.a_T \quad 2-13$$

where:

t_{red} = the reduced time

a_T = the horizontal shift factor for a given temperature T

T = temperature

T_{ref} = reference temperature

Materials that form a master curve following the time-temperature superposition are called thermorheological simple materials. In addition to a horizontal shifting, some materials require a vertical shifting. Such materials are referred as thermorheological complex. At low load levels, bituminous materials are usually considered as thermorheological simple. Higher load levels in bituminous materials can result in thermorheological complex behaviour [34].

a) Time-Temperature Shift Factor

The shift factor that is used in the time-temperature superposition principle is a basic material property. This implies that the same factor remains applicable for all other viscoelastic functions of the material, such as shear and bulk modulus. In literature, several models are proposed for obtaining shift factors. Some of

the commonly used models include the Log-polynomial, the Arrhenius and the Williams-Landel-Ferry models. The shift factor in the Log-polynomial model is given as:

$$\text{Log } a_T[\Gamma] = b_0 + b_1 T + b_2 T^2 + \dots \quad 2-14$$

The terms b_0 , b_1 and b_2 are model parameters for the polynomial function in temperature. For the Arrhenius model, the following relation is used.

$$\text{Log } a_T[\Gamma] = \frac{-E_a}{2.303R} \left[\frac{1}{T} - \frac{1}{T_R} \right] \quad 2-15$$

where:

$a_T[\Gamma]$ = shift factor for a given temperature T

E_a = activation energy [J/mol]

R = gas constant [J/mol/K]

T_R = reference temperature in K

Literature suggests that for temperatures below the glass transition temperature, which is the temperature below which the material behaves brittle, the Arrhenius model delivers good results [27].

The Williams-Landel-Ferry (WLF) model is given as:

$$\text{Log } a_T[\Gamma] = \frac{C_1(T - T_R)}{C_2 + T - T_R} \quad 2-16$$

where:

C_1, C_2 = model parameters

T_R = reference temperature in K

This model is applicable for ranges from just below glass transition to far above glass transition temperatures [10, 27].

b) Vertical Shift Factor

For thermorheological complex materials, the change in temperature can no longer be modelled only with a horizontal shift factor. For this, Ferry [15] introduced a vertical shift factor, b_T , applied to a corrected or reduced modulus E_p . The general formulation of this principle is given as:

$$E(t, T) = b_T E_p(t, a_T[T], T_R) \quad 2-17$$

where:

b_T = vertical shift factor for a given temperature T

T_R = reference temperature in K

$a_T[T]$ = horizontal shift factor for a given temperature T

E_p = reduced modulus(obtained after horizontal shifting)

2.3.2.6 Mechanical Models

a) General

From the previous sections, it is shown that information concerning the time dependent nature of the materials is contained in the viscoelastic material functions, such as relaxation and creep functions. To make use of these material properties in pavement performance prediction models, most of which are developed in numerical platforms, a relevant mechanical model needs to be utilized. Physical models, comprising of springs and dashpots, are commonly used to represent these material functions. There also exist analytic models that are used for describing the material functions. Such models, apart from their use in test result description, have limited applicability in a numerical environment [9, 40]. The applicability of any of the mechanical or analytical models to a particular problem in a numerical environment depends on the ability of the chosen model to accurately characterize the experimentally measured data, and also the model suitability for application in the chosen numerical platform.

Following the constitutive relation for pure elastic materials, the linear relationship between the applied stresses and the resulting strain in a material is modelled using a linear spring. Similarly for Newtonian fluids, where there exist a linear relationship between the applied stress and resulting strain rate, a linear dashpot is used. Since viscoelastic materials show a combination of viscous and elastic behaviour, a combination of linear springs and linear dashpots is usually used to model their response behaviour. Constitutive relations for such models are usually described by differential equations of an integer order.

Mechanical analogies for viscoelastic materials can also be obtained with a combination of springs and variable dashpots. The constitutive relation defining the variable dashpot differs from the linear dashpot in that the differential operators for the variable dashpots involve fractional (non integer) orders [39]. In the following sections a selective overview of the representative mechanical models in each category is presented.

b) Models with Linear Spring and Linear Dashpot Elements

Maxwell Model

The Maxwell model is the simplest model that can be obtained using a spring-dashpot combination (Figure 2-12). It is obtained by putting a linear spring in parallel with a linear dashpot. During loading, the stress in the spring and the dashpot remains always the same. However, the total deformation is obtained by summing the individual element contributions.

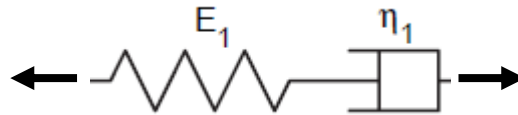


Figure 2-12 Maxwell model

Denoting the total strain and stress in the system as $\varepsilon(t)$ and $\sigma(t)$ respectively, the constitutive relation defining the Maxwell model, shown in Figure 2-12, becomes:

$$\varepsilon(t) = \varepsilon_s(t) + \varepsilon_d(t) \quad \text{and} \quad \sigma(t) = \sigma_s(t) = \sigma_d(t) \quad 2-18$$

where the subscript s and d in the stress and strain terms refer to the spring and dashpot element respectively. For a linear spring with spring constant, E_1 , and a dashpot with viscosity, η_1 , the stress and strain expressions given in Equation 2-18 can be merged together resulting in the following differential equation.

$$\sigma(t) + \frac{\eta_1}{E_1} \dot{\sigma}(t) = \eta_1 \dot{\varepsilon}(t) \quad 2-19$$

In Equation 2-19, the ratio E_1/η_1 is known as the relaxation time constant usually denoted as τ . Comparing this constitutive relation with the general form of the differential constitutive relation discussed in Section 2.3.2.2, it can be seen that for the Maxwell model only the first two terms in the polynomial series are required.

Solving the differential equation for a unit strain step and a unit stress step separately results in the relaxation and creep compliance functions of the Maxwell model.

$$E(t) = \frac{\sigma(t)}{\varepsilon_0} = E_1 \exp(-t/\tau) \quad \text{and} \quad D(t) = \frac{\varepsilon(t)}{\sigma_0} = \frac{t}{\eta_1} + \frac{1}{E_1} \quad 2-20$$

where:

ε_0 = constant strain

σ_0 = constant stress

$E(t)$ = relaxation function

$D(t)$ = creep compliance function

Figure 2-13 illustrates the response behaviour of a Maxwell material when subjected to a constant stress and constant strain. In the illustration a constant stress step of magnitude σ_0 is applied for a time duration $0 < t < t_1$ which results in a linear strain response. When the strain ε_1 obtained at time $t = t_1$ is kept constant for time $t > t_1$, an exponential decay of the stress is observed.

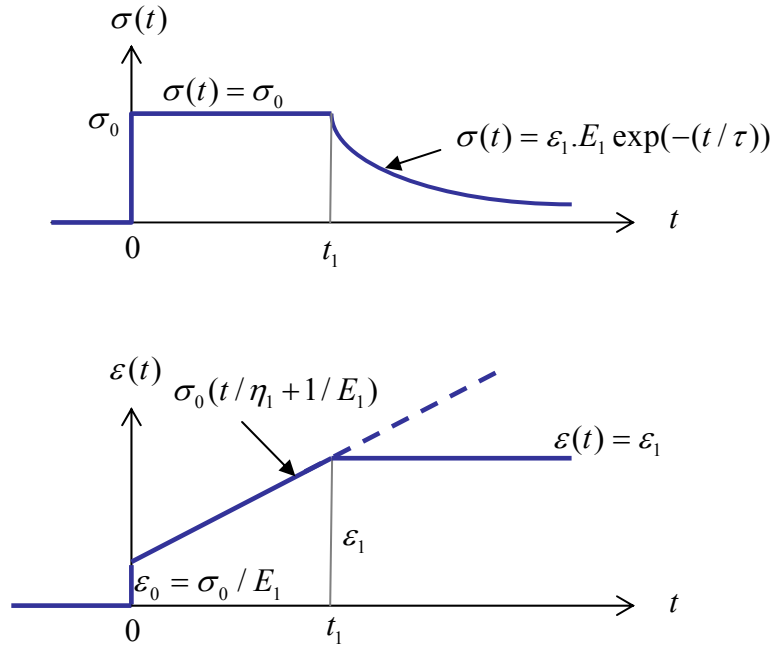


Figure 2-13 Maxwell model response

For frequency domain measurements, the time-frequency domain inter-conversion methods discussed in the previous section can be employed to obtain the material functions. The storage and loss modulus of a Maxwell model subjected to a dynamic strain with radial frequency, ω , are given as:

$$E'(\omega) = \frac{E_1 \omega^2 \tau^2}{1 + \omega^2 \tau^2} ; \quad E''(\omega) = \frac{E_1 \omega \tau}{1 + \omega^2 \tau^2} \tag{2-21}$$

$$\tan \theta = \frac{E''}{E'}$$

where:

- $E'(\omega)$ = storage modulus of the material
- $E''(\omega)$ = loss modulus of the material
- θ = phase angle
- E_1, τ = material parameters

Important features of the Maxwell model are the linear viscous flow for a constant stress and the exponential decay in stress for a constant strain. The decay in stress follows a simple exponential function with a single relaxation time. However, most real materials have different molecular constituents. The different molecules respond to deformation in a different manner which results in the material having a spectrum of various relaxation and creep/retardation times. Such a material behaviour cannot be modelled with a single Maxwell model and requires a combination of more response elements.

Voigt-Kelvin Model

Another model commonly obtained using a simple spring-dashpot combination is the Voigt-Kelvin Element. This model is obtained by placing a linear spring in parallel with a linear dashpot as shown in Figure 2-14. In this model, the total stress in the system is the sum of the stresses in the spring and dashpot element. The deformation in the spring and dashpot element remains equal.

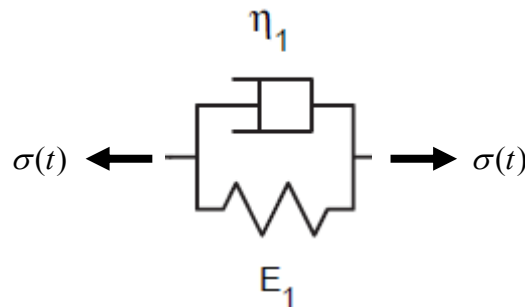


Figure 2-14 Voigt-Kelvin model

The governing constitutive equation for the Voigt-Kelvin model is given as

$$\sigma(t) = E_1 \varepsilon(t) + \eta_1 \dot{\varepsilon}(t) \quad 2-22$$

The response of the model for a strain step, $\varepsilon = \varepsilon_0 H(t)$ where $\dot{\varepsilon} = \varepsilon_0 \delta(t)$, or a stress step, $\sigma = \sigma_0 H(t)$, can be analyzed to obtain the relaxation modulus and the creep compliance functions of the following form.

$$E(t) = H(t)E_1 + \delta(t)\eta_1 = \begin{cases} \infty & t = 0 \\ E_1 & t > 0 \end{cases} \quad 2-23$$

$$D(t) = \frac{\varepsilon(t)}{\sigma_0} = \frac{1}{E_1} (1 - \exp(-t/\tau))$$

where:

$H(t)$ = unit step function

$\delta(t)$ = Dirac delta function

- σ_0 = constant applied stress
 E_1, η_1 = material parameters
 $E(t), D(t)$ = relaxation and creep functions

Figure 2-15 illustrates the response behaviour of the Voigt-Kelvin material when subjected to a constant stress and constant strain. In the illustration a constant step stress of magnitude σ_0 is applied for time duration $0 < t < t_1$ while the strain ε_1 , obtained at time $t = t_1$, is kept constant for time $t > t_1$ resulting in a constant stress. Unlike the Maxwell model where the stress decays with time, the single element Voigt-Kelvin model does not simulate a decaying stress, and hence is not suitable for modelling materials showing relaxation behaviour.

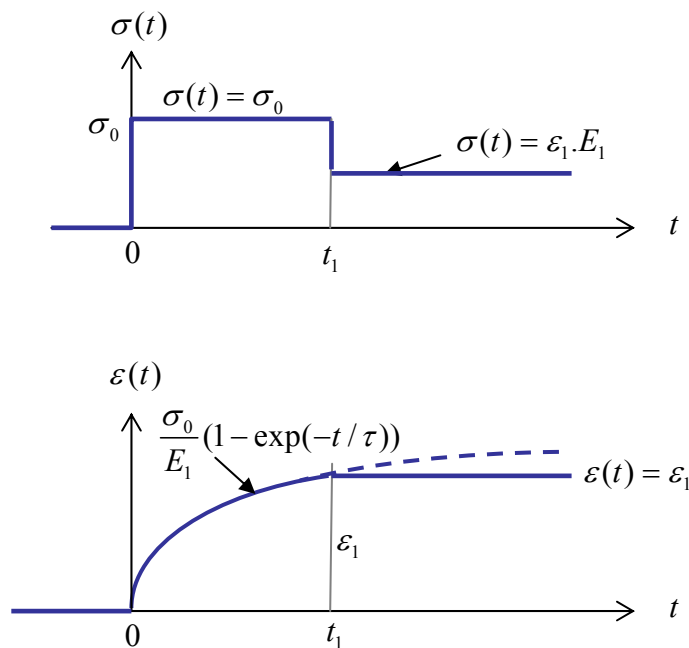


Figure 2-15 Voigt-Kelvin model response

Similar to the Maxwell model, the frequency domain expression for the storage and loss creep compliance for the Voigt-Kelvin model can be obtained as:

$$D'(\omega) = \frac{D_1}{1 + \omega^2 \tau^2} \quad \text{and} \quad D''(\omega) = \frac{D_1 \omega \tau}{1 + \omega^2 \tau^2}$$

2-24

$$\tan \theta = \frac{D''(\omega)}{D'(\omega)}$$

where:

- $D'(\omega)$ = storage creep compliance
 $D''(\omega)$ = loss creep compliance
 θ = phase angle

D_1, τ = material parameters

Unlike the Maxwell model, the Kelvin-Voigt model simulates the evolution of creep with a decreasing slope as is observed in most viscoelastic materials. However, as is the case for Maxwell model, a single retardation constant does not describe the behaviour of real viscoelastic materials. As a result most viscoelastic materials are modelled with a combination of Maxwell and Kelvin-Voigt models.

Generalized Maxwell and Voigt-Kelvin Models

Because the basic Maxwell and Voigt-Kelvin models have simple expressions for the relaxation and creep functions, they are not capable in characterizing most material behaviours. The material functions of these basic models are expressed by a single relaxation/retardation time. Real materials, however, have a much broader relaxation/retardation spectrum. To describe the response behaviour of such materials, a series of spring-dashpot combinations needs to be used.

One of the common rheological models obtained by placing a series of Maxwell elements in parallel is the Generalized Maxwell model, also known as Prony series. Since the deformations in the parallel elements are equal, the relaxation material function of this model can easily be obtained as a summation of the relaxation function of each of the individual Maxwell elements. The number of terms required for accurately modelling a given material response is determined based on the quality of fitting on the measured response data.

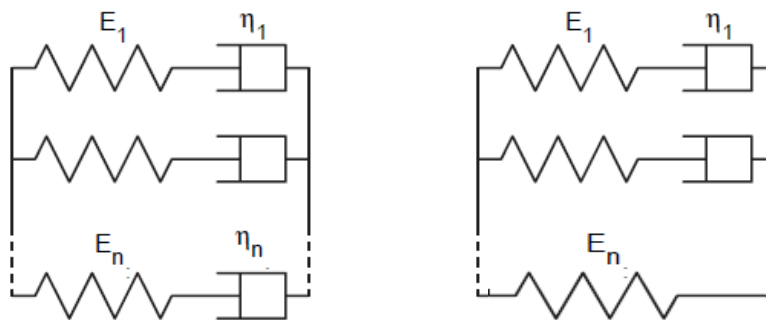


Figure 2-16 Generalized Maxwell model (left), and the form used in Abaqus (right)

Figure 2-16 illustrates the generalised Maxwell model. The built-in material model in the commercially available FE software Abaqus, on which the meso mechanics PA tool is developed, is of the form shown in the right figure. The presence of the parallel spring implies that the model is intended for viscoelastic solid materials. The parallel spring represents the rubbery modulus of the material.

Similar to the relaxation function for the single Maxwell model, the relaxation function for the generalized Maxwell model with n terms can easily be obtained as a summation of the functions of the individual terms as:

$$E(t) = \frac{\sigma(t)}{\epsilon_0} = \sum_{i=1}^n E_i \exp(-t / \tau_n) \tag{2-25}$$

Similarly for the frequency domain the corresponding expressions become

$$E'(\omega) = \sum_{i=1}^n \frac{E_i \omega^2 \tau_i^2}{1 + \omega^2 \tau_i^2} \text{ and } E''(\omega) = \sum_{i=1}^n \frac{E_i \omega \tau_i}{1 + \omega^2 \tau_i^2} \tag{2-26}$$

$$|E^*(\omega)| = \sqrt{(E'(\omega))^2 + (E''(\omega))^2}$$

where $E'(\omega)$ and $E''(\omega)$ are the storage and loss modulus of the material and $|E^*(\omega)|$ is the complex modulus. The mathematical simplicity of the relaxation functions makes this model suitable for characterizing material behaviours under strain controlled environments.

For stress controlled situations, deriving the creep compliance for the Generalized Maxwell model is cumbersome. In this case, the convenient way of modelling the creep behaviour is by using the Generalized Voigt-Kelvin model (Figure 2-17). This model is obtained by placing a number of Voigt-Kelvin models in series. In this model, the total strain in the system is obtained by summing up the individual contributions. Since the individual creep response of the each Voigt-Kelvin element is known, the creep compliance expression of the generalized model can easily be obtained using summation.

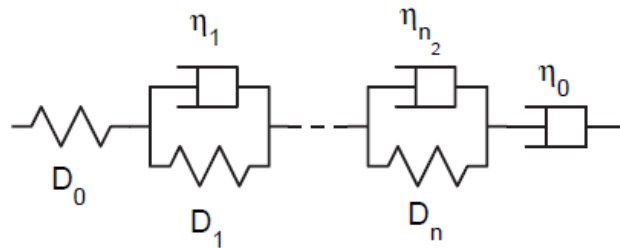


Figure 2-17. Generalized Voigt-Kelvin model

The generalised Voigt-Kelvin element, as described in most of the literature, contains only a series of Voigt-Kelvin elements. The form shown in Figure 2-17 with a single spring and dashpot is also alternatively used. Mathematically a spring response can be obtained when one of the Voigt-Kelvin elements dashpots parameter goes to nil. Similarly a dashpot response can be obtained when the spring value is set to zero. In reference to Figure 2-17, the instantaneous response is captured by the spring element, the creep evolution is

captured by the series of Kelvin-Voigt elements, and the single dashpot element captures the viscous deformation. A version of this model with a single Kelvin-Voigt element is called the Burgers' model. This model is widely used for modelling bituminous binder and mixture responses in the field of pavement engineering [1].

The time and frequency domain expression for the creep compliance are given as:

$$D(t) = D_0 + \sum_{i=1}^{i=n} D_i (1 - \exp(-t / \tau_i)) + \frac{t}{\eta_0}$$

$$D'(\omega) = D_0 + \sum_{i=1}^n \frac{D_i}{1 + \omega^2 \tau_i^2} \quad \text{and} \quad D''(\omega) = \frac{1}{\eta_0 \omega} + \sum_{i=1}^n \frac{D_i \omega \tau_i}{1 + \omega^2 \tau_i^2} \quad 2-27$$

$$|D^*(\omega)| = \frac{1}{|E^*(\omega)|} = \sqrt{(D'(\omega))^2 + (D''(\omega))^2}$$

If sufficient numbers of response elements are chosen, both the Generalized Maxwell and Generalized Kelvin-Voigt model can describe the response curves of most viscoelastic materials fairly well.

c) Models with Parabolic Dashpot Elements

The constitutive relationships of models that are formed using the linear spring-dashpot combinations result in a governing differential equation of an integer order. While the suitability of such models for numerical applications is highly commended, accurate description of material response with such models usually result in a number of model parameters. In the case of bituminous materials, the number of parameters in the order of 20 to 30 was observed [48].

The other alternative approach for modelling viscoelastic materials is by using spring and parabolic dashpot combinations, where the constitutive relations of the parabolic dashpot elements involve differential equations of non-integer order. The non-integer order differential equations are also called fractional derivatives. In comparison to models of linear differential orders, these models characterize the viscoelastic material response with a limited number of model parameters. Applications of such models in the field of pavement engineering are also common [19, 36, 38, 39]. In this section the most representative models, 2S2P1D model and its precursors, Huet-Sayegh and Huet models, are presented.

Huet Model

The Huet model [19] consists of a spring and two parabolic dashpots placed in series as shown in Figure 2-18. This model is also called a power law model,

mainly because its creep compliance, derived in the following sections, results in a form of a power law [10].

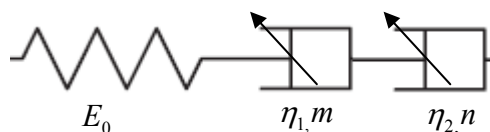


Figure 2-18 Huet Model

The parabolic dashpots in the Huet model have different response characteristics as compared to the linear dashpots. While the linear dashpot constitutive relation involves a differential equation of the first order to relate the applied stress to strain, the constitutive relation for the parabolic dashpot involves differential operators of non-integer order (fractional derivatives). Before the response characteristics of the Huet model are discussed, first the response behaviour of a single parabolic dashpot is treated here. The constitutive relation for the parabolic dashpot is given by the fractional derivative of the form [39]:

$$\sigma(t) = \eta_i \tau_i^{m-1} \frac{\partial^m}{\partial t^m} \{\varepsilon(t)\} = \eta_i \tau_i^{m-1} \Omega^m \{\varepsilon(t)\} \quad 2-28$$

where:

- η_i, τ_i, m = dashpot parameters with $0 \leq m \leq 1$
- Ω = fractional differential operator with $\Omega^m = \partial^m / \partial t^m$
- $\sigma(t)$ = stress as a function of time
- $\varepsilon(t)$ = strain as a function of time

When the values of the parameter, m , equals 1, the differential operator is equal to the normal first order differential operator $\partial / \partial t$ for the linear dashpot, and when m equals 0 Equation 2-28 reduces to the relationship between stress and strain for a linear elastic spring with a spring constant $E = \eta / \tau$. For intermediate values of m , the parabolic dashpot will have a viscoelastic response. This can best be illustrated in a frequency domain where the dashpot response will exhibit similar characteristics as a Kelvin-Voigt type element. Figure 2-19 illustrates the response of a single parabolic dashpot for a sinusoidal load. The resulting phase angle is denoted by a variable φ [39].

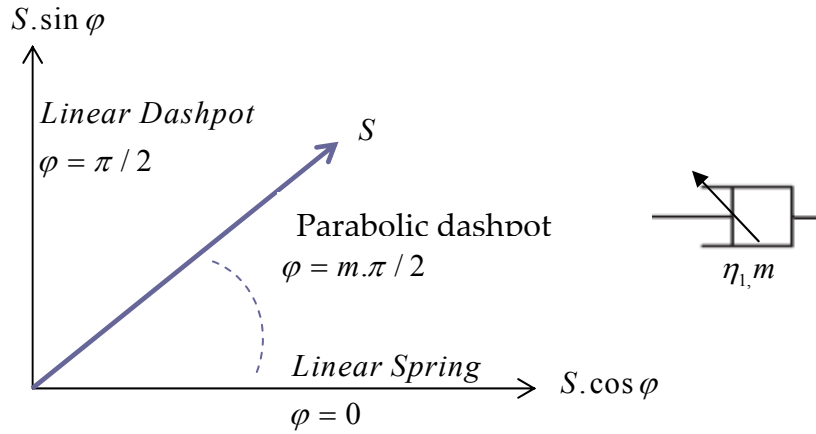


Figure 2-19 Response of a parabolic dashpot [39]

For parabolic dashpots all the deformations are fully recoverable once the loading is removed. Hence the creep like evolution observed during the loading phase will not result in permanent or viscous deformation.

The creep compliance of the Huet model is equal to the sum of the creep compliances of the individual response elements. Obtaining the creep compliance of the parabolic dashpot requires solving the fractional differential equation for a constant stress. This involves integration to a fractional order. Using classical fractional calculus, the Riemann-Liouville integral can be used to obtain the m order integration of a function $f(t)$ as:

$$I^m \{f(t)\} = \frac{1}{\Gamma(m)} \int_0^t (t-s)^{m-1} f(s) ds$$

where the integration operation $I^m \{f(t)\}$ represents the m order integration of a function and $\Gamma(m)$ is a gamma function. Thus for a constant applied stress σ_0 , the strain in the parabolic dashpot with model parameters, η_1, τ_1 and m , can be obtained as:

$$\sigma_0 = \eta_1 \tau_1^{m-1} \Omega^m \{\varepsilon_1(t)\} \rightarrow \Omega^m \{\varepsilon_1(t)\} = \frac{\sigma_0}{\eta_1 \tau_1^{m-1}} = \text{constant}$$

Applying the Riemann-Liouville integral, the strain response of the parabolic dashpot is obtained as:

$$\varepsilon_1(t) = I^m \left\{ \frac{\sigma_0}{\eta_1 \tau_1^{m-1}} \right\} = \frac{\sigma_0}{\eta_1 \tau_1^{m-1}} \frac{1}{\Gamma(m)} \int_0^t (t-s)^{m-1} ds$$

2-29

$$\varepsilon_1(t) = \frac{\sigma_0}{\eta_1 \tau_1^{m-1}} \frac{1}{\Gamma(m+1)} t^m$$

Equation 2-29 shows that the strain response of the parabolic dashpot follows a power form. Since the total strain in the Huet model is the sum of the strain

responses of each element, and the total stress is equal to the stress in the individual elements, the strain response of the Huet model for a constant applied stress can be obtained by summing the creep response of each response element as:

$$\varepsilon(t) = \sigma_0 \left[\frac{1}{E_0} + \frac{\tau_1^{1-m}}{\eta_1 \Gamma(m+1)} t^m + \frac{\tau_2^{1-n}}{\eta_2 \Gamma(n+1)} t^n \right]$$

The creep compliance, $D(t)$, of the Huet model then becomes:

$$D(t) = \frac{1}{E_0} + \frac{\tau_1^{1-m}}{\eta_1 \Gamma(m+1)} t^m + \frac{\tau_2^{1-n}}{\eta_2 \Gamma(n+1)} t^n \quad 2-30$$

The frequency domain response of the Huet model can be obtained from the time domain creep compliance using time-frequency domain conversion. The complex creep compliance and complex modulus expressions are given by:

$$D^*(\omega) = \frac{1}{E_0} + \frac{\tau_1^{1-m}}{\eta_1} (i\omega)^{-m} + \frac{\tau_2^{1-n}}{\eta_2} (i\omega)^{-n} \quad 2-31$$

$$E^*(\omega) = \frac{1}{D^*(\omega)} = \frac{E_0}{1 + \frac{E_0 \tau_1}{\eta_1} (i\omega \tau_1)^{-m} + \frac{E_0 \tau_2}{\eta_2} (i\omega \tau_2)^{-n}}$$

Huet-Sayegh Model

The Huet-Sayegh model is an improved version of the Huet model. It is obtained by placing a linear spring in parallel with the original Huet model. Similar to the parallel spring in the Prony series model, the parallel spring in the Huet-Sayegh model represents the rubbery modulus of the material; hence it represents a viscoelastic solid material behaviour. The physical representation of the model is given in Figure 2-20.

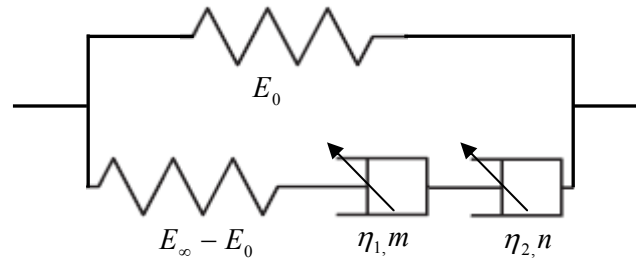


Figure 2-20 Huet-Sayegh Model

For the Huet-Sayegh model, the time domain expression for the creep compliance is not trivial. However, the frequency domain expression for the complex modulus can easily be derived from the corresponding expression obtained for the Huet model. Since the strains in the two parallel branches, the

branch with the parallel spring and the branch with Huet model are the same, and the total stress in the system is the sum of the stresses in the two branches, the complex modulus expression can be obtained as

$$E^*(\omega) = E_0 + \frac{E_\infty - E_0}{1 + \frac{(E_\infty - E_0)\tau_1}{\eta_1}(i\omega\tau_1)^{-m} + \frac{(E_\infty - E_0)\tau_2}{\eta_2}(i\omega\tau_2)^{-n}} \quad 2-32$$

If the value of the parallel spring constant is set to nil, $E_0 = 0$, the expression reduces to the original Huet model.

2S2P1D Model

The 2-spring, 2-parabolic-1-linear dashpot (2S2P1D) model of Di Benedetto and Olard [36] is the latest in the improved versions of the Huet model series. The 2S2P1D model differs with the Huet-Sayegh model in that it incorporates a linear dashpot in series with the parabolic dashpots. The physical representation for this model is shown in Figure 2-21.

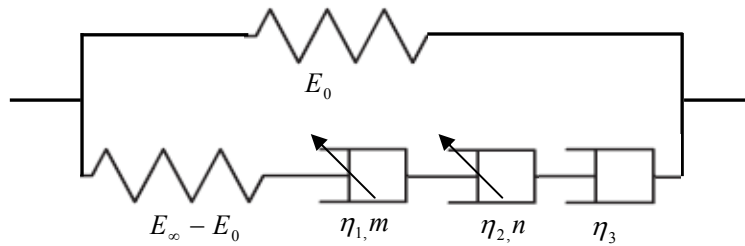


Figure 2-21 2S2P1D Model

The purpose of the linear dashpot is to improve the low frequency region fits of the model to experimentally obtained response data. For describing frequency domain measurements, the complex modulus expression can be obtained in a similar way as for the Huet-Sayegh model. The complex modulus is given by:

$$E^*(\omega) = E_0 + \frac{E_\infty - E_0}{1 + \delta_1(i\omega\tau)^{-m} + \delta_2(i\omega\tau)^{-n} + (\beta i\omega\tau)^{-1}} \quad 2-33$$

where:

$\delta_1, \delta_2, \beta$ = model parameters

m, n = parameters with $0 \leq m, n \leq 1$

E_0 = rubbery modulus, modulus value at near zero frequency

E_∞ = elastic modulus, modulus at high frequency values

Application of this model on the frequency domain response data of different asphalt concrete mixtures has shown improvement in the low frequency region. The model is used to simulate materials with a viscoelastic solid property, and hence no viscous deformation. However, the peculiar case of this model, which is obtained by removing the parallel spring, has been used in literature to

simulate viscous deformations in bituminous binders [36]. For simulating viscous deformations in asphalt concrete mixtures, addition of a linear dashpot element in series with Huet-Sayegh model is suggested [40].

2.3.3 Modelling Nonlinear Viscoelastic Materials

Assumption of linear viscoelasticity remains valid for small loads only. For large loads, most materials exhibit nonlinear behaviour [3, 4]. As a result, the superposition principle used in developing the constitutive relation for linear viscoelastic materials becomes inapplicable. Research work in the past has shown that the task of obtaining a universal nonlinear constitutive model, equivalent to those that exist in the linear theory, is challenging for various reasons [10, 16]. Some of the reasons include the extent of experimental work involved, the required computational power of computers, the ease of use for application, the material behaviour complexity etc. Workable solutions in dealing with nonlinear viscoelastic problems are therefore to seek for special forms of constitutive relations by making reasonable simplifications. Such models, even though not universal, can be adapted to deal with specific nonlinear problems. However, their applicability is mainly based on the ability of the models to describe the particular experimental data.

For viscoelastic materials, various nonlinear theories have been proposed in the past. Most referred and representative works in nonlinear viscoelasticity include Green-Rivlin's theory [18], Christensen's theory [10], modified superposition principle (Leaderman [31], Findley [16], Locket [32]) and Schapery's theory [43]. These theories have many features in common with the linear viscoelastic theory, and the most fundamental common aspect between linear and nonlinear theories is that of the memory hypothesis. This hypothesis, that the material has a memory for the past deformation events, is the basic point in the development of both linear and nonlinear viscoelastic theory. The most representative nonlinear theories from literature are discussed below.

2.3.3.1 Modified Superposition Principle

Leaderman's [31] model, referred to as modified superposition principle, for modelling nonlinear viscoelastic materials separates the creep behaviour of the material into time and stress dependent part, and are additive. The mathematical formulation of this model is given as [27]:

$$\varepsilon(t) = k\sigma + h(\sigma)D(t)$$

For a general case of loading in one dimension, the model is expressed in a single integral form as:

$$\varepsilon(t) = k\sigma(t) + \int_0^t D(t-\tau) \frac{d}{d\tau}(h(\sigma(\tau)))d\tau \quad 2-34$$

where:

k = material constant known as time independent compliance

$h(\sigma)$ = function representing the separation of stress dependent part

$D(t)$ = function representing the separation of time dependent part

It has been reported that the constitutive relation can be used for a particular type of nonlinear viscoelastic material, but the form is not sufficiently general to describe all time dependent materials. This is mainly due to the empirical nature of the functions in the constitutive relation. A form of the modified superposition principle explored later by Findley [16] and co-workers is given by means of Equation 2-35.

$$\varepsilon(t) = \int_0^t \frac{\partial \varepsilon[\sigma(\tau), t - \tau]}{\partial \sigma(\tau)} \frac{d\sigma(\tau)}{d\tau} d\tau \quad 2-35$$

The modified superposition principle can be described as follows. When the state of stress is abruptly changed from σ_1 to σ_2 at time t_1 , the creep response can be considered as if at this instant stress σ_2 is removed and at the same time stress σ_2 is applied to the material. It is assumed that both procedures are independent and are acting on an initially undeformed material. If the relation between the stress and strain is linear, the stress ratio in the hereditary integral reduces to the creep compliance of the material and hence linear viscoelasticity theory is obtained. Otherwise, the obtained creep compliance would be a function of stress to reflect the nonlinear behaviour of the material. The laboratory work required to obtain the strain dependent nature of the relaxation function is relatively simple for this approach. However, the fact that the approach extends the Boltzmann superposition principle beyond the range of its applicability without any rigorous theoretical support puts lots of uncertainty for its universal applicability.

2.3.3.2 Green-Rivlin's Theory

Green and Rivlin [18] described the nonlinear creep response of a viscoelastic material by a polynomial stress-function. For uni-axial testing at constant stress, their model is mathematically expressed as:

$$\varepsilon_0(t) = \Delta\sigma_0\varphi_1(t) + \Delta\sigma_0^2\varphi_2(t) + \Delta\sigma_0^3\varphi_3(t) + \dots \quad 2-36$$

where:

$\varphi_i(t)$ = time dependent material functions

$\Delta\sigma_0$ = applied constant stress

$\varepsilon_0(t)$ = the resulting creep strain

This theory states that for different stress increments applied at different times as shown in Figure 2-22, the resulting response is not only the direct superposition of the response of the individual increments, as is the case for linear viscoelastic materials, but also the sum of all the possible cross products to account for nonlinearity.

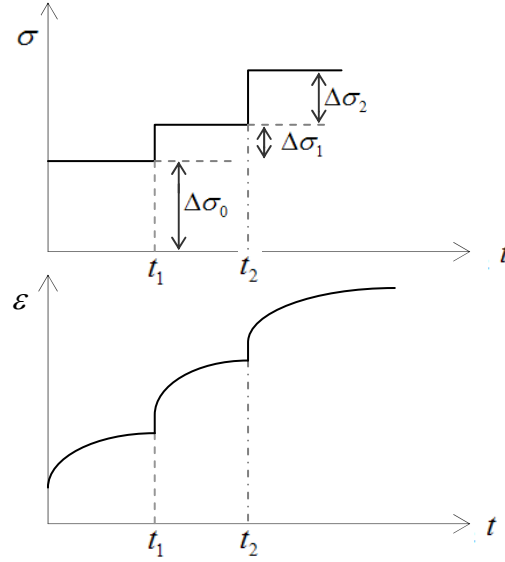


Figure 2-22 Creep response to multiple steps of stress

Introducing a representation of the form $\Delta\sigma_0\Delta\sigma_1\varphi_2(t, t-t_1)$ to describe the additional contribution to the time dependent strain in the nonlinear range due to the cross effect of $\Delta\sigma_0$ applied at $t=0$ and $\Delta\sigma_1$ applied at $t=t_1$, Equation 2-36 generalizes to the following form [16]:

$$\begin{aligned} \varepsilon(t) = & \sum_{i=0}^N (\Delta\sigma_i)\varphi_1(t-t_i) + \sum_{i=0}^N \sum_{j=0}^N (\Delta\sigma_i)(\Delta\sigma_j)\varphi_2(t-t_i, t-t_j) \\ & + \sum_{i=0}^N \sum_{j=0}^N \sum_{k=0}^N (\Delta\sigma_i)(\Delta\sigma_j)(\Delta\sigma_k)\varphi_3(t-t_i, t-t_j, t-t_k) + \dots \end{aligned} \quad 2-37$$

An arbitrarily varying stress can be considered as a limiting case of Equation 2-37 consisting of an infinite number of infinitesimal step wise stress inputs and can be written in general form in a multiple integral representations, the simplest form of which is obtained when the third order ($N=3$) is considered [32].

$$\begin{aligned} \varepsilon(t) = & \int_0^t \varphi_1(t-\tau_1) \frac{d\sigma}{d\tau_1} d\tau_1 + \int_0^t \int_0^t \varphi_2(t-\tau_1, t-\tau_2) \frac{d\sigma}{d\tau_1} \frac{d\sigma}{d\tau_2} d\tau_1 d\tau_2 \\ & + \int_0^t \int_0^t \int_0^t \varphi_3(t-\tau_1, t-\tau_2, t-\tau_3) \frac{d\sigma}{d\tau_1} \frac{d\sigma}{d\tau_2} \frac{d\sigma}{d\tau_3} d\tau_1 d\tau_2 d\tau_3 \end{aligned} \quad 2-38$$

In this approach, it can be seen that the first integral term describes the linear viscoelastic behaviour. Literature states that a minimum of two or more terms are needed to characterize nonlinear viscoelastic materials [32]. The material functions involved in this approach depend on several integration variables and require an impractical number of tests for the determination of material properties in the laboratory. Lockett [32] evaluated the experimental program for determining the material functions in the simplest three order approximation of the theory. It has been shown that the minimum number of experiments required to reasonably characterize a material, for the one dimensional case, is 78, some of which require two and three step deformations (see Figure 2-22). In cases where higher order terms need to be included, the experimental investigation becomes prohibitive.

2.3.3.3 Christensen's Theory

Using the basic theory of linear viscoelasticity, Christensen [10] has developed a nonlinear viscoelastic theory. The one dimensional form of the model is given as:

$$\sigma(t) = 3G_0\varepsilon(t) + \frac{3}{2}[1 + \varepsilon(t)] \int_0^t G_1(t - \tau) d \frac{\varepsilon(\tau)}{d\tau} d\tau \quad 2-39$$

where:

G_0 = the rubbery shear modulus

G_1 = transient part of the shear relaxation modulus

This model explicitly assumes the material as incompressible. The model reduces to the linear viscoelasticity form if the strain term, $\varepsilon(t)$, is set to zero. In the constitutive relation, the nonlinear effect is reflected through the multiplying term $[1 + \varepsilon(t)]$ in front of the integral. It can be intuitively seen that the multiplying factor is fixed in position and it approaches a value of one for small values of strain. Thus if the material exhibits nonlinear behaviour for small strain values, this model fails short to reflect the nonlinear behaviour. The model also lacks flexibility to incorporate other forms of nonlinearity that may arise due to aging, moisture and any other possible factors.

2.3.3.4 Schapery Nonlinear Theory

Schapery's nonlinear theory is the most widely used nonlinear theory for modelling time dependent materials. Its derivation is based on thermodynamics of irreversible processes. Only the final form of the theory, which is widely applied in nonlinear viscoelastic problems, is presented here. The one dimensional representation of the theory resembles the constitutive relation for the linear viscoelasticity, and as such can be considered as a direct extension of the linear viscoelastic theory. Schapery's theory in one dimension is given as:

$$\varepsilon(t) = g_0 D_0 \sigma(t) + g_1 \int_0^t \Delta D(\psi^t - \psi^\tau) \frac{d}{d\tau} (g_2 \sigma(\tau)) d\tau \quad 2-40$$

where:

D_0 = the instantaneous creep compliance

ΔD = the transient or time dependent part of the creep compliance

g_0, g_1, g_2 = model parameters functions of $\sigma(t)$

$\psi^\tau = \psi(\tau)$ is a reduced time

The reduced time is defined as:

$$\psi(t) = \int_0^t \frac{dt'}{a_\sigma(\sigma)}, \quad \psi(\tau) = \int_0^\tau \frac{dt'}{a_\sigma(\sigma)} \quad 2-41$$

where $a_\sigma(\sigma)$ is a stress shift factor. It should be noted that if all the nonlinear model parameters, g_0, g_1 and g_2 , are assigned a value of 1, Equation 2-40 reduces to the hereditary integral form of the linear viscoelastic relation derived in the previous section. The graphical representation for the transient and instantaneous component of the creep compliance is illustrated in Figure 2-23.

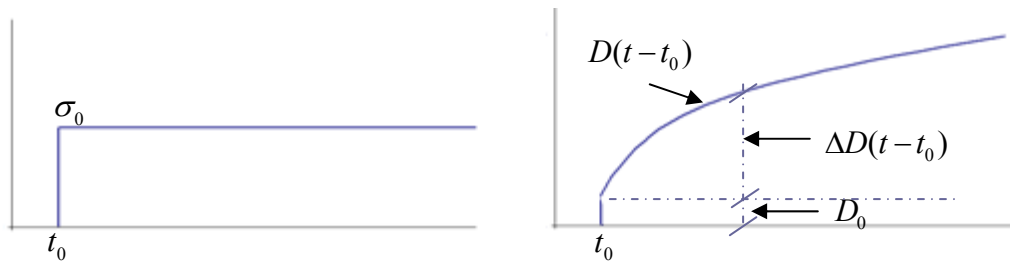


Figure 2-23 Transient and instantaneous creep response

The laboratory tests required for this model are simpler than that required for other nonlinear theories. The nonlinear model parameters for the Schapery model can be obtained from constant creep tests at various stress levels. For a given stress level, the nonlinear parameter $g_1 g_2$ can be obtained by measuring the vertical distance between the linear creep curve and the creep curve at particular stress level. The same principle is also used for the parameter g_0 which represents the nonlinear factor for the time independent part of the compliance curve. Separation of the parameters $g_1 g_2$ involves a two step creep test [43].

Schapery's theory is widely used for nonlinear viscoelastic modelling. This is due to its rigorous theoretical foundation, and the simplicity of the laboratory tests that are required for obtaining the model parameters. For bituminous materials, other forms of nonlinearity, such as aging and moisture effects, have also been suitably incorporated in the theory elsewhere [1, 2, 33].

2.4 Summary

2.4.1 Meso Mechanics

Meso mechanics rely on the fundamental properties of the constituent materials to predict the composite material behaviour. Its application in asphalt concrete modelling has shown promising results. The approach intrinsically allows a more realistic examination of meso structural material response behaviour, such as stresses and strains in the component materials. This analysis provides insight into damage initiation and propagation in asphalt concrete materials. It can therefore provide a powerful tool for optimizing mixture design on the basis of given performance criteria. Since surface distresses, like ravelling, rutting and cracking, are mostly mixture related problems, the resistance of a given asphalt mixture to any of these distress types can best be analyzed using this approach. Meso mechanics has also a potential to minimise the amount of costly asphalt mixture tests that are required for design and control purposes.

Results obtained using FEM or DEM for asphaltic concrete mixes have shown to be comparable. For applications where continuous elements are analyzed, FEM has an advantage over DEM. The later is advantageous to model large displacements where new contacts are created during the simulations.

2.4.2 Response Models

2.4.2.1 Linear Viscoelastic Models

The most commonly used viscoelastic response models in numerical applications are models that comprise linear spring-dashpot combinations. The suitability of any of these models for any particular problem is evaluated based on the model ability to explain laboratory measured response data. The generalized Voigt-Kelvin model and the generalized Maxwell model are the two most widely used models in numerical applications. For applications in bituminous material modelling, the generalized Voigt-Kelvin model and its derivatives (such as the Burgers' model) are widely used. The number of terms to be used is determined based on the quality of the model fit to experimentally obtained data. For bituminous materials, it has been observed that a minimum of 15 to 20 terms are required for proper description of the material behaviour for wide range of loading times.

An alternative approach for modelling viscoelastic materials is the use of models that constitute linear spring, linear dashpot and parabolic dashpot combinations. The constitutive relations for parabolic dashpots involve fractional derivatives of non integer order. As compared to linear spring-dashpot combination models, models that constitute parabolic dashpot have found to be very capable in describing the material response for a wide range of loading times with very few model parameters. Based on applications on bituminous binders, it has been shown that the "equivalent" number of model

parameters required by the generalized Maxwell model to give a comparable quality of fit similar to models that constitute parabolic dashpots is 4 to 5 fold higher. The tremendous reduction in model parameters and the excellent model ability to characterize the response for a wide range of loading times make such models very practical. However, their application in numerical environments is limited mainly due to the higher computational memory required for storing history effects. On the other hand, with the recent increase in computation power of computers, application of these models can be considered practical.

2.4.2.2 Nonlinear Viscoelastic Theory

Among the available nonlinear viscoelastic theories, Schapery's nonlinear theory is the most widely used. The theory is based on rigorous theoretical foundation. In terms of practical considerations, the number of laboratory tests that are required to obtain the nonlinear parameters is reasonable.

Its application in modelling the nonlinear behaviour of bituminous materials has shown good results. In addition to the effects of loading, the form of the theory also allows inclusion of other nonlinearity factors, such as aging and moisture effects on the properties of asphalt concrete materials [6].

Even though the creep and relaxation functions in the theory are commonly represented using the generalized Kelvin-Voigt and the generalized Maxwell models respectively (mainly for numerical reasons), the theory allows implementation of any other response model in the constitutive relation.

References

- [1]. Abbas, A., *Simulation of the Micro-mechanical behavior of Asphalt mixtures using the Discrete Element Method*. 2004, Washington state university.
- [2]. Abbas, A., Masad, E., Papagiannakis, T., and Harman, T., *Micromechanical Modeling of the Viscoelastic Behavior of Asphalt Mixtures Using the Discrete-Element Method*. International Journal of Geomechanics, 2007. 7(2): p. 131-139.
- [3]. Airey, G., Rahimzadeh, B., and Collop, A., *Viscoelastic linearity limits for bituminous materials*. Materials and Structures, 2003. 36(10): p. 643-647.
- [4]. Airey, G.D., Rahimzadeh, B., and Collop, A.C., *Linear Rheological Behavior of Bituminous Paving Materials*. Journal of Materials in Civil Engineering, 2004. 16(3): p. 212-220.
- [5]. Baars, S.v., *Discrete Element Analysis of Granular Materials*. 1996, Delft.
- [6]. Bahia, H., Zhai, H., Bonnetti, K., and Kose, S., *Nonlinear Visco-elastic and Fatigue Properties of Asphalt Binders*. J. Assoc. Asphalt Paving Tech., 1999. 68: p. 1-34.
- [7]. Buttlar, W. and You, Z., *Discrete Element Modeling of Asphalt Concrete: Microfabric Approach*. Transportation Research Record: Journal of the Transportation Research Board, 2001. 1757(-1): p. 111-118.
- [8]. Chang, K.-N.G. and Meegoda, J.N., *Micromechanical Simulation of Hot Mix Asphalt*. Journal of Engineering Mechanics, 1997. 123(5): p. 495-503.
- [9]. Christensen, D.W. and Anderson, D.A., *Interpretation of Dynamic Mechanical Test Data for Paving Grade Asphalt Cements*. J. Assoc. Asphalt Paving Tech., 1992. 61: p. 67-116.
- [10]. Christensen, R.M., *Theory of viscoelasticity: An introduction*. Second edition ed. 1982, New York: Academic press.

- [11]. Collop, A.C., McDowell, G.R., and Lee, Y., *Use of the Distinct Element Method to Model the Deformation Behavior of an Idealized Asphalt Mixture*. International Journal of Pavement Engineering, 2004. **5**(1): p. 1 - 7.
- [12]. Dai, Q. and You, Z., *Prediction of Creep Stiffness of Asphalt Mixture with Micromechanical Finite-Element and Discrete-Element Models*. Journal of Engineering Mechanics, 2007. **133**(2): p. 163-173.
- [13]. Dai, Q. and You, Z., *Micro-mechanical finite element framework for predicting visco-elastic properties of asphaltic mixtures*. J of Materials and Structures, 2008. **41**(6): p. 1025-1037.
- [14]. Dai, Q., Sadd, M.H., and You, Z., *A micro-mechanical finite element model for visco-elastic creep and visco-elastic damage behavior of asphalt mixture*. Int J Numeric Anal Meth Geomech, 2006. **30**: p. 1135-1158.
- [15]. Ferry, J.D., *Viscoelastic Properties of Polymers* 1961: John Wiley
- [16]. Findley, W.N., Lai, J.S., and Onaran, K., *Creep and Relaxation of Nonlinear Viscoelastic Materials with an Introduction to Linear viscoelasticity*. 1976, Amsterdam: North Holland publishing.
- [17]. Flügge, W., *Viscoelasticity*. Second Edition ed. 1975, Berlin.Heidelberg,New York: Springer-Verlag.
- [18]. Green, A.E. and Rivlin, R.S., *The mechanics of non-linear materials with memory*. Archive for Rational Mechanics and Analysis, 1957. **1**(1): p. 1-21.
- [19]. Huet, C., *Etude par une méthode d'impédance du comportement visco-élastique des matériaux hydrocarbonés*. 1963, Faculté des Sciences de Paris: Paris.
- [20]. Hurman, M., *Lifetime Optimisation Tool, LOT, Main Report*. 2008: Delft.
- [21]. Hurman, M., Milne, T.I., and Van de Ven, M.F.C., *Development of a structural FEM for road surfacing seals*, in ICCES. 2003: Curfu, Greece.
- [22]. Hurman, M., Mo, L.T., and Woldekidan, M.F., *Unravelling Porous Asphalt Concrete, Towards a Mechanistic Material Design Tool*. Road Materials and Pavement Design, 2009. **10**: p. 233-262.
- [23]. Hurman, M., Mo, L., and Woldekidan, M., *Mechanistic Design of Silent Asphalt Mixtures*. International Journal of Pavement Research and Technology, 2010. **3**(2): p. 56-64.
- [24]. Hurman, M., Scarpas, T., Kasbergen, C., and T, M. *Development of a structural FEM for Road Surfaceing Seals*. in *International Conference on Computational & Experimental Engineering & Sciences (ICCES' 03)*. 2003. Greece.
- [25]. Hurman, M., Mo, L., Woldekidan, M.F., Khedoe, R.N., and Moraal, J. *Overview of the LOT meso mechanical research into porous asphalt raveling*. in *Proceedings of the 7th Int. RILEM Symposium Advanced Testing and Characterization of Bituminous Materials*. 2009. Rhodes, Greece.
- [26]. Hurman, M., Mo, L., Woldekidan, M.F., Khedoe, R.N., and Moraal, J., *Overview of the LOT meso mechanical research into porous asphalt raveling*. *Advanced Testing and Characterisation of Bituminous Materials, Vols 1 and 2*, 2009: p. 507-518.
- [27]. Jansen, K.M.B., *Thermomechanical modeling and characterization of polymers*. 2006, Delft: TU Delft Lecture Book.
- [28]. Kim, H., Wagoner, M., and Buttlar, W. *Towards Realistic Heterogeneous Fracture Modeling of Asphalt Mixture Using Disk-Shaped Compact Tension Test Based on Discontinuum Approach*. in *Transport Research Board, 85 Annual Meeting*. 2006. Washington, DC, USA.
- [29]. Kose, S., Guler, M., Bahia, H., and Masad, E., *Distribution of strains within asphalt binders in HMA Using Image and finite element techniques*. Journal of Transportation Research Record National Research Council, 2000. **1728**: p. 21-27.
- [30]. Kringos, N., Scarpas, A., and Kasbergen, C., *Three Dimensional Elasto-Visco-Plastic Finite Element Model for Combined Physical-Mechanical Moisture Induced Damage in Asphalt Mixes*. Journal of the Association of Asphalt Paving Technologists 2007. **76**: p. 495-516.
- [31]. Leaderman, H., *Elastic and creep properties of filamentous materials and other high polymers*, in *The Textile Foundation*. 1943: Washington.
- [32]. Lockett, F.J., *Nonlinear viscoelastic solids*. 1972, London: Academic press.

- [33]. Masad, E. and Somadevan, N., *Microstructural Finite-Element Analysis of Influence of Localized Strain Distribution on Asphalt Mix Properties*. Journal of Engineering Mechanics, 2002. **128**(10): p. 1105-1114.
- [34]. Medani, T.O., *Design Principles of Surfacing on Orthotropic Steel Bridge Decks*. 2006, Delft University of Technology: Delft.
- [35]. Mo, L.T., Huurman, M., Woldekidan, M.F., Wu, S.P., and Molenaar, A.A.A., *Investigation into material optimization and development for improved ravelling resistant porous asphalt concrete*. Materials & Design, 2010. **31**(7): p. 3194-3206.
- [36]. Olard, F. and Di Benedetto, H., *General 2S2P1D model and relation between the linear viscoelastic behaviours of bituminous binders and mixes*. Vol. 4. 2003, Paris, FRANCE: Lavoisier. 40.
- [37]. Papagiannakis, A., Abbas, A., and Masad, E., *Micromechanical Analysis of Viscoelastic Properties of Asphalt Concretes*. Transportation Research Record: Journal of the Transportation Research Board, 2002. **1789**(-1): p. 113-120.
- [38]. Pellinen, T. and Oeser, M. *Creep and recovery of linear and nonlinear rheological bodies*. in *Proceedings of the International Conference on Advance Characterization of Pavement and Soil Engineering Materials*. 2007. Athens, Greece.
- [39]. Pronk, A.C., *The Variable Dashpot*. 2003, Ministry of water and transport, Rijkswaterstaat: Delft.
- [40]. Pronk, A.C. *The Huet-Sayegh Model: A Simple and Excellent Rheological Model for Master Curves of Asphaltic Mixes*. 2005. Baton Rouge, Louisiana, USA: ASCE.
- [41]. Rothenburg, L., Bogobowicz, A., Haas, R., Jung, R.W., and Kennepohl, G. *Micromechanical modelling of asphalt concrete in connection with pavement rutting problems*. in *Proceedings of the Seventh International Conference on the Structural Design of Asphalt Pavements*. 1992.
- [42]. Sadd, M.H., Dai, Q., Parameswaran, V., and Shukla, A., *Microstructural Simulation of Asphalt Materials: Modeling and Experimental Studies*. Journal of Materials in Civil Engineering, 2004. **16**(2): p. 107-115.
- [43]. Schapery, R.A., *On the characterization of nonlinear viscoelastic materials*. Polymer Engineering & Science, 1969. **9**(4): p. 295-310.
- [44]. Sepehr, K., Harvey, O.J., Yue, Z.Q., and El Hussein, H.M. *Finite Element Modeling of Asphalt Concrete Microstructure*. in *Proc. 3rd Intl. Conf. Computer-Aided Assessment and Control Localized Damage*. 1994. Udine, Italy.
- [45]. Tschoegl, N.W., *The Phenomenological Theory of Linear Viscoelastic Behavior: An Introduction*. 1989, Berlin, Germany: Springer.
- [46]. Ullidtz, P., *Distinct Element Method for Study of Failure in Cohesive Particulate Media*. Transportation Research Record: Journal of the Transportation Research Board, 2001. **1757**(-1): p. 127-133.
- [47]. Wang, L., Myers, L., Mohammad, L., and Fu, Y., *Micromechanics Study on Top-Down Cracking*. Transportation Research Record: Journal of the Transportation Research Board, 2003. **1853**(-1): p. 121-133.
- [48]. Woldekidan, M., Huurman, M., and Mo, L., *Testing and modeling of bituminous mortar response*. Journal of Wuhan University of Technology--Materials Science Edition, 2010. **25**(4): p. 637-640.
- [49]. Zelelew, H.M. and Papagiannakis, A.T., *Micromechanical Modeling of Asphalt Concrete Uniaxial Creep using the Discrete Element Method*. International Journal of Road Materials and Pavement Design, 2010. **11**(3): p. 613-632.

3

Research Methodology

Chapter 1 and 2 outlined the potential and advantages of meso mechanics approach for gaining insights into top layer distresses. The approach can be an excellent tool for designing better performing AC mixtures against top-layer distresses such as ravelling, rutting and cracking. Results that were obtained from meso mechanistic PA design tool have shown to be very capable in explaining the ravelling phenomenon in PA surface wearing courses [8].

It is known that regardless of the distress type being investigated, the results obtained from a meso mechanistic approach mainly rely on three important factors, which are:

- The loading
- The geometry
- The material behaviour

Based on the knowledge obtained during the development of a PA design tool, it has been shown that a fairly accurate representation of the traffic loading can be obtained by analyzing the contact stress distribution between the wheel and the pavement. The contact stress distribution has previously been studied in detail by De Beer et al. [3]. Effect of the environmental loading on the properties of the binders has also been investigated in detail by Hagos [5]. With regard to the meso scale geometry, reasonable representations can be made through a volumetric analysis [9]. More accurate 2D and 3D meso scale geometries of the mixture can also be obtained through CT scan analyses [1, 9]. The different components in the mixture need to be described using different material behaviour. Since the likelihood of aggregate crushing in the mixture is very low, a rigid body assumption was made for the aggregates in the mixture. Modelling interface layers were realized by assigning normal and shear

stiffness parameters to a thin adhesive layer around the aggregates. For the bituminous binder a linear viscoelastic assumption was made.

From the results, it has been learned that complex stress and strain signals occur in the bituminous mortar and adhesive zone within a PA mixture. The magnitude and shape of the stress signals vary from one location to the other. The wide ranging of loading rates within the mortar domain implies that the viscoelastic response models used in the PA design tool are required to reflect the change in response characteristics of the mortar accordingly. In addition to the loading rates, the material response models need to reflect the response characteristics of the mortar for any existence of stress dependent behaviour. For future application in solving rutting related problems, it has also been emphasized that response models that incorporate viscous deformation component are required. Based on these observations it was concluded that an appropriate response model that can fulfil the aforementioned demands needed to be sought. The response model available in the ABAQUS material library, the Prony series, does not fulfil all these demands for various reasons. As explained in the literature review section, the Prony series model in ABAQUS is meant for viscoelastic solid materials. In addition, the model is linear viscoelastic and hence does not incorporate any stress dependent behaviour of the mortar.

The research goal of this study is therefore focused in obtaining an appropriate response model for the bituminous mortar. The model is also required to be implemented in the commercially available FE program, ABAQUS. The response model is mainly meant for use in meso mechanics applications for asphalt concrete materials. However, it can also be equally applicable for other applications in modelling asphalt concrete materials.

3.1 Research Approach

3.1.1 Setting the Demands

Based on the literature review and the first findings of the LOT design tool for PA, the following points are regarded important in setting the demands for the mortar response model:

- In the majority of cases, surface distresses such as ravelling and surface cracking are observed after millions of single load repetition. In comparison to the total amount of damage, the damage as a result of a single load application can therefore be considered insignificant.
- In relation to the above point, material response characterization in the laboratory should exclude any presence of damage in the response data.
- Asphalt mixtures in general exhibit features of viscous, elastic and viscoelastic behaviour. Thus material response models need to incorporate elements that can simulate elastic, viscous and viscoelastic behaviour.

- For reasons of practicality, those types of response models are preferred that combine best response characterization features with the fewest possible model parameters.
- For material response characterization in the nonlinear viscoelastic range, simplicity in the required number of tests and model parameter determination, and the model accuracy are of paramount importance to guarantee practical application of the design tool.

It appears that the built-in viscoelastic material model in ABAQUS, the Prony series, does not fully fulfil the criteria set for the mortar response model. Its' first limitation is that it is a linear viscoelastic model, and hence it does not incorporate any nonlinear behaviour. The second drawback is the lack of a response element for simulating viscous deformation in bituminous materials. As discussed in the literature review, the Prony series in ABAQUS is fundamentally meant for modelling linear viscoelastic solids. To allow simulation of viscous deformations, the general form of the Prony series (the Prony series model with the absence of the parallel spring, also called the general Maxwell model) needs to be used. This can be practically achieved by assigning a small model parameter to the parallel spring. However, for characterizing stress controlled experimental data, the analytical form of the Prony series is not convenient. The alternative material model, with a suitable analytical expression for characterizing stress controlled response data, is the generalized Burgers' model. This model is commonly used for modelling bituminous material response. However, application of this model and inclusion of any additional nonlinearity effects in the ABAQUS material library requires writing separate user material subroutines.

3.1.2 Selected Response Models

There are a number of viscoelastic models available in literature. None of these models can be considered as being universal. Suitability of any of these models for a particular problem is judged based on the model ability to fulfil specified demands that are deemed important in addressing any particular problem. For asphalt concrete mixtures, most commonly used response models comprise elements of a linear spring-dashpot combination. These kinds of models are preferred for their efficiency in numerical environments. Other category of response models comprises elements of a linear spring-dashpot and a parabolic dashpot combination. Models of the later category are powerful in describing material response for wide range of loading times. They also require very few model parameters, and hence they are very practical for use. However, their computational power demand in numerical environments is higher.

For modelling mortar response, one candidate response model from each category is selected. In the selection process, more attention is given to the important points listed in Section 3.2.1. The two selected models are the

Burgers' model and the Huet-Sayegh model. These models are widely used for pavement design purposes; multilayer pavement design programs like VEROAD [6] and ViscoRoute [2] include either one or both models in their material model library.

For implementing the nonlinear behaviour of the mortar, a suitable nonlinear theory has also been selected from literature. A short review of the selected models and nonlinear theory are given below.

3.1.2.1 Burgers' Model

The Burgers' model shown in Figure 3-1 is a commonly used response model for modelling the response of asphalt concrete materials. Its preferred use is due to a number of reasons: first, it is capable in simulating all the important response characteristics asphalt concrete materials, i.e. elastic, viscous, and viscoelastic. The second reason, like all other spring-dashpot combination models is that it is computationally efficient in numerical environments. In addition, it is suitable for response characterization in stress controlled mode. The model is used in various viscoelastic pavement design programs [6, 17].

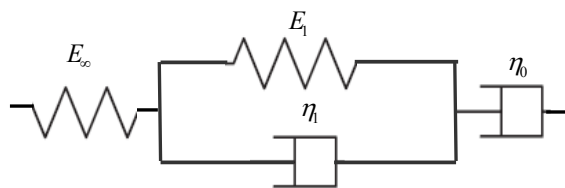


Figure 3-1 Burgers' model

The main drawback of the Burgers' model is that for a given set of model parameters it can correctly describe the response of the material only for a limited frequency window. For applications where the loading rate within the material varies tremendously from one location to the other, application of Burgers' model results in a very severe limitation.

3.1.2.2 Huet-Sayegh (HS) Model

The HS model is an excellent model for AC mixture modelling. Its distinct feature as compared to other response models is its ability to describe AC mixture response for wide range of loading rates with very few model parameters. In describing a master curve data covering wide range of temperatures, the number of model parameters required to obtain comparable quality of results can usually be 4 to 5 times higher if models of linear spring-dashpot combinations, such as Prony series, are used. The other advantage of the HS model is that the model parameters determination are straight forward and can easily be performed using regression analysis in spreadsheet programs like Excel.

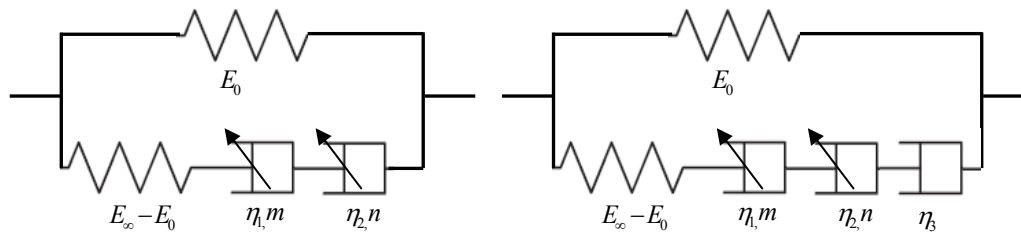


Figure 3-2 HS model (left) and 2S2P1D model (right)

The only disadvantage of the HS model is the absence of a response element to simulate viscous deformations. It is, therefore, fundamentally suited to model viscoelastic solid materials. A later version of HS model, the 2S2P1D model [15], has an additional linear dashpot element in one branch of the HS model (Figure 3-2). The purpose of this linear dashpot is to improve the low frequency fit of the model to an experimentally obtained response data. The general behaviour of the model is therefore fundamentally similar to the original HS model.

3.1.3 Schapery's Nonlinear Theory

At high stress levels, bituminous materials exhibit nonlinear behaviour. Among the available nonlinear viscoelastic theories in literature, Schapery's nonlinear theory is widely used. As presented in the literature review section, the theory is developed based on a sound theoretical background, and it is relatively simple in form as compared to other nonlinear theories [18]. Schapery's theory requires a reasonable number of laboratory tests for model parameter determination. In terms of practicality, this is advantageous as compared to other nonlinear theories, such as the Green and Rivlin theory [4], which requires an impractical number of laboratory tests for obtaining model parameters. Literature has also shown that the Schapery's theory is very convenient to incorporate nonlinearity arising from other factors such as aging and moisture effects [13]. Because of these advantages, the theory is selected for use in meso mechanics applications in this research.

3.2 Methodology

The research approach involves experimental and numerical works. The experimental part involves obtaining the response of the bituminous binders for various loading conditions. In this research only mechanical loadings are considered. Effects of environmental loadings such as aging and moisture effect on binder properties are discussed elsewhere [5, 11]. The numerical work makes use of response data obtained from the laboratory for developing the selected response models. The selected models need also be formulated in an incremental approach for implementation into the commercially available FE program, ABAQUS. The model's use in analyzing PA behaviour will be demonstrated. Effects of nonlinear behaviour on the computed results will also be evaluated. Figure 3-3 illustrates the general research layout.

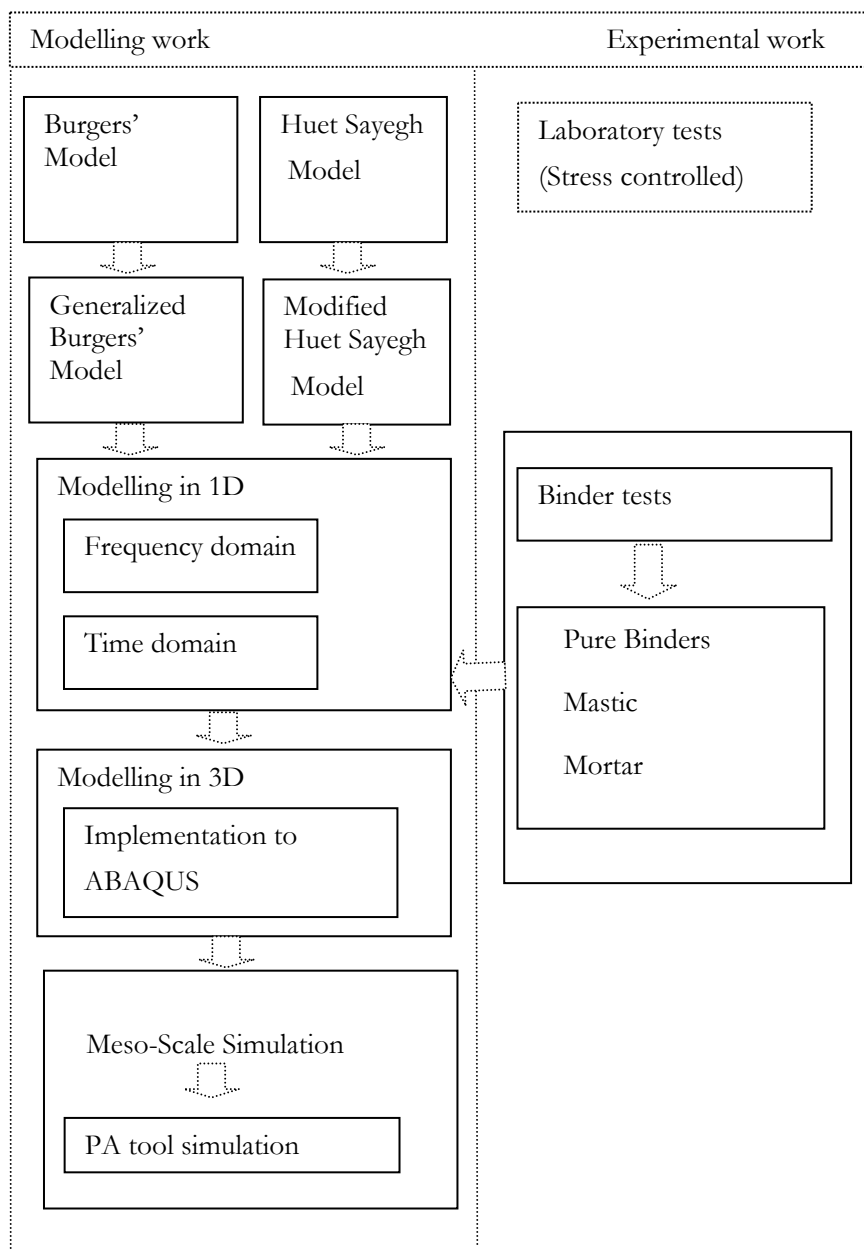


Figure 3-3 Research layout

3.2.1 Experimental Work

3.2.1.1 Stress Controlled vs. Strain Controlled Tests

Both stress controlled and strain controlled tests are widely used to obtain material response data in the laboratory. Since the material properties are intrinsic, different material properties obtained under different test conditions are related to each other. In cases where material response data are not feasible in strain controlled situation, stress controlled tests can provide the necessary information and vice versa. Its implication on the choice of mechanical models is that one model may appear analytically more convenient for describing a

stress controlled data while the other is better suited to describe strain controlled data. For example, the generalized Maxwell model is widely used for characterizing results from strain controlled tests while, the generalized Burgers' model is used for results obtained from a stress controlled test. In this research, the majority of the laboratory tests on the bituminous mortar are performed in the stress controlled mode.

3.2.1.2 Time Domain vs. Frequency Domain Tests

In general laboratory investigations of viscoelastic materials are conducted in the time and frequency domain. Time domain measurements provide material response data from intermediate to long loading durations. Frequency domain tests are used to obtain material response for short loading periods. It has been reported that applying a constant stress or strain to a test sample in practice takes a finite time (typically 0.1 to 1 second) [10]. As a result material response for short loading periods, less than 0.1 to 1 seconds, cannot be accurately obtained from time domain test data. In reality, the pavement layer is subjected to traffic loading at a high speed. The loading time for a vehicle travelling at 80 to 100 km/hr is in the order of 0.01 seconds. The relevant response data of the bituminous mortar should therefore be obtained at short loading periods. Because of this reason, the experimental works for obtaining response behaviour of the mortar and bituminous binders in this research are mainly conducted in the frequency domain.

3.2.2 Modelling Work

3.2.2.1 Basic Assumptions

When loads are applied to a bituminous material, time dependent deformation behaviour is observed. Practice has shown that in comparison to shear deformation, volumetric deformation component of a well compacted asphalt mixture is insignificant [14, 19, 20]. From this it follows that time dependency of the volumetric deformation can reasonably be considered to have little significance. In case of oily substances like bituminous binders the resistance to volumetric deformation is even higher due to the high bulk modulus of the material. The bulk modulus of the mortar can therefore be considered time independent. In modelling the mechanical behaviour of bituminous materials, only the shear modulus is commonly considered to possess time dependent behaviour [6, 7, 16].

The modelling assumption used in this research also follows a similar approach. In the constitutive formulations the stresses and strains within the loaded body are decomposed into shear and volumetric components. Based on the above discussion, the volumetric deformation of the mortar is considered time independent. The shear deformation will be modelled as time dependent.

3.2.2.2 Response Modelling

The response modelling work is divided in two sections. The first section deals with modelling of material response in the linear viscoelastic range. In this section the two candidate response models selected in the previous section will be used to describe experimentally obtained data. In the second section, the models will be incorporated to a nonlinear viscoelastic theory so as to describe any nonlinearity that might arise as a result of high stresses.

Linear Viscoelastic Range

The selected models will be used to explain the experimentally obtained data. Based on the demands set for the mortar response model, appropriate modifications are also made.

As discussed in previous section, the main drawback from the HS model is the lack of a viscous response element and its difficulty in numerical application. The model is however, capable in characterizing the response for a wide range of loading rates with few parameters. In the case of the Burgers' model, the main limitation is its response characterization for narrow frequency; its use in numerical environments on the other hand is efficient.

Considering the pros and cons of both models, the following two approaches are proposed to suit the demands set in the Section 3.2.1:

1. HS model

Modify the original HS model with a linear dashpot in series so as to provide viscous response component. Investigate ways to numerically implement the model in ABAQUS and evaluate the model efficiency in a FE environment.

2. Burgers' model

Utilize the generalized form of the Burgers' model so as to enable the model to simulate the response of the bituminous materials for a wide range of loading frequencies.

These two models will be made available in the ABAQUS material library. The availability of the alternative material models in ABAQUS library provides flexibility for the user in choosing between the generalized Burgers' model and modified HS model. The models' suitability in terms of numerical efficiency, model prediction accuracy and ease of use will also be discussed.

Nonlinear Viscoelastic Range

For modelling the nonlinear response of the bituminous mortar, Schapery's nonlinear theory will be used. For this theory, numerical formulation techniques are available in literature. These formulations incorporate the generalized Burgers' model in the nonlinear theory [12]. This formulation will be adopted for use. In this work, the modified HS model application is limited

to linear viscoelastic domain. Main reason for the limitation is attributed the model suitability (computational efficiency) in nonlinear analysis. Further details are given in the relevant chapters ahead.

References

- [1]. Abbas, A., Masad, E., Papagiannakis, T., and Harman, T., *Micromechanical Modeling of the Viscoelastic Behavior of Asphalt Mixtures Using the Discrete-Element Method*. International Journal of Geomechanics, 2007. **7**(2): p. 131-139.
- [2]. Chabot, A., Tamagny, P., Duhamel, D., and Poche, D. *Viscoelastic modeling for asphalt pavements- software ViscoRoute*. in *Proceedings of the 10th international conference on asphalt pavements*. 2006. Quebec, Canada.
- [3]. De Beer, M., Fisher, C., and Jooste, F.J. *Determination of Pneumatic/Pavement Interface Contact Stresses Under Moving Loads and Some Effects on Pavement with Thin Asphalt Surfacing Layers*. in *Proceedings of the Eighth International Conference Structural Design of Asphalt Pavements*. 1997. USA.
- [4]. Green, A.E. and Rivlin, R.S., *The mechanics of non-linear materials with memory*. Archive for Rational Mechanics and Analysis, 1957. **1**(1): p. 1-21.
- [5]. Hagos, E.T., *The Effect of Aging on Binder Properties of Porous Asphalt Concrete*. 2008, Delft.
- [6]. Hopman, P.C., Nilsson, R.N., and Pronk, A.C. *Theory, Validation and Application of the Visco-Elastic Multilayer Program VEROAD*. in *Proceedings of the eight International Conference on Asphalt Pavements*. 1997. Seattle, USA.
- [7]. Huang, Y.H. *Stresses and displacements in viscoelastic layered systems under circular loaded areas*. in *Proc.2nd Internat.Conf., Structural Design of Asphalt Pavements*. 1967. Univ.of Mich.
- [8]. Huurman, M., Mo, L., and Woldekidan, M.F., *Porous asphalt ravelling in cold weather conditions*, in *ENVIROAD 2009, 2nd International Conference on Environmentally Friendly Roads*. 2009: Warsaw, Poland.
- [9]. Huurman, M., Mo, L., and Woldekidan, M., *Mechanistic Design of Silent Asphalt Mixtures*. International Journal of Pavement Research and Technology, 2010. **3**(2): p. 56-64.
- [10]. Jansen, K.M.B., *Thermomechanical modeling and characterization of polymers*. 2006, Delft: TU Delft Lecture Book.
- [11]. Kringos, N., Scarpas, A., and Kasbergen, C., *Three Dimensional Elasto-Visco-Plastic Finite Element Model for Combined Physical-Mechanical Moisture Induced Damage in Asphalt Mixes*. Journal of the Association of Asphalt Paving Technologists 2007. **76**: p. 495-516.
- [12]. Lai, J. and Bakker, A., *3-D schapery representation for non-linear viscoelasticity and finite element implementation*. Computational Mechanics, 1996. **18**(3): p. 182-191.
- [13]. Masad, E. and Somadevan, N., *Microstructural Finite-Element Analysis of Influence of Localized Strain Distribution on Asphalt Mix Properties*. Journal of Engineering Mechanics, 2002. **128**(10): p. 1105-1114.
- [14]. Nilsson, R., Oost, I., and Hopman, P., *Viscoelastic Analysis of Full-Scale Pavements: Validation of VEROAD*. Transportation Research Record: Journal of the Transportation Research Board, 1996. **1539**(-1): p. 81-87.
- [15]. Olard, F. and Di Benedetto, H., *General 2S2PID model and relation between the linear viscoelastic behaviours of bituminous binders and mixes*. Vol. 4. 2003, Paris, FRANCE: Lavoisier. 40.
- [16]. Perloff, W.H. and Moavenzadeh, F. *Deflection of viscoelastic medium due to a moving load*. in *Proc.2nd Internat.Conf., Structural Design of Asphalt Pavements*. 1967. Univ.of Mich.
- [17]. Scarpas, A., *CAPA-3D Finite elements system-User's manual*. 1992, Delft.

- [18]. Schapery, R.A., *On the characterization of nonlinear viscoelastic materials*. 1969, Society of Plastics Engineers, Inc. p. 295-310.
- [19]. Weissmann, S., Harvey, J.T., Sackman, J.L., and Long, F. *Selection of Laboratory Test Specimen Dimension for Permanent Deformation of Asphalt Concrete Pavements*. in *Transportation Research Record 1681*. 1997. Washington D.C.
- [20]. Weissmann, S.L., *The Mechanics of Permanent Deformation in Asphalt-aggregate Mixtures: a Guide to Laboratory Test Selection*. 1997, Symplectic Engineering Corporation.

4

Materials, Experiments and Results

From the literature review presented in Chapter 2 it has been learned that complex stress and strain signals occur in the bituminous mortar within a PA mixture. The magnitude and rate of the stresses vary from one location to the other. The wide range in loading rates within the mortar implies that the response models need also to reflect the change in response characteristics of the mortar accordingly.

In order to obtain sufficient response data for the modelling work, an extensive experimental program has been carried out. The details of the laboratory investigation work are presented in this chapter. The chapter begins with a description of the materials that are used in the research. The sections that follow present a thorough description of the experimental setups and discuss the relevant data interpretation techniques. In the last sections of the chapter, the results of the experimental investigation are presented.

4.1 Materials

4.1.1 Bitumen

Two types of bitumen are used in this research; bitumen pen grade 40/60 (hereafter referred as B40/60) and bitumen pen grade 70/100 (hereafter referred as B70/100). These two binders are commonly used in road construction in the Netherlands. B70/100 is commonly used in PA surface layers. The source and properties of these two binders are given in Table 4-1 below.

Table 4-1 Source and types of bitumen used in the research

	Pen [0.1 mm]	Softening Point [°C]	Penetration Index	source
Bitumen 40/60	42	50	-1.57	Q8: Kuwait Petroleum B.V.
Bitumen 70/100	93	45	-1.01	Q8: Kuwait Petroleum B.V.

4.1.2 Mastic

Mastic is a combination of filler material and pure bitumen. For this research one type of mastic is considered in the test program. To match the type of the materials commonly used in PA layers, the B70/100 bitumen is selected for the mastic. The filler composition comprises of fine fractions with a maximum grain size of 63 microns. The weight percentages of the bitumen and filler in the mastic are determined based on the Dutch RAW specifications (RAW 2005 [12]) for PA mixtures. As per the standard a bitumen-filler ratio of 1:1 by weight is considered. The compositions of the mastic are given in Table 4-2.

Table 4-2 Mastic composition

	Type of Bitumen	Filler type	B:F ratio
Mastic	70/100	Wigro 60K	1:1

The filler type used in the mastic, Wigro 60K, is limestone filler with 25% calcium hydrate (lime).

4.1.3 Mortar

Mortar is a combination of bitumen, filler and fine sand. The fine sand in the mortar has a maximum grain size of 0.5mm. This is based on an earlier PA aggregate skeleton study [10] that showed the bituminous mortar in the top layer of a PA mixture contains sand fractions smaller than 0.5 mm. Similar to the procedure that was followed to determine the mastic composition, the RAW specifications [12] for PA is used to obtain the weight proportions. Table 4-3 shows the selected PA mixture composition as per the RAW specification, from which the mortar composition is derived.

Table 4-3 PA mixture composition [12]

Sieve size(mm)	Density (Kg/m ³)	RAW spec.% Retained	ret.by weight	Cumm. % ret.	%ret.w bit	Cumm.% ret.w.bit
C22.4-16.0	2778	0-5	2.5	2.5	2.40	2.39
C16.0-11.2	2774	15-30	20	22.5	19.14	21.53
C11.2-8.0	2762	50-65	35	57.5	33.49	55.02
C8.0-5.6	2765	70-85	20	77.5	19.14	74.16
C5.6-2.0	2677	85	7.5	85	7.18	81.34
2.0-0.063	2781	95.5	10.5	95.5	10.04	91.38
<0.063 (Filler)	2720	100	4.5	100	4.30	95.69
				100		95.69
Bitumen	1030	4.50%	4.5	104.5	4.30	100

The crushed sand with the gradation given in Table 4-4 (left) was used as a source. Through sieve analysis, a sand gradation with a maximum size of 0.5mm was obtained. The final composition of the mortar, by weight percentage, is given as shown in Table 4-4 (right).

Table 4-4 Crushed sand (left) and final mortar composition by weight (right)

Sieve size (mm)	% retained	Cumm. % ret.	Mortar components	% wt
2.0	8.2	8.2	Sand<0.5mm	34.8
0.5	49.0	57.2	Wigro 60K filler	32.6
0.18	28.4	85.7	Bitumen(B70/100)	32.6
0.063	12.6	98.2		
<0.063	1.8	100.0		

Like the case for the mastic, Table 4-4 also shows that for the mortar the filler-binder ratio of 1:1 by weight is kept unaltered.

4.2 Experimental Setups and Descriptions

4.2.1 Setting the Framework

To obtain good results from meso mechanistic performance models, it is important that laboratory response investigations reasonably cover the ranges of loading conditions the binder experiences in real pavements. Finite element

simulations of a moving wheel on PA mixtures showed that the mortar in the mixture is subjected to a complex 3D state of stress and strain. The magnitude and rate of the stresses and strains within the mortar varies from one location to the other within the mixture structure. This implies material response models used in PA performance models need to represent the material response behaviour for various loading conditions (stress levels, loading frequency and temperatures).

In characterizing the material response in the laboratory, it is also important that the field loading times are simulated as good as possible. The loading times for a single wheel passage are usually very short, in order of 0.01 seconds (for vehicle speed of 80 km/hr). Obtaining accurate material response data for such short loading times requires conducting frequency domain tests.

The experimental work in this research therefore aims to obtain the response of the binder, mastic and mortar for various stress levels at various loading rates and temperatures. For the reason discussed above, the major part of the experimental work is performed in the frequency domain. For this purpose the Dynamic Shear Rheometer (DSR) has been utilized. Detailed descriptions of the experimental setups used in testing the materials, i.e. the bitumen, mastic and mortar, are presented below. The result interpretation methods are also discussed.

4.2.2 The Dynamic Shear Rheometer

The DSR is commonly used to determine the rheological properties of viscoelastic materials. In road engineering the DSR is used to determine the complex shear modulus and phase angle of bituminous binders at different temperatures and frequencies. For this research, a DSR machine AR2000ex is used (Figure 4-1). This machine has a torque capacity of up to 0.2 Nm. The machine is equipped with an Environmental Test Chamber (ETC). The ETC is a test cabinet with an accurate temperature control system based on electrical heating and gas cooling (using a liquid nitrogen storage vessel). This allows a wide range of test temperatures varying from -150 °C up to +350 °C.



Figure 4-1 DSR environmental test chamber(left); Liquid Nitrogen vessel(right)

4.2.2.1 Standard Test Methods

The standard testing procedure to obtain the response of bituminous binders involves a small sample of bituminous binder sandwiched between two parallel plates, also called test geometries. The specimen size and plate diameter to be used depend upon the temperature. Usually a specimen size of 1 mm thickness and 25 mm in diameter is used for intermediate to high temperatures. For low to intermediate temperatures a specimen size with a thickness of 2 mm and an 8 mm plate diameter are used. During the test, a defined oscillating torque is applied on the upper plate while the lower plate remains fixed and the angular rotation is measured. Interpretation of the applied torque and the measured deformations provide the material response information. The interpretation process includes adjusting the raw data for the system factors that include inertia effects and machine compliance factors. These factors are determined in the calibration step before the test is executed. By taking into account all these factors the torque and angular rotation signals deliver fundamental material properties such as complex shear modulus $|G^*|$, complex shear compliance $|J^*|$, and the phase angle δ . Figure 4-2 illustrates the DSR test setup and the test principles.

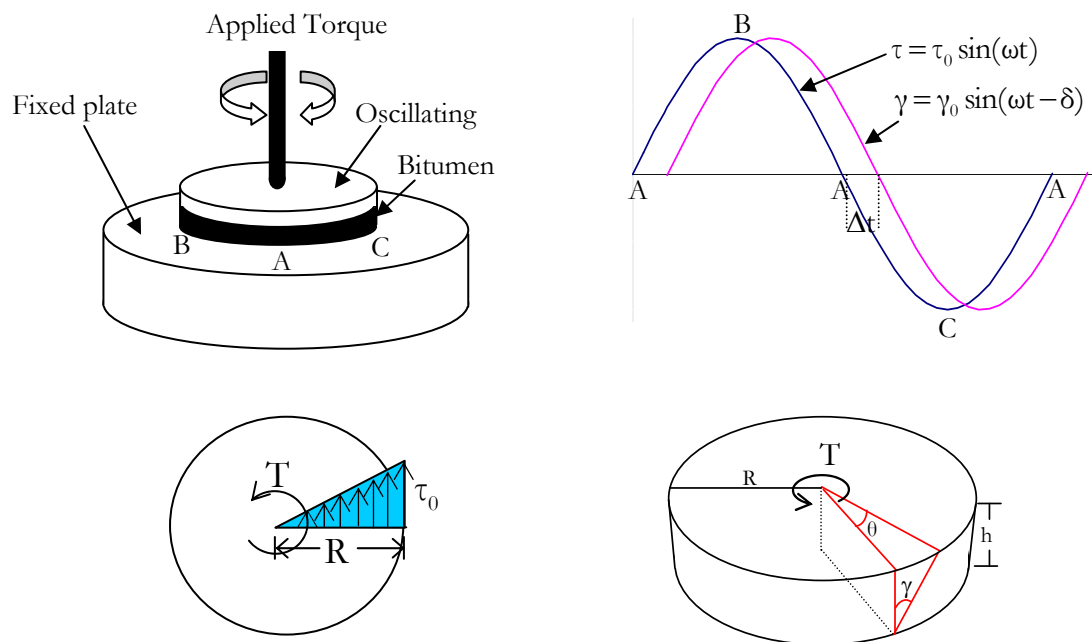


Figure 4-2 DSR test set-up and principles

The strain and the stress values reported by the DSR machine are those at the rim of the test sample. Equation 4-1 to Equation 4-3 present the basic relations used for obtaining the fundamental material properties.

$$\gamma_{\max} = \frac{\theta R}{h} \quad \text{and} \quad \tau_{\max} = \frac{2T}{\pi R^3} \tag{4-1}$$

$$|G^*(\omega)| = \frac{\tau_{\max}}{\gamma_{\max}} ; \tag{4-2}$$

$$G^*(\omega) = |G^*(\omega)| \cos \delta + i |G^*(\omega)| \sin \delta = G' + iG'' \tag{4-3}$$

$$\delta = \omega \Delta t = \text{atan}(G''/G') \tag{4-3}$$

where:

- R = radius of the cylindrical sample [mm]
- h = height of the cylindrical sample [mm]
- T = is the applied Torque [N.mm]
- θ = rotation [rad]
- τ_{max} = maximum shear stress [MPa]
- γ_{max} = maximum shear strain [-]
- |G*| = magnitude of the complex shear modulus [MPa]
- G' = storage shear modulus [MPa]

- G'' = loss shear modulus [MPa]
 i = complex notation
 Δt = phase lag between the stress and strain signals [s]
 δ = phase angle of the material for a given frequency, ω , [°]

For stress controlled tests, the creep compliance of the material is of interest. The following relations are used to determine the shear compliance in a DSR test.

$$|J^*(\omega)| = \frac{\gamma_{\max}}{\tau_{\max}} \quad 4-4$$

$$J^*(\omega) = |J^*(\omega)| \cos \delta + i |J^*(\omega)| \sin \delta = J' + iJ''$$

where:

- τ_{\max} = maximum shear stress [MPa]
 γ_{\max} = maximum shear strain [-]
 $|J^*|$ = magnitude of the complex creep compliance [MPa]
 J' = storage creep compliance [MPa]
 J'' = loss creep compliance [MPa]
 i = complex notation
 δ = phase angle of the material for a given frequency, ω , [°]

As illustrated in Figure 4-2 the shear stress and shear strain distribution across the diameter of the cylindrical test sample is not uniform. The test setup is basically meant for response measurements at very low stress levels where the material is assumed to have linear viscoelastic behaviour. However, for measurements at higher stress levels, where the bitumen response is likely to become nonlinear, the non uniform nature of the stress distribution across the sample geometry makes interpretation very difficult. One possibility to obtain a uniform stress distribution across the diameter of the sample is to conduct uniaxial dynamic tests. However, this option is not possible with the available AR2000ex DSR machine with which only dynamic shear can be conducted. With this limitation, the second possibility is to utilize a different test-geometry to obtain a uniform shear stress distribution. Due to the geometrical advantage, a cone and plate setup geometry has been used for this purpose.

4.2.2.2 The Cone and Plate Setup

A) Description of the Test Setup

The geometrical advantage of the Cone and Plate (CP) setup is that it provides a uniform shear rate and uniform shear stress distribution throughout the test sample. When cone angles are low, the variation of the shear rate across the diameter is very small. As the cone angle increases, the accuracy decreases. The setup is commonly used for viscosity measurements for homogeneous samples. The disadvantage of this setup is that the gap between the cone and plate cannot be varied. The shear rate factor for each cone is therefore fixed. The standard angles provided for viscosity measurements are 0.5°, 1.0°, 2.0° and 4.0° with a 40 mm diameter plate. The tip of the cone is usually trimmed to avoid possible variations in results associated with the sharp contact area. Figure 4-3 illustrates the setup for the cone and plate test.

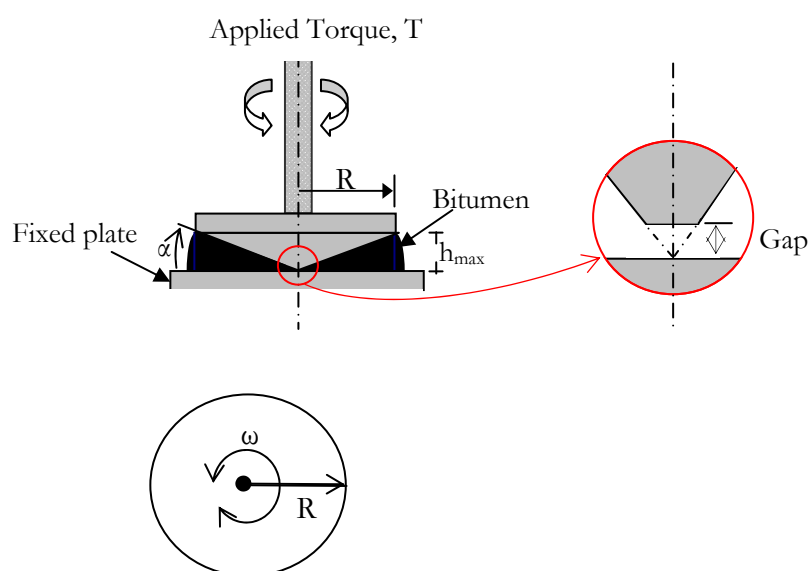


Figure 4-3 Cone and Plate test set-up

For the CP setup the shear strain rate can be obtained as a function of the cone angle at a given rotational speed. The shear stress is obtained from the applied torque. Equation 4-5 and Equation 4-6 present the relationships that are used to obtain the shear strain rate and shear stress respectively.

$$\dot{\gamma} = \frac{\omega}{\tan \alpha} \quad 4-5$$

$$\tau = \frac{3T}{2\pi R^3} \cos \alpha \quad 4-6$$

where:

R = cone radius [mm]

α = cone angle [°]

T = is the applied torque [N.mm]

τ = shear stress [MPa]

For measurements at intermediate and low temperature regions, the standard cone geometries with 40 mm diameter would require a much higher torque capacity than what is possible with the AR2000ex DSR machine. Table 4-5 presents the maximum shear capacity that can be achieved when the various standard geometries are used.

Table 4-5 Maximum shear stress for standard CP geometries

Torque [N-mm]	R [mm]	τ_{\max} [MPa]	Cone angle [°]
200	12.5	0.0489	0.5-4
200	20	0.0119	0.5-4
200	30	0.0035	0.5-4

The maximum values of the shear stresses that can be obtained using the standard geometries are well below the desired values. From previous meso mechanistic computations [6], much higher shear stress values are reported in the mortar domain of PA mixture. To achieve higher shear stress values in the DSR test, smaller diameter cones are developed for this project. Similar to the standard PP geometries, an 8 mm diameter and a 25 mm diameter cones were designed for measurements at low and high temperature regions respectively. The maximum sample height at the rim of the cones is 2 mm and 1 mm for the 8 mm diameter and 25 mm diameter cone respectively. Figure 4-4 shows the 8 mm and 25 mm diameter geometries in a DSR setup.

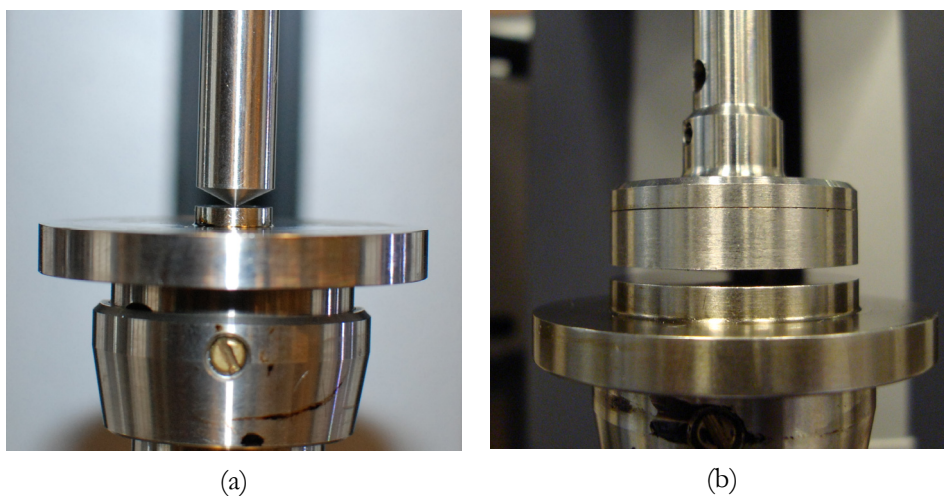


Figure 4-4 CP setup, 8 mm diam. (left) and 25 mm diam. (right)

For the selected geometries Table 4-6 presents the maximum shear stress that can be achieved in the test setup.

Table 4-6 Maximum shear stress for the 8 mm and 25 mm diameter CP geometries

Torque [N-mm]	R [mm]	τ_{\max} [MPa]	Cone angle [°]	h_{\max} [mm]	Gap [μm]
200	4	1.33	26.565	2	65
200	12.5	0.05	4.574	1	65

B) Numerical Evaluation

A Finite Element (FE) model has been utilized to evaluate the stress uniformity within the test sample. For this purpose FE models of the cone and plate setup were prepared. By applying an oscillating torque, the resulting stress and strain distribution within the sample can be evaluated. Figure 4-5 illustrates the FE model for the 8mm diameter CP setup.

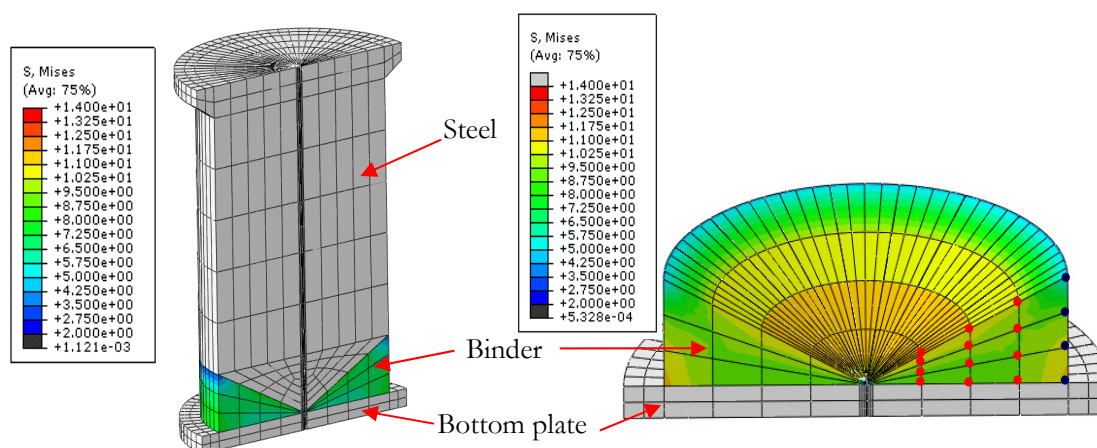


Figure 4-5 von Mises stress in a CP setup (left: section of the test setup, right: part of the test material with the top steel rod removed)

For a sinusoidal varying applied torque the resulting shear stress values at various nodal locations, which are marked with dots in Figure 4-5, are plotted together in Figure 4-6 and Figure 4-7. Due to edge effects, the stress value obtained for the nodal points at the outer periphery, located at a height of 2 mm from the bottom plate, is nearly half the value obtained for other nodal points (Figure 4-6). Apart from these locations, the shear stress values obtained at all the other nodes are very comparable. Figure 4-6 presents the stress values obtained at all nodal points plotted together. When the nodal points located in the outer periphery of the sample are excluded, Figure 4-7 is obtained.

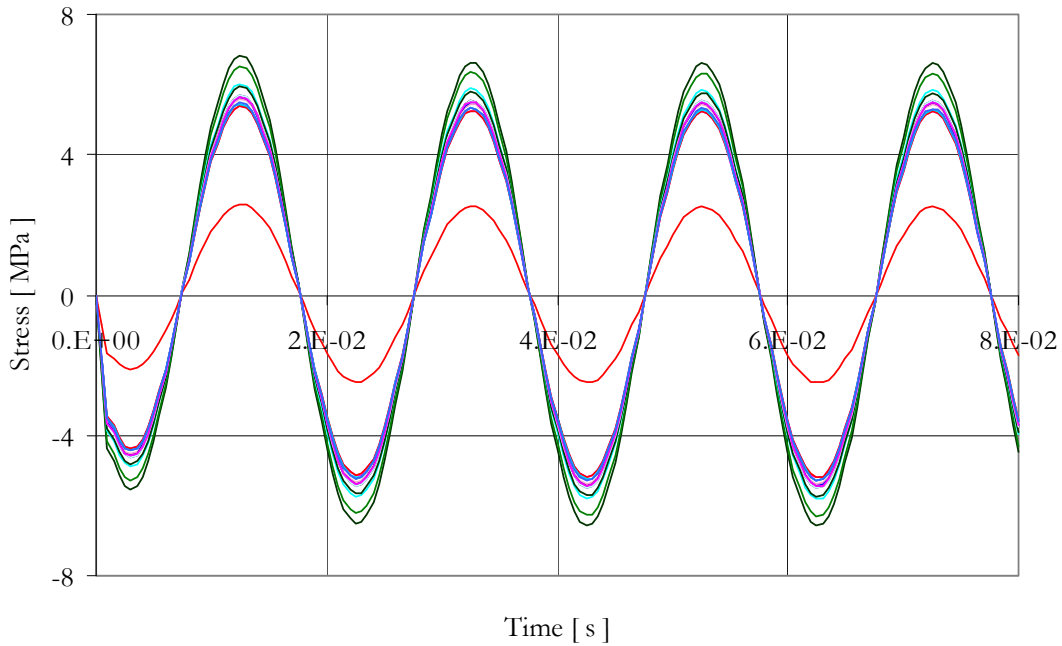


Figure 4-6 Shear stress signals obtained at various nodal points

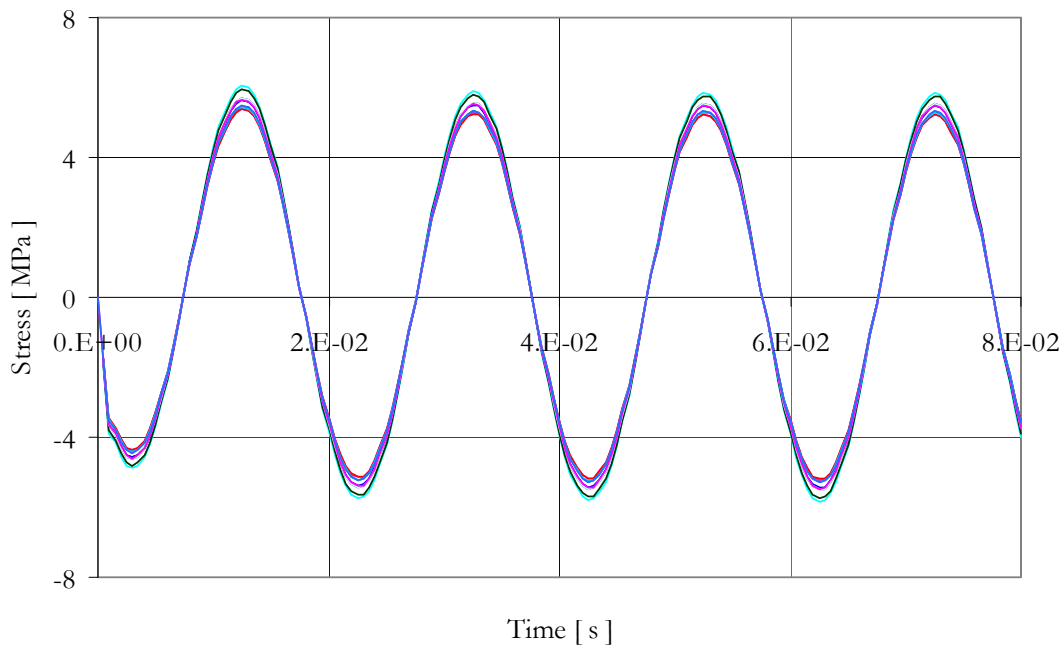


Figure 4-7 Shear stress signals obtained at various nodal points (results at the outer periphery of the sample excluded)

From Figure 4-6 and Figure 4-7 it can be seen that the CP setup delivers a uniform shear stress distribution within the test specimen. Apart from the stress distribution at the nodal points located at the outer periphery of the test sample, the stress distribution inside the test sample is quite uniform. Thus from the numerical evaluation it can be concluded that the CP geometry can indeed be used to conduct constant stress measurements in a DSR setup.

C) Sample Preparation

The procedure for test sample preparation is similar to the standard procedures followed for the PP geometries. A silicone mould has been used to prepare the 8 mm and 25 mm diameter cylindrical samples. The 8 mm and the 25 mm moulds produce a sample with a height of 3 mm and 2 mm respectively. In the pouring procedure the binder is first heated to a temperature of 150°C. The hot binder is then stirred for uniformity and poured into the mould. After cooling the samples at room temperature the mould is placed in a refrigerator for about 10 minutes. The samples are finally extracted and are made ready for placement in the DSR setup (see Figure 4-8).

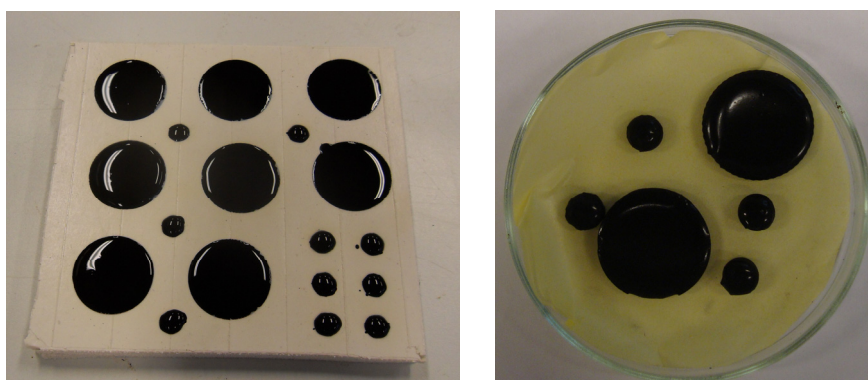


Figure 4-8 DSR test samples (left: binder in a mould, right; extracted samples)

In the DSR machine the sample is placed on the bottom plate, and the top cone-shaped plate is slowly lowered until a preset gap is reached. Similar to the PP settings an extra 50 μm thickness is allowed; hence the preset gap is set to 115 μm . The excess binder that has been squeezed out is then trimmed with a hot spatula. Before the test is run, the final gap is set to 65 μm . Once the testing procedure is started the applied torque and rotational deformation are recorded.

To interpret the applied torque and measured deformation into stress and strain within the sample, transfer functions need to be developed. The relevant test interpretation methods for the different cone geometries are presented below.

D) Test Interpretation Methods

The built-in transfer functions within the TA instrument for obtaining the shear complex modulus and phase angle of the material are valid for the PP geometries. As a result different transfer functions needed to be used for interpreting the measured applied torque and measured angular displacement in the CP setup. The transfer functions relating the applied torque with the shear stress, and the shear strain with the angular deformation, can be given as

$$\tau = k_1 \frac{3T}{2\pi R^3} \quad 4-7$$

$$\gamma = k_2 \frac{\theta.R}{h} \quad 4-8$$

where:

- T = is the applied Torque [N.mm]
- τ = shear stress [MPa]
- k_1 = constant
- R = cone radius
- γ = shear strain [-]
- θ = rotation [rad]
- h = specimen height at outer periphery
- k_2 = constant

FE simulations showed that a radial deformation angle of 0.00492 rad is obtained when a torque of 3.6 N-mm is applied. Accordingly the computed shear stress and shear strain for a representative location in the test sample, being a node located at 4/3 mm high from the bottom plate on the outer periphery, are 2.53E-2 MPa and 9.85E-03 respectively. Combining these values the transfer equation constants given in Equation 4-7 and Equation 4-8 can be obtained. For plate diameters of 8 mm and 25 mm the values of these constants are given in Table 4-7.

Table 4-7 Constants in the transfer function

Plate diameter [mm]	Transfer functions values	
	k_1	k_2
8	0.942	0.99
25	0.992	1.0

4.2.2.3 The DSR Mortar Column Setup

A) Description of the Test Setup

The mortar contains bitumen, filler and sand particles with fine fraction of the sand. The CP setup does not give consistent results for test samples containing particulate materials. As a result the CP setup for DSR cannot be used for response testing. Therefore, the special mortar test sample geometry developed during the first phase of the PA design tool project [5] has been adopted for this research. The mortar sample geometry is presented in Figure 4-9. The specimen

has a total height of 20 mm. The sample ends are enclosed in a 4 mm steel ring to allow clamping of the specimen into the DSR machine. Over the central 10 mm length, the specimen has a constant diameter of 6 mm.

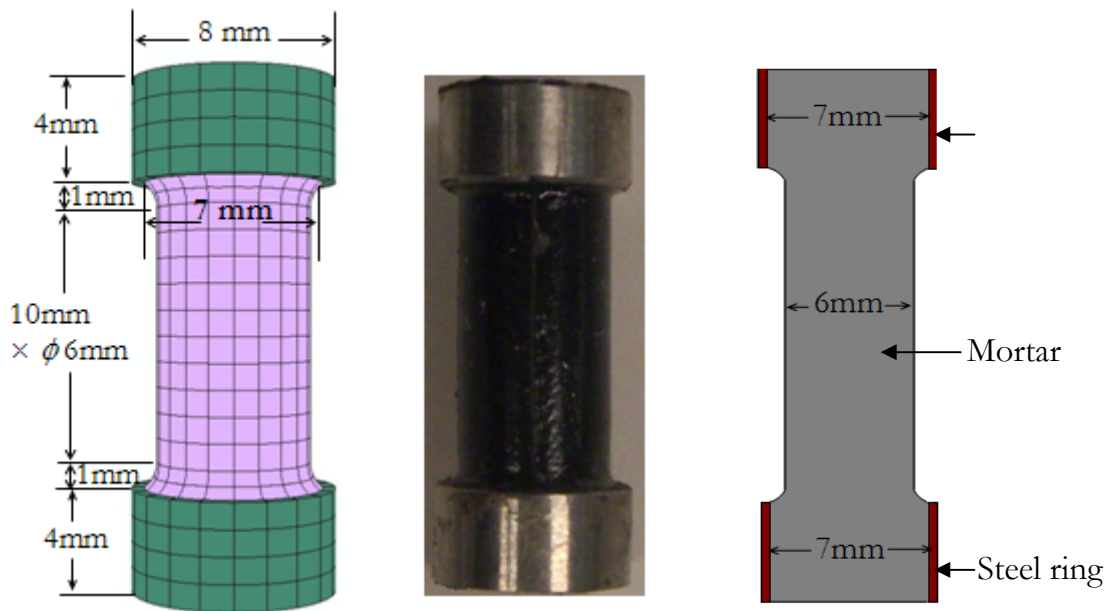


Figure 4-9 Mortar specimen (Left: FE model, Middle: Real specimen, Right: specimen section)

The test procedure involves mounting the mortar sample into the DSR machine. In the test procedure, two types of mounting procedures can be followed. The first is using the steel end clamps. In this mounting procedure the mortar column is fastened to the top rotating rod using the steel end clamp that is designed to fit the steel rings which are used at the two ends of the mortar column. The top rotating rod is then slowly lowered until the bottom end of the mortar column is placed into the other steel end clamp that is firmly fixed with the bottom plate (see Figure 4-10). In this procedure it is important that the samples are kept straight for easy alignment into the end clamps. It is also crucial that the screws are sufficiently tightened to ensure the sample is firmly fixed at the two ends.

The second mounting procedure utilizes a two-component fast curing adhesive glue (X60). In this mounting method, the sample is first glued to the top rotating rod. On the bottom plate sufficient glue is placed, and the top rod (with the mortar sample attached to it) is slowly lowered till the bottom end of the sample comes in contact with the bottom plate. Additional glue is put at the ends as required. Similar to the previous procedure mortar samples need to be straight and enough glue needs to be used at the ends to ensure sufficient bond. Figure 4-10 shows mortar samples mounted in a DSR machine using the two mounting procedures. In the test, a sinusoidal torque is applied to the top bar. The applied torque and the rotational deformation of the specimen are measured and the phase difference between these two signals is determined.

The difference in results between the two mounting procedures will be discussed later on.

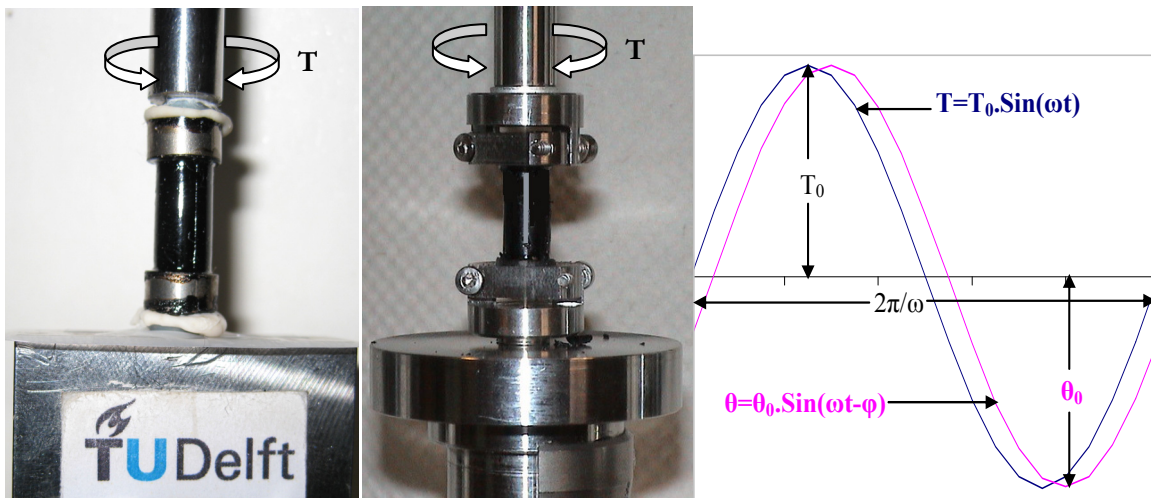


Figure 4-10 Mortar specimen in a DSR test (left: glued ends, middle: steel end clamps, right: typical load and displacement signals).

B) Sample Preparation

The sample preparation procedure involves heating the component materials to a mixing temperature of 170°C. The bitumen, filler and sand are then thoroughly mixed with a hot spatula to obtain a uniform mixture. The heated mortar is then carefully poured into a special designed pre-heated mould made of a silicone plastic. After filling, the mould is placed back in an oven for about 5 minute to remove air voids from the specimen. The mould is cooled down at room temperature and then stored in a freezer, at a temperature of -10°C, before the mortar columns are extracted. Figure 4-11 shows the pouring and extraction of the mortar column samples.

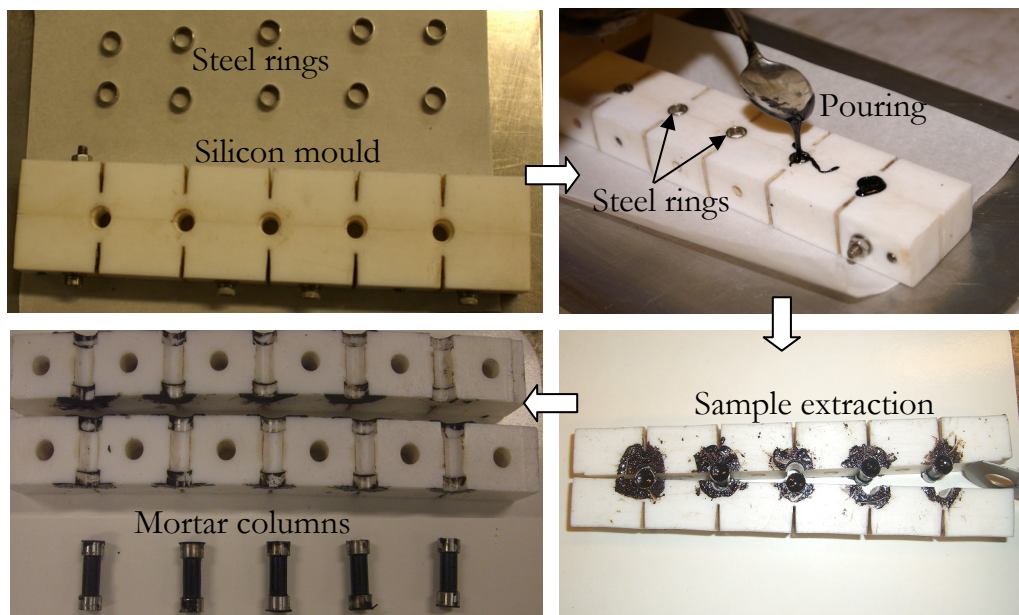


Figure 4-11 Mortar specimen preparation

After cooling down, for about 2 hours in the freezer, the mould is split and the samples are removed carefully. The samples are visually inspected to assure that no air pockets or damages are present. Only undamaged samples with no visual air pockets are used in the test program. Additional CT scan measurements were also made on a randomly selected mortar sample to examine the presence of air voids inside the mortar (Figure 4-12). The CT scan results showed the presence of a small air void content, about 0.22% by volume, in the mortar samples. For samples extracted without putting the mortar-filled mould back to the oven, as part of the air void removal procedure, a higher air void content of about 1.5% is obtained. Hence for this research the air void removal procedure has been followed consistently.

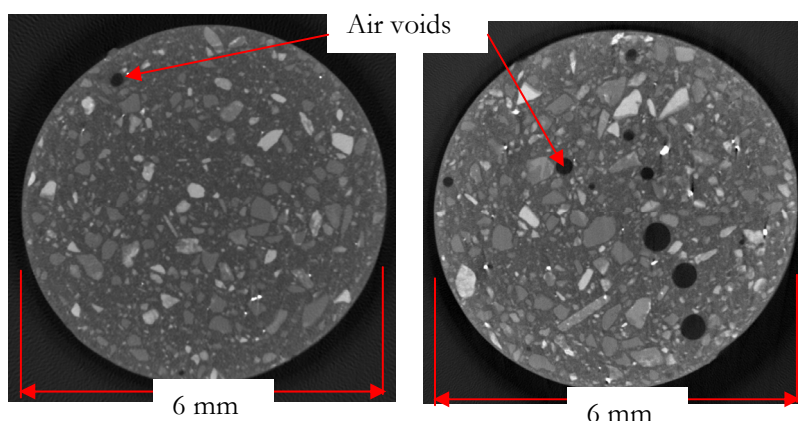


Figure 4-12 CT scan images showing air voids in mortar samples

C) Test Interpretation Methods

Since the geometry of the mortar column is different from the standard DSR geometries, relevant transfer functions need to be applied to obtain stresses and strains in the test sample based on the measured torque and rotational deformations. The effect of specimen geometry is analyzed by means of a FE model. On the basis of the FE model the transfer function that relates the stress and strain in the test specimen to the torque and rotational deformation were obtained.

The transfer function to relate the applied torque with the shear stress, and the shear strain with the angular deformation, was obtained based on the following relations.

$$\tau = k_1 \frac{2T}{\pi R^3} \quad 4-9$$

$$\gamma = k_2 \frac{\theta.R}{h_{\text{eff}}} \quad 4-10$$

where:

- T = is the applied Torque [N.mm]
- τ = shear stress [MPa]
- k_1 = constant
- R = specimen radius, 3mm
- γ = shear strain [-]
- θ = rotation [rad]
- h_{eff} = effective height of the test specimen, 12.74mm
- k_2 = constant

The constants in the relations were determined from FE model simulations. Material properties for the mortar were set to have a shear modulus value of 100 MPa and a Poisson's ratio of 0.45. A torque of 70 N.mm acting on the upper steel ring was applied. The computed shear stress and strain at the outer edge of the middle-straight section of the mortar column were 1.645 MPa and 0.0164 respectively. The corresponding rotational displacement of 0.06951 rad was computed. Combining the applied torque with the induced stress, the stress factor that accounts for the sample geometry can be calculated. In a similar manner, the strain factor accounting for the sample geometry was obtained. These constants are given in Table 4-8. The factor k_2 is taken unity for response measurement. For fatigue tests, this factor can be adjusted to take into account the stress concentration factor based on the observed location of fatigue failure in the sample.

Table 4-8 Constants used in the transfer function

Transfer functions values		
k_1	k_2	h_{eff} [mm]
0.997	1.00	12.742

It can be seen from Table 4-8 that the effective height of the sample is a little higher than the total height of the mortar column, which is 12.0 mm. This is a combined effect of the slight contribution of the mortar deformation in the steel rings, and also the geometrical effects at the end sections where the diameter of the sample gradually changes from 6 mm to 7 mm. The geometrical effect can be seen from the relatively high shear stress concentrations at the two ends of the mortar column as shown in Figure 4-13.

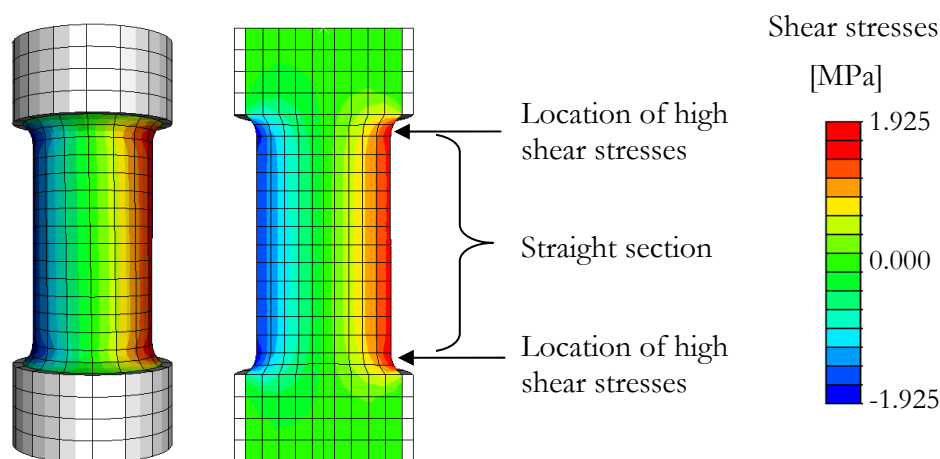


Figure 4-13 Shear stress distribution along the height of the mortar sample

Figure 4-13 also shows that the stress distribution across the diameter of the mortar sample is not uniform. As discussed in the previous sections, obtaining uniform stress distribution across the sample diameter is important especially for response characterization at higher stress levels. The convenient setup for obtaining uniform stress distribution for the mortar sample in a DSR setup is uni-axial testing. However, the available DSR machine was not capable of performing uni-axial dynamic testing. Because of this limitation, it was decided to conduct the mortar response measurements in the shear mode, and numerically estimate the effects of the non uniform stress distribution on the measured results. However, for measurements conducted at higher shear stress levels, evaluation of the non uniform shear stress distribution on the measured results requires relevant nonlinear models which are not readily available at this stage. From a literature it became clear that nonlinear response measurements for bituminous mortar with composition similar to this research were not available. Hence, it was decided to conduct the numerical evaluation

at a later stage when relevant nonlinear model and response data for the mortar are available.

4.3 Experiments and Results

4.3.1 Experimental Plan

In this section the experiments that were carried out on the various binders are presented. For the bitumen and mastic, the first series of experiments that were conducted were for evaluating the quality of data from the CP setup. For evaluation, a comparative approach was utilized, where CP response data within the linear viscoelastic range are compared with similar data obtained from the standard PP setup. Table 4-9 shows the experiments conducted for this purpose. Two materials, i.e. pen grade bitumen and mastic, are used.

Second category of tests includes response testing at higher shear stress levels. Table 4-10 shows the experiments performed to investigate the stress dependent behaviour of the binders. Stress controlled tests at various stress levels and various temperatures were conducted. Tests on B70/100 bitumen, B70/100 mastic and B70/100 mortar were made. It is known that, the maximum shear stress level reached in each of the tests is limited either by the maximum torque capacity of the machine or the maximum torque level that the material could carry. For the data analysis stage however, response data with the presence of little or no damage are sought. This is to imitate the practical observation that pavements last millions of load repetition; and thus the damage incurred by a single wheel load on the pavement is insignificant.

To evaluate the effect of the shear stress level on the fatigue life of the binders, supplementary fatigue and stress sweep tests were also conducted. This test plan is presented in Table 4-11.

The last group of tests, the result of which will be presented in the relevant sections in the next chapter, are time domain tests. These tests were mainly conducted at low stress/strain levels to check the time-frequency domain relationship. The types of tests conducted in this category were creep and relaxation tests (see Table 4-12).

Table 4-9 Tests carried out for CP result verification

Materials	Test type	Geometry	Temperature		Remark
				[°C]	
B40/60	Frequency sweep	PP and CP		-10 to 60	Linear viscoelastic
B70/100 Mastic	Frequency sweep	PP and CP		-10 to 60	Linear viscoelastic

Table 4-10 Response tests at various stress levels (frequency domain)

Materials	Test type	Geometry	Temperature [°C]	Stress range ¹
B70/100	Frequency sweep	CP	-10 to 50	Low to high
B70/100 Mastic	Frequency sweep	CP	-10 to 50	Low to high
Mortar	Frequency sweep	Cylindrical columns	-10 to 40	Low to high

Table 4-11 Tests carried out to determine fatigue life cycles

Materials	Test type	Geometry	Temperature [°C]
B70/100	Stress/Time sweep	CP	10 - 20
B70/100 Mastic	Stress/Time sweep	CP	10 - 20
Mortar	Stress/Time sweep	Cylindrical columns	10 - 20

Table 4-12 Time domain response tests

Materials	Test type	Geometry	Temperature [°C]	Remark
Mortar	Creep/relaxation	Cylindrical columns	10 - 20	Linear viscoelastic

4.3.2 Bitumen and Mastic Response at Low Stress Levels

4.3.2.1 Results from CP and PP Setups

In order to evaluate the quality of the response data from the CP setup, frequency sweep tests were conducted using the CP and the PP geometries. Since binder response at low stress levels is linear viscoelastic, the response obtained from the CP and the PP setups is expected to show good agreement.

Following the standard frequency sweep testing procedure, the 8 mm and the 25 mm parallel plate diameters were used for low and high temperature regions respectively. Similarly for the CP setup, the 8 mm and 25 mm diameter cone were used for the low and high temperature regions respectively. Table 4-13 summarizes the geometries used for the various temperature regions.

¹ The maximum stress varies for each temperature. For defining the lower stress limit, the stress value that can provide measurable deformation is used.

Table 4-13 Test geometries used at various temperatures

Type of test	Temperature [°C]	Diameter [mm]	Geometry
Frequency sweep	-10°C to 20°C	8	Parallel plate
	30°C to 60°C	25	Parallel plate
	-10°C to 20°C	8	Cone and Plate
	30°C to 60°C	25	Cone and Plate

From the frequency sweep test, the magnitude of the dynamic shear modulus, G^* , and the phase angle, δ , were obtained. In processing the data, appropriate transfer functions that were presented in the previous sections were utilized. Figure 4-14 to Figure 4-17 present the comparison between the results from the CP and PP setups for B40/60 binder and B70/100 mastic.

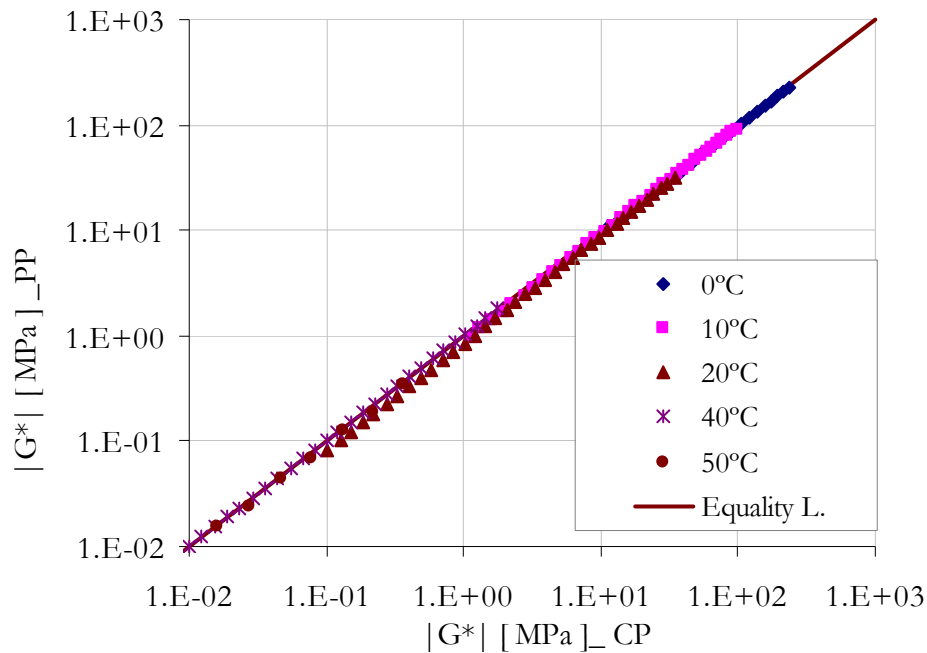


Figure 4-14 Comparison of complex modulus data, results obtained at various temperatures using the CP and PP setups (B40/60)

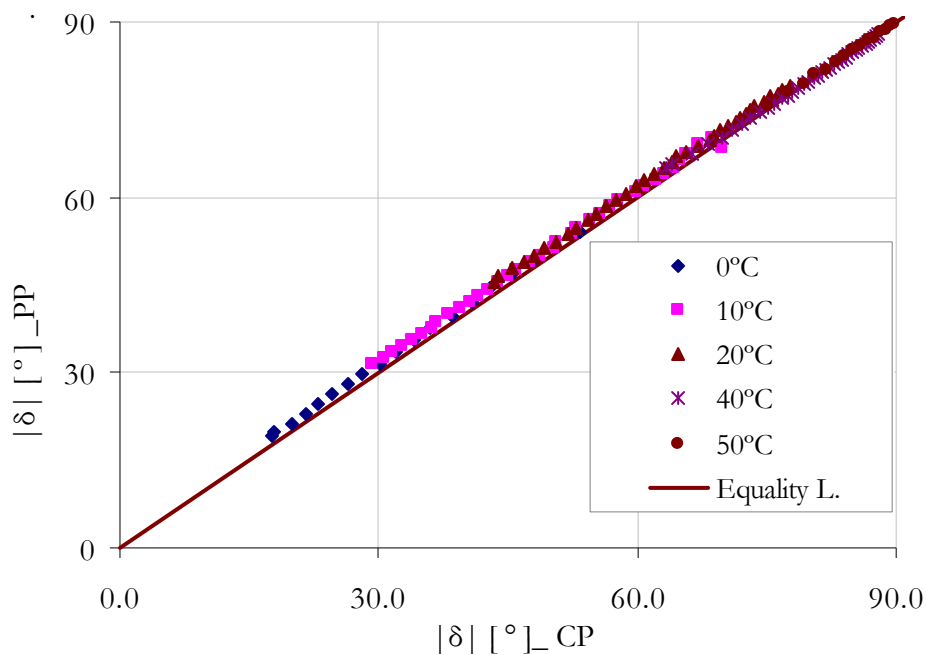


Figure 4-15 Comparison of phase angle data, results obtained at various temperatures using the CP and PP setups (B40/60)

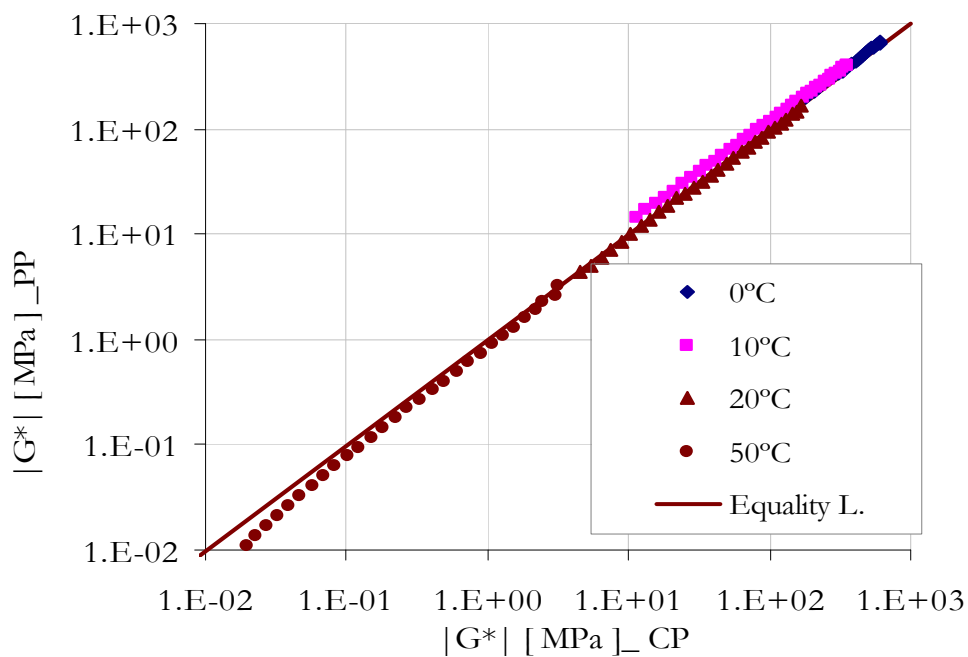


Figure 4-16 Comparison of complex modulus data, results obtained at various temperatures using the CP and PP setups (B70/100 mastic)

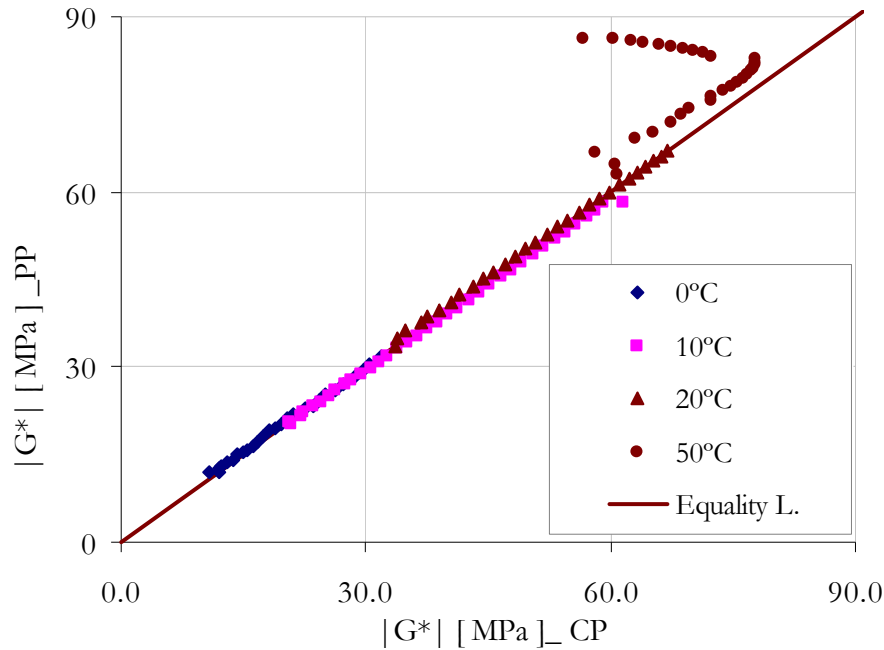


Figure 4-17 Comparison of phase angle data, results obtained at various temperatures using the CP and PP setups (B70/100 mastic)

For the penetration grade bitumen, B40/60, Figure 4-14 and Figure 4-15 show that the complex modulus and phase angle measurements obtained from the CP and PP setups are in a good agreement. Figure 4-16 and Figure 4-17 show the comparison between the CP and PP test results for the mastic. For the measurements conducted at the lower temperatures, the CP setup appears to deliver a relatively lower complex modulus in comparison to results from the PP setup. The CP measurements conducted at higher temperatures, where the 25 mm diameter cone was used, show inconsistent (out-of-trend) results. This can be seen from the phase angle data at a temperature of 50°C (Figure 4-17). The observed variation in test results is believed to be due to the gap settings and the cone angles used for the 25 mm diameter. At the tip of the cone and in its vicinity, the particles in the test specimen, i.e. the filler materials, might possibly get jammed. This effect is thought to be less for higher cone angles and larger gap settings. Further investigations to find optimum gap setting and cone angle have not been carried out. As a result, only the response data obtained at low to intermediate temperatures, i.e. measurements made using the 2 mm cone diameter, are chosen for use in this project.

A) Master Curve using Time-Temperature Superposition Principle

For the results obtained from the CP and the PP setup, master curves were constructed using the Time-Temperature superposition principle. This principle allows shifting the response data obtained at various temperatures with respect to time or frequency to a selected reference temperature. The curve obtained in this manner can be plotted as a function of reduced time or frequency. The

amount of shifting required at each temperature can be obtained using the Williams-Landel-Ferry (WLF) equation [4].

$$\text{Log } a_T = \frac{-C_1(T - T_0)}{C_2 + (T - T_0)} \quad 4-11$$

where:

- C_1, C_2 = constants
- T = temperature [°C]
- T_0 = reference temperature [°C]
- a_T = shift factor

For describing the resulting master curves for the shear complex modulus, G^* , and the phase angle, δ , the Christensen Anderson (CA) model was chosen [3].

$$|G^*(\omega)| = G_g \left[1 + \left(\frac{\omega_c}{\omega} \right)^{\frac{\log 2}{R}} \right]^{\frac{-R}{\log 2}} \quad \text{and} \quad |\delta(\omega)| = 90 \left[1 + \left(\frac{\omega}{\omega_c} \right)^{\frac{\log 2}{R}} \right]^{-1} \quad 4-12$$

where:

- $|G^*(\omega)|$ = magnitude of the complex shear modulus
- G_g = glassy modulus
- ω_c = location parameter (cross over frequency) [rad /s]
- ω = reduced frequency [rad /s]
- R = rheological index, $R = \log (G_g / G(\omega_c))$
- $\delta(\omega)$ = phase angle

Figure 4-18 and Figure 4-19 present the master curve plots for B40/60 bitumen and B70/100 mastic respectively. The CP data used for the construction of the master curve for the B70/100 mastic was from measurements conducted at low to intermediate temperature regions only. The master curves were constructed at a reference temperature of 20°C. For comparison purposes the data from the CP and the PP setups are presented together.

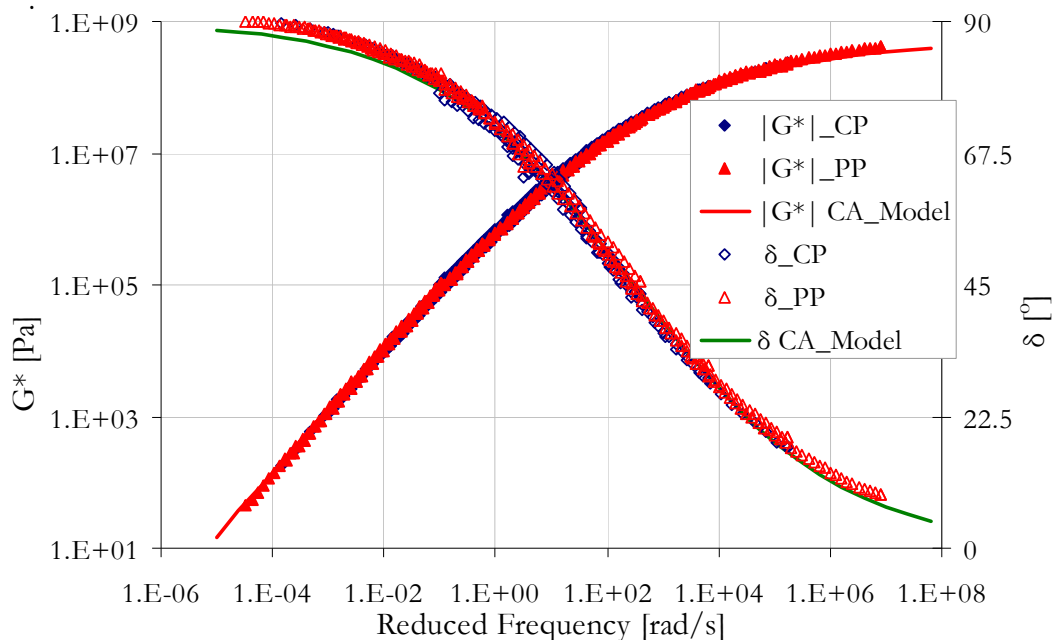


Figure 4-18 Master curve for B40/60 bitumen at 20°C

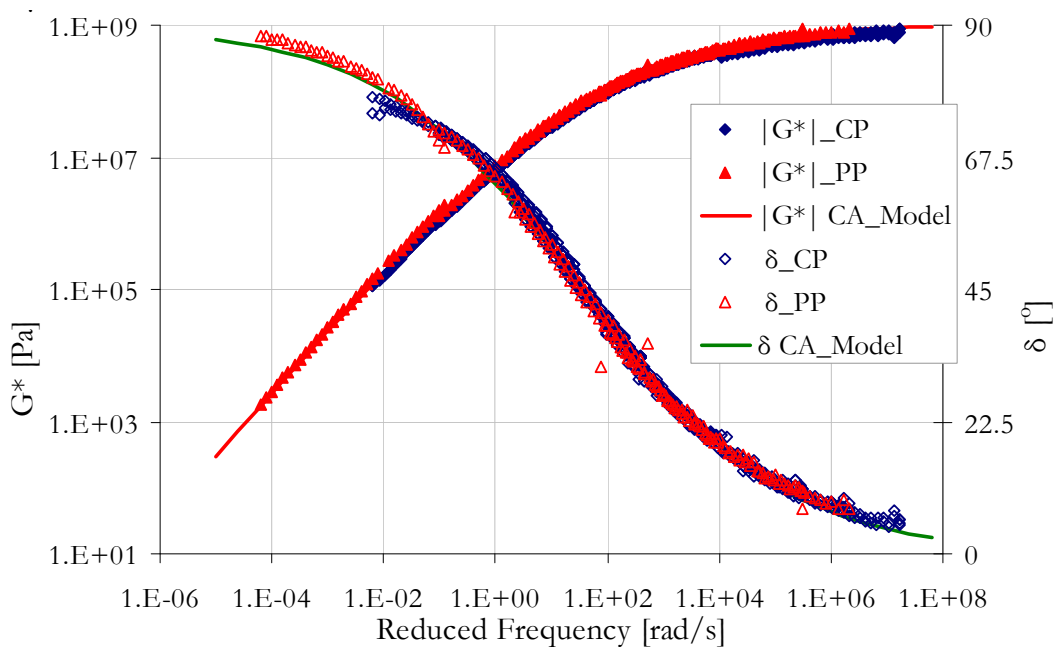


Figure 4-19 Master curve for B70/100 mastic at 20°C

The shift factors that were used to construct the master curves and the CA model parameters are given in Table 4-14. The parameters were determined based on response data from the PP and CP setups.

Table 4-14 Master curve parameters at reference temperature of 20°C

	WLF Factors		CA model parameters			R ²	
	C ₁	C ₂	G _g	ω_c	R	G*	δ
	[-]	[-]	[MPa]	[rad/s]	[-]	[-]	[-]
B40/60	15.718	135.546	480	303.564	1.268	0.999	0.996
B70/100 Mastic	20.796	164.832	1100	34.47	1.259	0.989	0.997

B) Summary and Discussions

The master curve for the mastic shown in Figure 4-19 was constructed using the results from the 8 mm diameter cone covering temperature ranges between 0°C and 30°C. The 25 mm diameter cone with a cone angle of 26.6° provided good quality data for the pen grade bitumen at higher temperatures; the corresponding results for the mastic in the same temperature range appeared to be unrealistic (see Figure 4-17). Consequently, it was decided not to use the 25 mm diameter cone for mastic testing. The 8 mm diameter cone with a cone angle of 2.29° was used to cover temperature ranges up to 30°C for the mastic.

From Figure 4-18 and Figure 4-19 it is observed that the master curves are well described by the CA model. Master curves obtained from the CP and PP setups showed a very good agreement. The good agreement between the two sets of data indicates that the selected geometries for the CP setup can be used for response testing. For low stress measurements it can reproduce the results from the standard PP setup.

4.3.3 Bitumen and Mastic Response at High Stress Levels

4.3.3.1 B70/100 Bitumen

In the previous section the applicability of the CP setup for obtaining material response at low stress levels for various temperatures were investigated. Using the selected geometries the response investigation of the binders at higher stress levels is discussed in this section.

Various DSR frequency sweep tests were conducted using the CP geometries. Due to the limitation in the DSR maximum torque capacity, the maximum stress level reached during the test is different at different temperatures. At low temperatures the stiffer nature of the binders implies that higher stresses or torque values can be achieved. In such cases the DSR maximum torque capacity would be the limiting factor for determining the highest stress level during the test. Due to the viscoelastic nature of the binders, the stiffness of the binders decreases as the temperature increases. Thus large deformations are obtained for relatively lower torque magnitudes in the intermediate to higher temperature ranges. For such cases the material ability to sustain higher shear

stresses would be the limiting factor for determining the highest stress level during the test.

A) General Considerations

In obtaining the response data at various stress levels for a given temperature, it was decided to use a single test specimen. This is mainly for two reasons. The first reason is to avoid possible variations in test results that may arise due to test sampling procedures. If different samples are used for different stress levels, the effect of the stress on the response and variation in test results due to sampling methods would be mixed. The second reason is the time consuming nature of the frequency sweep test. Changing the test sample for each stress level would require a considerable amount of time to cover various stress levels and temperatures. For these reasons, it was decided to obtain material response data as a function of stress level on a single specimen at a given temperature.

Another point of interest is the variation of the linear range with temperature for bituminous materials. Airey et al. [1, 2] showed that the linear range of bituminous binders decreases as temperature increases. The relationship between loading time and temperature also implies that the linear range will also decrease as the frequency decreases. Depending on the chosen frequency window for the frequency sweep test, the material response for a given stress level could therefore go through the nonlinear and linear responses at the lower and higher frequency regions respectively. At extreme cases, especially for a very high stress levels, the low frequency region loadings may introduce damage to the test sample.

To filter out response data that may include damage, two control mechanisms were introduced. The first is to optimize the frequency window based on trial experiments. In determining the frequency window, consideration was also given to frequency regions that are of interest for PA layer performance computations. A frequency window of 1 Hz to 50 Hz was chosen for this study. The second control mechanism that was used in this study is to monitor damage in the test sample after each stress increment by conducting response measurements at very low stress level. By comparing the response obtained at the low stress level with the linear viscoelastic response, damage introduced to the sample was monitored.

B) Frequency Sweep Test

The frequency sweep tests were conducted such that the measurement at a given temperature begins with the smallest torque level and then progresses to the higher torque levels in steps. After each torque increment the amount of damage introduced to the sample was monitored by conducting a frequency sweep measurement at the lowest torque level. By comparing the response obtained at lowest torque level with the linear viscoelastic response data, an

indication of damage incurred to the sample was obtained. Table 4-15 presents the range of shear stress covered at each temperature for B70/100 bitumen.

Table 4-15 Stress ranges for B70-100 bitumen

Temperature [°C]	0	10	20	40	50
Stress range [kPa]	20-850	15-850	10-210	0.4-32	0.2-10

Test results have shown a stress dependent behaviour both at low and high temperature regions. For low temperature range, using the data at 0°C as an example, Figure 4-20 and Figure 4-21 illustrate the complex modulus and phase angle results for various shear stress levels. The corresponding results for higher temperature regions are illustrated using the results obtained at 40°C (see Figure 4-22 and Figure 4-23). Similar results covering the whole temperature range varying from 0°C to 50°C are attached in Appendix A. In all these plots, response data from test specimens in which damage reduces the low-stress complex modulus values with more than 10% are excluded. The approach used to define this damage limit will be discussed later on.

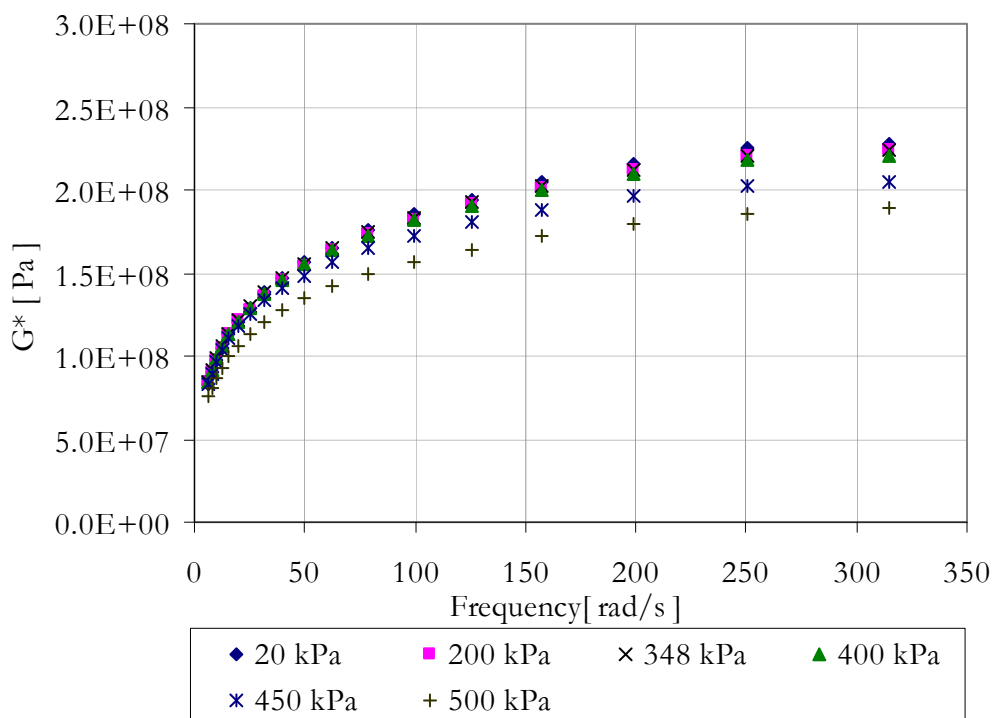


Figure 4-20 Results at 0°C, complex modulus for B70/100

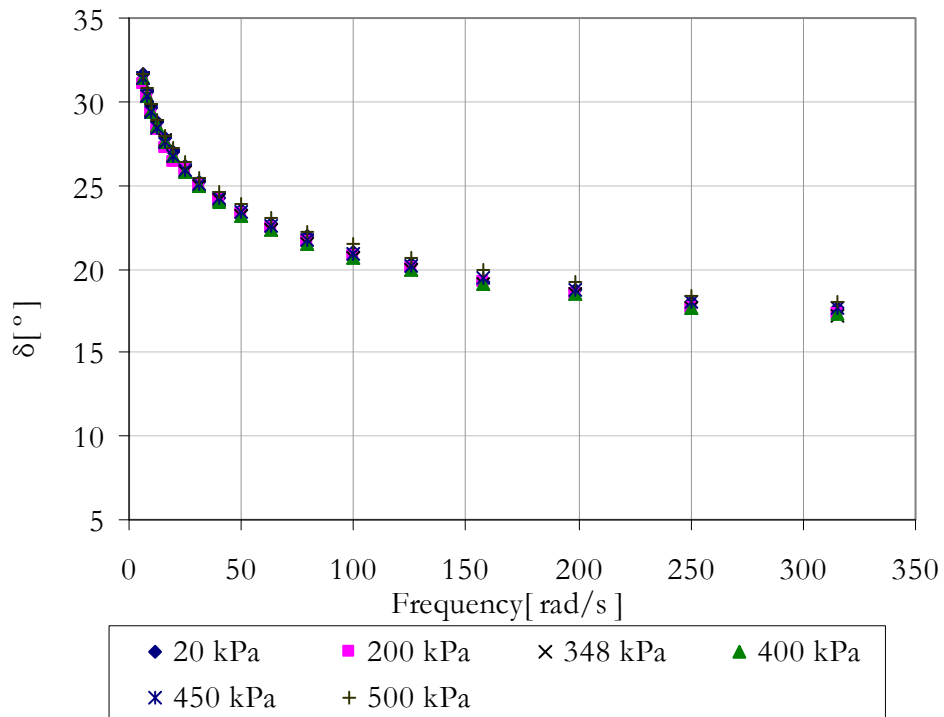


Figure 4-21 Results at 0°C, phase angle for B70/100

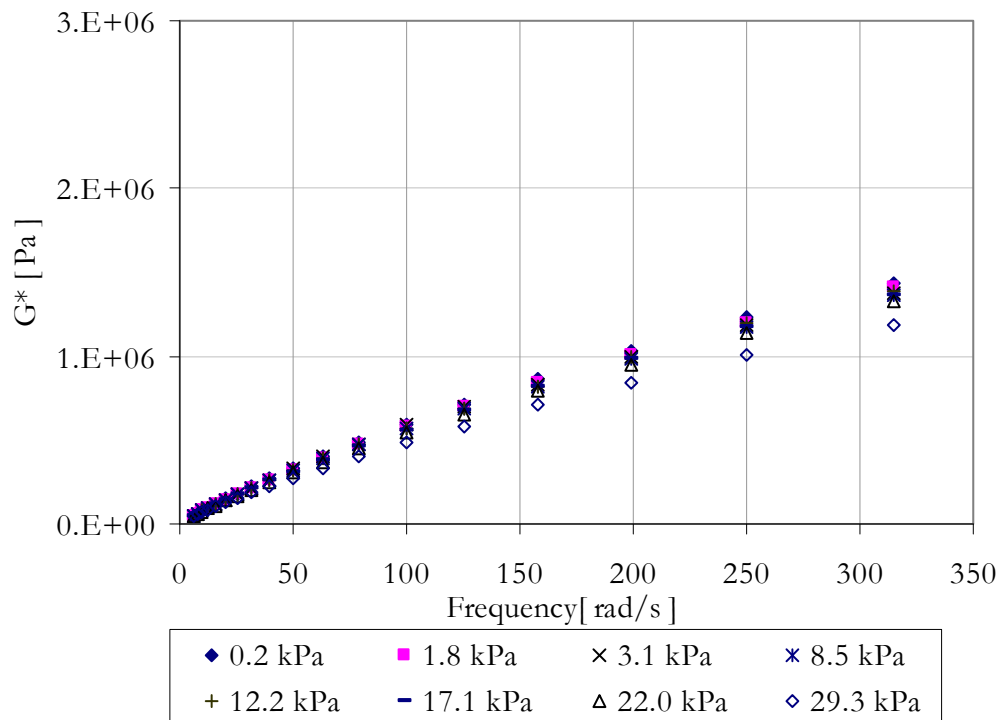


Figure 4-22 Results at 40°C, complex modulus for B70/100

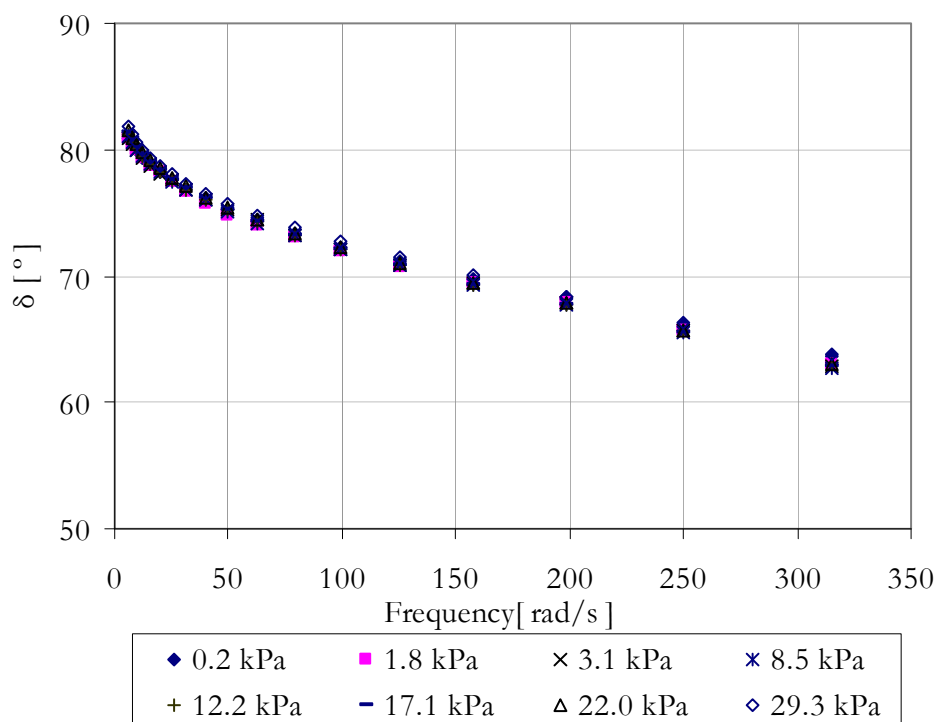


Figure 4-23 Results at 40°C, phase angle for B70/100

Figure 4-20 to Figure 4-23 show a decreasing trend for the complex modulus for an increasing shear stress. It is also evident from the results that the reduction in complex modulus value for higher shear stress levels is accompanied by an increase in phase angle.

To evaluate the reduction of the modulus values at the various frequencies the normalized values have been used. When the G^* values obtained at the various frequencies at a given stress levels were normalized by the corresponding linear viscoelastic G^* values, Figure 4-24 and Figure 4-25 were obtained corresponding to the results presented in Figure 4-20 and Figure 4-22 respectively. A normalized G^* value of 1 represents response data obtained at the linear viscoelastic range. For higher shear stresses, a reduction in G^* values result in a normalized G^* value of less than unity.

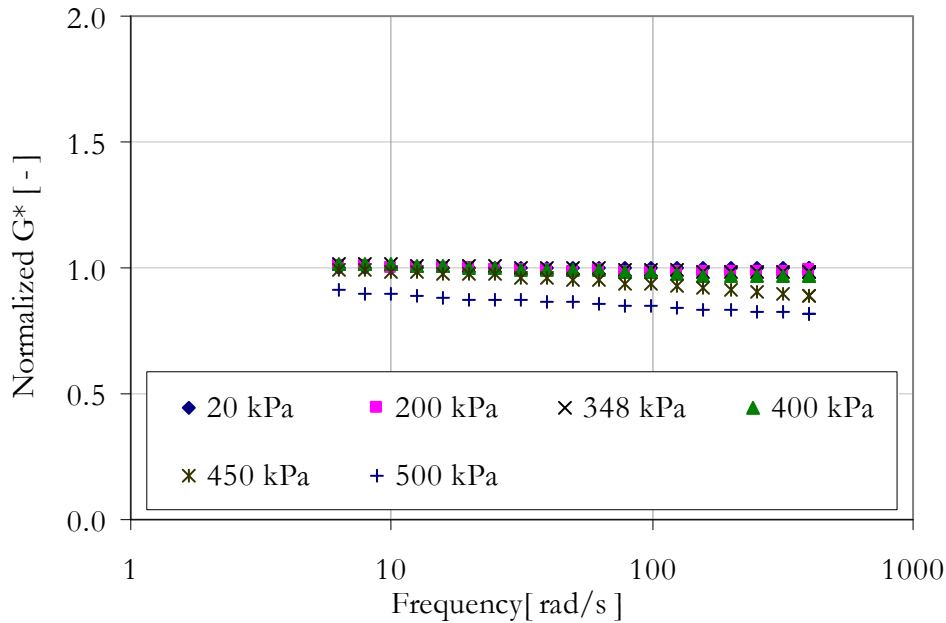


Figure 4-24 Normalized G^* at 0°C for B70/100

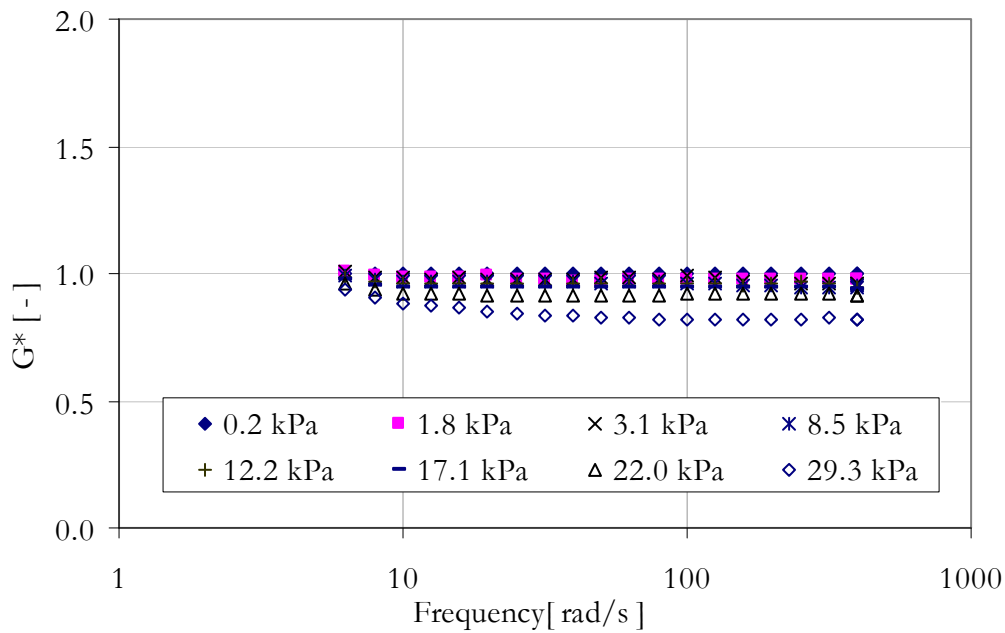


Figure 4-25 Normalized G^* at 40°C for B70/100

From the normalized G^* plots shown in Figure 4-24 and Figure 4-25, it is evident that the normalized G^* values for a given stress level are not constant for all frequencies. This indicates that the effect of the stress on the G^* property also depends on the loading frequency. This effect will be covered in detail in the nonlinear modelling section in Chapter 5.

C) Monitoring Damage in the Test Sample

In performing the frequency sweep tests at various torque/shear levels, damage on the test sample was monitored. For each test, following each torque

increment the binder response at the lowest torque level were measured. The checks were made at selected frequencies (see Figure 4-26). By comparing these results with the linear viscoelastic material property the presence of damage in the test sample were evaluated. Detailed explanation for this procedure is given below.

For each sample placed in the DSR machine, first a frequency sweep in the linear viscoelastic range is conducted. The complex modulus value obtained at various frequencies in the linear measurement is denoted as $G^*(T_0)$, where T_0 is a torque in the linear range. On the same specimen, a second frequency sweep test at a higher torque level, T_1 , is conducted. To monitor the presence of damage in the test sample due to the previously applied torque, T_1 , a third frequency sweep test at few selected frequencies is conducted at a torque level of T_0 . The complex modulus values obtained here are denoted as $G_1^*(T_0)$. Then again a frequency sweep at a higher torque value, $T_2 > T_1$, is conducted followed by a check test at the lower torque level and so on.

To formulate it in a mathematical notation, after the i^{th} torque increment the complex modulus that is obtained at the lowest torque level is denoted as $G_i^*(T_0)$, and the corresponding linear viscoelastic complex modulus value is $G^*(T_0)$. For a given stress level and frequency, a parameter to monitor damage (stiffness reduction ratio), r_i , can be defined. It is given by:

$$r_i = \frac{G_i^*(T_0)}{G^*(T_0)} \quad 4-13$$

In Equation 4-13, the complex modulus values, $G_i^*(T_0)$ and $G^*(T_0)$, are both obtained at the same torque level, T_0 , which is a torque level in the linear viscoelastic range of the material. The only difference between the two complex modulus values is that the first value, $G_i^*(T_0)$, represents the low stress property which is determined after the sample has previously been subjected to a higher torque level. The latter complex modulus value, $G^*(T_0)$, represents the low stress material property which is determined prior to any application of higher torque levels to the test sample.

For the stiffness reduction ratio, r_i , a value of 1 implies that after the i^{th} torque application the material still retains its linear viscoelastic property, hence no damage is incurred to the material. A stiffness reduction ratio less than 1 indicates a change in the linear viscoelastic property. To illustrate results obtained at low, intermediate and high temperature regions, Figure 4-26 to Figure 4-28 present the stiffness reduction ratios obtained at 0°C, 20°C and 40°C at various stress levels for B70/100. The stiffness reduction ratios were obtained at discrete frequencies.

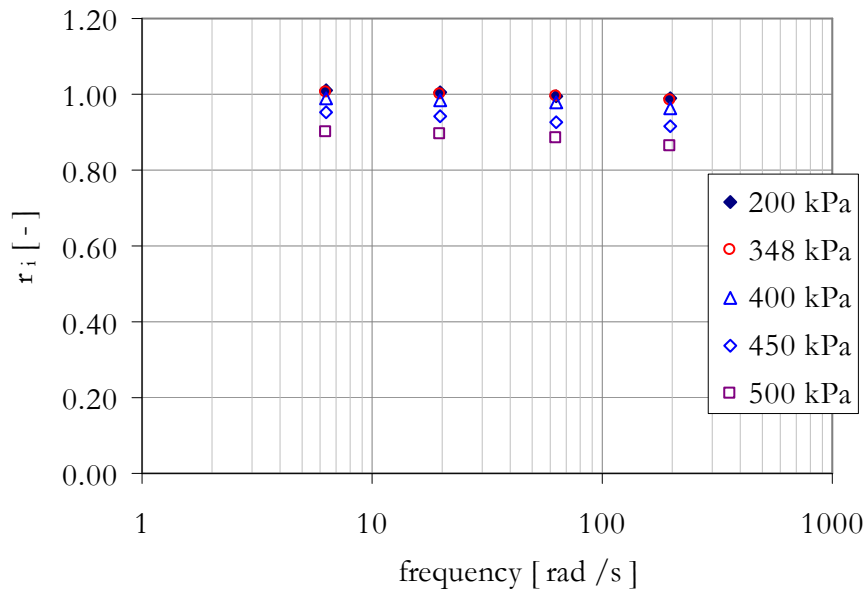


Figure 4-26 Stiffness reduction ratios at 0°C for B70/100

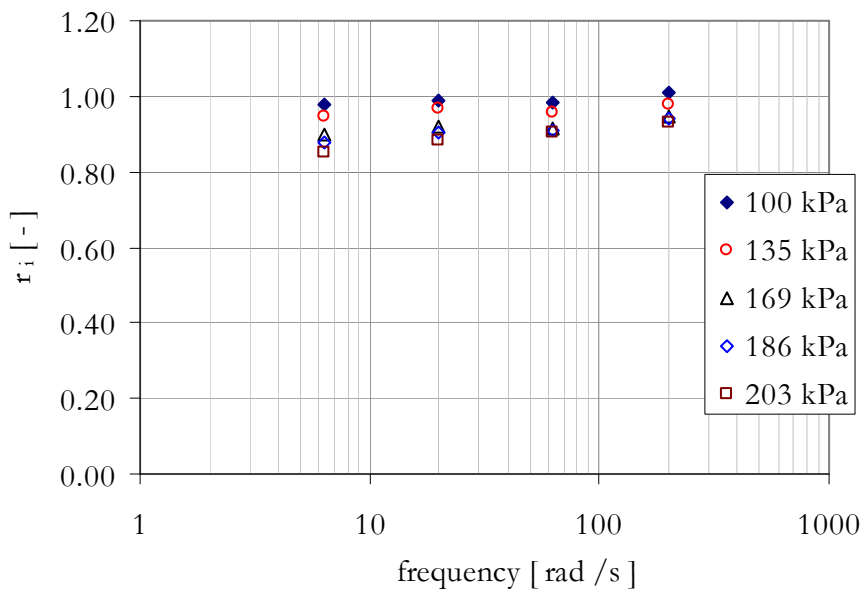


Figure 4-27 Stiffness reduction ratios at 20°C for B70/100

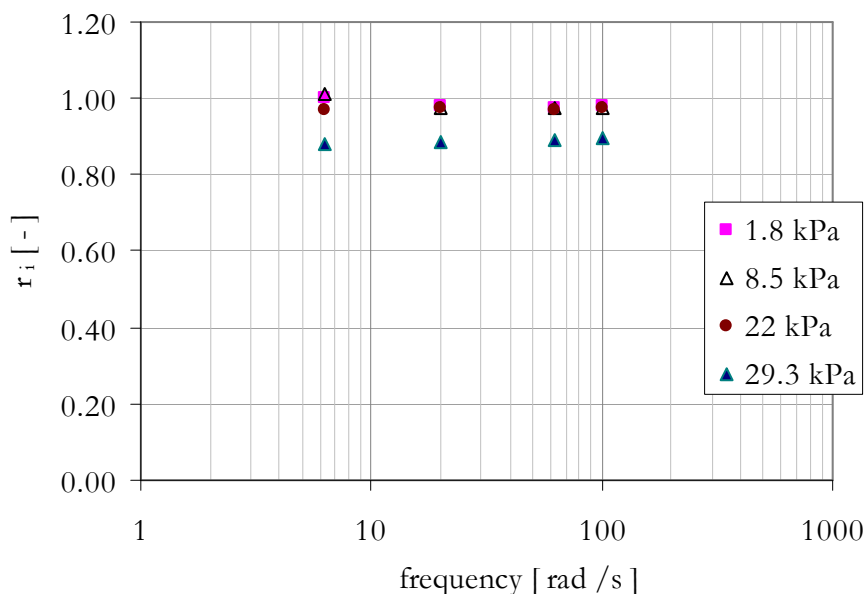


Figure 4-28 Stiffness reduction ratios at 40°C for B70/100

Figure 4-26 to Figure 4-28 show stiffness reduction ratios of less than 1 for higher shear stress levels. This implies that the complex modulus of the binder does not completely return to its original linear viscoelastic value once the material experiences higher torque values. In other words, each torque application practically introduces a limited damage to the test specimen. The results also show that the values of the stiffness ratios, r_i , obtained at various frequencies corresponding to a given stress level are not constant. This indicates that the damage by a given stress level to the test specimen is different at different rates of loading. Further investigation on the effects of the applied stress and load rate on the material damage are beyond the scope of this study and are not covered here. For the data analysis in this work, a stiffness ratio limit was chosen to avoid inclusion of data that included substantial amount of damage to the response analysis. For this purpose the mean value of the stiffness ratio at a given stress level was decided not to exceed 10%. The mean value (r_m) of the stiffness ratios for a given shear stress level is calculated as:

$$r_m = \frac{1}{n} \sum_{i=1}^n r_i \quad 4-14$$

To further examine the practicality of the 10% stiffness reduction criterion, supplementary fatigue tests were carried out. Practice has shown that fatigue failure in pavements occurs after millions of load repetitions. Stress values that result in a few number of fatigue load cycles can therefore be considered impractical, and hence may be excluded from the response data. Following this practical assumption, some stress-controlled fatigue tests were conducted on B70/100 bitumen. The stress values for the fatigue testing were selected from the

stress region where nonlinear behaviour is apparent. This range was first determined based on stress sweep tests. These tests are discussed below.

D) Stress Sweep and Fatigue Tests

The stress sweep results were meant to provide additional information to the ranges of stress values where the nonlinear behaviour of the material is evident. These tests were conducted at four selected frequencies; 0.1Hz, 1Hz, 5Hz and 10Hz. The fatigue results were then used to examine practical stress ranges for the response modelling work. It is also used to evaluate the 10% stiffness reduction criterion that was used to filter the frequency sweep response data.

I. Stress Sweep Results

The stress sweep tests were conducted at two selected temperatures. Figure 4-29 and Figure 4-30 present the stress sweep results obtained for B70/100 at 10°C and 20°C at four selected frequencies.

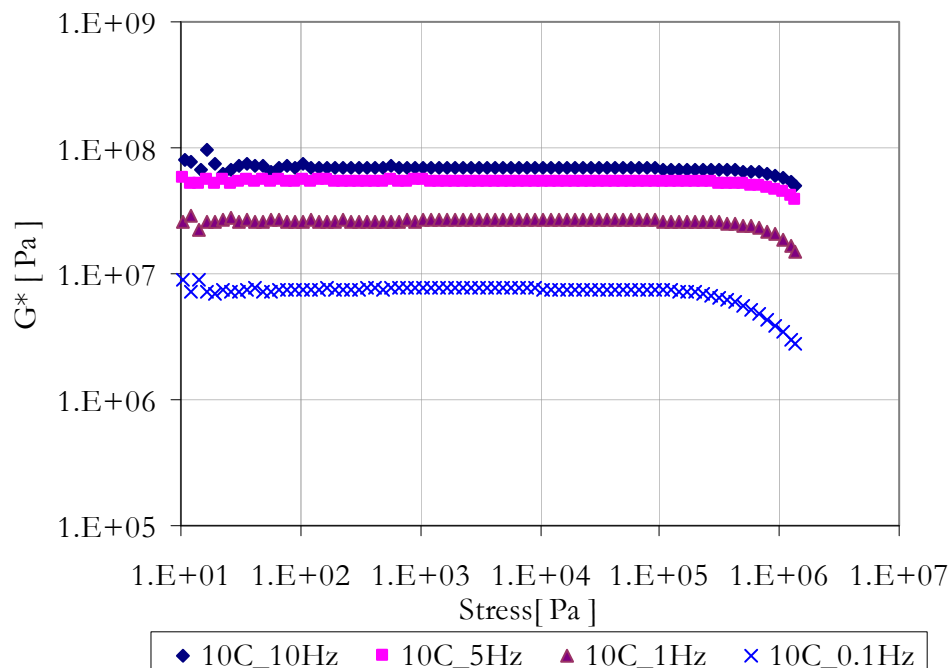


Figure 4-29 Stress sweep results at 10°C for B70/100

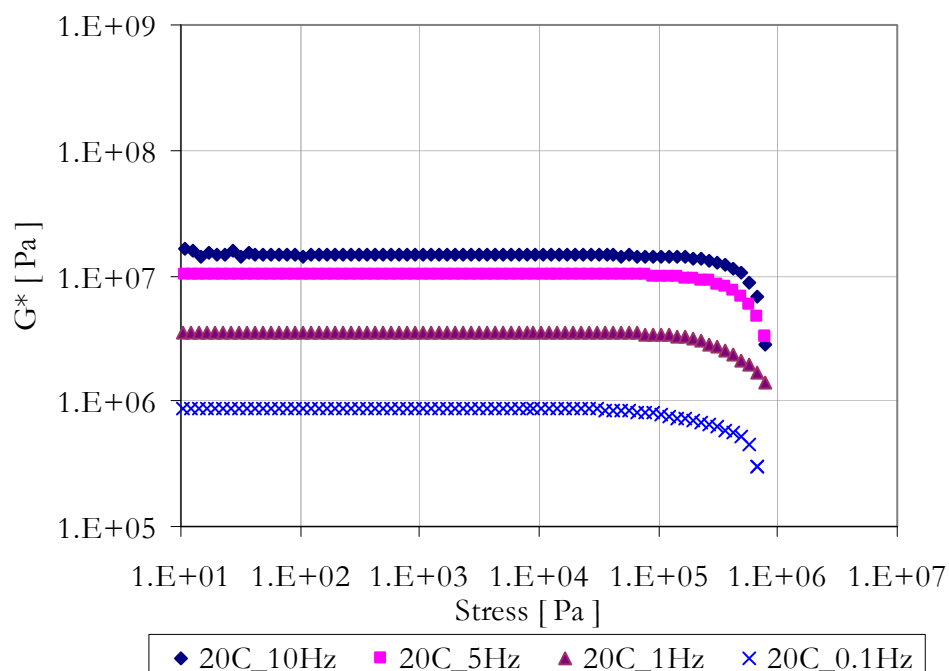


Figure 4-30 Stress sweep results at 20°C for B70/100

From Figure 4-29 and Figure 4-30 it can be seen that the nonlinear behaviour is evident in the stress window ranging between 10 kPa to 1000 kPa. For selected stress levels in this range, fatigue tests were conducted. The fatigue results were analyzed using the dissipated energy approach, and the fatigue relation was determined. Before bringing all the data together, the data processing is first discussed.

II. Fatigue Test Results

In analyzing the fatigue data, the Dissipated Energy Ratio (DER) were utilized [11]. In this approach, the first step is the calculation of the energy lost per unit volume during one complete cycle.

$$\Delta W = \int_0^T \tau \cdot \dot{\gamma} \cdot dt \quad 4-15$$

where:

ΔW = The energy loss per unit volume per cycle

τ = Shear stress [MPa]

$\dot{\gamma}$ = Shear strain rate

The energy loss per unit volume per cycle is obtained as:

$$\Delta W = \pi \tau_0 \gamma_0 \sin \delta \quad 4-16$$

where:

- τ_0 = Shear stress amplitude
- γ_0 = Shear strain amplitude
- δ = Phase angle

The DER, which can be used to evaluate the fatigue evolution process of a material (Pronk et al. [11]), was obtained by dividing the cumulative dissipated energy at the n^{th} cycle with the dissipated energy at the n^{th} cycle as:

$$\text{DER} = \frac{\sum_{i=1}^n \Delta W_i}{\Delta W_n} \quad 4-17$$

where:

- DER = Dissipated Energy Ratio
- ΔW_i = Dissipated Energy per cycle per unit volume at the i^{th} cycle
- ΔW_n = Dissipated energy at the n^{th} cycle

In this method, the fatigue life to crack propagation (N_p) marking the transition from the crack initiation to crack growth can be obtained from the plot of DER vs. the number of load cycles. Figure 4-31 and Figure 4-32 present the DER vs. number of load cycles plot for B70/100 for a selected stress values at 10°C and 20°C.

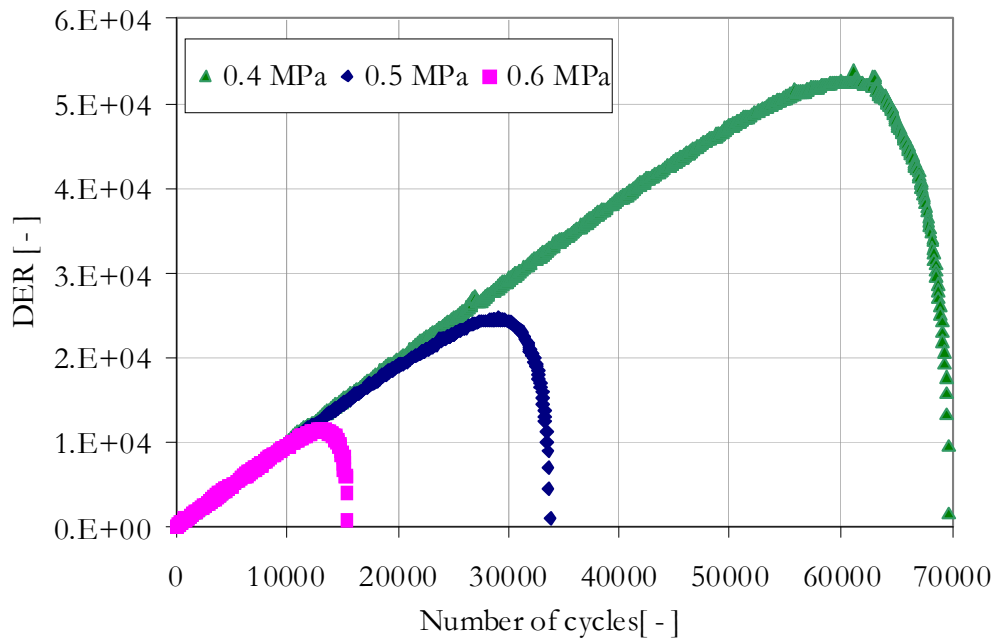


Figure 4-31 DER vs. number of load cycles at 10°C, frequency 10Hz

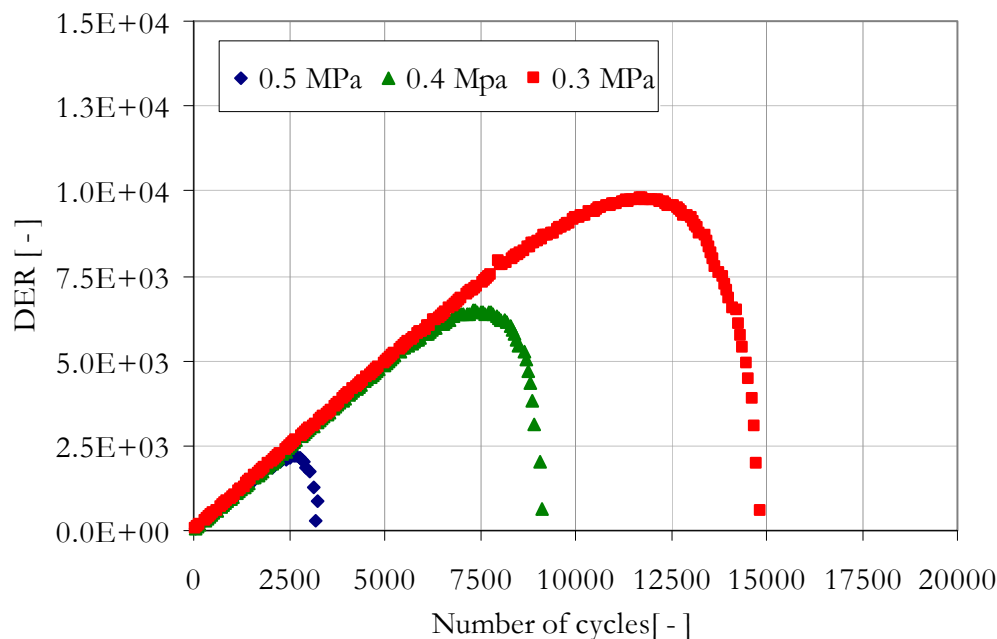


Figure 4-32 DER vs. number of load cycles at 20°C, frequency 10Hz

To obtain the fatigue life to initiation of cracking, N_p , from the DER plots first a tangent line was drawn to the initial straight section of the DER plot. The intersection of this line with a horizontal tangent drawn to the maximum value of the DER curve (see Figure 4-33) gives an indication to the fatigue life resistance of the binder [11]. This value was used as the fatigue life in determining the fatigue relation using the Wöhler approach.

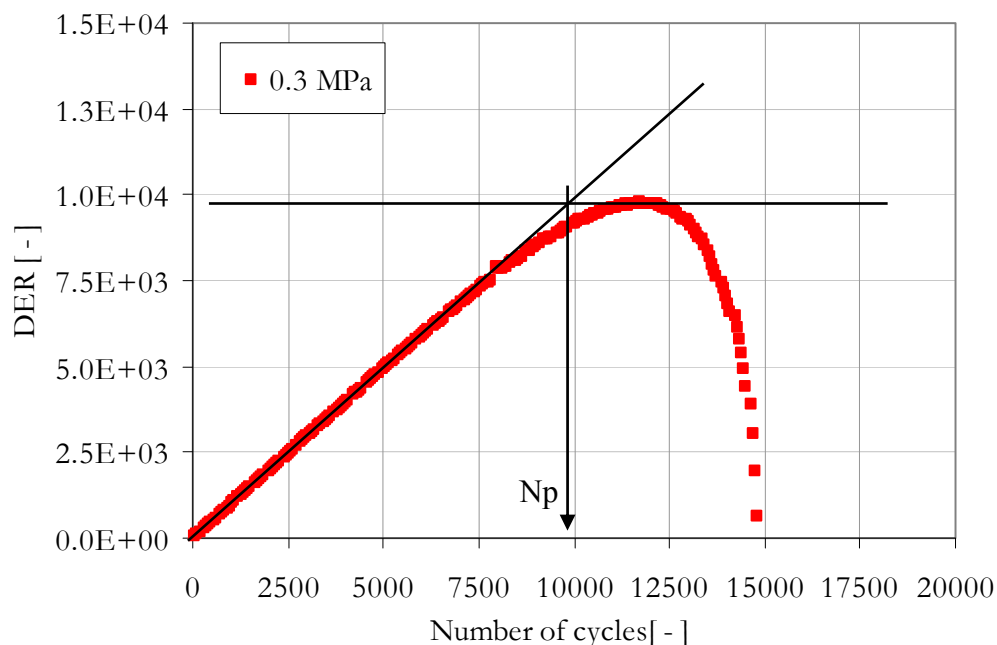


Figure 4-33 Illustration; method of obtaining Fatigue life to crack initiation

Fatigue Relation using the Wöhler Approach

Following the Wöhler’s approach, a logarithmic relation between the applied stress and number of cycles to failure was established. Using the limited number of fatigue tests conducted at temperatures of 10°C and 20°C, the parameters for the fatigue relation given in Equation 4-18 were determined using regression analysis.

$$N_f = A.\tau^{-n} \tag{4-18}$$

where:

N_f = number of cycles to failure [-]

A, n = regression constants [-]

τ = shear stress [MPa]

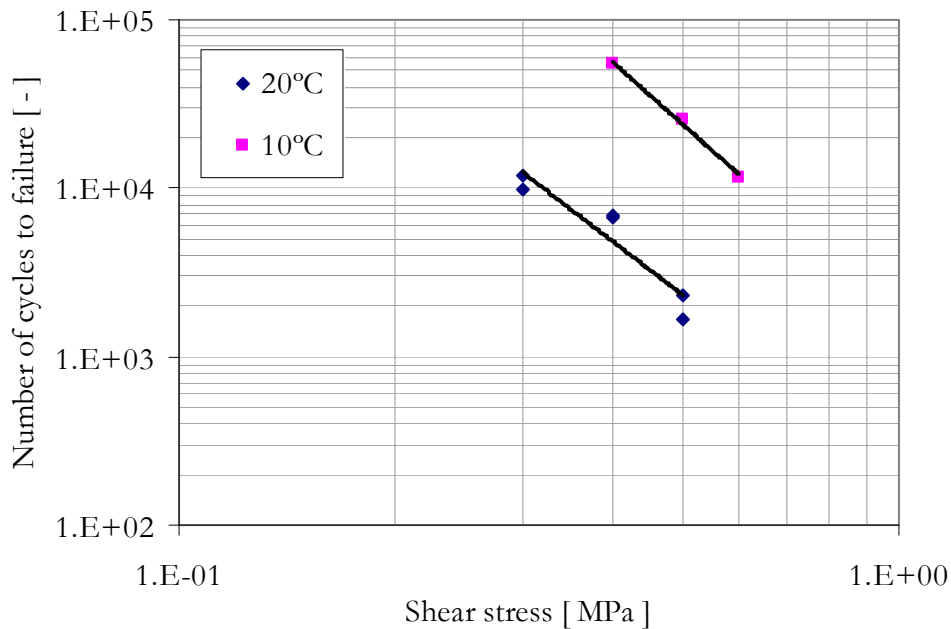


Figure 4-34 Fatigue relations, stress controlled, 10 Hz

The model parameters for the Wöhler’s approach are given in Table 4-16.

Table 4-16 Parameters for the fatigue relation using the Wöhler’s approach

Temperature [°C]	n	A	R ²
10	3.79	1740.2	0.996
20	3.26	243.82	0.876

The fatigue relations were then used to estimate practical shear stress levels that need to be incorporated in modelling the response. The fatigue relations were also used to evaluate the 10% stiffness reduction criterion that was used for

filtering purpose while analyzing the frequency sweep test. All the results are brought together in the summary and discussion presented below.

E) Summary of Results and Discussions

From the frequency sweep tests, a decrease in the complex modulus is observed for an increasing level of shear stress. From Figure 4-24 and Figure 4-25 it is observed that the normalized G^* values for a given stress level are not constant at all frequencies. In order to analyze the data at different temperatures, the normalized G^* values at the various frequencies at a given stress level were averaged. Using the mean of the normalized G^* values, the frequency sweep data obtained at various stress levels for various temperatures is summarized in Figure 4-35.

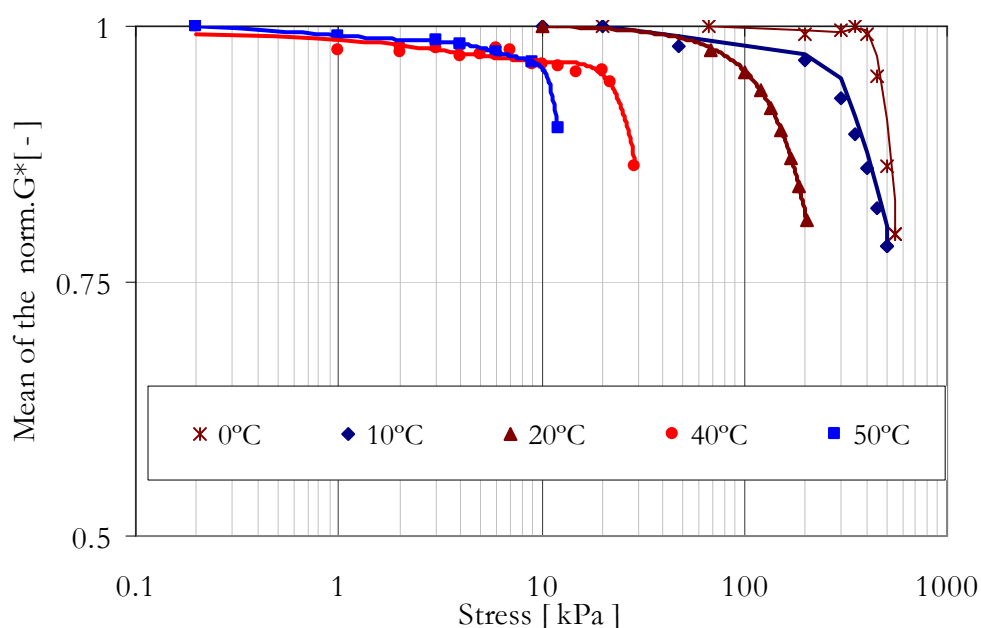


Figure 4-35 Mean of the normalized G^* values at various stress levels for various temperatures, B70/100

A normalized G^* value of 1 represents linear viscoelastic behaviour. For very low shear stress levels, in the order of 1 kPa or less, Figure 4-35 shows that the binder behaviour can practically be considered linear viscoelastic. For temperatures of 20°C and below, nonlinear behaviour is evident for shear stress values above 100 kPa. At high temperatures, the nonlinear behaviour is evident at a much smaller stress level of about 10 kPa. These shear stress ranges for the nonlinear behaviour of the binder are in good agreement with results reported in literature [2].

It is to be remembered that the data points used in Figure 4-35 were obtained using a damage limit of 10% (see Figure 4-26 and Figure 4-27). For similar work in literature a different criterion has been used. In the work of Masad et al. [8] the response data with a criterion of 25-30% stiffness reduction from the linear viscoelastic stiffness value have been used. In reference to Figure 4-35, the

minimum value for the mean of the normalized G^* is about 0.78. This value is equivalent to a 22% stiffness reduction from the linear viscoelastic value. This shows that that the criterion used in this research lies in the lower margin of the values used in literature.

I. Evaluation in Relation to Fatigue

The fatigue life of pavements in practice is known to be in millions. This implies that shear stress values that result in a very short fatigue life are not of practical significance in evaluating the long term performance of a pavement. To examine the fatigue life cycles corresponding to the shear stress levels that were incorporated in the response data, the fatigue relations at 10°C and 20°C were utilized. Figure 4-36 presents the binder response for the various shear stress levels together with the fatigue performance lines for the binder at 10°C and 20°C.

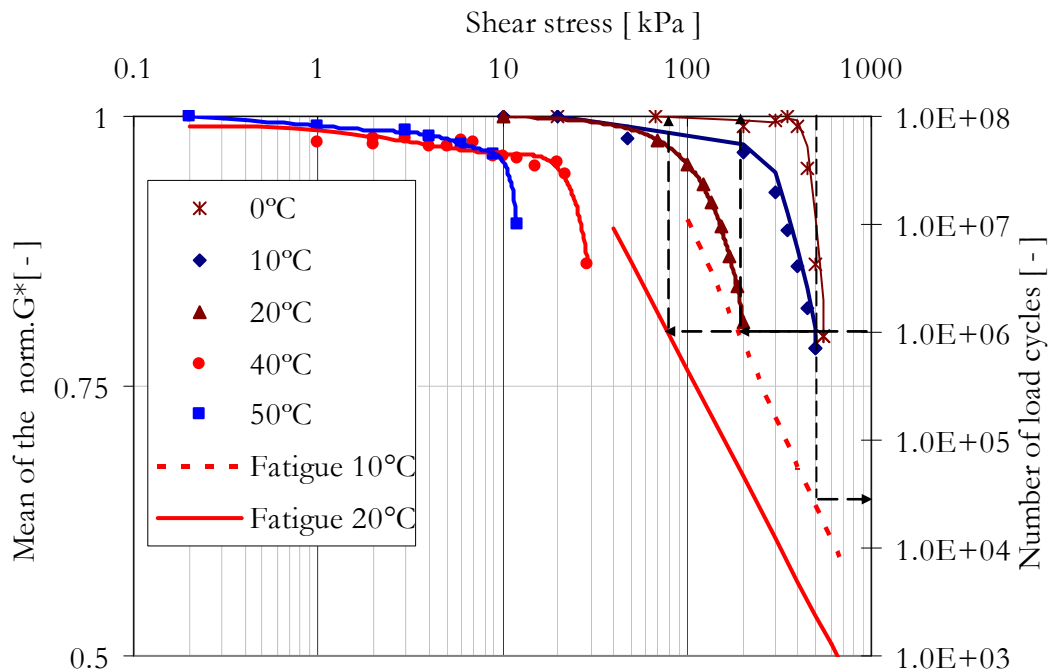


Figure 4-36 Fatigue relations and mean of the normalized G^* at various stress levels for various temperatures, B70/100

If a laboratory fatigue life of 1 million load cycles is assumed, the field fatigue life can be estimated by applying healing and lateral wander factors. With a healing factor of 4 and lateral wander factor 1.5, the fatigue life in practice would be about 6 million load cycles, which is realistic for heavy duty pavements. For 10°C and 20°C, from Figure 4-36 a fatigue life of 1 million load cycles corresponds to a shear stress level in the range of 80 kPa to 200 kPa. Looking at the mean of the normalized G^* at 10°C, for shear stress levels of 200 kPa or less, the nonlinear behaviour is very limited, and linear viscoelastic behaviour can be assumed. From this, it can be argued that the nonlinear behaviour of the binder may not have any practical significance in relation to

the fatigue performance of the binder. The nonlinear response data at 10°C that were obtained using the 10% damage criterion (covering shear stresses up to 500 kPa) may not thus be encountered in practice, as it results in a very short fatigue life cycle (about 30,000 cycles at 10°C). However, this fatigue-related evaluation is relevant only for low temperature regions. For higher temperatures, other distress types such as rutting are important. For this kind of distresses literature reported that linear viscoelastic assumption is not good enough [10]. Similar to the low temperatures, evaluations to determine practical stress limits at higher temperatures were not possible. Comprehensive evaluation on the importance of the nonlinear behaviour for the various temperatures was therefore decided to be made at a later stage with the help of FE modelling work. Hence to obtain sufficient response data for all the binders, it was decided to proceed with the 10% damage criterion.

4.3.3.2 B70/100 Mastic

A) Frequency sweep

Similar to the procedure followed for the B70/100 bitumen, a number of frequency sweep tests were performed on the B70-100 mastic. For the reasons discussed in Section 4.3.2.1, the 8 mm diameter cone was used to cover low to intermediate temperature ranges, i.e. 0°C up to 30°C. From the linear viscoelastic response results presented in Section 4.3.2.1, it was shown that the 25 mm diameter did not provide good results for mastic testing. The response behaviour for higher temperature regions for the mastic is therefore not investigated. However, the data obtained at low to intermediate temperature regions is considered sufficient for the modelling work in this research. Table 4-17 presents the range of shear stresses applied at the various test temperatures on the B70/100 mastic.

Table 4-17 Stress ranges for B70/100 mastic

Temperature [°C]	0	10	20	30
Stress range [kPa]	50-1268	20-1268	2-700	1-270

Figure 4-37 to Figure 4-40 illustrate the complex modulus and phase angle data at various stress levels for temperatures of 0°C and 30°C.

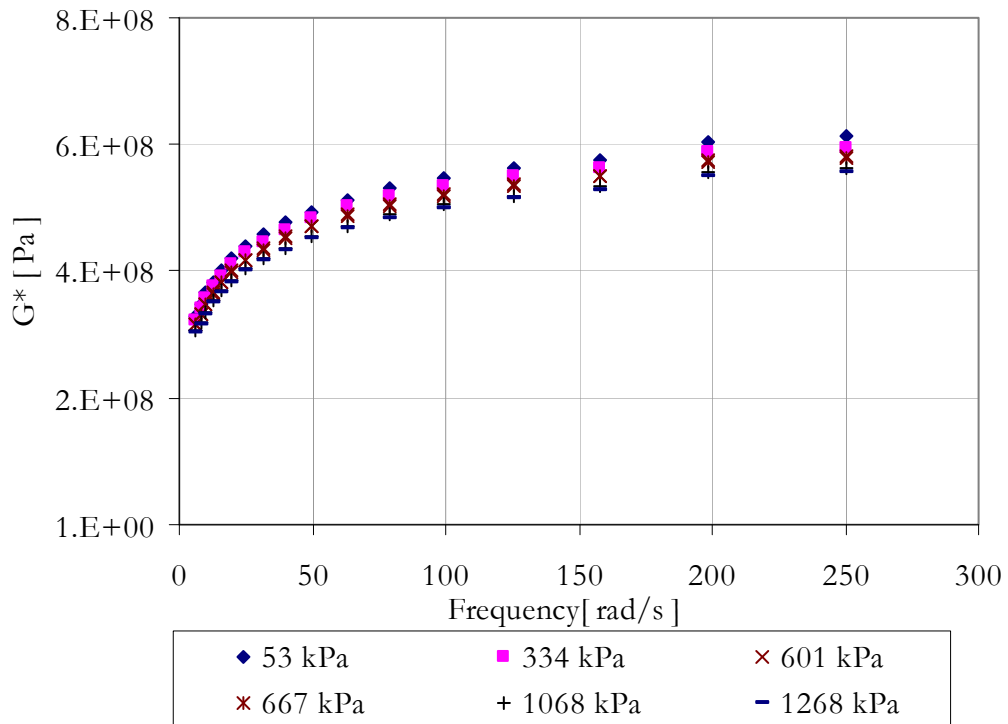


Figure 4-37 Frequency sweep results at 0°C; complex modulus for B70/100 mastic

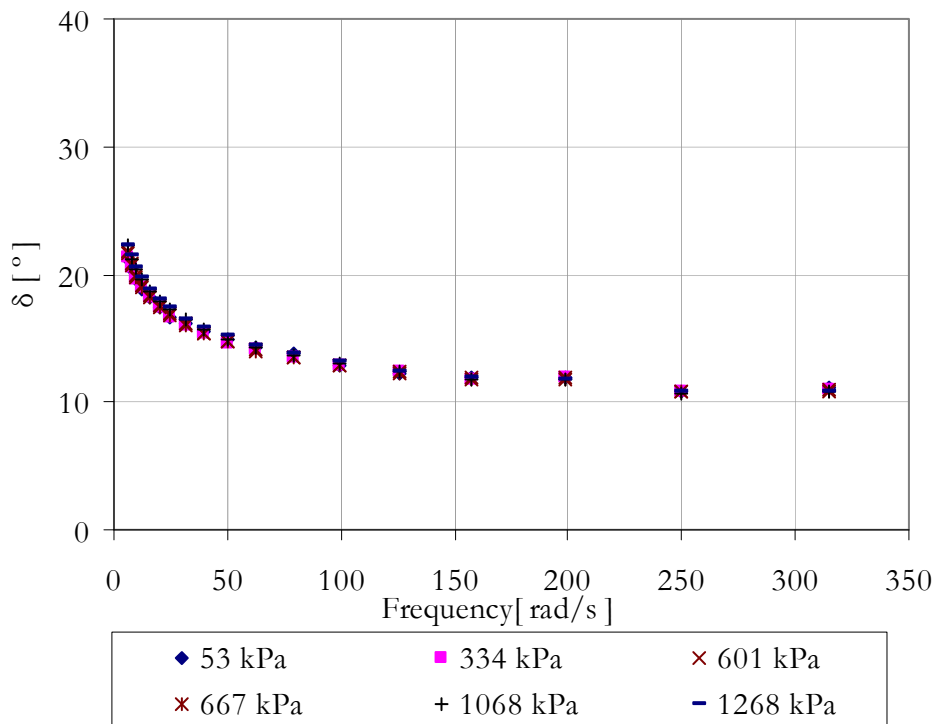


Figure 4-38 Frequency sweep results at 0°C; phase angle for B70/100 mastic

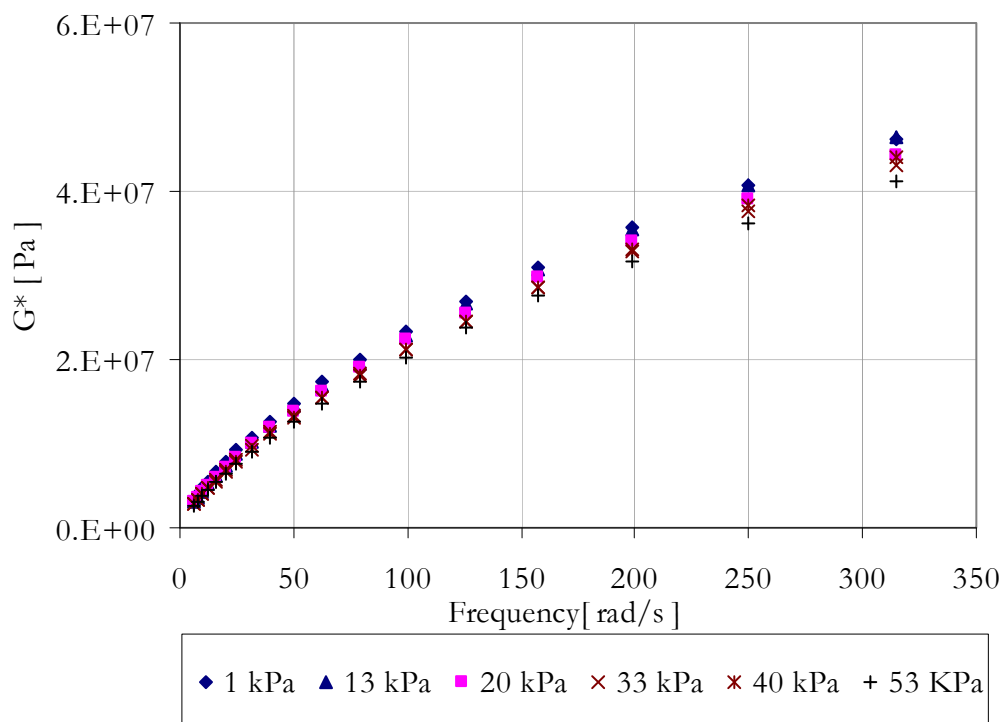


Figure 4-39 Frequency sweep results at 30°C; complex modulus

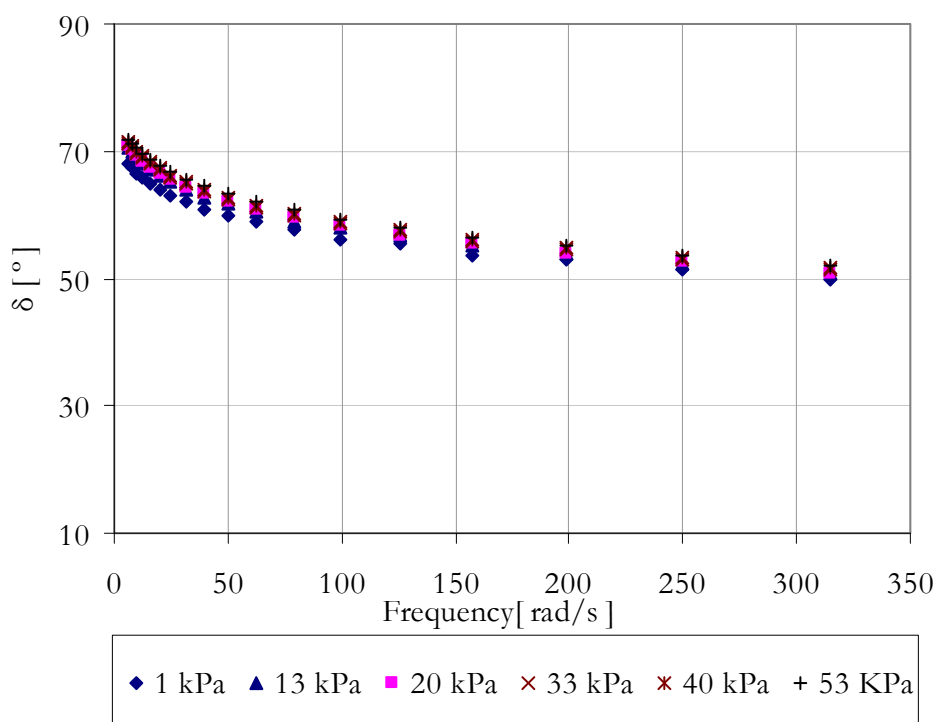


Figure 4-40 Frequency sweep results at 30°C; phase angle

Similar results obtained for other temperatures, ranging from 0°C to 30°C, are attached in Appendix B. For analyzing the effect of stress levels on the mastic response at various temperatures, the normalized response data were used. Corresponding to the results obtained at 0°C and 30°C, Figure 4-41 and Figure 4-42 present the normalized G^* values at various stress levels.

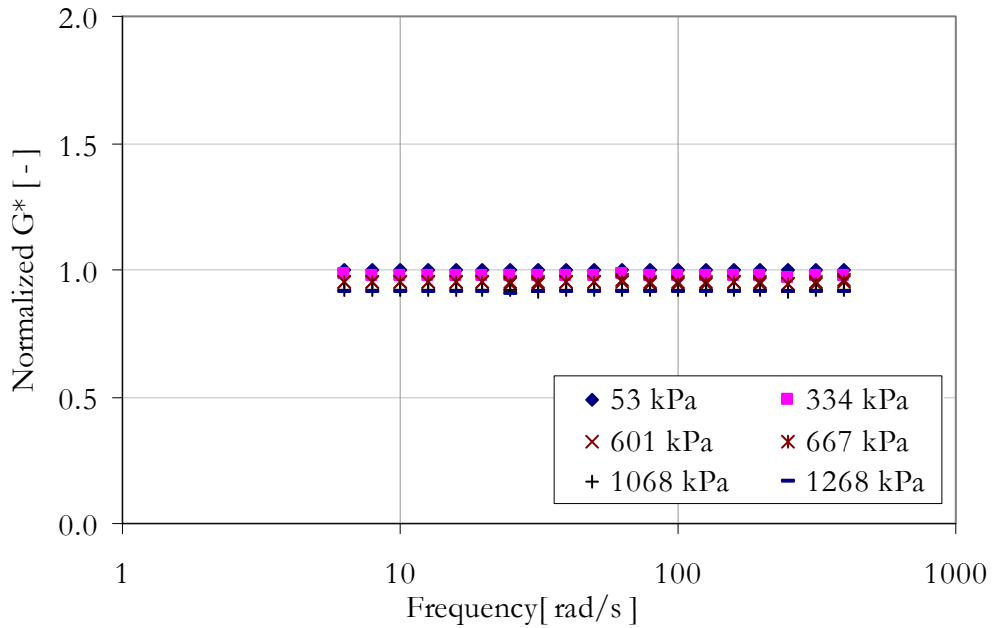


Figure 4-41 Normalized G^* values at 0°C for B70/100 mastic

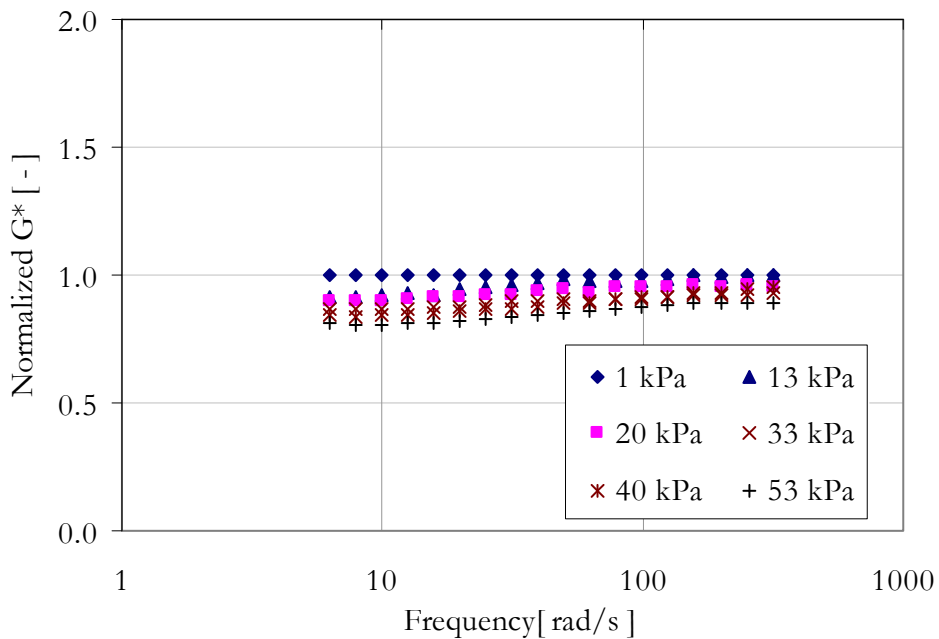


Figure 4-42 Normalized G^* values at 30°C for B70/100 mastic

From Figure 4-41 it can be seen that a shear stress of 1.2 MPa causes the complex modulus of the mastic to change by about 10%. However, at higher temperatures, see Figure 4-42, a much smaller shear stress level of 53 kPa causes the complex modulus to change by about 20%. This result has a practical implication in pavement design computations. Since for all temperatures trucks loads are constant, this implies that the effect of the nonlinear behaviour is significant at higher temperatures.

B) Summary of Results and Discussions

In this section the response data of the mastic obtained at various temperatures are summarized. The utilized approach is similar to the one used for the analysis of the B70/100 bitumen. At each stress levels, the mean of the normalized G^* values were calculated. Figure 4-43 summarizes the results obtained at various temperatures.

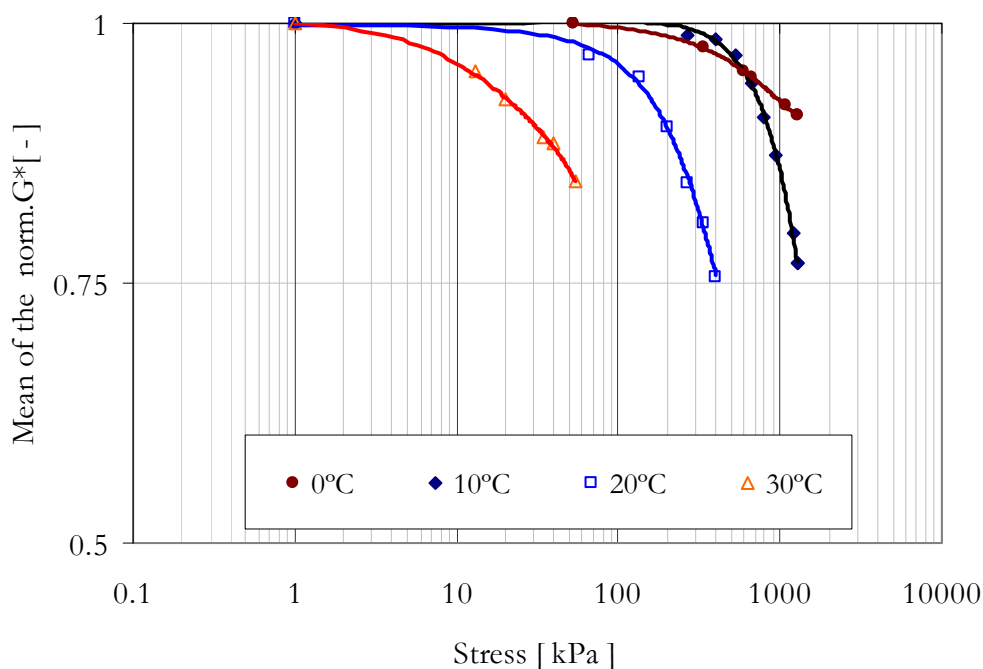


Figure 4-43 Mean of the normalized G^* at various stress levels, B70/100 mastic. For a temperature of 20°C, Figure 4-43 shows that shear stress values in the order of 100 kPa or more result in nonlinear behaviour. For lower temperatures, 10°C and 0°C, relatively higher shear stress in the range of 300 kPa and above result in a nonlinear response. Higher temperature data are only available at 30°C. However, it can be seen from the trend that shear stress values in the order of 10 kPa cause nonlinear behaviour at higher temperatures.

In Figure 4-44 the results obtained for the B70/100 bitumen are compared with the mastic results. From the graph it can be seen that the shear stress range at which nonlinear behaviour is evident appears to be similar for both the mastic and the B70/100 bitumen.

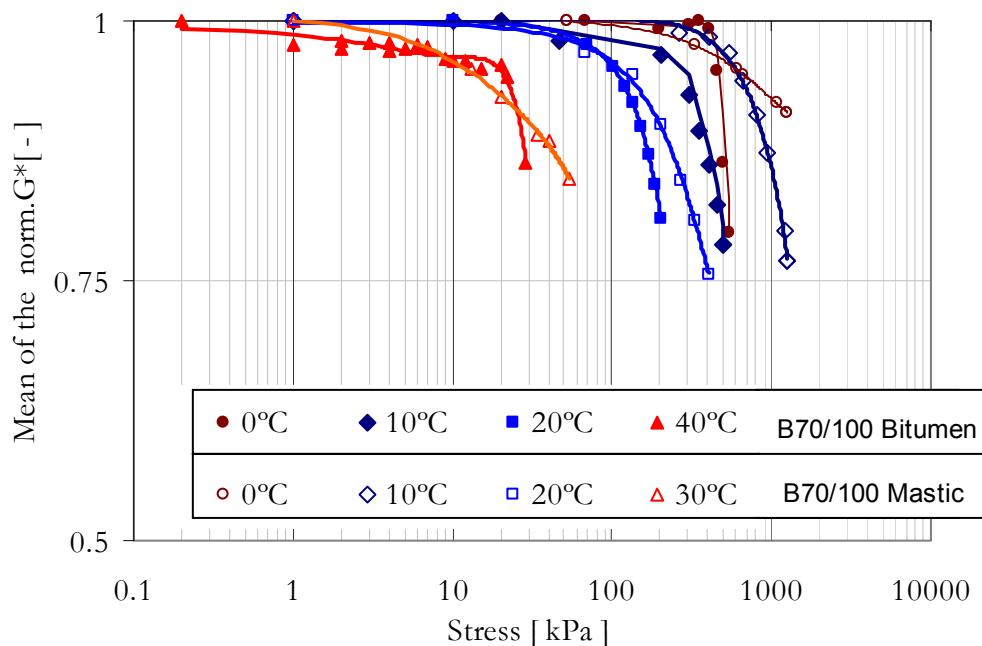


Figure 4-44 Mean of the normalized G^* (open and filled marks represent the B70/100 mastic and the B70/100 bitumen data respectively)

4.3.4 Mortar Response at Low Stress Levels

The previous sections have shown the response of the pure B70-100 bitumen binder and B70-100 mastic for various shear stress levels at various temperatures. In this section, results obtained for the mortar testing at low stress levels are presented. As discussed in Section 0, the mortar column samples can be mounted to a DSR machine following two mounting procedures. Both procedures were used to obtain the response at low stress levels. The mounting procedure which gave less scatter in response data was adopted for response measurements conducted at higher stress levels. First the results from the two setups at low shear stress level are discussed.

4.3.4.1 Frequency Sweep Results; Setup with Steel End Clamps

The steel end clamps were developed in the first phase of a PA design tool project [7]. The purpose of the end clamps is to hold the mortar test specimen firmly during testing. The mounting procedure involves first inserting the mortar column to the top clamp. Then the screws on the steel clamp are tightened. The top rotating bar is slowly lowered and the mortar column is centred. Slowly the bottom end of the mortar column is inserted to the slot in the bottom clamp. The mortar sample should be straight for easy alignment with the bottom slot. All the screws holding the sample at the top and bottom need to be securely fastened. Figure 4-45 shows the mortar sample and end clamps in the DSR test setup.

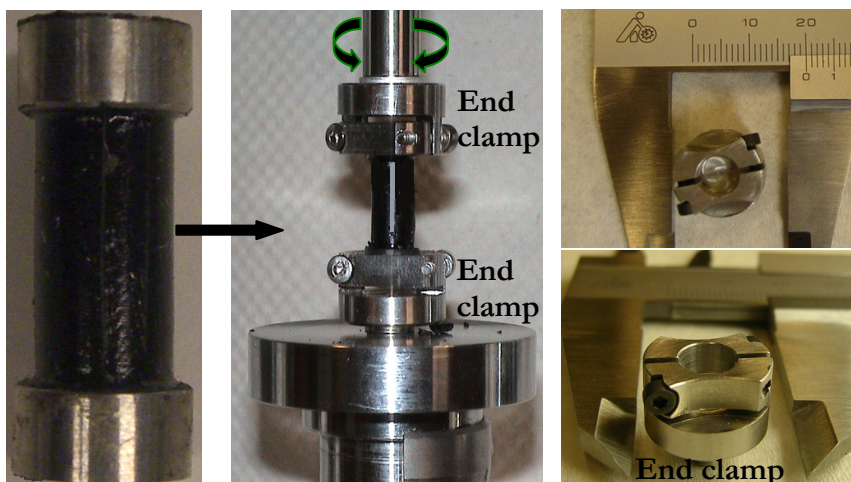


Figure 4-45 Mortar column DSR setup (left; test sample, middle; mounted specimen, right; steel end clamps)

Using this setup torque controlled frequency sweep tests were conducted on 5 different samples. Temperature ranges from -10°C to 30°C were covered. The results were used to form a master curve at a reference temperature of 10°C . Figure 4-46 presents the master curve for the mortar based on results from 5 different tests.

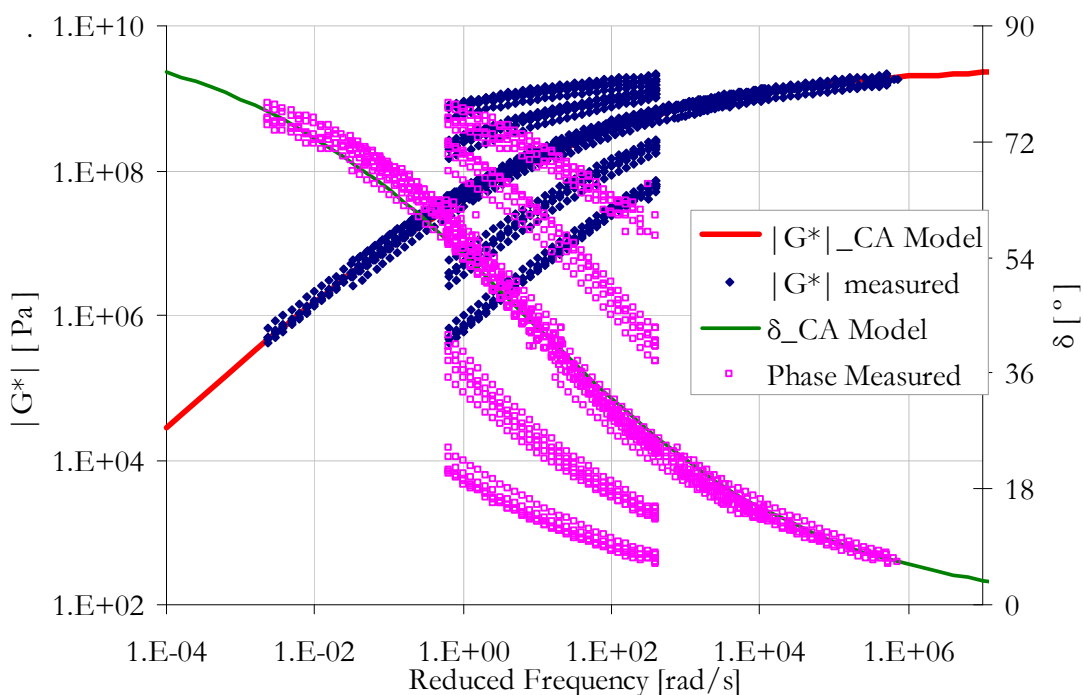


Figure 4-46 Master curves at $T_{ref}=10^{\circ}\text{C}$ obtained for different samples

The solid lines in Figure 4-46 represent the Christensen Anderson (CA) model fit to the master curve data. Quality of fit in terms of R square values were obtained for the G^* and δ . The shift factors used to obtain the master curve were also described by the WLF formula. The parameters for the WLF formula, the

CA model parameters and the regression coefficients for the master curve are presented in Table 4-18.

Table 4-18 Master curve parameters at $T_{ref} = 10^{\circ}\text{C}$

	WLF Factors		CA model parameters			R ²	
	C ₁	C ₂	G _g	ω_c	R	G*	δ
	[-]	[-]	[MPa]	[rad/s]	[-]	[-]	[-]
Mortar	21.88	160.98	2760	6.83	1.37	0.974	0.991

A) Observations

Figure 4-46 shows that a slight scatter has been observed for the complex modulus and phase angle data. The source of the scatter can be attributed to various reasons. The sampling methods and the mounting procedure are among the main possible sources for the data scatter. In the sample preparation stage, great care was taken to avoid samples containing too much air voids. To allow easy placement of the mortar sample into the clamps, the outer surface of the steel rings needed to be cleaned with Heptane ('Wasbenzine'). In this stage great care is needed to avoid any contact between the mortar sample and the cleaning substance. During mounting, the centring of the mortar samples and the fastening of the screws also involved a delicate procedure. It was observed that when the steel rings are not perfectly circular in shape, difficulty was encountered in inserting the rings into the end clamps. This process is believed to introduce unaccounted deformation into the mortar sample.

Visual observation at the end of the testing also showed that, sometimes, the steel end clamps fail to grip the sample firmly. This is also another possible source for the scatter observed in the results.

4.3.4.2 Frequency Sweep Results; Setup with Glued Ends

Similar measurements on the mortar were conducted using the DSR setup with glued ends. The mounting procedure involves gluing the mortar sample to the top rotating rod of the DSR machine. For ease of handling the mortar samples were first kept at a low temperature, in the range of 0°C to 10°C , before mounting. The mortar column is glued on to the top rotating rod. Then glue is placed in the bottom plate and the top rod is lowered till the sample touches the glue on the bottom plate. Additional glue is put around the bottom ring to provide good bond. The glued-end and the clamped-end setup in a DSR machine were shown in Figure 4-10.

Five different mortar samples were tested under the same condition as in the tests conducted with the steel end clamps. The frequency sweep results obtained for these tests were used to form a master curve at a reference temperature of 10°C . The CA model was used to describe the complex modules

and the phase angle master curve data. Figure 4-47 presents the master curve data from the glued end setup.

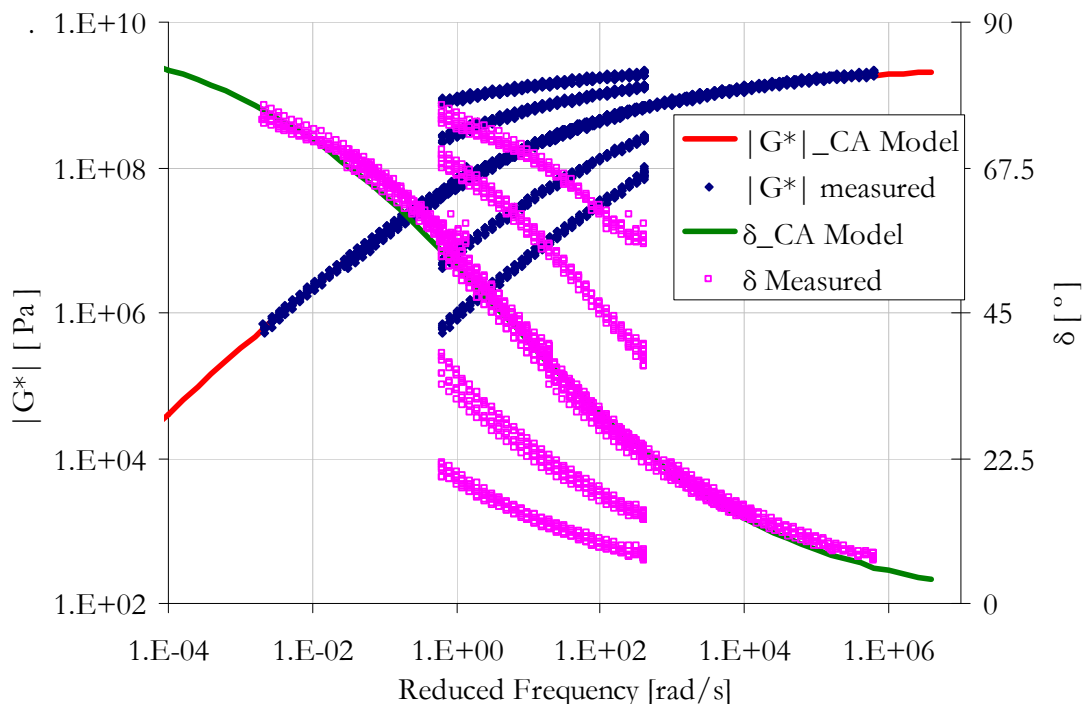


Figure 4-47 Master curves at $T_{ref}=10^{\circ}\text{C}$ obtained for 5 different samples. The shift factors that were used to construct the master curve are described by the WLF equation. The WLF factors together with the CA model parameters are given in Table 4-19.

Table 4-19 Master curve parameters at $T_{ref}= 10^{\circ}\text{C}$

	WLF Factors		CA model parameters			R^2	
	C_1	C_2	G_g	ω_c	R	G^*	δ
	[-]	[-]	[MPa]	[rad/s]	[-]	[-]	[-]
Mortar	21.86	157.14	2460	4.16	1.32	0.994	0.995

A) Observations

As compared to Figure 4-46 the results presented in Figure 4-47 have shown a better repeatability. This can also be seen from the higher R^2 values reported in Table 4-19. The better repeatability observed in case of the glued end setup can be attributed to many factors. In comparison with the steel end clamp setup, the mounting procedure for the glued end setup involved a less delicate procedure. The loosening of the end grips observed in the testing phase when using the steel end clamp was avoided by using the glue.

The relative disadvantage in using the glued end setup is that vertical alignment (centring) of the mortar sample is ensured with visual observation,

whereas in the setup with the steel end clamp the circular slots guarantee precise centring of the mortar sample. In spite of this, the glued end setup has provided better repeatability, and it is therefore chosen for carrying out further tests on the mortar with higher shear stress levels in this research.

4.3.5 Mortar Response at High Stress Levels

4.3.5.1 Frequency Sweep Test Results

Similar to the B70/100 bitumen and mastic testing procedures, a single mortar test specimen was used to investigate the stress dependency at a given temperature. As previously discussed, after each stress increment the potential presence of damage was monitored by conducting response measurements at a low stress level (linear viscoelastic range). With this method, the change in the linear viscoelastic property is constantly monitored. Using the same criterion as used for the B70/100 bitumen and mastic, a maximum of 10% reduction in the complex modulus value (linear viscoelastic value) is used as a criterion to define the maximum shear stress level. A frequency window of 1 Hz to 50 Hz was chosen. Table 4-20 presents the range of stress covered at each temperature for the mortar.

Table 4-20 Shear stress ranges covered in mortar response tests

Temperature [°C]	-10	0	10	20	30
Shear stress range [kPa]	10 – 2,420	10 - 2,420	1 - 1,115	1 - 911	1 - 300

For temperatures of 0°C and 20°C, Figure 4-48 to Figure 4-51 illustrate the complex modulus and phase angle plots at various shear stress levels. Similar plots for other temperatures are given in Appendix C.

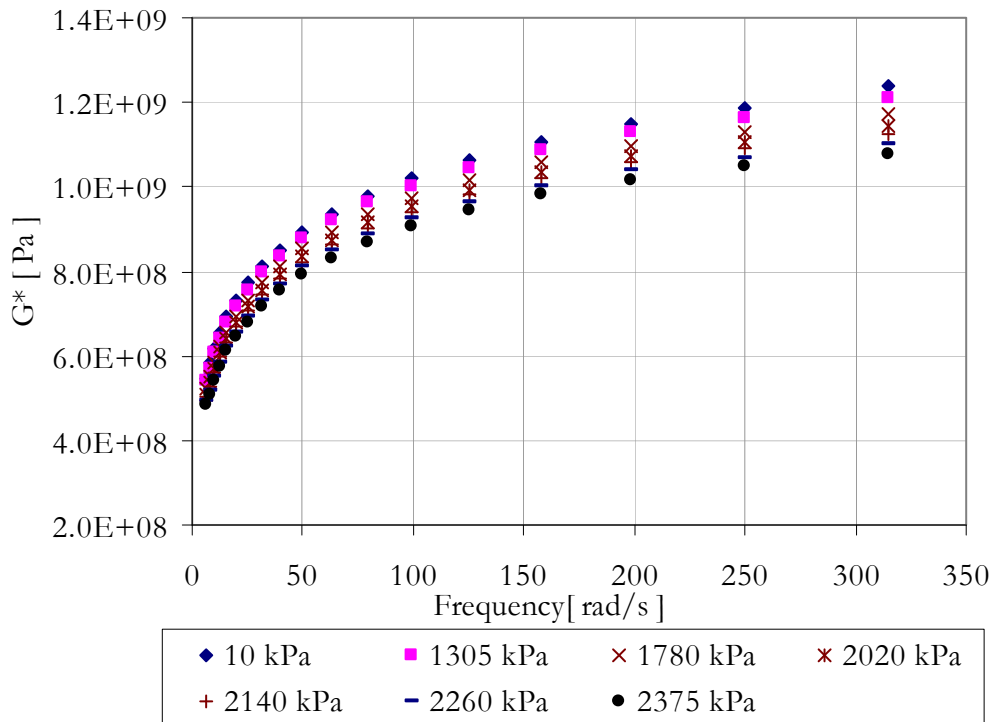


Figure 4-48 Frequency sweep result; complex modulus for mortar at 0°C

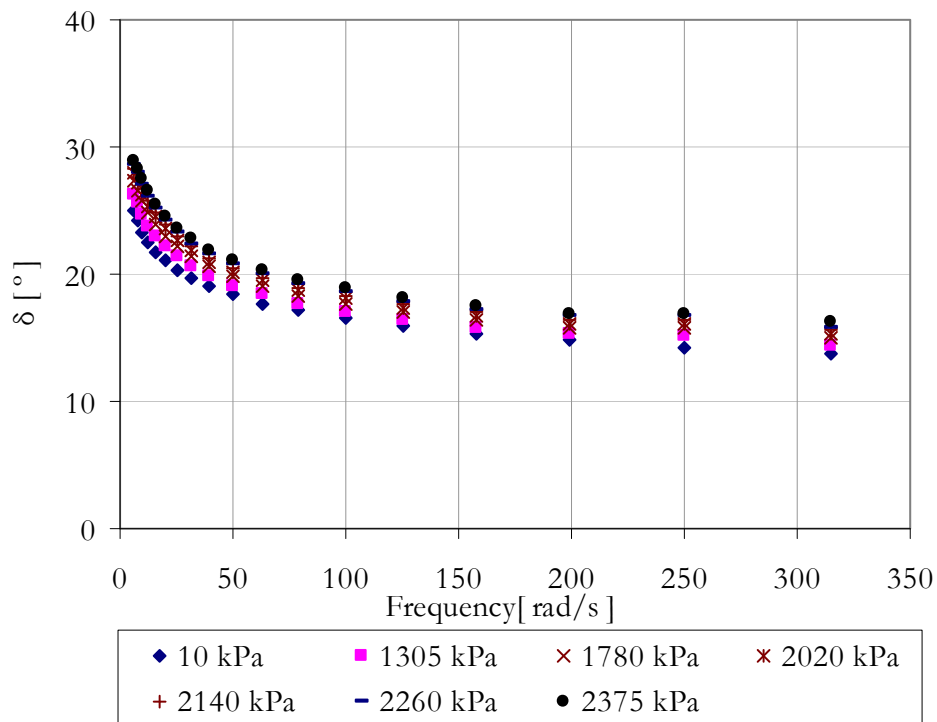


Figure 4-49 Frequency sweep result; phase angle for mortar at 0°C

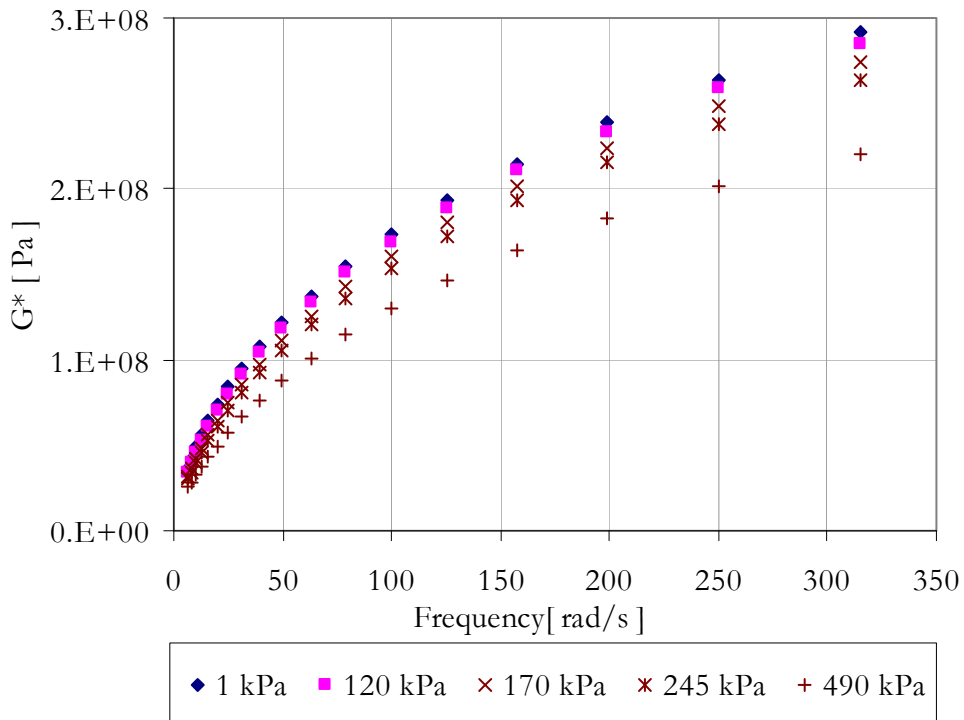


Figure 4-50 Frequency sweep result; complex modulus for mortar at 20°C

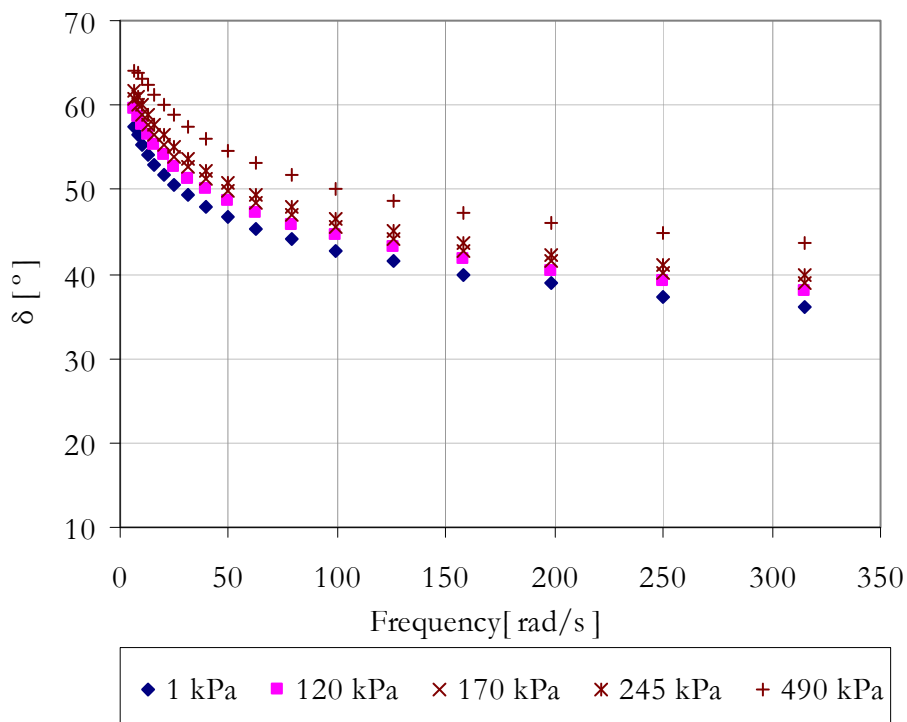


Figure 4-51 Frequency sweep result; phase angle for mortar at 20°C

Following the procedure used for the B70/100 binder and the B70/100 mastic, the G^* values obtained at various shear stress levels for the mortar were normalized with the corresponding G^* values obtained at the lowest shear stress level, i.e. the linear viscoelastic G^* . As an example, the normalized G^*

values at various shear stress levels at 0°C and 20°C are presented in Figure 4-52 and Figure 4-53 respectively.

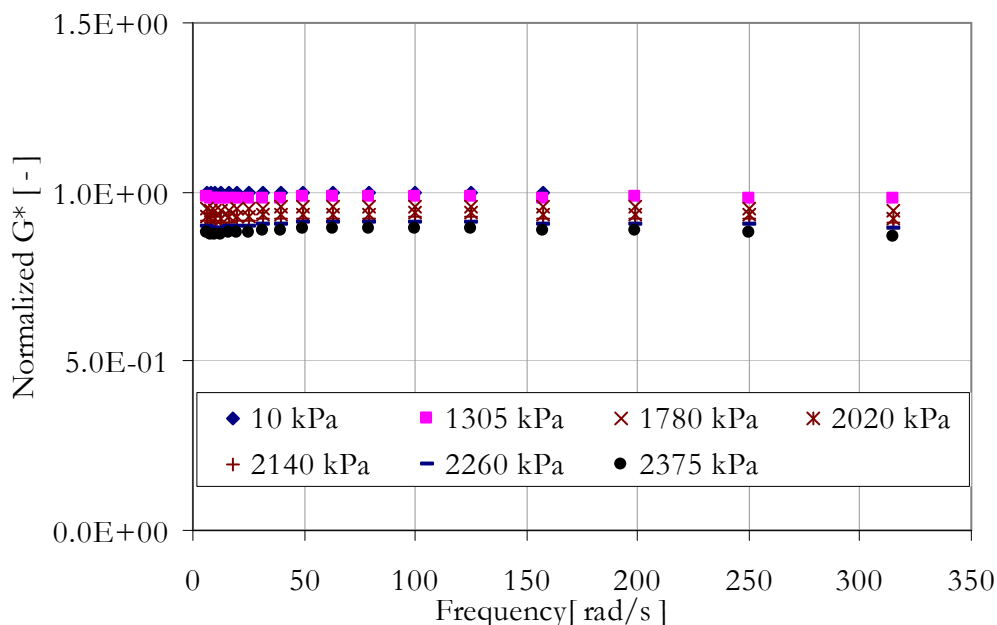


Figure 4-52 Normalized G^* at various stress levels for mortar at 0°C

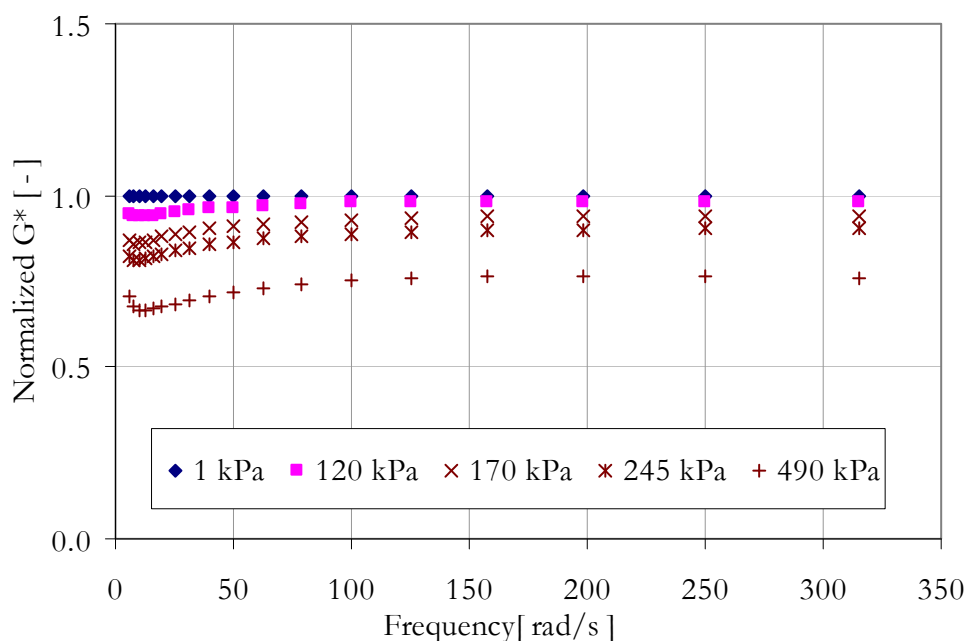


Figure 4-53 Normalized G^* at various stress levels for mortar at 20°C

From the data at 20°C in Figure 4-53, it can be seen that a normalized G^* value of about 0.75 is obtained for a shear stress of 490 kPa. In terms of the linear viscoelastic complex modulus value, it translates to a 25% reduction. For the results at 0°C (see Figure 4-52) a much higher shear stress level of 2.4 MPa gives a normalized G^* value of 0.9. This implies that at 20°C the mortar exhibit highly nonlinear behaviour at a smaller shear stress levels as compared to the behaviour at 0°C.

A) Summary of Results and Discussions

In the above discussions, the mortar response results obtained at 0°C and 20°C were used to illustrate the mortar response behaviour at low and intermediate temperatures. Here the results obtained for all temperatures are summarized. To allow evaluation of the shear stress ranges where nonlinear behaviour of the mortar is evident at various temperatures, the mean of the normalized G^* values were calculated at the various stress levels. For temperatures varying from 0°C to 30°C, Figure 4-54 summarizes the results obtained at various shear stress levels for the mortar.

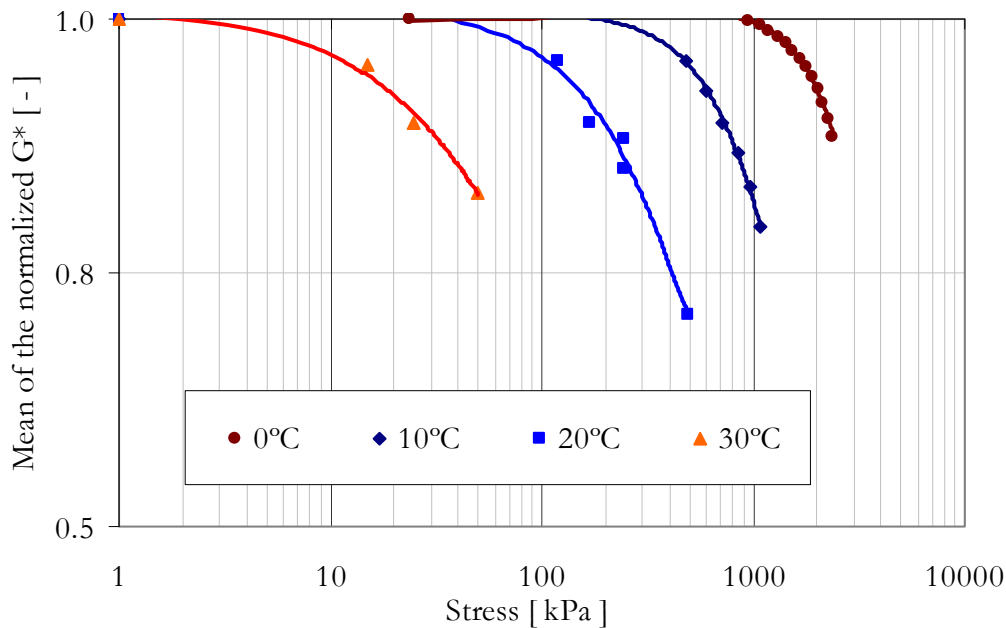


Figure 4-54 Mean of the normalized G^* values for the mortar

Figure 4-54 shows that at a temperature of 20°C shear stress values of 100 kPa and above result in a nonlinear behaviour. For 10°C a relatively higher shear stress in the range of 300 kPa causes a nonlinear response. At 0°C the mortar shows nonlinear behaviour for shear stresses above 1 MPa. It can also be seen that a much smaller shear stress value in the range of 10 kPa causes nonlinear behaviour of the mortar at 30°C. These results appear to be similar with the results obtained for the mastic in the previous section. For the sake of comparison the normalized G^* values for the mastic and the mortar are presented together in Figure 4-55.

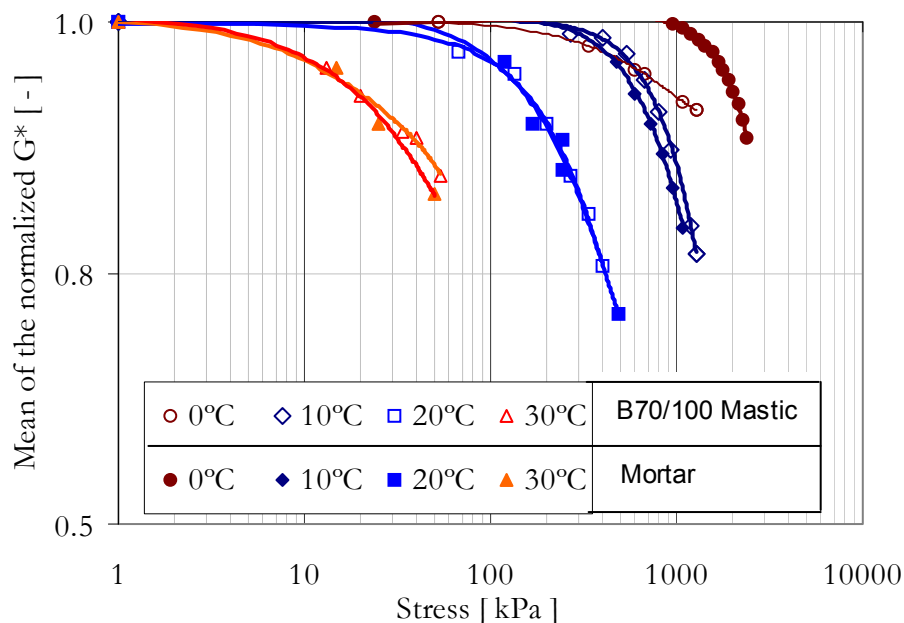


Figure 4-55 Mean of the normalized G^* ; mortar and mastic

Figure 4-55 shows that with the exception of the 0°C data, the shear stress range where the mortar and the mastic exhibit nonlinear behaviour is very similar. In addition to the shear stress range, the values of the normalized G^* at the various shear stress levels also appear to be the same. Since the filler-binder ratio used in the mastic and the mortar is the same, the above results may indicate that the observed nonlinear behaviour of the mortar at intermediate and high temperature regions is highly governed by the mastic behaviour.

Analysis of the mortar and mastic response data obtained at low stress levels also lead to a similar conclusion. As shown in Figure 4-56, the master curves that were obtained for the mastic and the mortar at a reference temperature of 10°C reveal similar response behaviour for frequencies lower than 1 rad/s . From the time-temperature superposition principle that were used to construct the master curve, the data corresponding to the reduced frequencies in the range of $1\text{E-}4\text{ rad/s}$ to 1 rad/s in Figure 4-56 represent the response for temperatures of 20°C and 30°C . For obtaining the master curve parameters for the mastic and mortar, reference is made to Table 4-14 and Table 4-19 respectively.

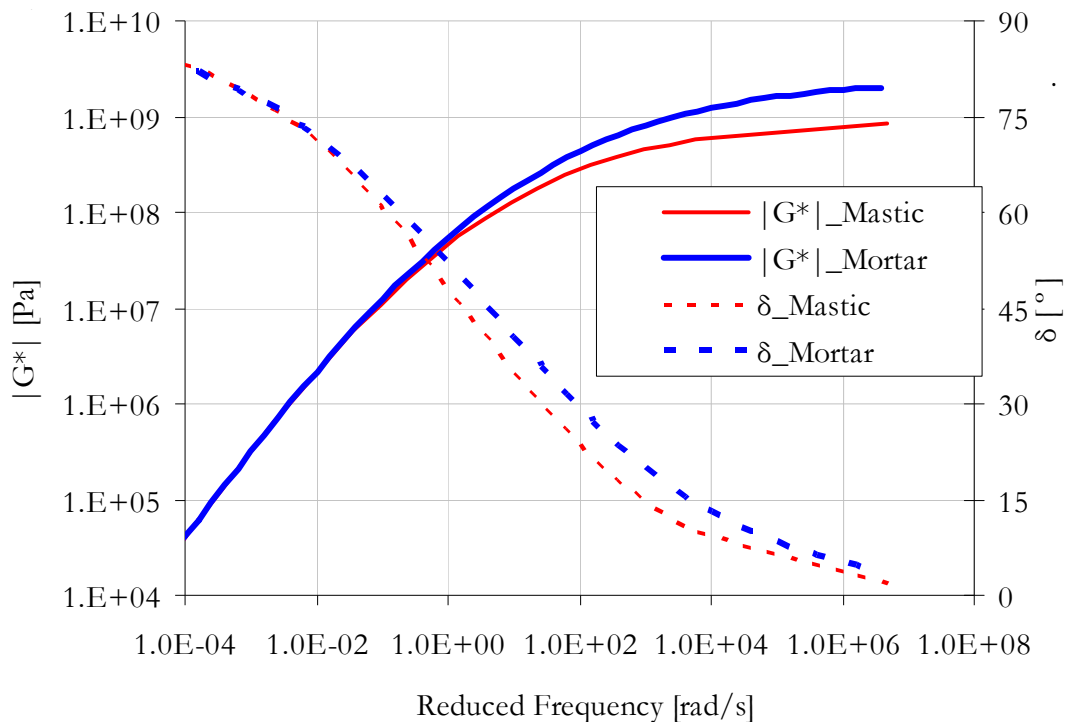


Figure 4-56 Master curves for the mortar and mastic at 10°C.

In contrary to the trend observed at higher temperatures, the nonlinear behaviour of the mortar at 0°C is rather different as compared to the mastic. From Figure 4-55 it can be seen that the mastic exhibit a nonlinear behaviour for shear stress values of 300 kPa and above, whereas the nonlinear behaviour of the mortar is evident for shear stress values greater than 1MPa. In terms of the shear stress range covered in the test, it can also be seen that much higher shear stress values have been realized in the mortar at 0°C. This difference in response behaviour is also observed on the master curve results shown in Figure 4-56, i.e. higher complex modulus values for the mortar at lower temperatures. For the materials considered in this study, the above discussion implies that in terms of the response, the presence of fine fractions of sand in the mortar influenced the low temperature behaviour. For temperatures of 20°C and above, the mastic and mortar response appeared to be similar both in the linear as well as the nonlinear range.

B) Experimental observations

Specimen Geometry

The mortar column geometry was found to be suitable for response testing for temperatures up to 30°C. Experimental attempts to apply the same geometry for response investigations at higher temperatures were not successful. It was observed that for temperatures of 40°C and above the mortar column showed excessive creep due to temperature effects. Because of this reason the response investigations conducted at higher temperatures were excluded from the analysis.

Testing and Data Processing

Due to inertia and machine compliance factors, the torque that is applied by the DSR machine (raw torque) is not the same as the torque in the test sample. This also applies to the raw deformations measured by the machine and the resulting deformation in the test sample. The raw torque and raw deformations measured by the machine therefore need to be adjusted for inertia and machine compliance factors to obtain the true torque and true deformation in the test sample. This has been extensively discussed elsewhere [9]. Following this procedure, it has been observed that at higher frequencies (in the range of 200 rad/s and above) inertia and compliance factor corrections on a constant raw torque resulted in a varying torque in the test sample. This has been illustrated using the mortar test data at 10°C as shown in Figure 4-57 and Figure 4-58.

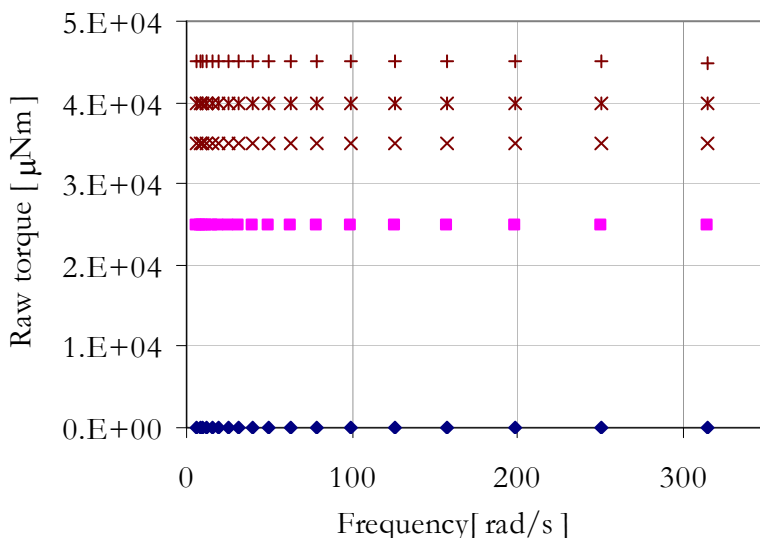


Figure 4-57 Applied (raw) torque; mortar test conducted at 10°C

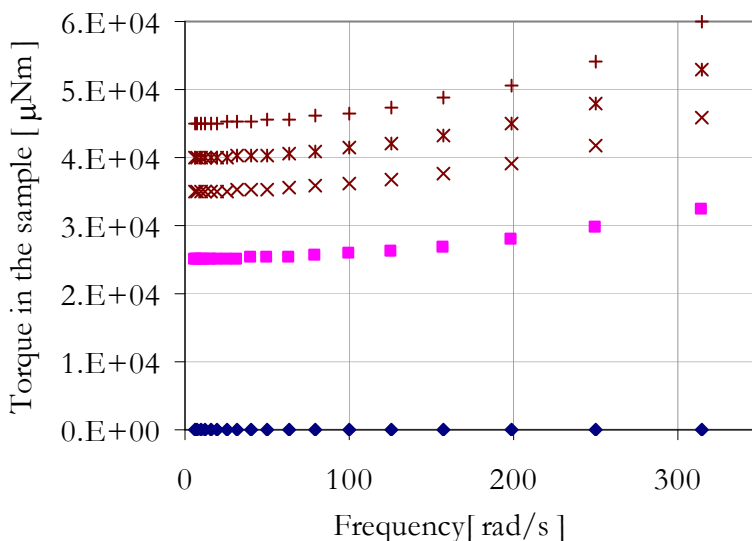


Figure 4-58 Real torque in the mortar sample, test conducted at 10°C

The main reason for the variation in torque observed at higher frequencies is due to the resonance effect. This effect on mortar test results for frequencies in the range of 150 rad/s to 200 rad/s has also been reported elsewhere [9]. Analysis of the data points for frequencies less than 200 rad/s showed that the variation in torque lies within the range of $\pm 5\%$ from the mean value. Since it is desired to characterize the mortar behaviour for constant torque covering a range of frequencies, it has been decided that a $\pm 5\%$ variation in torque magnitude is acceptable. Therefore, for the nonlinear response modelling work, which is to be covered in Chapters 5 and 6, the data points corresponding to the frequency range of 200 rad/s and above are excluded.

The above discussion also implies that mortar response and fatigue measurements that are obtained at loading rates which lie in the vicinity of the resonance frequency may lead to misleading results.

4.4 Conclusions

4.4.1 Experimental Setups

Two different experimental setups, i.e. the cone and plate and the mortar column setup, were used in this research. For testing the penetration grade bitumen and the mastic the cone and plate setup was used. For the mortar, the DSR setup with a cylindrical shaped specimen was utilized. With these setups response investigations were made at low and high shear stress levels. With regard to the test setups the following conclusions were reached:

Cone and Plate Setup

- The cone and plate setup provides fairly uniform shear stress distribution in the test samples.
- For B40/60 bitumen, the response results obtained from the 8 mm and 25 mm diameter cone and plate setups were found to be comparable with the results obtained from the standard parallel plate geometries.
- For the mastic, the 25 mm diameter cone, with a cone angle of 4.57° , has delivered inconsistent result (see Figure 4-17). The inconsistency is believed to be a result of the small cone angle and small gap. In comparison to the maximum size of the filler material in the mastic, higher gap settings and higher cone angles may provide better results. This can possibly avoid jamming of filler materials in the vicinity of the tip of the cone, where the distance between the surface of the cone and the bottom plate is small.
- The 8 mm diameter cone, which has a larger cone angle of 26.57° , has provided comparable results with the data obtained from the parallel plate geometries (Figure 4-16). However, better quality response data may also be obtained if higher gap setting (2~5 times the maximum size of the filler) is used.

Mortar Column Setup

- For mortar testing, either the steel end clamp or the glue can be used to mount the sample into the DSR machine. The repeatability of the test results were found relatively better in case of the glued ends.
- For the setup with steel end clamp a contact slip between the end clamps and the steel rings on the mortar has been observed in limited cases. This introduces variability in the test results.
- For mortar column testing, excessive creep due to temperatures effects was observed at high temperatures. Because of this the mortar column setup is not recommended for testing temperatures in the range of 40°C and above. For lower temperature regions, 30°C and below, the test setup delivered good results.
- Due to resonance frequency effects the mortar column setup does not provide good results for frequencies larger than 200 rad/s (Figure 4-58).

4.4.2 Test Results

Binder response investigations at various stress levels were performed. Following each shear stress application the test sample has been monitored for existence of any possible damage. A change in the complex modulus value of 10% was used as a threshold value to filter out response data that may possibly include damage. Based on the data analysis, the following conclusions were reached:

- Nonlinear behaviour was observed at high shear stress levels for all the binders.
- The stress range where nonlinear behaviour is observed varies with temperature. At higher temperatures, i.e. above 30°C, shear stresses as low as 10 kPa causes nonlinear behaviour in the mortar. At 0°C, nonlinearity is apparent for shear stress values of 1 MPa and above.
- In the intermediate temperature range shear stresses within the range of 100 kPa to 300 kPa cause nonlinear behaviour in the binders. Shear stress levels greater than 300 kPa cause nonlinear behaviour at 10°C for the mastic and mortar. At 20°C, nonlinear behaviour is observed for shear stresses greater than 100 kPa.
- The response behaviour of the mortar and the mastic has been found to be similar for temperatures of 20°C and above. This observation has been found valid for data obtained from the low stress as well as the high stress measurements (Figure 4-55 and Figure 4-56).

4.4.3 Implications

- The nonlinear behaviour observed at high shear stress levels implies material response models used in meso mechanics design programs need to incorporate the observed nonlinear behaviour.
- In view of constant axle loads on a pavement, both at low and high temperatures, the effect of nonlinear behaviour on the pavement response is expected to be highly pronounced at higher temperatures. This is because at high temperatures the binders behave nonlinear at small shear stress levels.

References

- [1]. Airey, G., Rahimzadeh, B., and Collop, A., *Viscoelastic linearity limits for bituminous materials*. Materials and Structures, 2003. **36**(10): p. 643-647.
- [2]. Airey, G.D., Rahimzadeh, B., and Collop, A.C., *Linear Rheological Behavior of Bituminous Paving Materials*. Journal of Materials in Civil Engineering, 2004. **16**(3): p. 212-220.
- [3]. Christensen, D.W. and Anderson, D.A., *Interpretation of Dynamic Mechanical Test Data for Paving Grade Asphalt Cements*. J. Assoc. Asphalt Paving Tech., 1992. **61**: p. 67-116.
- [4]. Ferry, J.D., *Viscoelastic properties of Polymers*. 3rd edition ed. 1980, New York.
- [5]. Huurman, M., *Lifetime Optimisation Tool, LOT, Main Report*. 2008: Delft.
- [6]. Huurman, M., Mo, L., and woldekidan, M.F., *Unravelling Porous Asphalt Concrete, Towards a Mechanistic Material Design Tool*. Int. Journal Road Materials and Pavement Design, 2009. **10**(Special Issue).
- [7]. Huurman, M., Mo, L., Woldekidan, M.F., Khedoe, R.N., and Moraal, J. *Overview of the LOT meso mechanical research into porous asphalt raveling*. in *Proceedings of the 7th Int. RILEM Symposium Advanced Testing and Characterization of Bituminous Materials*. 2009. Rhodes, Greece.
- [8]. Masad, E. and Somadevan, N., *Microstructural Finite-Element Analysis of Influence of Localized Strain Distribution on Asphalt Mix Properties*. Journal of Engineering Mechanics, 2002. **128**(10): p. 1105-1114.
- [9]. Mo, L., *Damage Development In The Adhesive Zone and Mortar of Porous Asphalt Concrete*. 2010, Delft.
- [10]. Muraya, P.M., *Permanent Deformation of Asphalt Mixtures*. 2007, Delft Univeristy of Technology: Delft.
- [11]. Pronk, A.C. and Hopman, P. *Energy Dissipation: The leading factor for Fatigue*. in *Strategic Highway Research Program (SHRP): Sharing the Benefits*. 1990. London, UK.
- [12]. RAW, *Standaard RAW Bepalingen 2005*. 2005: Ede.

5

Modelling Linear Viscoelastic Response of Binders

In Chapter 4 the response of bituminous binders for various shear stress levels has been investigated. From the results it has been observed that the response of the binders at high shear stress levels is nonlinear. Modelling the nonlinear response of the binders will be treated in detail in the next chapter. In this chapter, modelling the response of the binders in the linear viscoelastic range is presented. For this purpose the two selected response models, the Huet-Sayegh and the Burgers' model, have been utilized. In the first half of the chapter, the ability of the Huet-Sayegh model to describe the binder response in the frequency domain will be analyzed. Modifications that are deemed necessary are discussed, and methods of obtaining model parameters from experimental data are presented. For applications in numerical environments the time domain formulation of the model is presented. The relationships between the time and frequency domain responses of the binders have also been discussed. For these relations, numerical and experimental verifications have been performed using a number of creep-recovery and relaxation tests. The second half of the chapter covers similar modelling work with the Burgers' model. Based on the obtained results the pros and cons of the models are summarized, and the practical implications are discussed.

5.1 Response of Bituminous Materials

Bituminous materials have time dependent mechanical properties. The creep compliance and the relaxation modulus functions are two commonly used material functions that are used to characterize the time dependent behaviour. In the frequency domain, the corresponding material functions are known as

the dynamic creep compliance and the dynamic modulus. These functions are unique and serve as the fingerprint of the material. It follows from the theory of linear viscoelasticity that these material functions are interrelated. Hence, if the relaxation modulus of a material is known the creep compliance can be derived and vice versa.

Various forms of analytical expressions (models) are usually used to describe the relaxation modulus and creep compliance data obtained from laboratory tests [3, 10, 13]. The required model parameters to describe a given response data can be determined by performing a regression analysis on experimental data. For the Huet-Sayegh and the Burgers' model, the ability of the models to describe experimentally obtained data is investigated in the following sections.

5.2 The Huet-Sayegh (HS) model

The HS model is an excellent model for AC mixture response modelling. It is obtained by placing a parallel spring to the original Huet model [8]. Its distinct feature as compared to other rheological models is its ability to describe AC mixture response for a wide range of loading rates with a limited number of model parameters [13, 17]. The physical representation of the HS model is given in Figure 5-1.

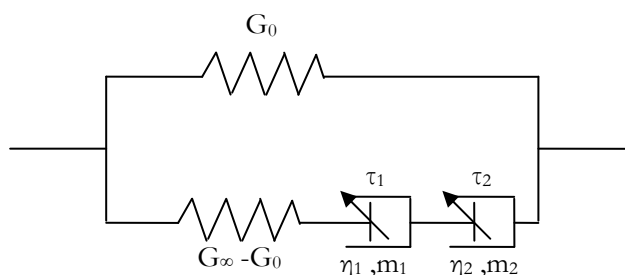


Figure 5-1 Huet-Sayegh model

5.2.1 The Model Behaviour in Frequency Domain

The mathematical representation of the HS model in frequency domain (for the shear modulus G) is given by:

$$G^*(\omega) = G_0 + \frac{G_\infty - G_0}{1 + \delta_1 (i\omega\tau_1)^{-m_1} + \delta_2 (i\omega\tau_2)^{-m_2}} \quad 5-1$$

where:

G_∞ = instantaneous shear modulus value

G_0 = rubbery shear modulus value

τ_1, τ_2 = time constants

m_1, m_2 = parabolic dashpot coefficients

δ_1, δ_2 = model parameters

i = complex number notation

The constants δ_1 and δ_2 are defined as:

$$\delta_i = \frac{\tau_i(G_\infty - G_0)}{\eta_i} \quad 5-2$$

Where η_i denotes model parameters for the parabolic dashpots. This model has a total of six parameters and two time constants. For asphalt concrete response modelling only one time constant is often used and the model parameter δ_2 is taken as unity [8]. Consequently only six parameters are used to describe the complete response of asphalt concrete covering various temperature and frequency regions.

At extreme low and high values of frequencies, the model approaches to limiting threshold values. For complex shear modulus data, these threshold values are the rubbery shear modulus, G_0 , and the instantaneous shear modulus, G_∞ , values (Figure 5-2). For intermediate values of frequencies, the shape of the master curve is dictated by the parabolic dashpot parameters. Parabolic dashpot coefficients values close to unity tends to make the S-curve steeper. This results in a narrow spectrum of relaxation times. Dashpot coefficient values close to nil tends to flatten the curve, implying less sensitivity of the material response for loading frequency. Coefficients between zero and one result in an S-shape curve with a moderate slope that describes the material behaviour within wide relaxation spectrum.

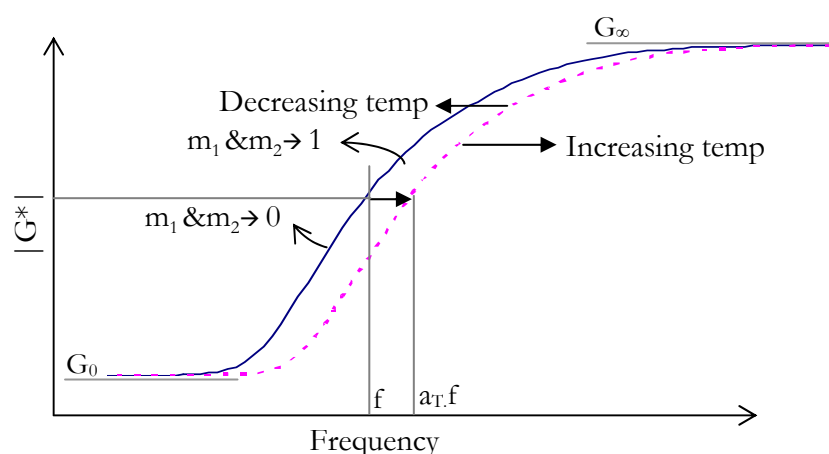


Figure 5-2 The HS model characteristics

For materials obeying the time-temperature superposition principle, the effect of temperature on the HS model parameters can be explained by applying the

appropriate shift factors to the time related model variables, i.e. the dashpot parameters.

5.2.2 Viscous Response Element

As discussed in the literature review section, for small loads asphaltic mixtures exhibit a mix of elastic, viscoelastic and viscous properties. While the HS model is capable of describing the response of such materials for wide frequency and temperature ranges very well, the model principally lacks a response element for simulating viscous deformation in asphalt mixtures.

In bitumen rich asphalt mixtures, such as dense asphalt concrete, the large stone aggregates in the mixture more or less float in the bituminous mortar. In such mixtures the contribution of the viscous deformation of the bituminous mortar to the overall mixture deformation is significant. In this case, the only disadvantage of the HS model, in contrast with the familiar Burgers' model, is the lack of a viscous response element. In this regard, the wider use of the Burgers' model for modelling permanent deformation characteristics of asphalt mixture is partly attributed to its ability to capture viscous deformation [20]. As an attractive alternative to the Burgers' model, the inclusion of a viscous deformation element in the HS model will make the model more comprehensive for broader application. To capture linear viscous deformations, the original HS model is therefore modified by adding linear dashpot element in series.

5.3 A Modified HS Model (MHS)

The MHS model is obtained by placing a linear dashpot in series with the original HS model. The linear dashpot element is for improving the low frequency region fit of the model to experimental data. It also allows the model to simulate viscous deformations. The physical representation of the model is shown in Figure 5-3.

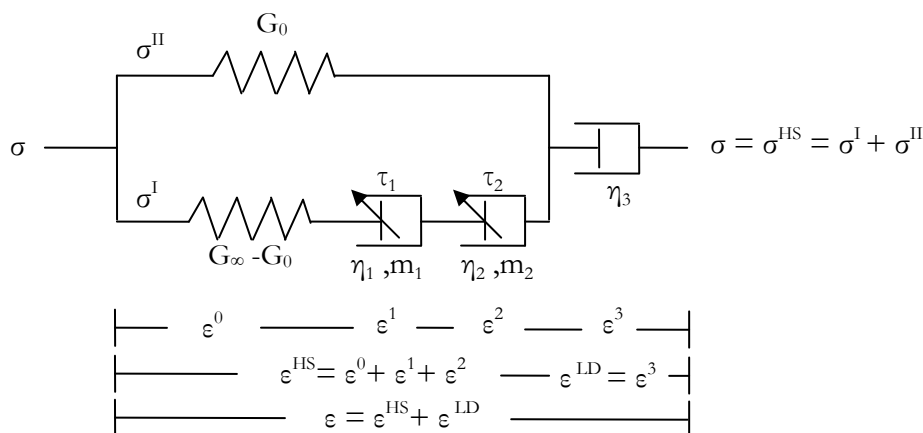


Figure 5-3 MHS model

5.3.1 The Model in Frequency Domain

The general behaviour of the model in frequency domain is similar to that of the original HS model. However, the behaviour of the MHS model at very low frequency regions resembles that of the Burgers' model. Unlike the original HS model, where the limiting value at the lower frequency region is a non-zero rubbery modulus value G_0 , the MHS model approaches a limiting value of nil at very low frequencies. This is due to the presence of the linear dashpot element which enables the model to simulate viscous deformations.

5.3.1.1 Model Parameter Determination

For model parameter determination from frequency domain data, the analytical expression of the model in frequency domain is required. Since the total strain in the MHS model is the sum of the strain in the linear dashpot and the strain in the original HS model (Figure 5-3), the creep compliance of the MHS model can be obtained by adding the compliances of the linear dashpot and the original HS model as:

$$J^*(\omega)_{\text{MHS}} = \frac{G'}{|G^*|^2} - i \left[\frac{G''}{|G^*|^2} + \frac{1}{\eta_3 \omega} \right] = J'(\omega) - iJ''(\omega) \quad 5-3$$

In Equation 5-3 the term η_3 is the linear dashpot parameter. The terms $J^*(\omega)_{\text{MHS}}$, $J'(\omega)$ and $J''(\omega)$ denote the complex, storage and loss creep compliances of the MHS model. The terms G' , G'' and $|G^*(\omega)|$ denote the expression for the loss shear modulus, storage shear modulus and magnitude of the complex shear modulus for the original HS model.

The expression for the storage and loss modulus values of the original HS model is given by[17]:

$$G' = G_0 + A \frac{G_\infty - G_0}{A^2 + B^2} \quad \& \quad G'' = B \frac{G_\infty - G_0}{A^2 + B^2} \quad 5-4$$

Further, the variables A and B in the storage and loss modulus expression are obtained as:

$$A = 1 + \delta_1 \frac{\cos\left(m_1 \frac{\pi}{2}\right)}{(\omega\tau)^{m_1}} + \delta_2 \frac{\cos\left(m_2 \frac{\pi}{2}\right)}{(\omega\tau)^{m_2}} \quad \& \quad B = \delta_1 \frac{\sin\left(m_1 \frac{\pi}{2}\right)}{(\omega\tau)^{m_1}} + \delta_2 \frac{\sin\left(m_2 \frac{\pi}{2}\right)}{(\omega\tau)^{m_2}} \quad 5-5$$

Given a set of data comprising the dynamic modulus and the phase angle values, Equation 5-3 to Equation 5-5 can be used to determine the parameters for the MHS model using simple regression analysis in an excel sheet. The following procedure can be followed in the model parameter determination:

- Define the error as the square of the relative difference between the experimentally determined and model predicted values for all the data points. This is done for the loss and storage compliances of the MHS model.
- Define the objective function as the sum of the squared standard errors obtained for all the data points.
- Minimise the objective function (Equation 5-6) using multi-dimensional non-linear least square regression techniques to determine all the model parameters.

$$\text{Objective function} = \sum_{i=1}^N \left(\left[\frac{J'_i}{J_i{}^0} - 1 \right]^2 + \left[\frac{J''_i}{J_i{}^0} - 1 \right]^2 \right) \quad 5-6$$

In Equation 5-6, J'_i and J''_i denote the predicted storage and loss compliances for the MHS model at the i^{th} frequency. The notations $J_i{}^0$ and $J_i{}^0$ represent the measured storage and loss compliance at the i^{th} frequency.

5.3.1.2 Model Application to Describe Frequency Domain Data

The MHS model has been used to describe several experimental data including those obtained on penetration grade bitumen, mastic, virgin mortar, aged mortar and bituminous mixtures. The response data obtained for the penetration grade bitumen, the mastic and the virgin mortar are described in Chapter 4. The response data for the aged mortar have been taken from a prior research project. This particular mortar contains Cariphalte XS (polymer modified) bitumen [9]. To illustrate the model's ability to simulate the response of asphalt mixtures, asphalt mixture data from literature have been used. The two asphalt mixture response data that were obtained from literature include the following:

- STAB 0/22 mixture response data that were obtained at temperatures ranging from -10°C to 20°C . The stiffness modulus was measured in a four point bending test (4PB) in the controlled displacement mode. The data cover frequency ranges from 2 to 29.3 Hz [17].
- Response data for a Recycled Asphalt mixture (RAP) obtained at temperatures ranging from -10°C to 50°C . The modulus was obtained from dynamic tests in the uni-axial mode. The data covers a frequency window ranging from 0.1 Hz to 25 Hz [19].

Figure 5-4 and Figure 5-5 illustrate the MHS model ability to describe frequency domain response data for the mortar and mastic. In these figures the model prediction with the absence of the linear dashpot is also included to illustrate the contribution of the linear dashpot at low frequencies.

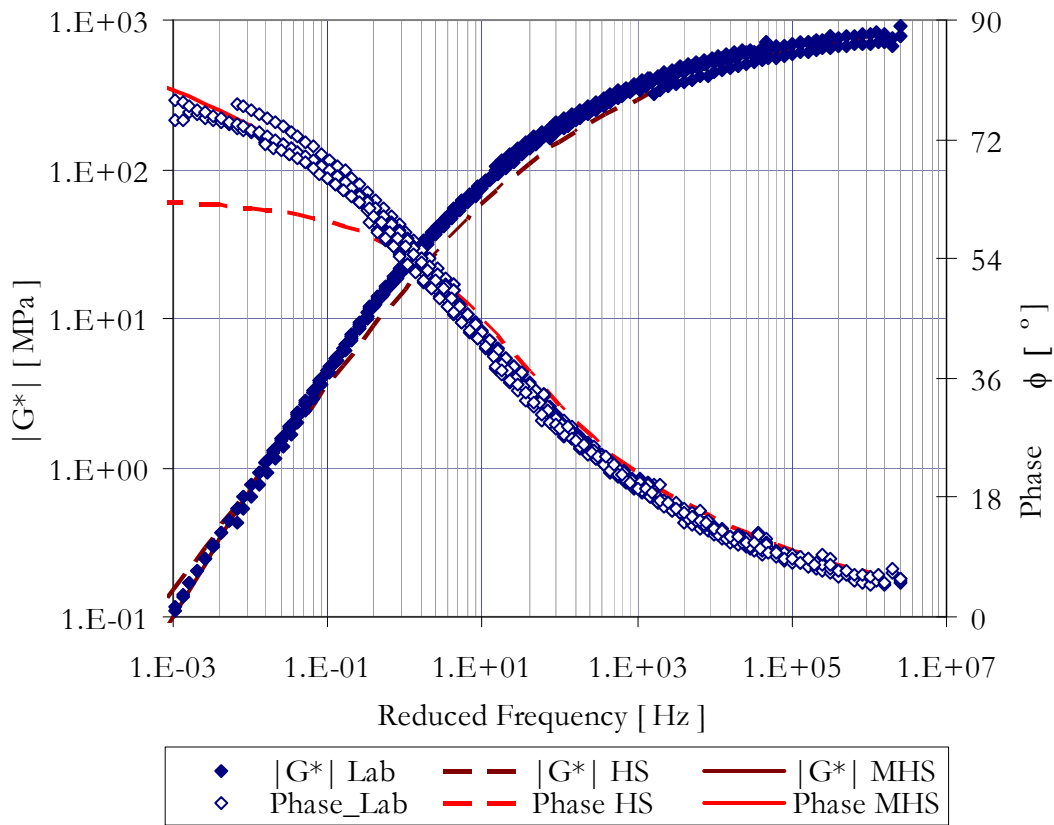


Figure 5-4 MHS and HS model fit to a mastic master curve ($T_{ref}= 20^{\circ}\text{C}$)

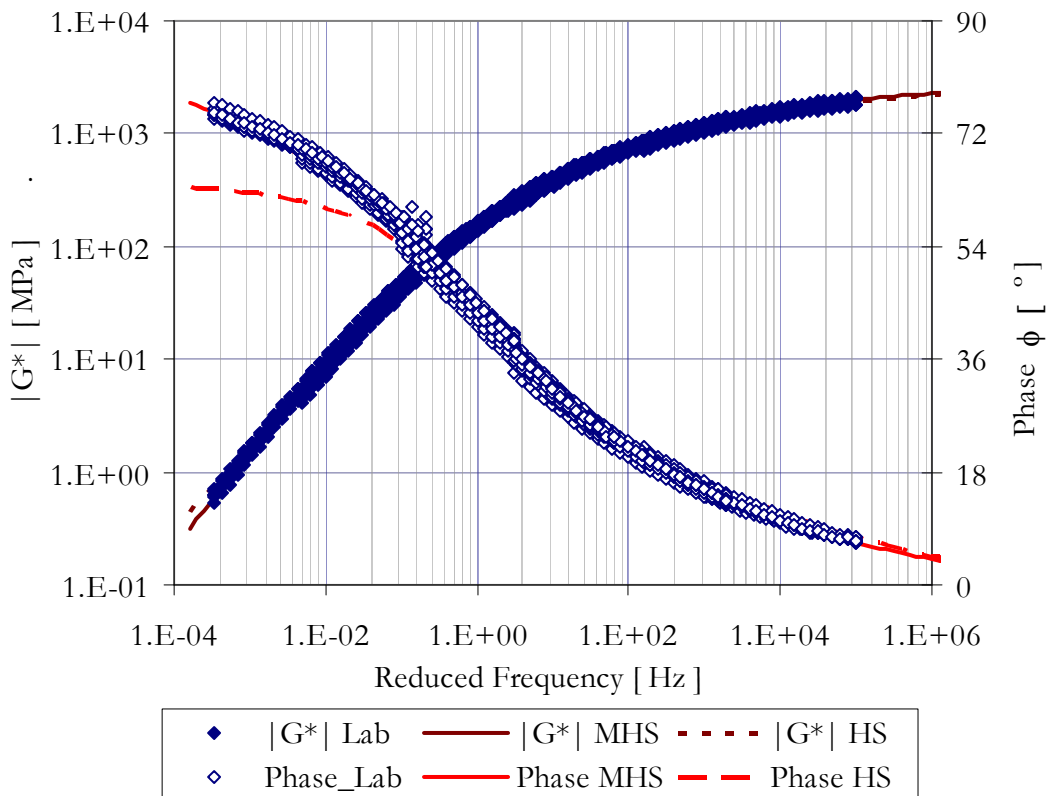


Figure 5-5 MHS and HS model fit to a mortar master curve ($T_{ref}= 10^{\circ}\text{C}$)

The improvement in the phase angle fit of the MHS model at low frequencies is attributed to the linear dashpot element. It should be noted that for Figure 5-4 and Figure 5-5, changing the parabolic dashpot parameters can provide better fits for the MH model. However, in such approach the viscous deformations at low frequencies would not be captured as true viscous deformations, rather it would be captured as pseudo deformations. Hence, upon the removal of applied loads all deformations are fully recoverable. The MHS model parameters for the various binders are given in Table 5-1. It can be seen that the G_0 value for the binders is nearly zero. For these binders it implies that the parallel spring in the MHS model can be eliminated. In such case, the resulting model is the same as the peculiar case of the 2S2P1D model [1, 13].

Similar model fits were also made on the asphalt mixtures. For the asphalt mixtures, the shift factors used to construct the master curve were obtained using the Arrhenius equation given in Equation 5-7. The MHS model fits to the asphalt mixture response data are presented in Figure 5-6 and Figure 5-7.

$$a_T = \exp\left(\frac{\Delta H}{R}\left(\frac{1}{T} - \frac{1}{T_{\text{ref}}}\right)\right) \quad 5-7$$

$$f_r = a_T \cdot f$$

where:

a_T = the shift factor

$R, \Delta H$ = model parameters

T = the temperature in Kelvin

T_{ref} = the reference temperature in Kelvin

f = the frequency

f_r = the reduced frequency

From Table 5-1, it can be seen that the model parameter corresponding to the series dashpot element, η_3 , is relatively very high for the RAP mixture. Nevertheless, the contribution to the phase angle fit is reflected in Figure 5-6. For the STAB mixture, due to the dense asphalt like behaviour of the mixture, the linear dashpot contribution is more significant. It can also be seen that for the STAB mixture the E_0 value is close to nil indicating the viscous nature of the mixture behaviour at higher temperatures (low frequencies).

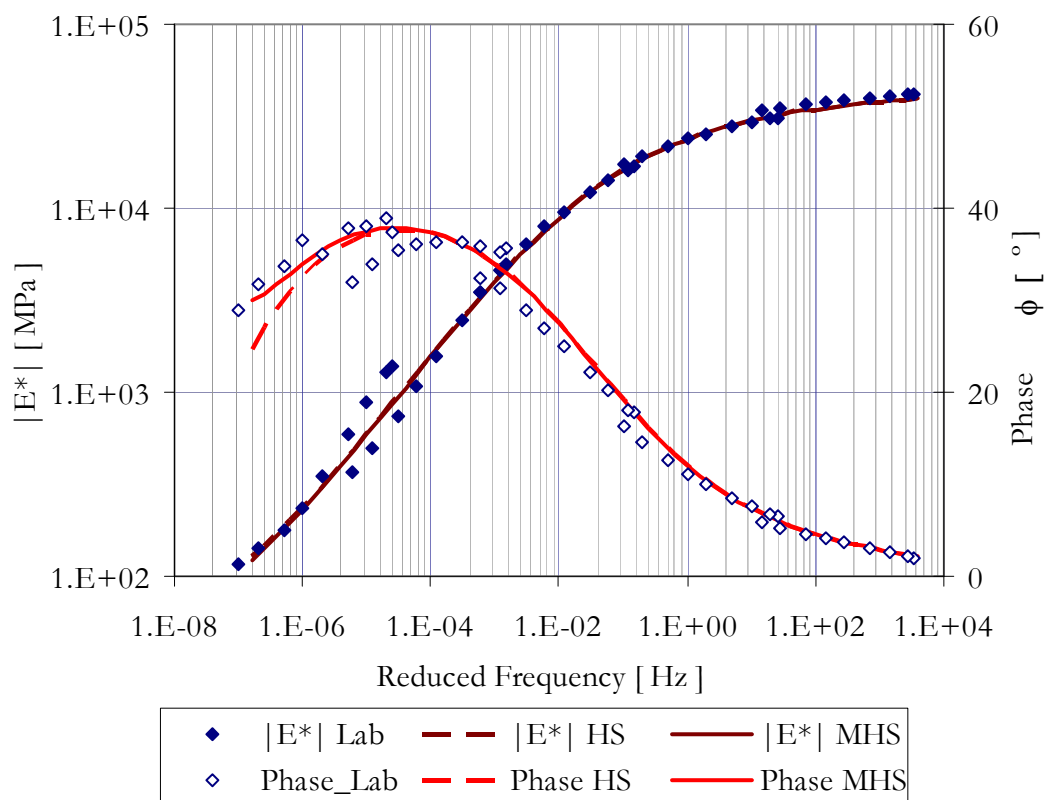
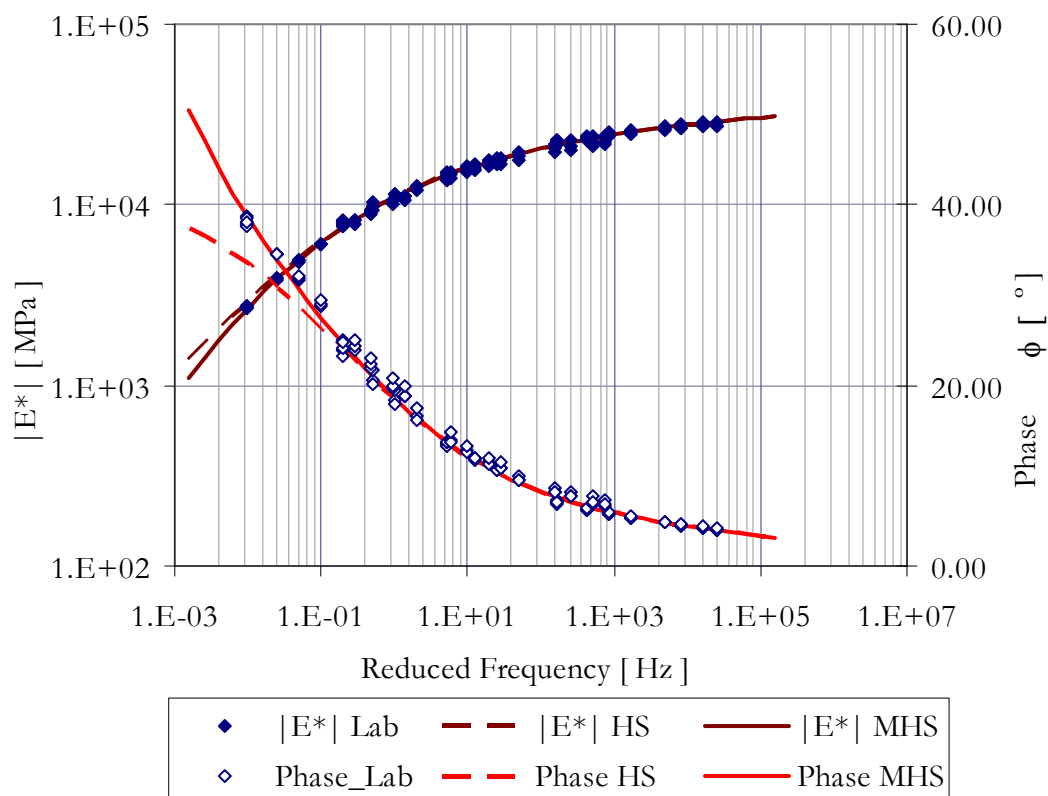

 Figure 5-6 MH and MHS model fit to RAP mixture response ($T_{ref} = 4.4^\circ\text{C}$)

 Figure 5-7 MH and MHS model fit to STAB mixture response ($T_{ref} = 10^\circ\text{C}$)

Table 5-1 MHS model parameters for various materials

Materials	MHS model parameters							
	T_{ref} [°C]	m_1 [-]	m_2 [-]	δ_1 [-]	τ [s]	E_∞ [MPa]	E_0 [MPa]	η_3 [MPa.s]
RAP	4.4	0.47	0.17	0.996	1.71	45137	57.93	121.0E7
STAB	10	0.14	0.477	1.646	1.21E-1	40480.5	1E-9	392.0E3

	T_{ref} [°C]	m_1 [-]	m_2 [-]	δ_1 [-]	τ [s]	G_∞ [MPa]	G_0 [MPa]	η_3 [MPa.s]
	B 70-100	20	0.57	0.182	0.25	2.03E-6	622.25	0
Mastic	20	0.699	0.259	0.046	1.36E-5	1052	1E-9	25.1
Virgin mortar	10	0.711	0.272	2.87E-2	5.41E-5	2699	1E-9	585.44
Aged mortar	10	0.460	0.189	8.9E-2	2.14E-5	3414.68	3E-9	9778.0

Table 5-2 Quality of fit to experimental data (R^2 values)

	B 70-100	Mastic	Virgin mortar	Aged mortar	STAB Mix	RAP Mix
G^*, E^*	0.989	0.998	0.994	0.989	0.991	0.996
ϕ	0.997	0.992	0.997	0.961	0.995	0.984

The shift factor parameters for the binders and mixture data, as described by the Arrhenius and WLF equations, are given in Table 5-3.

Table 5-3 Parameters for Arrhenius and WLF equations

Materials	C_1	C_2	T_{ref}	Materials	ΔH	R	T_{ref}
	[-]	[-]	[°C]		[-]	[-]	[°C]
B 70-100	16.91	144.45	20	RAP	216.18	8.62	4.4
Mastic	20.69	164.8	20	STAB	192.00	7.64	10
V. mortar	21.88	160.9	10				
A. mortar	42.67	281.98	10				

As shown in

Table 5-2, for all binders and asphalt mixtures high R^2 values have been obtained. This shows the good agreement between the MHS model prediction and the measured data. For the RAP mixture, the reduction in phase angle observed at high temperatures is also well described by the model. In asphalt mixtures, this phenomenon is observed at higher temperatures, and it is

attributed to the viscous nature of the binder which results in a change of the load transfer mechanism (aggregate interlock) within the asphalt mixture.

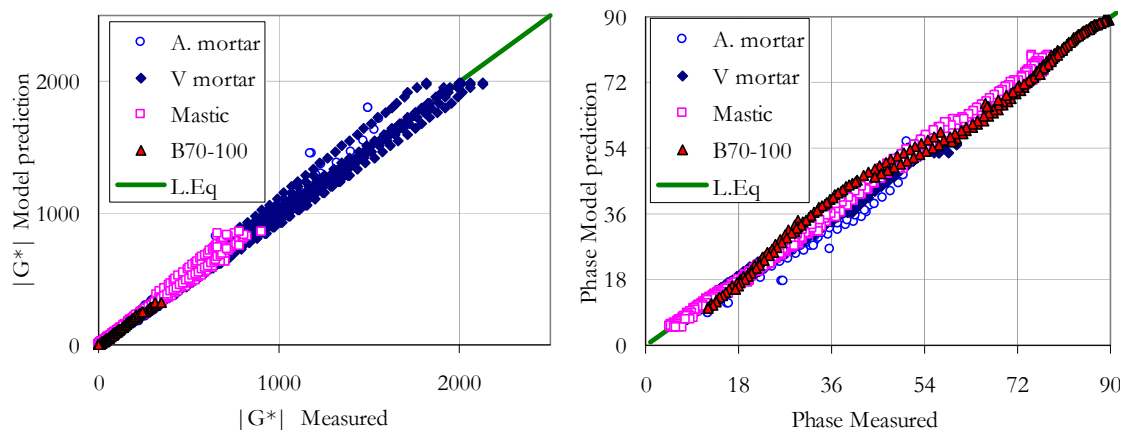


Figure 5-8 Comparison of predicted and measured response for binders

For the entire set of available binder data, i.e. 4 different master curves, Figure 5-8 presents the experimentally obtained values of the shear and phase angle data plotted against the model prediction values as predicted by the MHS model. In Figure 5-8 the solid line represents the line of equality (L.Eq).

Similarly for the STAB and RAP mixtures, excellent fits have been obtained. Figure 5-9 summarizes the results obtained for the asphalt mixtures.

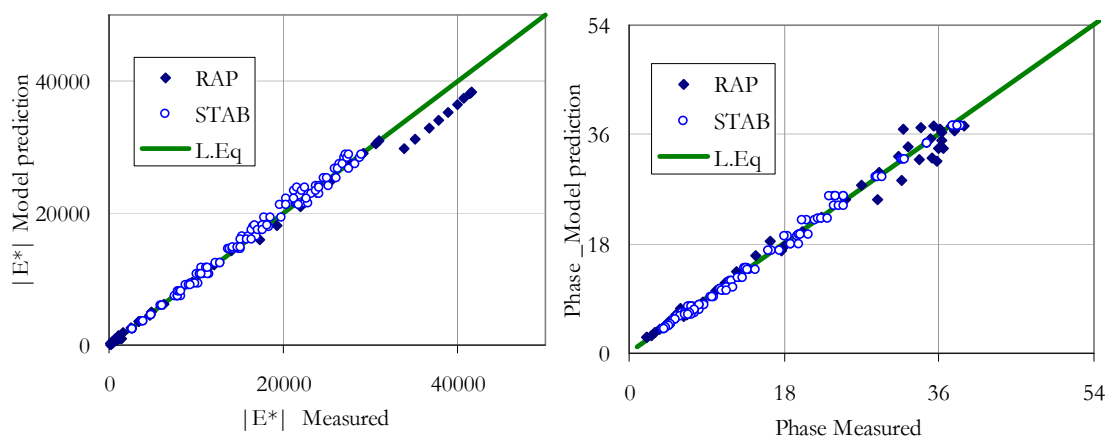


Figure 5-9 Comparison of predicted and measured response for mixtures

Based on the above results, the following remarks can be made about the MHS model in frequency domain.

- The good quality of fit, reflected in high R^2 values obtained for both the complex modulus and phase angle data, suggests the model's excellent ability in describing bituminous materials response for wide range of frequencies and temperatures.

- For all cases of the binders, the parameter corresponding to the parallel spring, G_0 , is close to nil. This suggests that the parallel spring in the modified HS model can be eliminated in modelling the response of binders. The resulting simplified model for the binders will therefore be the Huet model with a linear dashpot in series, which is also a particular case of the 2S2P1D model.

5.3.2 The Model in Time Domain

It has been shown in previous section that the analytical expression for the dynamic creep compliance, hence the dynamic modulus, of the MHS model can be obtained. This expression has been used for model parameter determination in the frequency domain. For time domain use, analytical material function for the Huet model exists, i.e. power functions. However, to the best of the author's knowledge, the analytical form of the time domain material functions for the original HS, the 2S2P1D and the MHS models are complex to obtain. In multilayer programs, such as VEROAD and ViscoRoute, application of such models in time domain is based on the possibility of Fourier decomposition for a moving constant load with constant speed [2, 7].

Application of the MHS model in time domain therefore requires a numerical approach. In this work a different numerical approach is proposed. In the following section, the time domain treatment of the MHS model is presented.

5.3.2.1 Numerical Approach

To allow implementation of the MHS model in numerical environments, the differential form of the linear viscoelastic theory can be used. In order to do so first the numerical approach for treating the parabolic dashpot element needs to be obtained. For this reason the numerical formulation of the parabolic dashpot element is first discussed. The section that follows generalizes the numerical formulation of the MHS model.

A) The Parabolic Dashpot

It has been discussed in the literature review that the parabolic dashpot can have a response in between the linear dashpot ($m=1$ and $\phi = \pi/2$) and the linear spring ($m = 0$ and $\phi = 0$). Instead of the common differentiation of integer order a kind of differentiation of a non-integer order appears in the constitutive relation for this response element [8, 16, 17]. The constitutive relation for the parabolic dashpot element is given as:

$$\sigma(t) = \eta \tau^{m-1} \Omega^m \{ \varepsilon(t) \} \quad 5-8$$

where:

$$\Omega^m = \partial^m / \partial t^m \text{ is a special differential operator}$$

m = parabolic dashpot coefficients

η = parabolic dashpot parameter

From Equation 5-8 it can be seen that when m equals 1 the special differential operator reduces to the first order differential operator d/dt for the linear dashpot element. Furthermore for m equals 0 Equation 5-8 reduces to the relationship between the stress and strain for the linear elastic spring with a constant $E = \eta/\tau$. For intermediate cases ($0 < m < 1$) the operator reduces to a derivative of non integer order, called fractional derivative. Analytically, the time domain treatment of this response element for arbitrarily applied strain signals is extensively covered by Pronk [16]. The approach utilizes Fourier transforms of load signals to obtain the time domain response.

In this research, a different approach for solving the fractional derivative is utilized. For this purpose the Grünwald-Letnikov definition of fractional derivatives is used [15]. At time step $t+1$, the m order fractional derivative of the strain function (Equation 5-8) can be given as:

$$\Omega^m(\varepsilon_{t+1}) = \lim_{\Delta t \rightarrow 0} \frac{1}{\Delta t^m} \sum_{j=0}^N b_j(m) \cdot \varepsilon(t_{t+1-j}) \quad 5-9$$

Here $b_j(m)$ denotes the Grünwald coefficients (multiplying factors for the strain history), j is the time history index, N is the time history length. The formulation requires that equal time steps are taken. The time step and time history index notations are further illustrated in Figure 5-10. The Grünwald coefficients are given as:

$$b_j(m) = (-1)^j \binom{m}{j} = \binom{j-m-1}{j} = \frac{\Gamma(j-m)}{\Gamma(-m)\Gamma(j+1)} \quad 5-10$$

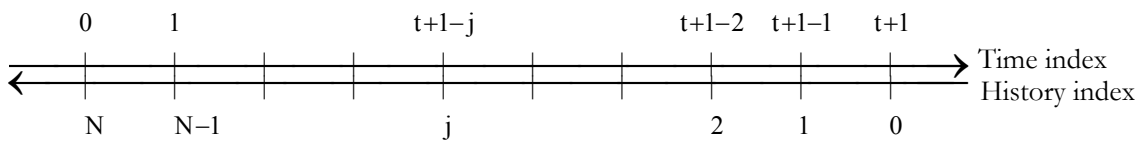


Figure 5-10 Notations used to refer the time step and the time history

Due to the nature of the gamma function, numerical problems can arise when calculating the Grünwald coefficients if m is close to an integer or if large values of j occur. This problem can be avoided if the coefficients are obtained in a recursive manner. Defining $b_0(m)$ as 1, the equivalent form for obtaining the Grünwald coefficients recursively is given as:

$$b_j(m) = \frac{\Gamma(j-m)}{\Gamma(-m)\Gamma(j+1)} = \left[1 - \frac{1+m}{j}\right] b_{j-1}(m) \quad 5-11$$

Using a short hand notation b_j for $b_j(m)$ the Grünwald coefficients can be obtained as:

$$b_0 = 1; b_1 = -m.b_0; b_2 = \frac{(1-m)}{2} b_1 \dots\dots b_n = \frac{(n-1-m)}{n} b_{n-1} \quad 5-12$$

Consequently, the fractional derivative of the strain function given in Equation 5-9 can be rewritten in the following form:

$$\Omega^m(\varepsilon_{t+1}) = \frac{\varepsilon_{t+1} + \sum_{j=1}^N b_j(m)\varepsilon_{t+1-j}}{\Delta t^m} \quad 5-13$$

Equation 5-8 and 5-13 can now be combined to obtain a numerical form for obtaining the stress and the strain for the parabolic dashpot as:

$$\sigma_{t+1} = \eta \tau^{m-1} \frac{\varepsilon_{t+1} + \sum_{j=1}^N b_j(m)\varepsilon_{t+1-j}}{\Delta t^m} \quad 5-14$$

$$\varepsilon_{t+1} = \frac{\Delta t^m}{\eta \tau^{m-1}} \sigma_{t+1} - \sum_{j=1}^N b_j(m)\varepsilon_{t+1-j} \quad 5-15$$

The numerical formulations given in Equation 5-14 and Equation 5-15 require the entire past history of the parabolic dashpot to be stored. This is depicted in the equation by the summation form for the strains. The Grünwald coefficients multiplying the strain histories of the parabolic dashpot can be obtained using the recursive relationship given in Equation 5-12.

The Grünwald coefficients follow a decreasing trend for an increasing time history index, j . This implies that the strain histories which are far from the current time step have less effect on the computed stress for the current time step than those strain histories in the near past. This is in conformity with the fading memory hypotheses for viscoelastic materials, which states that real materials have a fading memory with time [4]. For the parabolic dashpot, the rate at which the memory fades with time is a function of the dashpot coefficient, m . When the value of the parabolic dashpot coefficient, m , is close to 1, the Grünwald coefficients for distant past histories are much smaller than the corresponding values obtained for smaller parabolic dashpot coefficients. This implies that small parabolic dashpot coefficients mean longer memory effects.

Figure 5-11 shows the trend of the Grünwald coefficients as a function of time history index j , where $j = 0$ denotes current time step, $j=1$ previous step etc.

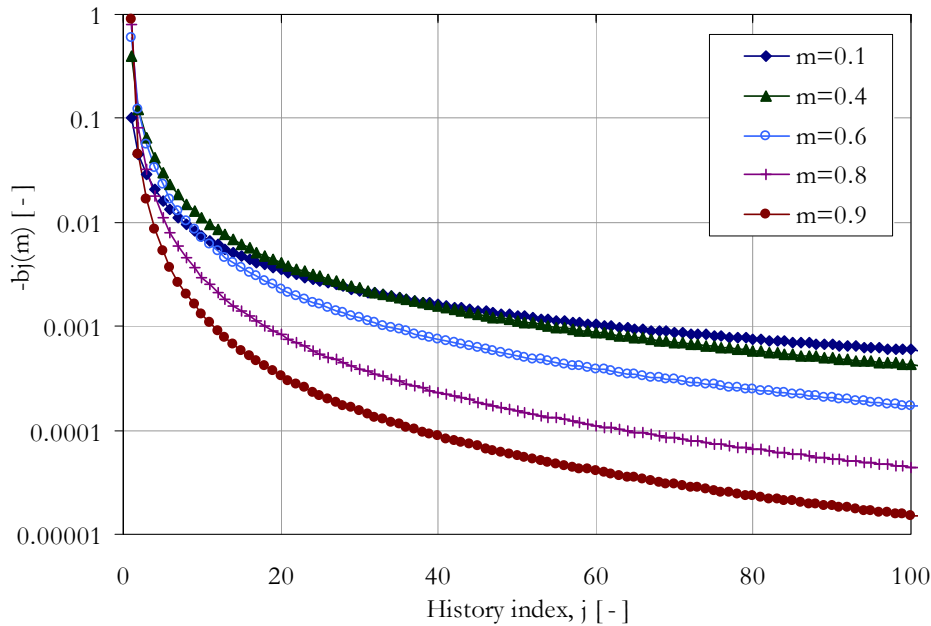


Figure 5-11 Grünwald coefficients for various parabolic dashpot coefficients

Numerical Example

Here an illustration for the time domain response of a parabolic dashpot is given. To compare numerical results with analytic solutions, data from literature have been used. Analytical formulation of the response of a single parabolic dashpot for a block pulse load in time domain has been given elsewhere [14]. For a single parabolic dashpot with model parameters m , η and τ the analytical time domain response for a block pulse stress σ_0 applied in a time window between t_0 and t_1 is given by:

$$\varepsilon = \frac{\sigma_0 \tau^{1-m}}{\eta \Gamma(1+m)} \left\{ (t-t_0)^m - (t-t_1)^m \right\} \quad 5-16$$

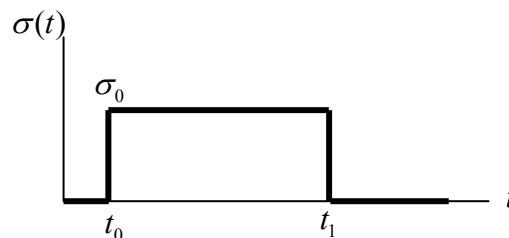


Figure 5-12 Block pulse stress

For dashpot parameters η and τ of 1 MPa.s and 1 second respectively, and an applied block pulse stress $\sigma_0 = 1$ MPa (Figure 5-12), the resulting strain in the parabolic dashpot is computed numerically. The numerical result is then

compared with the analytic solution that is obtained using Equation 5-16. Comparisons of the analytic and numerical results for various dashpot coefficients (m) are presented in Figure 5-13.

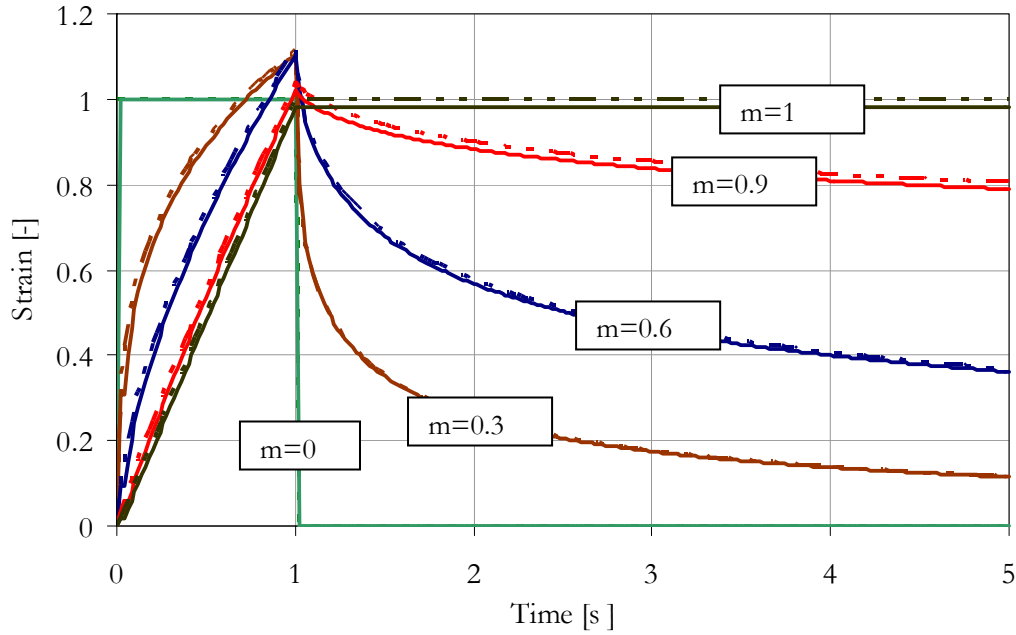


Figure 5-13 Parabolic dashpot response (solid lines; analytical [16], dashed lines; numerical)

Figure 5-13 shows that the numerical and analytical results are in good agreement. From the plot it can also be seen that the parabolic dashpot simulates a linear spring and a linear dashpot when the dashpot coefficients assume extreme values of 0 and 1 respectively. In between these two values, a delayed elastic response is observed.

B) The MHS Model

Since the numerical formulation for obtaining the stress and strain in the parabolic dashpot is known, similar procedures can be followed to derive expressions for the stress and strain in the MHS model. In reference to Figure 5-3, the strain in the original HS element ($\varepsilon_{t+1}^{\text{HS}}$) can be obtained by summing up the individual strain contributions from the linear spring (ε_{t+1}^0) and the two parabolic dashpots (ε_{t+1}^1 and ε_{t+1}^2). Denoting the stress in these elements as σ_{t+1}^I , the strain in the original HS element can be formulated as:

$$\varepsilon_{t+1}^{\text{HS}} = \frac{1}{G_{\infty} - G_0} \sigma_{t+1}^I + \frac{\Delta t^{m_1}}{\eta_1 \tau_1^{m_1-1}} \sigma_{t+1}^I + \frac{\Delta t^{m_2}}{\eta_2 \tau_2^{m_2-1}} \sigma_{t+1}^I - \sum_{j=1}^N b_j(m_1) \varepsilon_{t+1-j}^1 - \sum_{j=1}^N b_j(m_2) \varepsilon_{t+1-j}^2 \quad 5-17$$

Referring to Figure 5-3, the total stress in the original HS model is obtained as:

$$\sigma_{t+1}^{\text{HS}} = \sigma_{t+1}^{\text{I}} + G_0 \varepsilon_{t+1}^{\text{HS}} \quad 5-18$$

Substitution and rearranging yields:

$$\varepsilon_{t+1}^{\text{HS}} = \frac{\chi}{1 + \chi \cdot G_0} \sigma_{t+1}^{\text{HS}} - \frac{1}{1 + \chi \cdot G_0} \left(\sum_{j=1}^N b_j(m_1) \varepsilon_{t+1-j}^{\text{I}} - \sum_{j=1}^N b_j(m_2) \varepsilon_{t+1-j}^2 \right) \quad 5-19$$

The parameter χ is given by:

$$\chi = \frac{1}{G_\infty - G_0} + \frac{\Delta t^{m_1}}{\eta_1 \tau_1^{m_1-1}} + \frac{\Delta t^{m_2}}{\eta_2 \tau_2^{m_2-1}}$$

The numerical constitutive form given in Equation 5-19 can be used for obtaining the strain in the original HS response element. To obtain the total strain for the MHS model, the strain contribution from the linear dashpot ($\varepsilon_{t+1}^{\text{LD}}$) needs to be taken into account. The numerical formulation for the stress and the strain in the linear dashpot is given as:

$$\sigma_{t+1}^{\text{HS}} = \left[\frac{\eta_3}{\Delta t} \right] \cdot \left[\varepsilon_{t+1}^{\text{LD}} - \varepsilon_t^{\text{LD}} \right] \quad ; \quad \varepsilon_{t+1}^{\text{LD}} = \left[\frac{\Delta t}{\eta_3} \right] \sigma_{t+1}^{\text{HS}} + \varepsilon_t^{\text{LD}} \quad 5-20$$

It is important to note that the linear dashpot can be considered as the parabolic dashpot with the dashpot coefficient of one, $m = 1$, which leads to a Grünwald coefficients, $b_1 = -1$ and $b_j = 0$ for $j \geq 2$. This implies that all the multiplying coefficients for the strain histories are zero except b_1 . This in turn implies that only the strain history at the previous time step is sufficient for numerical computations, which is consistent with the numerical form obtained in Equation 5-20.

The final formulation for the strain in the MHS model ($\varepsilon_{t+1}^{\text{MHS}}$) can now be obtained by adding the strain in the linear dashpot and the strain in the original HS model as:

$$\varepsilon_{t+1}^{\text{MHS}} = \sigma_{t+1}^{\text{HS}} \left[\frac{\chi}{1 + G_0 \cdot \chi} + \frac{\Delta t}{\eta_3} \right] + \left[\varepsilon_t^{\text{LD}} - \frac{1}{1 + G_0 \cdot \chi} \left[\sum_{j=1}^N b_j(m_1) \varepsilon_{t+1-j}^{\text{I}} + \sum_{j=1}^N b_j(m_2) \varepsilon_{t+1-j}^2 \right] \right] \quad 5-21$$

The numerical form given in Equation 5-21 can be used to compute the strain in the MHS model for stress controlled situation. For strain controlled conditions the relation needs to be rewritten to obtain a suitable expression for obtaining the stress as:

$$\sigma_{t+1}^{HS} = \left[\frac{\chi}{1+G_0\chi} + \frac{\Delta t}{\eta_3} \right]^{-1} \left[\varepsilon_{t+1}^{MHS} - \varepsilon_t^{LD} + \frac{1}{1+G_0\chi} \left(\sum_{j=1}^N b_j(m_1)\varepsilon_{t+1-j}^1 + \sum_{j=1}^N b_j(m_2)\varepsilon_{t+1-j}^2 \right) \right] \quad 5-22$$

The above formulations require that for each incremental time step a strain update need to be made for the linear dashpot element (ε_{t+1}^{LD}). This can be performed using Equation 5-20. In addition, the strain values for the two parabolic dashpots ($\varepsilon_{t+1}^i, i=1,2$) need to be computed and stored. Since the stress (σ_{t+1}^{HS}) and the strain (ε_{t+1}^{MHS}) are known, the following relations can be used to compute the strains for storage:

$$\sigma_{t+1}^I = \sigma_{t+1}^{HS} - G_0\varepsilon_{t+1}^I \quad ; \quad \varepsilon_{t+1}^I = \varepsilon_{t+1}^{MHS} - \varepsilon_{t+1}^{LD} \quad 5-23$$

$$\varepsilon_{t+1}^1 = \frac{\Delta t^m}{\eta_1\tau_1^{m-1}}\sigma_{t+1}^I - \sum_{j=1}^N b_j(m_1)\varepsilon_{t+1-j}^1 \quad 5-24$$

$$\varepsilon_{t+1}^2 = \frac{\Delta t^n}{\eta_2\tau_2^{n-1}}\sigma_{t+1}^I - \sum_{j=1}^N b_j(n_1)\varepsilon_{t+1-j}^2 \quad 5-25$$

5.3.2.2 Notes on Practical Implications

The time domain formulation of the MHS model involves memory effects. This has a practical limitation when very large numbers of time step are involved in the numerical computations. Depending on the available computational memory, when such situations are encountered, the history length needs to be truncated for practical purposes. Effects of truncation in the computed results may vary depending on the material properties. It can generally be deduced from Figure 5-11 that history truncation for a parabolic dashpot with dashpot coefficient close to nil would have a bigger influence on the computed results than those with a higher dashpot coefficient. For solving numerical problems involving fractional derivatives, literature suggests various correction methods to minimize the truncated history effect on the computed results [18]. However, these correction methods which are developed for elastomeric materials are not universal. Relevant correction methods need to be obtained for other material types.

Investigation for obtaining relevant correction methods for the materials in this research has not been made. Hence the MHS model is used in this research without any history truncation. After the model is implemented into ABAQUS (Chapter 6), limitations specific to meso mechanics applications will be assessed. Depending on the required computational memory and the computational time, the need for history truncation will be assessed.

5.3.3 Frequency vs. Time Domain Response

5.3.3.1 General

Frequency domain experiments are conducted to obtain material response information corresponding to short loading times. As discussed in the literature review section, various inter conversion methods are then used to obtain the time domain material functions. It is therefore expected that the material response information obtained from the frequency domain test would be sufficient to simulate the time domain response of the material for short loading times.

In this research a limited number of time domain tests were carried out to obtain the creep-recovery and relaxation behaviour of the binders. Using the MHS model parameters that were obtained from the response data in frequency domain, relaxation and creep-recovery tests were simulated. The simulation results have been compared with the experimental data. To allow a reasonable comparison, the following two points are deemed important.

- Ensure uniform test sampling and test setup procedures for both frequency domain and time domain tests.
- Ensure stress/strain levels are low to guarantee measurements are conducted in the linear viscoelastic range

Stress and strain levels within the linear viscoelastic range can be determined based on the stress and strain sweep test results. To ensure uniform sampling and setup procedures for both frequency and time domain tests, it has been decided to carry out both tests on the same test specimen. Hence from one test specimen, both the frequency and time domain responses of the material are obtained. The details of the test procedures and simulation results are presented below.

5.3.3.2 Relaxation Tests on Mortar

Displacement controlled time domain tests were carried out on five different mortar specimens. A linearly increasing angular displacement (strain) was applied on the mortar for time step, T_1 , of 1 second, 2.5 seconds, 5 seconds and 10 seconds (Figure 5-14). The angular displacement obtained at the end of each time step is kept constant for 60 seconds. During the entire period the torque (stress) response of the material is measured. Table 5-4 summarizes the conditions for the relaxation tests performed on the mortar.

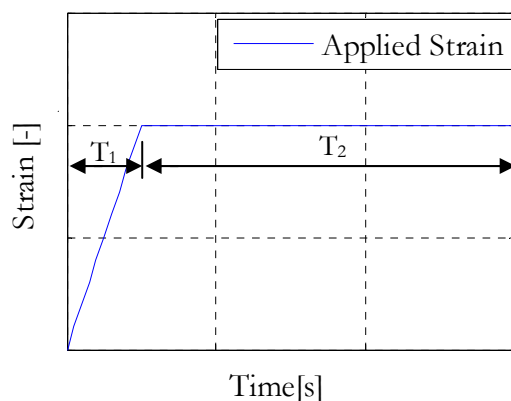


Figure 5-14 Shape of the strain signal used for relaxation tests

Table 5-4 Relaxation tests conducted on the mortar

Temperature [°C]	Max strain [-]	Time step T_1 [s]	Relaxation period, T_2 [s]	Sample no
10	2.08E-3	1, 2.5, 5 and 10	60	1
20	2.08E-3	1, 2.5, 5 and 10	60	2
20	2.05E-4	1, 2.5, 5 and 10	60	3
20	6.12E-4	1, 2.5, 5 and 10	60	4
20	7.6E-4	1, 2.5, 5 and 10	60	5

In performing the relaxation tests, the following procedures were followed:

- A frequency sweep test on the mortar sample is first conducted. The same test specimen is then conditioned at the desired test temperature for half an hour before the relaxation tests are started.
- A linearly increasing angular displacement is applied for a time step of 1 second and the maximum displacement is kept constant for 60 seconds. The stress response of the material is measured for the entire time period. In the procedure a zero displacement is set at the end of the test to minimize viscous deformation effects on the next test.
- Allow 15 minute conditioning time for the residual stress to relax.
- Repeat the second and the third procedures with time steps of 2.5 seconds, 5 seconds and 10 seconds each with a relaxation period of 60 seconds.

In order to check whether or not the material response information that was obtained from the frequency domain test can simulate the time domain response, numerical simulations were performed. The comparison between the

numerically simulated and experimentally obtained data is presented in the next section.

5.3.3.3 Relaxation Simulations

In this section the results of the numerical simulations that were made for the relaxation tests at 10°C and 20°C are presented. The incremental formulation of the MHS model discussed in the previous sections has been used. The relevant MHS model parameters that were obtained from frequency domain measurements for the reference temperature of 10°C are given in Table 5-1. To obtain the MHS model parameters at 20°C, appropriate shift factors from Table 5-3 were used.

Before performing the simulations, the numerical formulation of the MHS model requires that the simulation period need to be divided in to N equal time intervals (Figure 5-10). Consequently, from the strain that was applied during the relaxation testing, N strain readings were made at equal time intervals. The N strain readings are then used as input in Matlab to simulate the stress response of the material. Figure 5-15 to Figure 5-20 present the simulated and measured relaxation curves for the mortar.

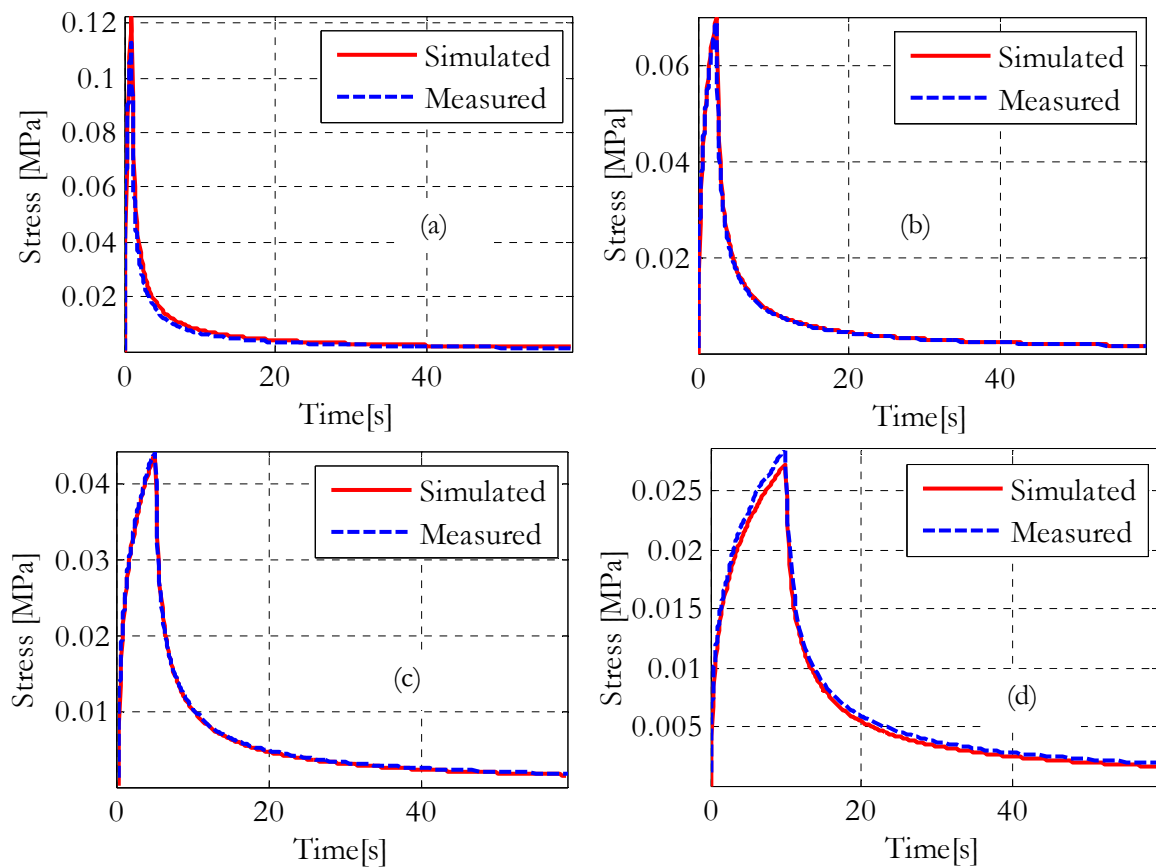


Figure 5-15 Measured and simulated relaxation curves for the mortar at 10°C , sample no 1. (Time step: 1 s (a), 2.5 s (b) , 5 s (c) and 10 s (d))

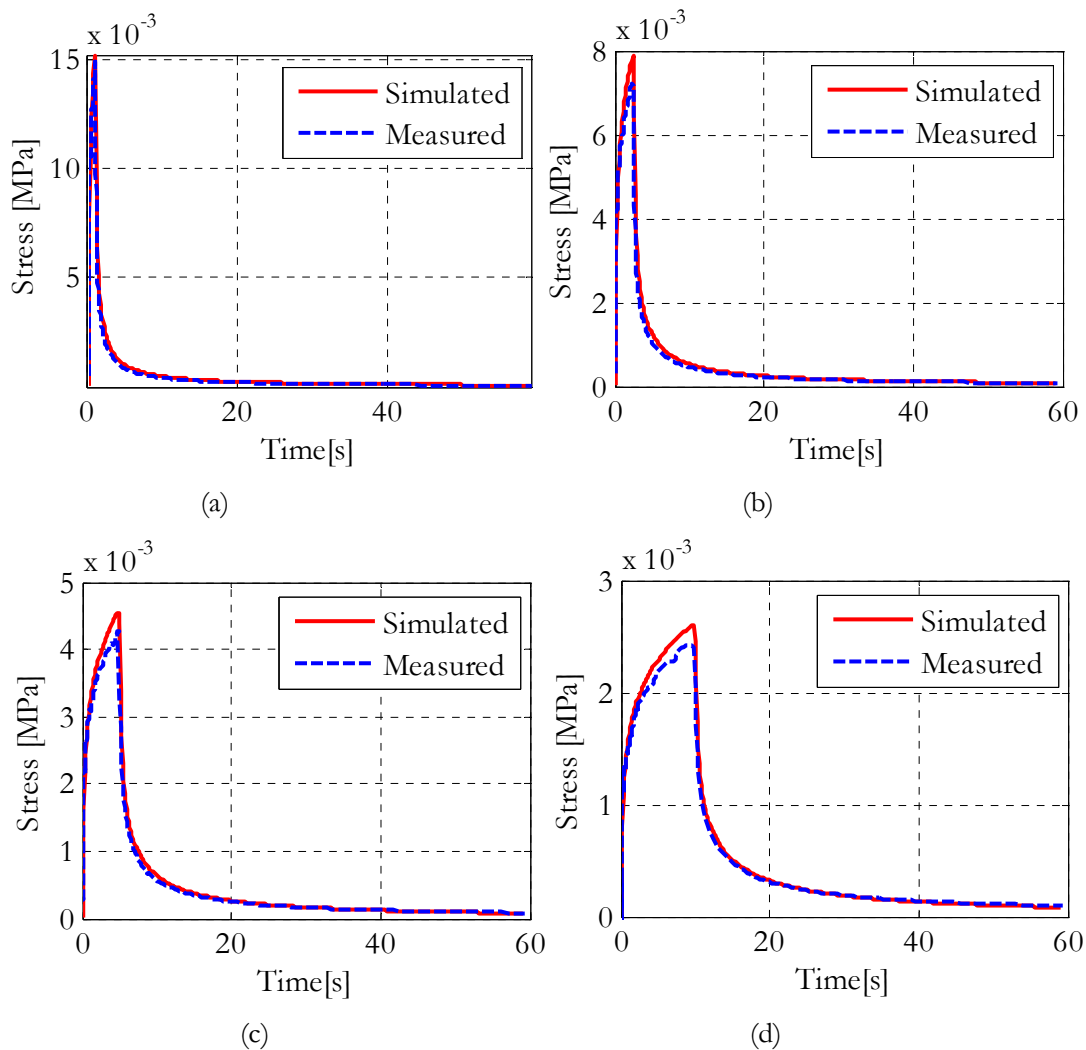


Figure 5-16 Measured and simulated relaxation curves for the mortar at 20°C, sample no 2. (Time step: 1 s (a), 2.5 s (b), 5s (c) and 10 s (d))

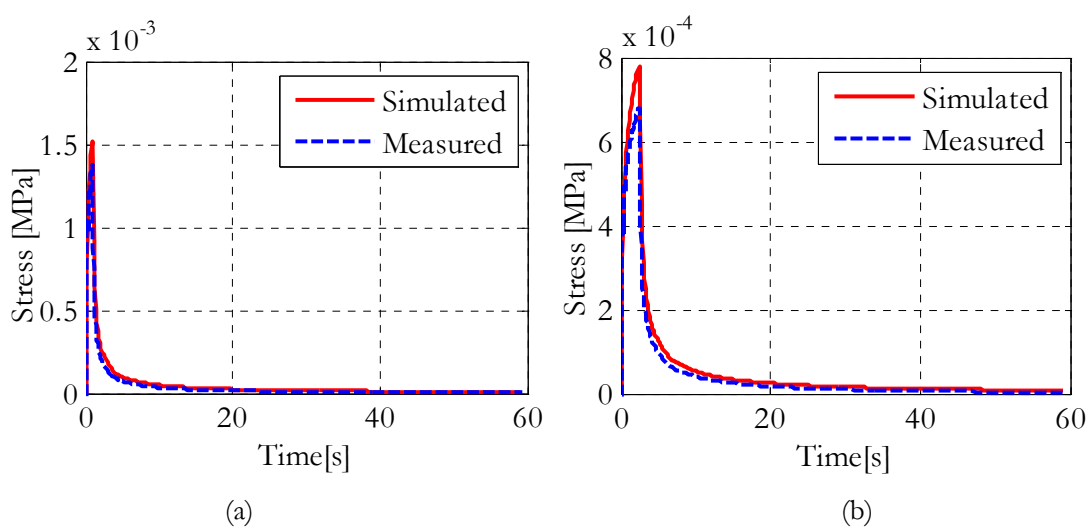


Figure 5-17 Measured and simulated relaxation curves for the mortar at 20°C, sample no 3. (Time step: 1 s (a), 2.5 s (b))

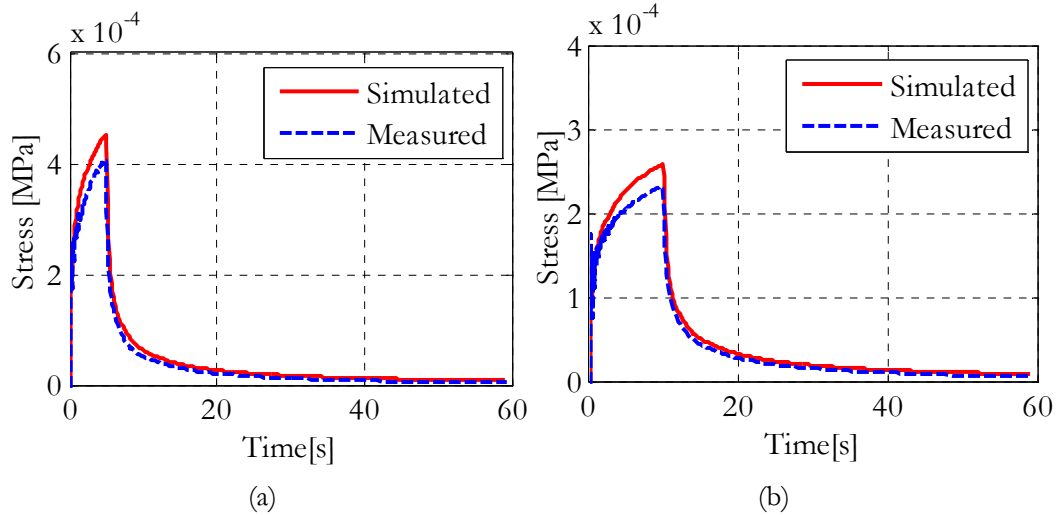


Figure 5-18 Measured and simulated relaxation curves for the mortar at 20°C, sample no 3. (Time step: 5 s (a) and 10 s (b))

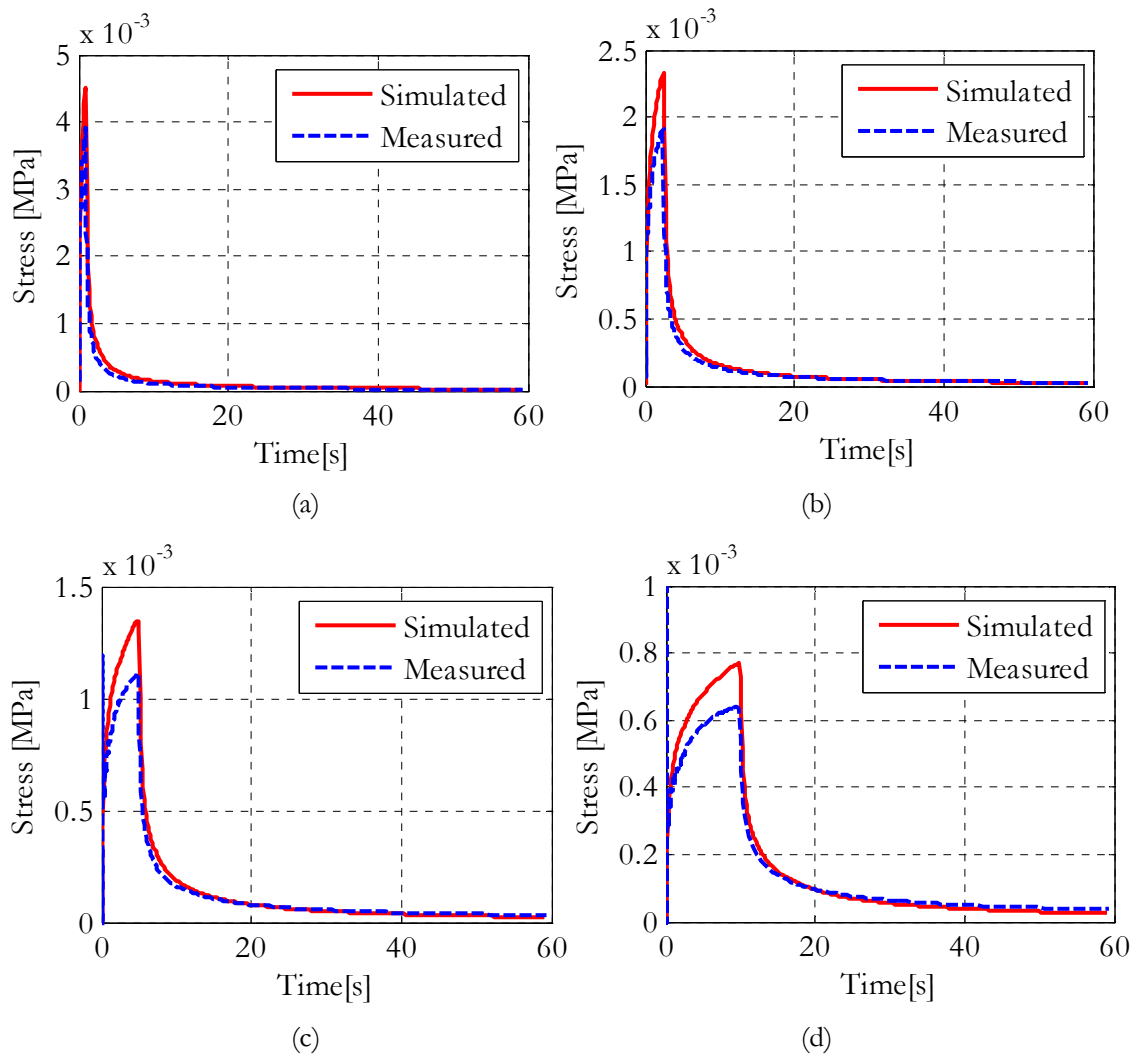


Figure 5-19 Measured and simulated relaxation curves for the mortar at 20°C, sample no 4. (Time step: 1 s (a), 2.5 s (b), 5 s (c) and 10 s (d))

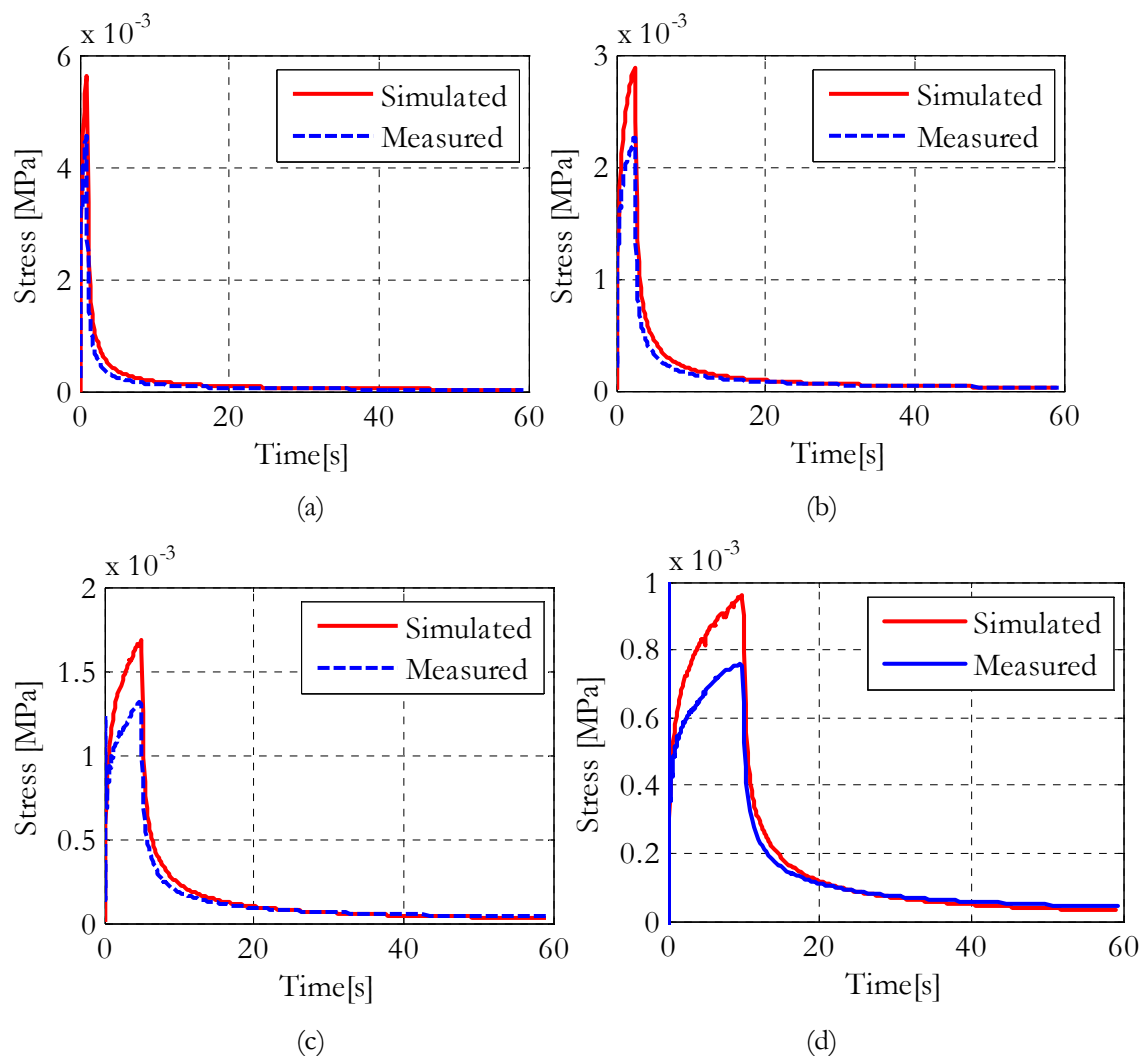


Figure 5-20 Measured and simulated relaxation curves for the mortar at 20°C, sample no 5. (Time step: 1 s (a), 2.5 s (b), 5 s (a) and 10 s (b))

5.3.3.4 Creep-Recovery Tests on Mortar

Creep-recovery tests at 10°C were conducted on mortar samples. A constant torque was applied for time steps varying from a minimum of 5 seconds to maximum duration of 15 seconds. Similar to the procedures that were followed for the relaxation tests, one test specimen has been used for both tests conducted in the frequency and time domain. For the same loading condition, the test has been conducted on two different mortar samples. The following procedures were followed in performing the creep-recovery tests at a chosen torque level:

- After the frequency sweep tests are performed in the linear viscoelastic range, the same test sample is conditioned at 10°C for half an hour before creep-recovery tests are started.

- A torque is applied for duration of 5 seconds and the creep-recovery behaviour of the material is measured. A recovery phase of 60 seconds is selected.
- A 15 minute conditioning phase is allowed for the residual stress to relax.
- Then the second creep-recovery test is performed with a time step of 10 seconds and a rest period of 60 seconds. This is also followed by a 15 minute conditioning phase for the next test.
- The third creep-recovery test is performed with a time step of 15 seconds and rest period of 60 seconds.
- Using the second torque level, the above procedures are repeated.

At the end of each creep-recovery tests, a zero displacement is set to minimize possible effects of viscous deformation on the test results. Figure 5-21 shows the shape of the measured response for an applied shear stress of 0.825 kPa and time step, T_1 , of 5 seconds.

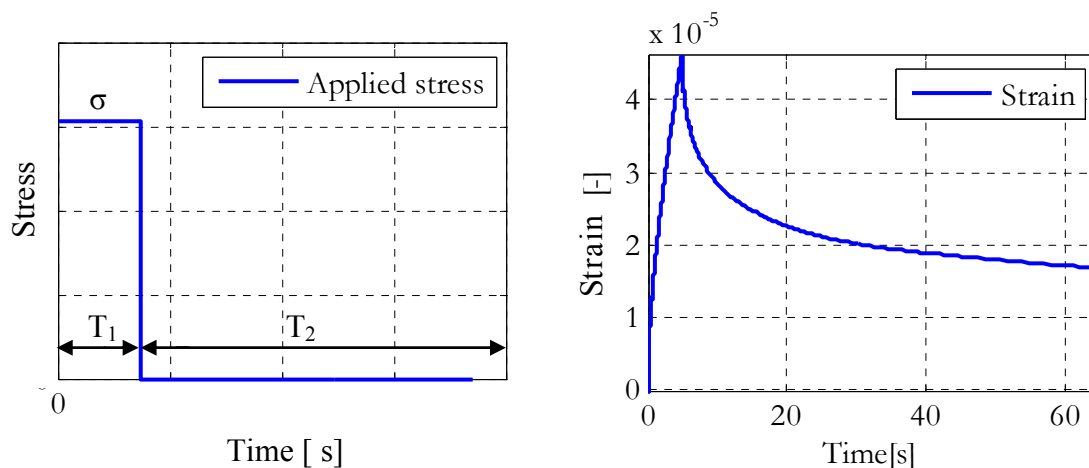


Figure 5-21 Loading for the creep-recovery test (left), typical creep-recovery result (b)

For combinations of three different time steps (5 seconds, 10 seconds and 15 seconds) and two torque levels (35 μNm and 65 μNm), a total of six creep-recovery test data were obtained from one test sample. For the second sample the same number of data was obtained. These test results were used for comparing numerically simulated creep-recovery tests.

5.3.3.5 Creep-Recovery Simulations

Using the MHS model parameters that were obtained from the frequency domain tests (Table 5-1), the creep-recovery response of the mortar were

numerically simulated using Matlab. The incremental formulation of the MHS model discussed in the previous sections has been used for this purpose.

Figure 5-22 present the comparison between the measured and simulated creep-recovery test for an applied shear stress of 0.825 kPa.

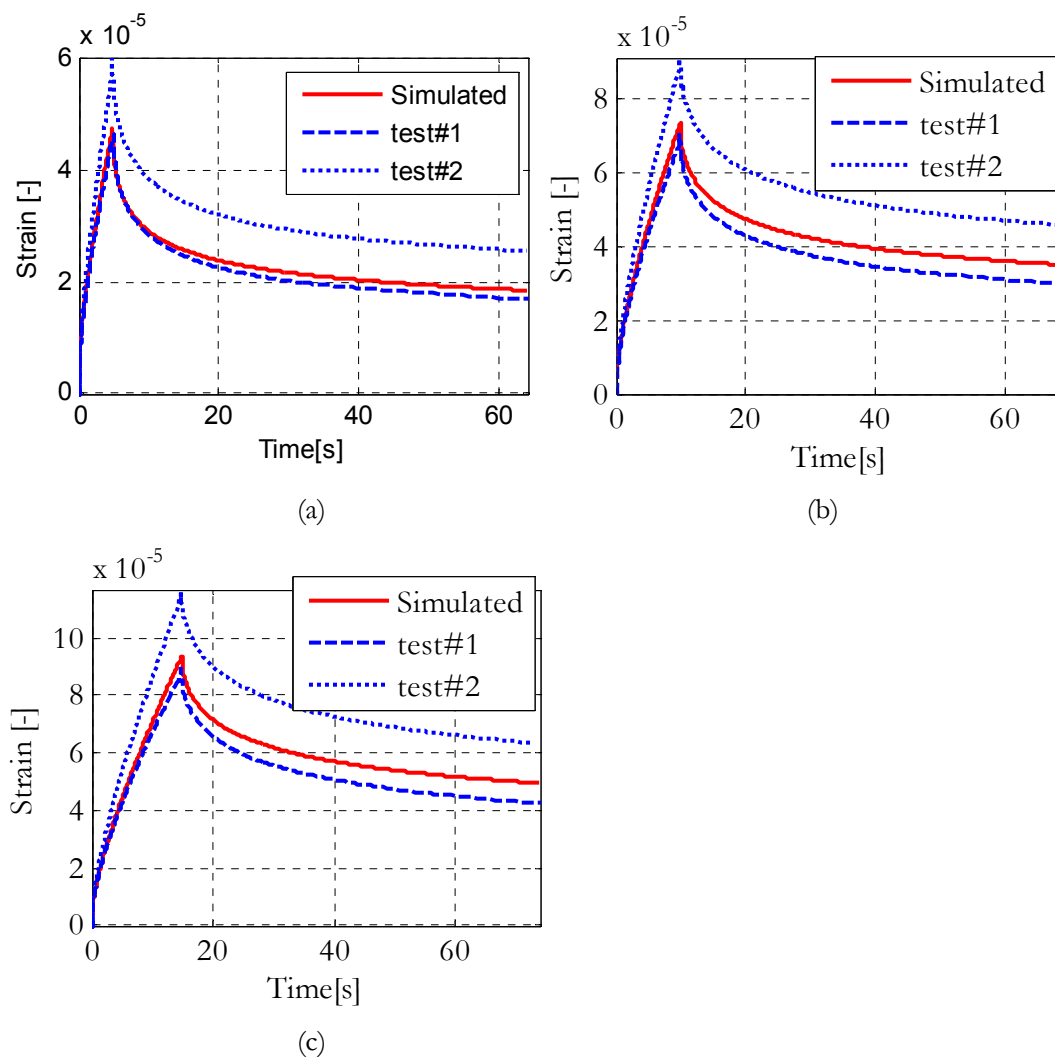


Figure 5-22 Measured and simulated creep-recovery data for an applied stress of 0.825 kPa (Time step: 5s (a), 10s (b) and 15s (c))

The first plot represents the results obtained for time step, T_1 , of 5 seconds. The second and third plots correspond to time steps of 10 seconds and 15 seconds respectively. Similar plots for a shear stress level of 1.53 kPa are presented in Figure 5-23. In each of the plots the two dashed lines (test#1 and test#2) represent the experimentally obtained creep-recovery data for the two mortar samples.

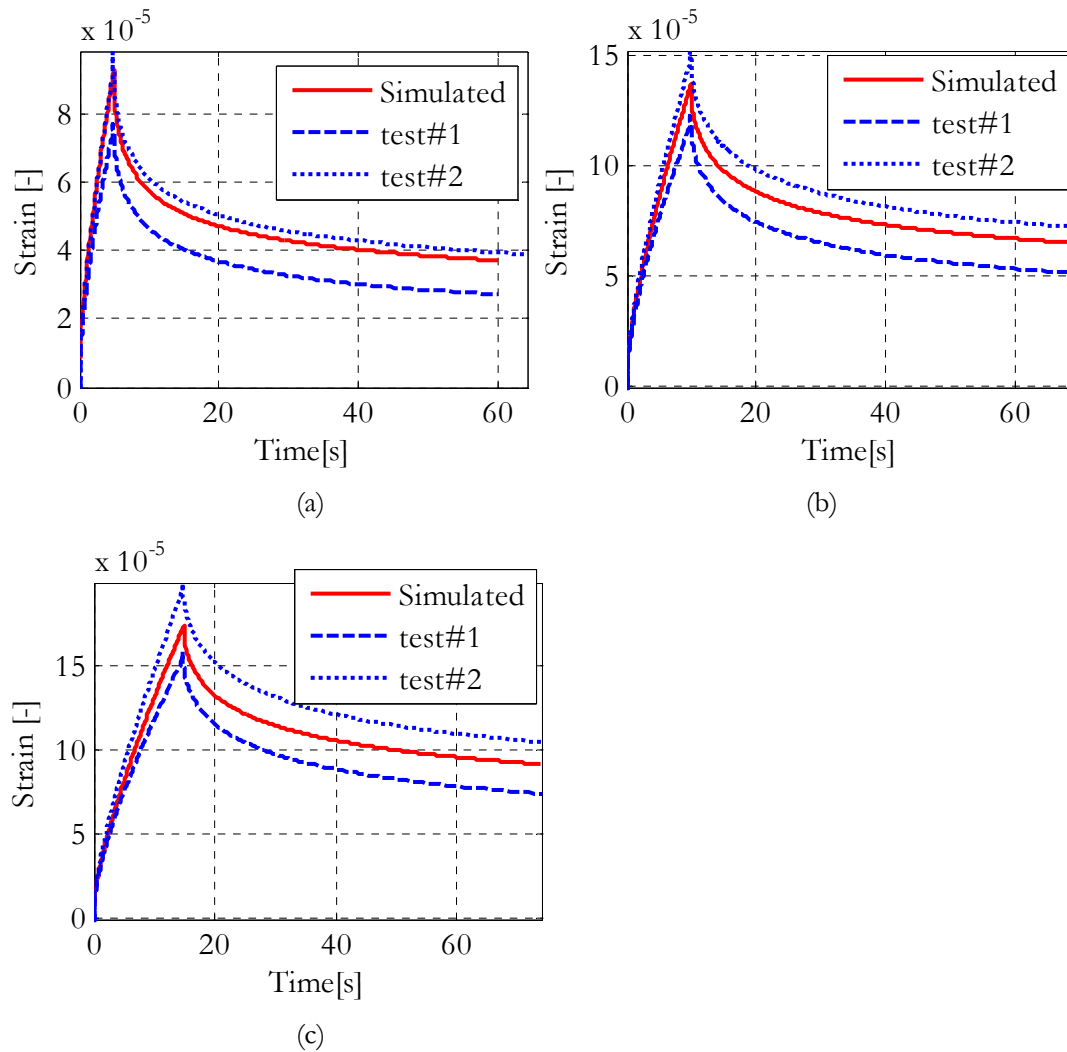


Figure 5-23 Measured and simulated creep-recovery data for an applied stress of 1.53 kPa (Time step: 5s (a), 10s (b) and 15s (c))

5.3.3.6 Discussions

As stated before, the frequency domain master curve data covering a wide range of frequencies were used to obtain the MHS model parameters. The model parameters were then used to simulate the time domain responses. The good agreement observed between the simulated and measured response data confirm that the frequency domain master curve data contained relevant material response information for short to long loading times. Which implies that one set of model parameters can be used to simulate both time and frequency domain responses. In relation to the response model, the results also show that the MHS model can be utilized for time domain simulations.

In terms of accuracy, the relaxation simulations appear relatively more accurate than the creep/recovery simulation results. The creep/recovery test results, test #1 and test #2, also did not show good repeatability. The main reason for this was not clear due to the testing phase. Possible reason could be in relation to the applied shear stress levels. In reference to the relaxation simulations at 10°C,

where very good agreement between the simulated and measured data is observed, maximum shear stress levels are in the range of 25 kPa to 120 kPa. For the relaxation tests conducted at 20°C, the maximum shear stresses vary from 0.8 kPa to 15 kPa; and relatively better agreement between simulated and measured data were observed for cases where the maximum shear stress is in the range of 4 kPa to 15 kPa. For very low shear stress levels (see Figure 5-19 (c, d) and Figure 5-20 (c, d)), the simulated results appear less accurate. Hence, the relatively less accurate simulation results obtained for the creep/recovery response could be a result of the low shear stress applied on the specimen. This may indicate that the machine requires relatively higher torque level for more accurate measurements.

With regard to practical use, the above simulation results are very reasonable. For fatigue based simulation in practice, the loading time for a wheel load on a pavement is in a fraction of seconds. In the simulations above, loading times of up to 15 seconds were considered with reasonably accurate simulated results. This also shows that very accurate material information is obtained from the frequency domain data. For creep performance criteria, supplementary time domain tests with long loading times are necessary.

5.4 The Burgers' model

The Burgers' model is widely used for modelling the response of bituminous materials [5, 12, 20]. The model is obtained by placing a single Maxwell element in series with a Kelvin-Voigt element (Figure 5-24). Its wide application for modelling bituminous materials comes from a number of reasons. One of the main reasons is that the model comprises response elements for describing the elastic, viscoelastic, and viscous components of the material response. These three response phenomena are observed in bituminous materials. Like most spring-dashpot combination models, the model is suitable and computationally efficient in numerical applications. The disadvantage of this model as compared to the MHS model is that it describes the response of the material only for a narrow frequency range. Hence different parameters needed for different loading rates [11].

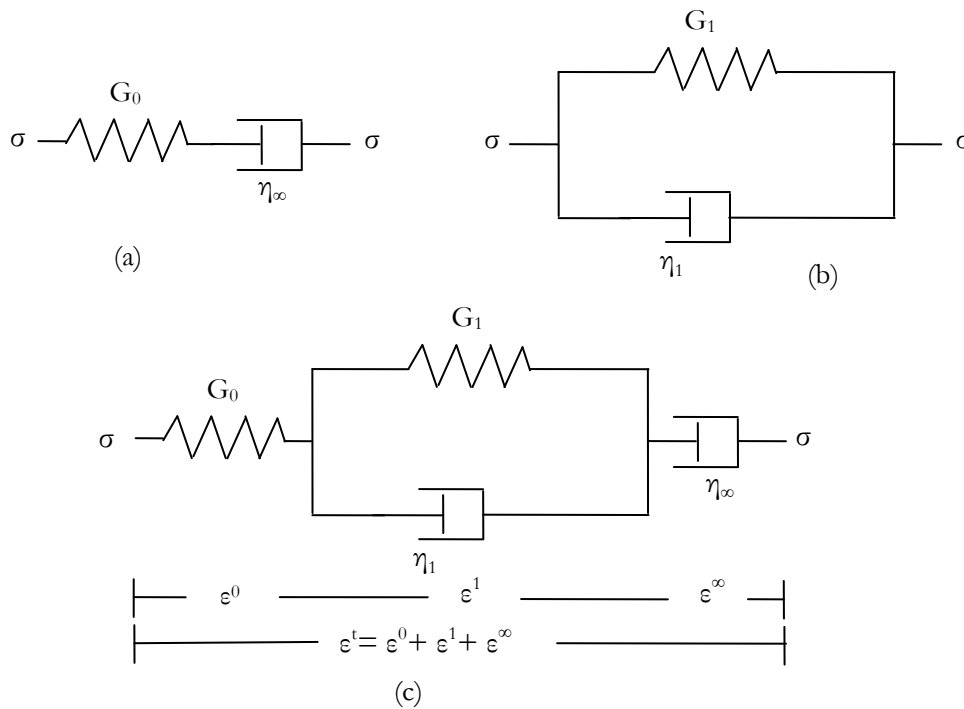


Figure 5-24 Maxwell model (a), Kelvin-Voigt model (b), Burgers' model (c)

A more comprehensive form of the Burgers' model is the generalized Burgers' model. This model contains a series of Kelvin-Voigt elements in series (Figure 5-25). The different Kelvin-Voigt elements represent different retardation spectra. It can therefore describe the response of a material over a wide frequency range.

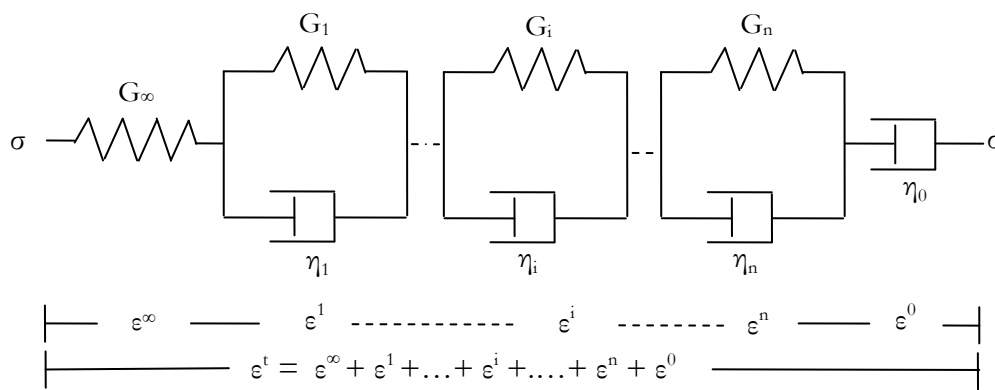


Figure 5-25 Generalized Burgers' model

5.4.1 The Model in Frequency Domain

The model behaviour in the frequency domain is similar to that of the MHS model. At higher frequencies and lower temperatures the model is asymptotic to a limiting value of G_∞ . At lower frequencies and higher temperatures the model approaches a limiting value of nil. In the frequency domain the

mathematical representation of the model for the creep compliance J in shear mode is given by:

$$J^*(\omega) = J_\infty + \sum_{n=1}^N \left(\frac{J_n}{1 + (\omega\tau_n)^2} \right) - i \left[\sum_{n=1}^N \left(\frac{J_n\omega\tau_n}{1 + (\omega\tau_n)^2} \right) + \frac{1}{\eta_0\omega} \right] \quad 5-26$$

where:

- $J^*(\omega)$ = complex creep compliance, $(1/G^*(\omega))$
- J_∞ = instantaneous shear compliance value, $(1/G_\infty)$
- J_n = model parameters for Kelvin-Voigt elements $(1/G_n)$
- τ_n = time constants for the various Kelvin-Voigt elements (η_i/G_i)
- η_0 = coefficient for the series dashpot

It should be noted that for characterizing a viscoelastic solid, the series dashpot element can be removed. Hence similar to the original HS model, the model predicts a finite rubbery compliance value equal to the sum of all the J_n values. Each Kelvin-Voigt element in the generalized model describes the material response over a narrow frequency window. To describe the material response for a wide frequency range, a number of Kelvin-Voigt elements with different retardation spectra are used. A minimum of 10 to 15 Kelvin-Voigt elements (equivalent to 22 to 32 model parameters) is usually required to describe bituminous response data over a wide frequency range [22].

5.4.1.1 Model Parameter Determination

A) General Approach

Various methods for determining the generalized Burgers' model parameters are reported in literature [1, 6, 14, 21]. The common approach for obtaining the model parameters involve optimizing the error between a given data set, which comprises the loss and storage compliance at various frequencies $(\omega_i, J'_i, \text{ and } \omega_i, J''_i)$, $i = 1 \dots M$, and the corresponding model prediction values. The model prediction values for the storage compliance (J') and loss (J'') compliance can be obtained from Equation 5-26 as:

$$J'(\omega) = \sum_{n=1}^N \left(\frac{J_n}{1 + (\omega\tau_n)^2} \right) \quad \& \quad J''(\omega) = \sum_{n=1}^N \left(\frac{J_n\omega\tau_n}{1 + (\omega\tau_n)^2} \right) \quad 5-27$$

For simplicity, in the loss and storage compliance equations the parameters of the series spring and series dashpot are included indirectly. It should be noted that the series spring can be obtained by setting the retardation constant (τ_n) for one of the Kelvin-Voigt element to nil. Similarly the series dashpot can be

represented by setting one of the elastic constants ($G_n = 1/J_n$) for one of the Kelvin-Voigt elements to nil, which corresponds to a very high retardation constant ($\tau_n \rightarrow \infty$).

For M data points, the loss and storage compliance relation can be written in a matrix form as:

$$J'(\omega_m) = S_{mn} \cdot J_n \quad \& \quad J''(\omega_m) = L_{mn} \cdot J_n \quad 5-28$$

where:

$J'(\omega_m)$ = measured storage compliance

$J''(\omega_m)$ = measured loss compliance

S_{mn} = m by n matrix for storage compliance with matrix elements given by:

$$\frac{1}{1 + (\omega_m \tau_n)^2}$$

L_{mn} = m by n matrix for loss compliance with matrix elements given by:

$$= \frac{\omega_m \tau_n}{1 + (\omega_m \tau_n)^2}$$

J_n = refers to elements of a column vector (corresponding to the model parameter for the n^{th} Kelvin-Voigt element)

For better convergence during the optimization procedure, retardation times are chosen first. For chosen retardation times τ_n ($n=1, \dots, N$) that are spaced equally in logarithmic scale, Equation 5-28 is used to perform the regression analysis to obtain the corresponding model parameters J_n ($n=1, \dots, N$). If chosen retardation times are not used, a total of $2N$ unknowns ($\tau_n, J_n; n=1, \dots, N$) need to be determined from the regression analysis, however, convergence problems are often encountered. The previous approach with chosen N retardation times is usually preferred.

Another common problem in the model parameter determination is the sensitivity of the regression analysis to scatter in the experimental data. Literature showed that better results are obtained when pre-smoothing of the experimental data using a power-law is made before the regression analysis is performed [14]. For bituminous material response data in literature, pre-smoothing of master curve data using the 2S2P1D model has also been used to determine the DBN model parameters [1]. In addition to the power law models other analytical equations such as the CA model can also be used for pre-smoothing. In this research the MHS model is chosen to perform pre-smoothing of the experimental data. This choice has been made because of the excellent ability of the model to describe the experimental data over a wide frequency window.

B) Pre-Smoothing the Experimental Data

For the purpose of obtaining a smooth curve representing the frequency domain data, the MHS model is first fitted to the experimental data. The fitting procedure for the MHS model in frequency domain has been discussed in previous sections. After a good fit is obtained for the dynamic creep compliance and phase angle data, discrete spectrum of frequencies is chosen matching the frequency window of the response data. For the chosen spectrum of frequencies, the MHS model parameters are used to generate a loss and storage compliance data. The generated loss and storage compliance data are used in the regression analysis for obtaining the generalized Burgers' model parameters. The procedure used to obtain the model parameters is discussed below.

C) Optimization Procedure

For obtaining the parameters of the generalized Burgers' model, nonlinear optimization techniques that are available in Matlab have been used. Given a set of pre-smoothed data comprising the loss and storage compliances at various frequencies, Equation 5-28 is used for obtaining the N set of Kelvin-Voigt model parameters (J_n, τ_n). For this purpose, the Matlab optimization technique (fmincon) that finds a constrained minimum of a scalar function of several variables starting at an initial estimate has been used. For the initial estimate, values can be specified manually. In this work specifying the initial estimate is made automatic by using trial solutions from least square analysis with non negative solutions. Thus in the Matlab program a two step analysis is performed.

1. In the first step, optimization is made based on a chosen set of retardation times. In Matlab the optimization technique with least square methods with non negative solutions, lsqnonneg, is used. This optimization step provides reasonable starting values for a constraint multi-variable nonlinear optimization to be performed in the second step.
2. In the second step the model parameters obtained from step 1 (J_n and τ_n) are used as initial estimates and further optimization is performed using the constrained nonlinear multi-variable optimization technique (fmincon). This step provides the final values for J_n and τ_n parameters.

In the constrained multi-variable optimization, the objective function given in Equation 5-29 is minimized.

$$\text{Objective function} = \sum_{i=1}^N \left(\frac{W_L}{V(J_i^0)} [J_i' - J_i'^0]^2 + \frac{W_s}{V(J_i''^0)} [J_i'' - J_i''^0]^2 + \frac{W_G}{V(G_i^{*0})} [G_i^* - G_i^{*0}]^2 + \frac{W_\phi}{V(\phi_i^0)} [\phi_i - \phi_i^0]^2 \right) \quad 5-29$$

where:

J' = predicted storage compliance at the i^{th} frequency

J'' = predicted loss compliance at the i^{th} frequency

J_i^0 = measured storage compliance at the i^{th} frequency

$J_i''^0$ = measured loss compliance at the i^{th} frequency

w_L, w_s, w_G, w_ϕ = weighting factors for loss modulus, storage modulus, complex modulus and phase angle (default value is set to 1)

$V(J_i^0), V(J_i''^0), V(G_i^{*0}), V(\phi_i^0)$ = variance for loss, storage, complex modulus and phase angle data

The parameter determination procedure is incorporated in a user friendly graphical user interface program (GUI) in Matlab (see Figure 5-26). With this tool, by changing the number of Kelvin-Voigt elements, optimization can be performed until a satisfactory fit is obtained. With regard to the GUI program, the procedure for the parameter determination can be summarized as follows:

- Import the master curve data (frequency, complex modulus, Phase angle) to the Matlab GUI program; in a comma delimited file
- In the program interface, fill in the number of Kelvin-Voigt elements
- Run the optimization
- Change the number of Kelvin-Voigt terms and re-run the optimization till satisfactory fit is obtained. The weighting factors for G^* , phase angle, loss and storage modulus can also be altered from the program interface helping to obtain better fits (Figure 5-26)

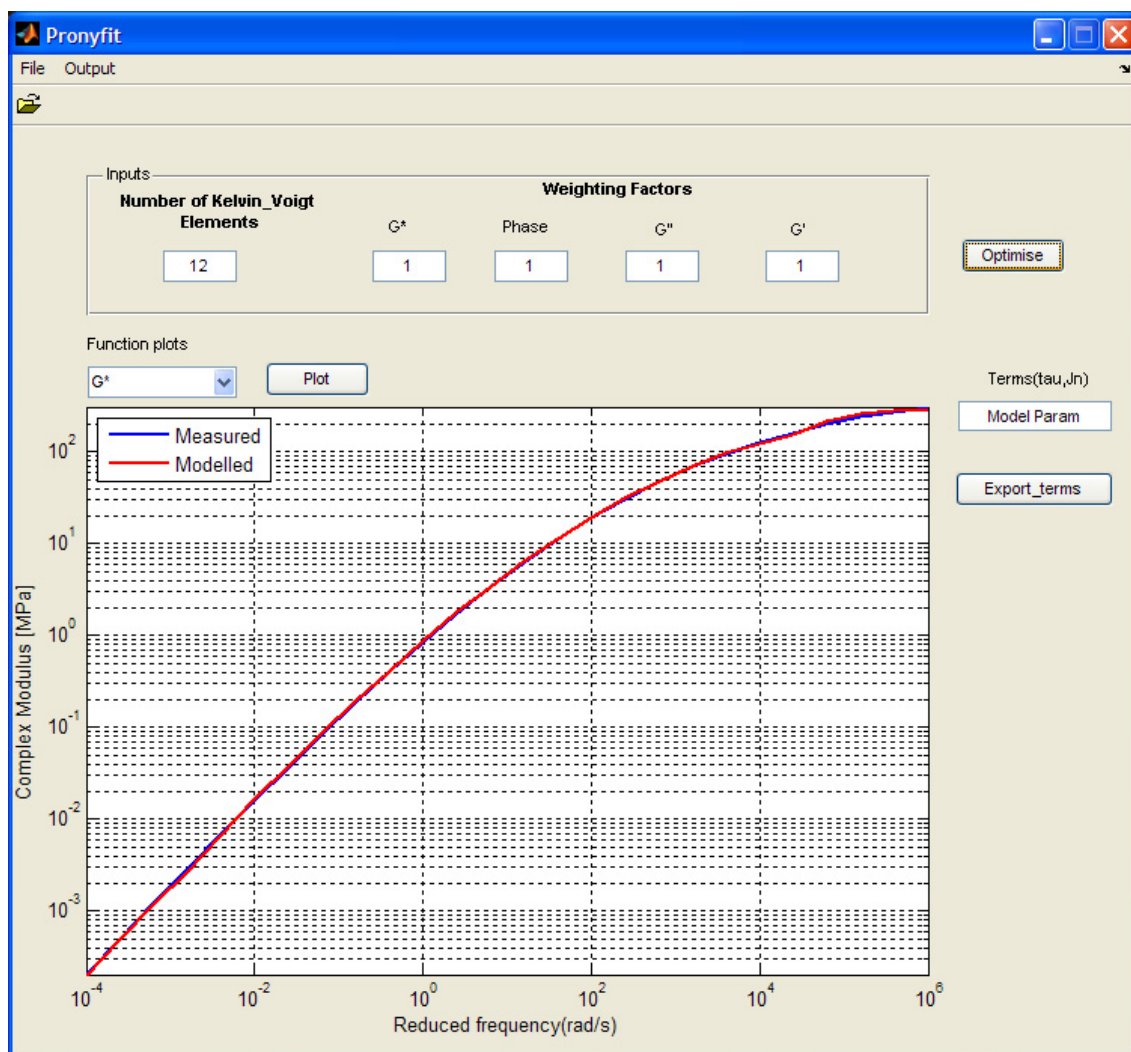
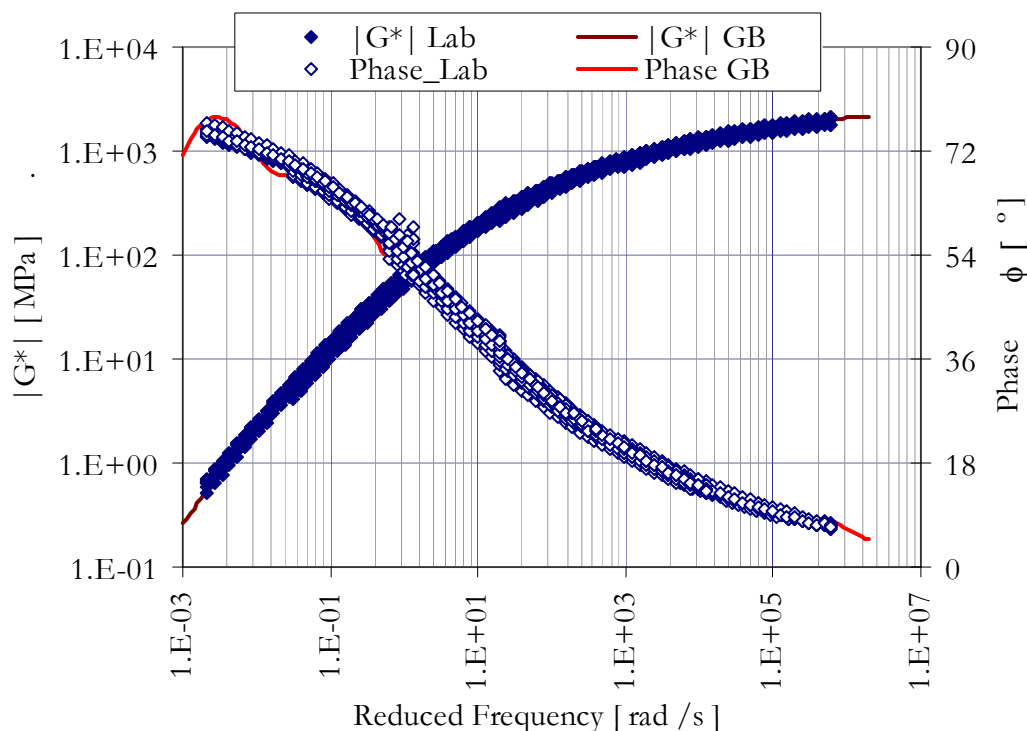
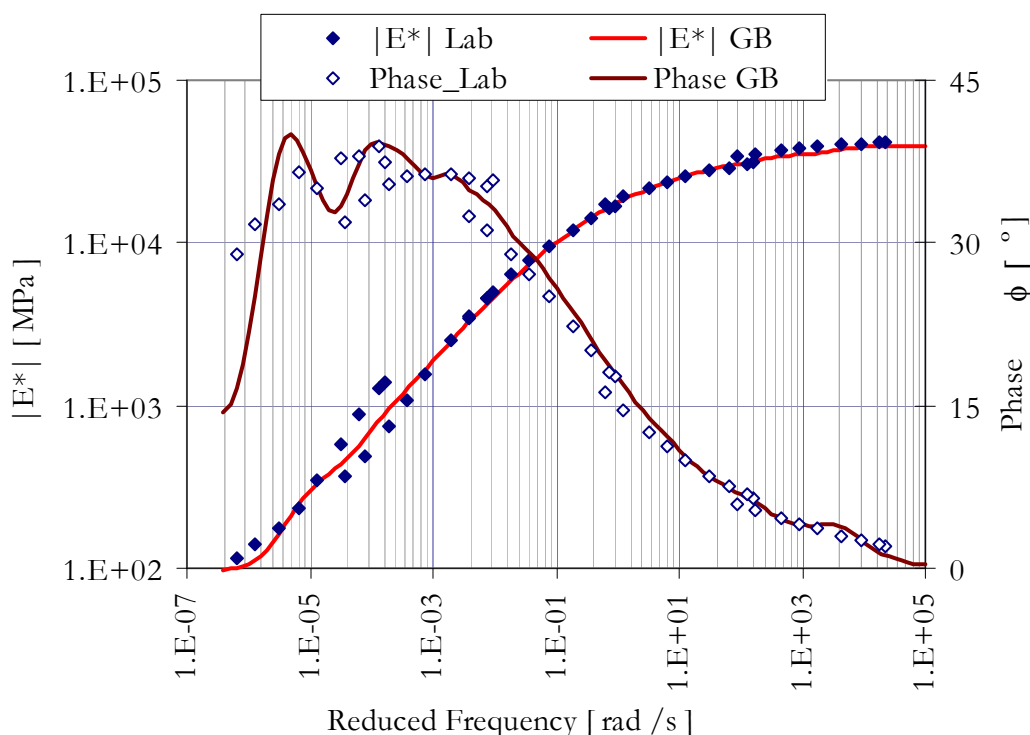


Figure 5-26 Matlab GUI for model parameter determination

5.4.1.2 Application to Describe Frequency Domain Data

Similar to the MHS model, the master curves of two asphalt mixtures and four binders are used in the analysis. The reference temperature and the corresponding shift factors for each material are presented in the previous section (Table 5-3).

Analysis results have shown that the number of model parameters required to properly describe the materials response over a wide frequency window is much higher than that of the MHS model. For the materials considered in this research, a minimum of 10 to 12 Kelvin-Voigt terms, which correspond to a total number of model parameters ranging from 22 to 26, were needed. Figure 5-27 and Figure 5-28 illustrate the quality of fit obtained for the mortar and RAP mixture respectively.


 Figure 5-27 Generalized Burgers' model fit, mortar master curve ($T_{ref} = 10^{\circ}\text{C}$)

 Figure 5-28 Generalized Burgers' model fit, RAP mixture ($T_{ref} = 4.4^{\circ}\text{C}$)

For brevity, the corresponding fits obtained for all the binders and asphalt mixtures data are not presented. However, the quality of fit for these materials is illustrated by plotting the experimental obtained values of the complex modulus and phase angle data versus the model prediction values. Figure 5-29

and Figure 5-30 summarize the results obtained for the binders and mixtures respectively. In these figures the solid line represents the line of equality (L.Eq).

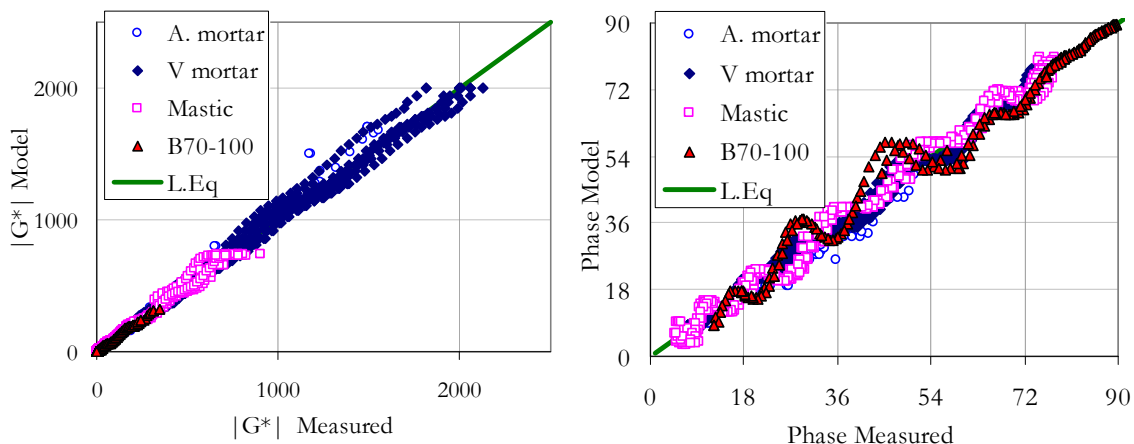


Figure 5-29 Comparison of predicted and measured response for the binders

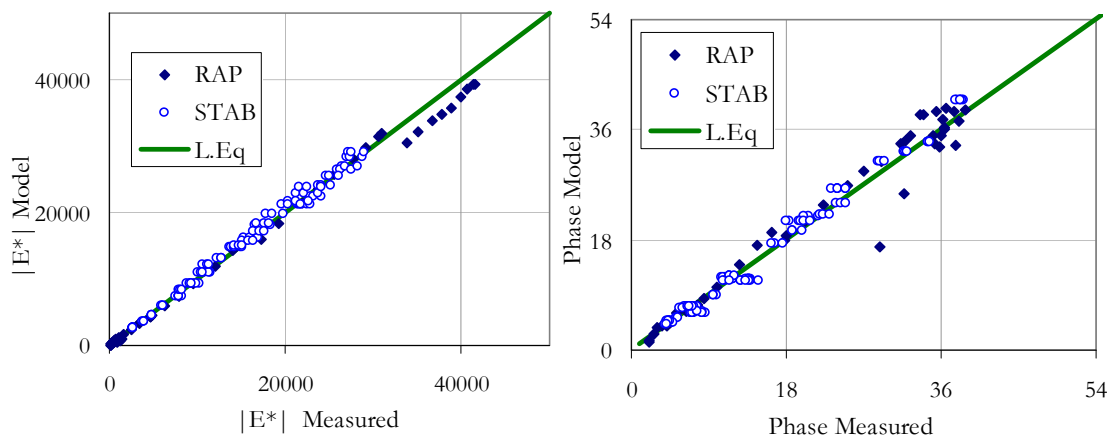


Figure 5-30 Comparison of predicted and measured response for the mixtures

From Figure 5-29 and Figure 5-30, it can be seen that the generalized Burgers' model description of the complex modulus is of similar quality in comparison to the MHS model (see Figure 5-8 and Figure 5-9). For the phase angle description however, the MHS model provides a better description of the experimental data. This can be seen from the phase angle plots in Figure 5-8 and Figure 5-9).

The generalized Burgers' model parameters for the binders as well as asphalt mixtures are given in Table 5-5 and Table 5-6. Table 5-7 presents the R^2 values obtained for all materials. In obtaining these values the model's fit on the phase angle and complex modulus is analyzed.

Table 5-5 Generalized Burgers' parameters for binders, $T_{\text{ref}} = 20^\circ\text{C}$

	B 70-100		Mastic		Virgin mortar	
n	τ_n	J_n	τ_n	J_n	τ_n	J_n
1	9.15E-06	2.21E-03	2.96E-06	4.86E-04	9.68E-06	1.80E-04
2	4.92E-05	1.14E-03	1.52E-05	2.11E-04	4.50E-05	6.63E-05
3	2.65E-04	5.53E-03	7.81E-05	7.47E-04	2.10E-04	2.56E-04
4	1.43E-03	9.93E-03	4.01E-04	9.84E-04	9.76E-04	3.12E-04
5	7.67E-03	2.78E-02	2.06E-03	2.00E-03	4.54E-03	5.79E-04
6	4.12E-02	6.50E-02	1.06E-02	3.97E-03	2.11E-02	1.01E-03
7	2.22E-01	1.89E-01	5.44E-02	9.09E-03	9.84E-02	1.89E-03
8	1.19E+00	3.65E-01	2.80E-01	2.52E-02	4.58E-01	4.61E-03
9	6.42E+00	1.86E+00	1.44E+00	5.87E-02	2.13E+00	8.35E-03
10	1.86E+02	1.84E+01	7.38E+00	2.79E-01	9.92E+00	3.86E-02
11			1.95E+02	4.49E+00	4.62E+01	1.19E-02
12					2.15E+02	4.85E-01
J_∞	3.10E-03		1.29E-03		4.90E-04	
η_0	1.17E+00		1.94E+01		3.29E+02	

Table 5-6 Generalized Burgers' model parameters for various materials¹

	Aged mortar $T_{\text{ref}}=10^\circ\text{C}$		STAB Mixture $T_{\text{ref}}=10^\circ\text{C}$		RAP mixture $T_{\text{ref}}=4.4^\circ\text{C}$	
n	τ_n	J_n	τ_n	D_n	τ_n	D_n
1	1.39E-04	2.99E-04	1.39E-05	5.45E-06	4.25E-04	3.18E-06
2	1.93E-03	3.87E-04	5.18E-05	7.88E-08	2.77E-03	2.12E-06
3	7.20E-03	2.52E-04	1.93E-04	5.11E-06	1.81E-02	4.88E-06
4	2.68E-02	6.44E-04	7.20E-04	3.62E-06	1.18E-01	7.77E-06
5	1.00E-01	8.18E-04	2.68E-03	6.42E-06	7.69E-01	1.48E-05
6	3.73E-01	1.40E-03	1.00E-02	8.70E-06	5.01E+00	3.02E-05
7	1.39E+00	2.58E-03	3.73E-02	1.12E-05	3.27E+01	6.26E-05
8	5.18E+00	3.21E-03	1.39E-01	2.29E-05	2.13E+02	1.50E-04
9	1.93E+01	9.75E-03	5.18E-01	2.21E-05	1.39E+03	2.89E-04
10	7.20E+01	4.26E-03	1.93E+00	8.25E-05	9.06E+03	9.59E-04
11	2.68E+02	4.33E-02	7.20E+00	2.92E-05	5.91E+04	7.83E-04
12			2.68E+01	3.75E-04	3.85E+05	6.81E-03
D_∞, J_∞	5.91E-04		3.30E-05		2.56E-05	
η_0	6.60E+03		1.97E+05		2.30E+09	

¹ Given binder properties reflect the shear behaviour while the mixture properties correspond to the bending behaviour

Table 5-7 Quality of fit to experimental data (R^2 values)

	B 70-100	Mastic	Virgin mortar	Aged mortar	STAB mix	RAP mix
G^*, E^*	0.986	0.995	0.994	0.990	0.989	0.996
ϕ	0.985	0.975	0.992	0.947	0.986	0.960

Based on the model fits obtained in frequency domain, the following remarks can be made about the generalized Burgers' model.

- A number of Kelvin-Voigt elements are required to describe the response data over wide temperature and frequency range. A total of 10 to 12 terms were required for the materials considered in this study.
- Model parameter determinations with chosen retardation times, which are equally spaced in logarithmic scale, provide better fits during optimization.
- Phase angle descriptions of the generalized Burgers' model are less accurate as compared to the MHS model.

5.4.2 The Model in Time Domain

As discussed in the literature review section, inter conversion methods can be applied to obtain time domain material functions from frequency domain data. For the generalized Burgers' model, the time domain creep compliance expression is given by:

$$J(t) = J_{\infty} + \sum_{n=1}^N J_n \left[1 - \exp\left(\frac{-t}{\tau_n}\right) \right] + \frac{t}{\eta_0} \quad 5-30$$

where:

$J(t)$ = creep compliance (shear mode)

J_{∞} = instantaneous shear compliance ($1/G_{\infty}$)

J_n = model parameters for Kelvin-Voigt elements ($1/G_n$)

τ_n = retardation time for the various Kelvin-Voigt elements (η_i/G_i)

η_0 = coefficient for the series dashpot

This analytical expression can be used to describe time domain creep compliance data. Similar to the frequency domain analysis, time domain curve

fitting can also be performed to determine the model parameters based on experimental data. For general application in numerical environment, the model needs to be formulated in an incremental approach.

5.4.2.1 Numerical Approach

To allow simulation of time domain responses for an arbitrarily shape of the applied stress signal, an incremental formulation of the model needs to be obtained. In reference to Figure 5-25, the total deformation in the generalized Burgers' model is the sum of the elastic, viscoelastic and viscous deformations. Hence the incremental strain in the system can be obtained as:

$$\Delta\varepsilon(t) = \Delta\varepsilon_e(t) + \Delta\varepsilon_{ve}(t) + \Delta\varepsilon_v(t) \quad 5-31$$

From the theory of viscoelasticity discussed in Chapter 2, the constitutive relation for a viscoelastic material in one dimensional form is given as:

$$\varepsilon(t) = \int_0^t J(t-\tau) \frac{d(\sigma)}{d\tau} d\tau \quad 5-32$$

where:

- $\varepsilon(t)$ = strain
- $\sigma(t)$ = applied stress
- $J(t-\tau)$ = creep compliance
- τ = integration variable

Applying the integral formulation for the elastic, viscoelastic and viscous components, the incremental formulation for the various deformation components can be obtained. For the elastic component, the incremental strain $\Delta\varepsilon_e$ that follows from an incremental stress $\Delta\sigma$ is given by:

$$\Delta\varepsilon_e = J_0 \Delta\sigma \quad 5-33$$

Denoting the creep compliance for the viscous element as $J_v(t)$, and applying the properties of the hereditary integrals, the constitutive relation for obtaining the viscous strain in the linear dashpot is given by:

$$\varepsilon_v(t) = \int_0^t J_v(t-\tau) \dot{\sigma} d\tau = \int_0^t \left[\dot{J}_v(t-\tau) \right] \sigma(\tau) d\tau \quad 5-34$$

where:

$$J_v(t-\tau) = \frac{t-\tau}{\eta_0}$$

$$\dot{J}_v(t-\tau) = \frac{dJ_v(t-\tau)}{d(t-\tau)} = \frac{1}{\eta_0}$$

Substituting and dividing the integral limits into two parts one obtains:

$$\varepsilon_v(t) = \int_0^t \dot{J}_v(t-\tau) \sigma(\tau) d\tau = \frac{1}{\eta_0} \int_0^{t-\Delta t} \sigma(\tau) d\tau + \frac{1}{\eta_0} \int_{t-\Delta t}^t \sigma(\tau) d\tau \quad 5-35$$

The first integral in the above expression corresponds to the viscous deformation in the previous time step, $\varepsilon_v(t-\Delta t)$. The second integral can be evaluated using a trapezoidal rule. After some mathematical manipulation the change in viscous strain can be computed as:

$$\Delta\varepsilon_v(t) = \frac{\Delta t}{\eta_0} \left(\sigma(t-\Delta t) + \frac{\Delta\sigma}{2} \right) \quad 5-36$$

In a similar manner, substituting the creep compliance expression for the Kelvin-Voigt elements to the integral formulation in Equation 5-31, the viscoelastic strain can be calculated as:

$$\varepsilon_{ve}(t) = \int_0^t \sum_{n=1}^N J_n \left[1 - \exp\left(\frac{-(t-\tau)}{\tau_n}\right) \right] \dot{\sigma} d\tau \quad 5-37$$

Which can be rewritten as:

$$\varepsilon_{ve}(t) = \varepsilon^1(t) - \sum_{n=1}^N \varepsilon^n(t) \quad 5-38$$

where:

$$\varepsilon^1(t) = \sum_{n=1}^N J_n \cdot \sigma(t)$$

$$\varepsilon^n(t) = \int_0^t J_n \left[\exp\left(\frac{-(t-\tau)}{\tau_n}\right) \right] \dot{\sigma} d\tau$$

For a time step Δt , the integral for the variable $\varepsilon^n(t)$ can be divided into two terms as:

$$\varepsilon^n(t) = \int_0^{t-\Delta t} J_n \left[\exp\left(\frac{-(t-\tau)}{\tau_n}\right) \right] \dot{\sigma} d\tau + \int_{t-\Delta t}^t J_n \left[\exp\left(\frac{-(t-\tau)}{\tau_n}\right) \right] \dot{\sigma} d\tau \quad 5-39$$

The first integral can be simplified as:

$$\int_0^{t-\Delta t} J_n \left[\exp\left(\frac{-(t-\tau)}{\tau_n}\right) \right] \dot{\sigma} d\tau = \exp\left(\frac{-\Delta t}{\tau_n}\right) \varepsilon^n(t-\Delta t)$$

Assuming that the stress rate is constant for an infinitesimal time step Δt , evaluation of the second integral in Equation 5-39 results:

$$\int_{t-\Delta t}^t J_n \left[\exp\left(\frac{-(t-\tau)}{\tau_n}\right) \right] \dot{\sigma} d\tau = J_n \cdot \frac{\Delta\sigma}{\Delta t} \tau_n \left[1 - \exp\left(\frac{-\Delta t}{\tau_n}\right) \right]$$

The variable $\varepsilon^n(t)$ can then be written in a recursive manner as follows:

$$\varepsilon^n(t) = \exp\left(\frac{-\Delta t}{\tau_n}\right) \varepsilon^n(t-\Delta t) + J_n \cdot \frac{\Delta\sigma}{\Delta t} \tau_n \left[1 - \exp\left(\frac{-\Delta t}{\tau_n}\right) \right] \quad 5-40$$

The change in the variable $\Delta\varepsilon^n(t)$ can be calculated as:

$$\Delta\varepsilon^n(t) = \varepsilon^n(t-\Delta t) \left(\exp\left(\frac{-\Delta t}{\tau_n}\right) - 1 \right) + J_n \cdot \frac{\Delta\sigma}{\Delta t} \tau_n \left[1 - \exp\left(\frac{-\Delta t}{\tau_n}\right) \right] \quad 5-41$$

Substituting Equation 5-41 into Equation 5-38 the change in viscoelastic strain $\Delta\varepsilon_{ve}$ that follows from a change in applied stress $\Delta\sigma$ is expressed as:

$$\Delta\varepsilon_{ve}(t) = \Delta\varepsilon^1(t) - \Delta \sum_{n=1}^N \varepsilon^n(t) \quad 5-42$$

where:

$$\Delta\varepsilon^1(t) = \sum_{n=1}^N J_n \cdot \Delta\sigma$$

$$\Delta\varepsilon^n(t) = \varepsilon^n(t-\Delta t) \left(\exp\left(\frac{-\Delta t}{\tau_n}\right) - 1 \right) + J_n \cdot \frac{\Delta\sigma}{\Delta t} \tau_n \left[1 - \exp\left(\frac{-\Delta t}{\tau_n}\right) \right]$$

For the generalized Burgers' model, Equation 5-33, Equation 5-36 and Equation 5-42 in combination allows computation of the incremental strain for an incrementally applied stress. The incremental formulation requires an update of

the variable $\varepsilon^n(t)$ at each time step increment. The value of $\varepsilon^n(t)$ at each time step can be calculated in a recursive manner using Equation 5-40.

5.4.2.2 Notes on Practical Implications

Unlike the MHS model which requires storage of the entire strain history in numerical applications, the incremental formulation for the generalized Burgers' model takes into account history effects in a recursive manner (Equation 5-40). This allows efficient utilization of computer memory. This attribute is common to most linear spring-dashpot combination models.

On the other hand it has previously been shown that the phase angle fits of the model to the experimental data is less accurate. From a practical point of view, the large number of model parameters to describe material response data over a wide frequency range is also a disadvantage.

5.4.3 Frequency vs. Time Domain Response

Using the MHS model, it has been shown that one set of model parameters can be used to simulate both the frequency and time domain response of the mortar. In this section similar computations have been made to simulate the creep-recovery and relaxation response of the mortar using the generalized Burgers' model. The model parameters used in the simulations have been obtained from the frequency domain measurements. The test conditions for the creep-recovery and relaxation tests have already been discussed in Section 5.3.3.2 and Section 5.3.3.3. In the following sections the simulation results are presented.

5.4.3.1 Relaxation Simulations

Using the generalized Burgers' model, relaxation tests for the mortar were simulated. The simulations correspond to the relaxation tests presented in Table 5-4. The simulation results were compared with the experimental data. Similar to the MHS model, the time domain simulations show a very good agreement with the experimental results. For brevity only the simulation at 10°C is presented. The remaining simulations that were made at 20°C are given in the Appendix D.

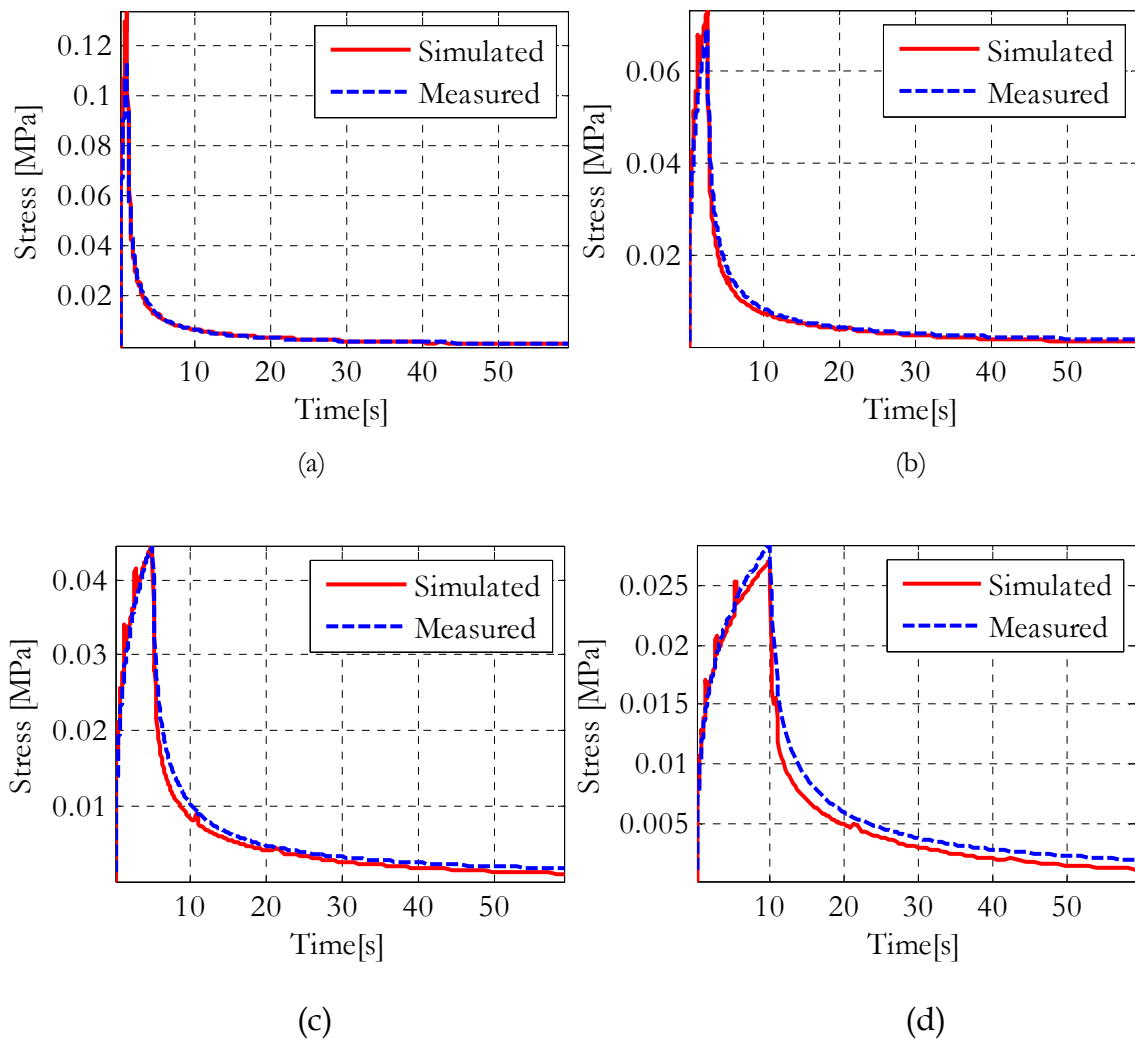


Figure 5-31 Measured and simulated relaxation tests for mortar at 10°C, sample no 1 (Time step: 1.25 s (a), 2.5s (b), 5 s (c) and 10 s (d))

5.4.3.2 Creep-Recovery Simulations

Using the block pulse stress signals from the creep-recovery experiment as input, the creep-recovery phase of the mortar was simulated numerically using the Matlab program. The generalized Burgers' model parameters that were determined from the master curve data in the frequency domain were used. The parameters are given in Table 5-5. These properties were determined based on response data obtained from 5 different mortar samples. Figure 5-32 presents the comparison between the measured and simulated creep-recovery tests for an applied stress of 0.825 kPa. The first plot represents the results obtained for a time step, T_1 , of 5 seconds. The second and third plots correspond to time steps of 10 seconds and 15 seconds respectively. Similar plot for a stress level of 1.53 kPa is presented in Figure 5-33. In each of the plots the dashed lines represent the experimentally obtained creep-recovery curve for the two different mortar samples. The solid line represents the simulated result with material properties obtained from the frequency domain response data.

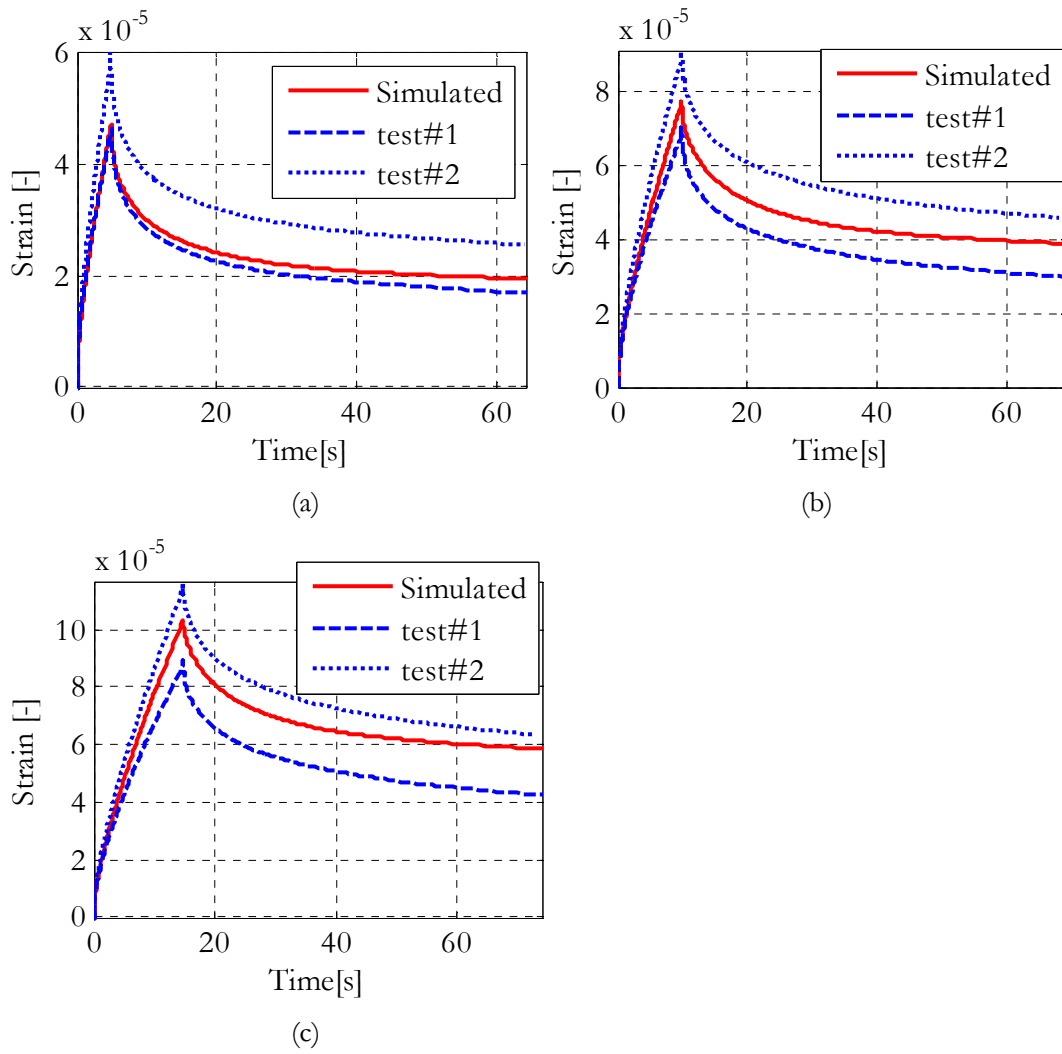


Figure 5-32 Measured and simulated creep-recovery data for an applied stress of 0.825 kPa (Time steps: 5 s (a), 10 s (b) and 15 s (c))

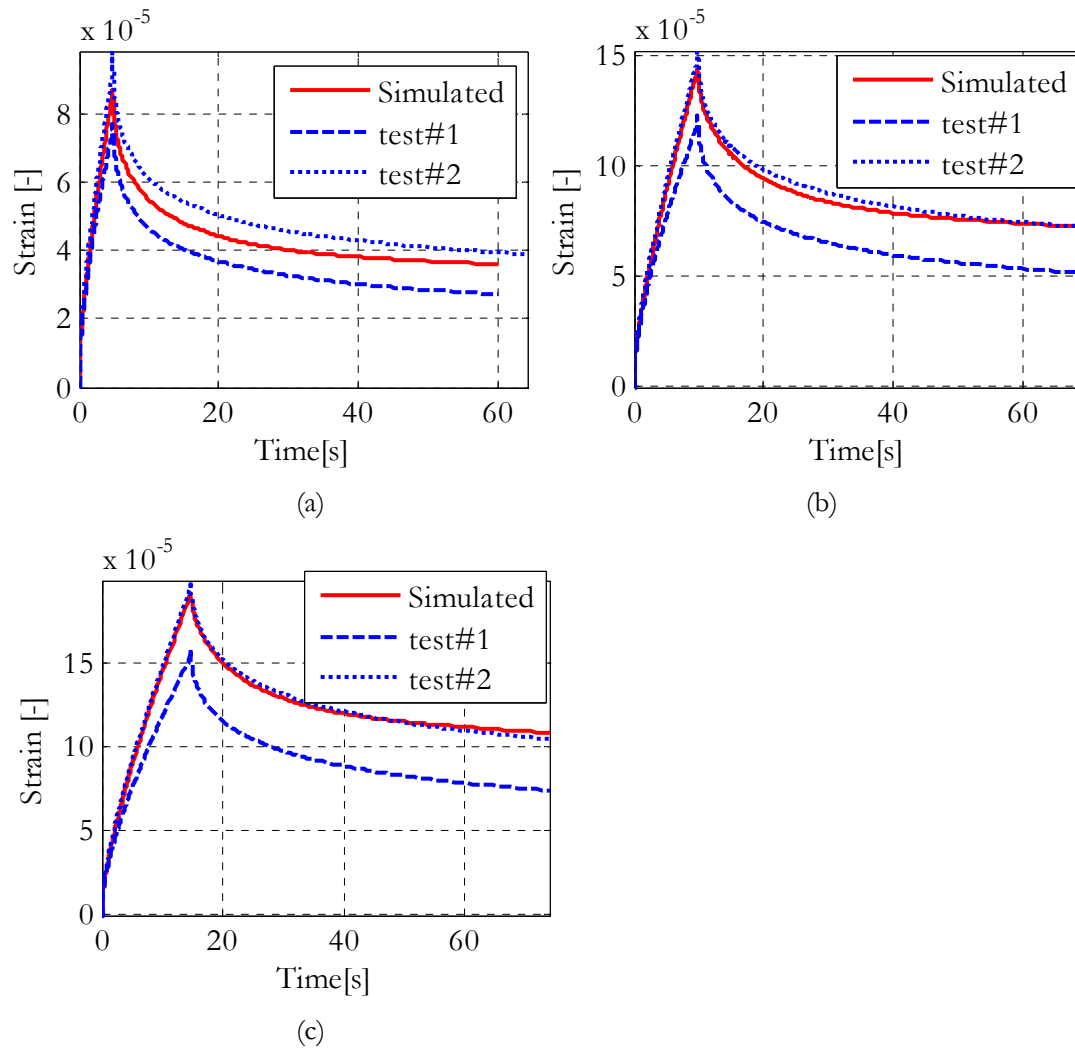


Figure 5-33 Measured and simulated creep-recovery data for an applied stress of 1.53 kPa (Time steps 5 s (a), 10 s (b) and 15 s (c))

5.4.3.3 Discussions

Similar to the MHS model, the generalized Burgers' model was used to simulate time domain results. Due to the computational efficiency of the model, memory storage is not required. Because of this the load signals obtained from the laboratory were directly used to simulate the relaxation and creep/recovery tests. The numerical noises observed in the simulations (see Figure 5-31) are a reflection of the noises observed in the actual measurement of the applied deformation.

In terms of accuracy, it can be seen that the simulation results are as accurate as the case for the MHS model. This indicates that regardless of the models, the frequency and time domain responses are well related. In this particular case, both the MHS and the generalized Burgers' models described the frequency domain response data of the mortar very well. Hence, good description of the response data in frequency domain leads to good prediction of the time domain responses. Since similar experimental data was used here, other observations

that were discussed in Section 5.3.3.6, for the MHS model, are not repeated for clarity. The summary of the findings for both models is summarized below.

5.5 Summary of Findings

The main findings that can be drawn from the material presented in this chapter are summarized below.

5.5.1 The MHS model

- The original HS model was modified with addition of a linear dashpot in series. This is to allow viscous deformation simulations.
- The MHS model has been used to describe the frequency domain response of bituminous binders as well as mixtures. The results have shown that the model is capable in describing the response over a wide frequency window. The model has very few model parameters which is very desirable for practical use.
- Model parameter determination from the frequency domain can be performed using the analytical expression of the model in simple spreadsheet programs like excel. Model parameter determination from time domain tests require a numerical approach. This is because the time domain analytical expression for the relaxation and creep material functions of the MHS model are complex to obtain.
- For time domain applications, the numerical formulation of the MHS model has been obtained. The Grünwald definition of fractional derivatives was utilized in formulating the model for time domain applications. The formulation requires that the entire strain history for the parabolic dashpots to be stored. In terms of the required amount of computational memory, this may result in a serious limitation when the model is applied for computations that involve too many time steps. The numerical formulation also requires equal time steps to be taken which is a disadvantage for long computations that need to be performed with varying time steps.

5.5.2 The Generalized Burgers' Model

- Similar to the MHS model, the generalized Burgers' model has also described the response of binders and mixtures over a wide frequency window. However, in comparison to the MHS model the phase angle description of the generalized Burgers' model has been found to be less accurate. This behaviour is intrinsic to spring-dashpot combination models, and it is mainly related to the nature of the resulting analytical expression (consisting of exponential functions) that is used to describe the material functions.

- Appropriate description of the material response over a wide frequency window requires the use of many Kelvin-Voigt elements. This results in a large number of model parameters. For the materials used in this research a minimum of ten Kelvin-Voigt elements, which results in a total of 22 model parameters, were required to describe the response over a wide frequency window.
- In determining the model parameters from frequency domain response data, it has been observed that the optimization analysis is very sensitive to data scatter. Hence prior data smoothing is required for best results. Analytical expressions used to describe the master curves of binders and mixtures can be used for data smoothing. Due to the excellent description of the complex modulus and phase angle data of the materials, the MHS model has been used as a tool for performing data smoothing in this research.
- Unlike the MHS model, the numerical formulation of the generalized Burgers' model does not require storage of the entire history. It is, therefore, efficient in terms of computational memory. The formulation also does not require equal time steps to be used, hence the incremental time step can be varied during a computation, which is not possible for the case of the MHS model.

5.5.3 Frequency and Time Domain Responses

Frequency domain response data that were obtained at various temperatures were used to construct the master curve for the materials. For this purpose, the time-temperature superposition principle was utilized. The master curve represents the response of the material over a wide frequency window. Hence, in time domain it is expected that the response data corresponds to a wider window in the time of loading.

In order to establish the relation between the frequency domain response and the time domain response, frequency domain response data have been used to simulate time domain responses. First, for the selected reference temperatures, the MHS and the generalized Burgers' model parameters were determined from the frequency domain master curve data using regression analysis. These parameters have been used to simulate creep-recovery and relaxation tests in time domain. The results of the simulations have been compared with experimental data. Loading times of up to 15 seconds were considered with a rest period of 60 seconds. The results of the simulation showed that one set of parameters can be used to simulate both the frequency and time domain response of the material. For loading times of 10 to 15 seconds a good agreement between the simulated and measured response has been obtained.

5.5.3.1 Practical Implication

The time of wheel loading for a pavement is essentially very short. For trucks travelling at a speed of 80 km/ hr, the loading time on a pavement is in fractions of seconds. Hence the good agreement that is observed between the frequency and time domains responses (for long loading times of up to 10 seconds) implies that very accurate material information is obtained from frequency domain data that can provide appropriate representation of the material behaviour for loading times corresponding to a wide range of truck loading speeds. However, it is important to note that for other computations involving very long loading times, the frequency domain data may lack the material response information corresponding to long loading times. Depending on the purpose, the relevant material response information in such cases may need to be obtained from time domain tests (such as creep tests).

5.5.4 Choice of Models

It has been shown that the generalized Burgers' model and the MHS model can describe the response of the materials for wide frequency window. The advantage of the MHS model over the generalized Burgers' model is that the MHS model requires only a few number of model parameters to describe the material response over a wide frequency window. In addition the model provides better quality of fit for the phase angle. In view of model selection for practical use, the few number of model parameters required for the modified HS is very attractive. One of the model disadvantages is the relatively high computational memory required in numerical environments. Furthermore, the equal time step requirement in the numerical formulation limits the model application for cases where use of different time steps is mandatory for computational efficiency (example for highly nonlinear analysis).

With regard to the generalized Burgers' model, the number of model parameters is dependent on the range of frequency considered. The model description of the phase angle data has been found to be less accurate. The model parameter determination is also less straight forward as compared to the MHS model. However, its computational efficiency in numerical environments is excellent. In contrary to the MHS model, the numerical formulation of the generalized Burgers' model allows the use of different time steps in a computation, which is advantageous for computational efficiency.

The attractiveness of the models for practical use can therefore be evaluated based on the ease of use, accuracy, computational efficiency etc. However, these factors also depend on the scale of the problem that is to be dealt with. Hence absolute model selection can not be made. However, based on the work performed in this research the author believes that for linear viscoelastic computations, the MHS model offers equivalent or more benefit than the generalized Burgers' model. For nonlinear computations, the requirements to

use equal time steps in the numerical formulation and to store the entire strain histories for the parabolic dashpots are serious limitations. For meso mechanistic applications, the performance of the models in terms of accuracy and computational efficiency will be further discussed in Chapter 7.

References

- [1]. Benedetto, H.D., Mondher, N., Sauzèat, C., and Olard, F., *Three-dimensional Thermo-viscoplastic Behaviour of Bituminous Materials. The DBN Model*. Road Materials and Pavement Design, 2007. **8**(2): p. 285-315.
- [2]. Chabot, A., Tamagny, P., Duhamel, D., and Poche, D. *Viscoelastic modeling for asphalt pavements- software ViscoRoute*. in *Proceedings of the 10th international conference on asphalt pavements*. 2006. Quebec, Canada.
- [3]. Christensen, D.W. and Anderson, D.A., *Interpretation of dynamic mechanical test data for paving grade asphalt cements*. Journal of Assoc. Asphalt Paving Technol., 1992. **61**: p. 67-116.
- [4]. Christensen, R.M., *Theory of viscoelasticity: An introduction*. Second edition ed. 1982, New York: Academic press.
- [5]. Collop, A.C., Scarpas, A., Kasbergen, C., and Bondt, A., *Development and Finite Element Implementation of A Stress Dependent Elasto-Visco-Plastic Constitutive Model with Damage for Asphalt*, in *Transport Research Board (TRB) Annual Meeting*. 2003: Washington DC.
- [6]. Cost, T.L. and Becker, E.B., *A multidata method of approximate Laplace transform inversion*. International Journal for Numerical Methods in Engineering, 1970. **2**(2): p. 207-219.
- [7]. Hopman, P.C., Nilsson, R.N., and Pronk, A.C. *Theory, Validation and Application of the Visco-Elastic Multilayer Program VEROAD*. in *Proceedings of the eight International Conference on Asphalt Pavements*. 1997. Seattle, USA.
- [8]. Huet, C., *Etude par une méthode d'impédance du comportement visco-élastique des matériaux hydrocarbonés*. 1963, Faculté des Sciences de Paris: Paris.
- [9]. Huurman, M., Mo, L., Woldekidan, M.F., Khedoe, R.N., and Moraal, J., *Overview of the LOT meso mechanical research into porous asphalt raveling*. Advanced Testing and Characterisation of Bituminous Materials, Vols 1 and 2, 2009: p. 507-518.
- [10]. Medani, T.O., Huurman, M., and Molenaar, A.A.A., *A unified model to describe the time-temperature dependency characteristics of several bound road materials*. Vol. 8. 2007, Paris, France: Lavoisier. 27.
- [11]. Muraya, P.M., *Permanent Deformation of Asphalt Mixtures*. 2007, Delft Univeristy of Technology: Delft.
- [12]. Nilsson, R., Oost, I., and Hopman, P., *Viscoelastic Analysis of Full-Scale Pavements: Validation of VEROAD*. Transportation Research Record: Journal of the Transportation Research Board, 1996. **1539**(-1): p. 81-87.
- [13]. Olard, F. and Di Benedetto, H., *General 2S2PID model and relation between the linear viscoelastic behaviours of bituminous binders and mixes*. Vol. 4. 2003, Paris, FRANCE: Lavoisier. 40.
- [14]. Park, S.W. and Kim, Y.R., *Fitting Prony-series viscoelastic models with power-law presmoothing*. Vol. 13. 2001, Reston, VA, ETATS-UNIS: American Society of Civil Engineers.
- [15]. Petras, I., *The fractional-order controllers: Methods for their synthesis and application*. J.of Elect.Eng., 2000. **50**(1999): p. 284-288.
- [16]. Pronk, A.C., *The Variable Dashpot*. 2003, Ministry of water and transport, Rijkswaterstaat: Delft.
- [17]. Pronk, A.C. *The Huet-Sayegh Model: A Simple and Excellent Rheological Model for Master Curves of Asphaltic Mixes*. 2005. Baton Rouge, Louisiana, USA: ASCE.

- [18]. Ramrakhyani, D.S., Lesieutre, G.A., and Smith, E.C., *Modeling of elastomeric materials using nonlinear fractional derivative and continuously yielding friction elements*. International Journal of Solids and Structures, 2004. **41**(14): p. 3929-3948.
- [19]. S.P.Wu and J.Qiu, *Rheological and mechanical characterization of recycled asphalt mixture*, in *8th International Conference of Eco-Materials*. 2007: Brunei University, West London, UK.
- [20]. Scarpas, A., *CAPA-3D Finite elements system-User's manual*. 1992, Delft.
- [21]. Schapery, R.A., *A simple Collocation Method for Fitting Viscoelastic Models to Experimental Data*. 1961, California Institute of Technology: Pasadena, California.
- [22]. Woldekidan, M., Huurman, M., and Mo, L., *Testing and modeling of bituminous mortar response*. Journal of Wuhan University of Technology--Materials Science Edition, 2010. **25**(4): p. 637-640.

6

Modelling Nonlinear Viscoelastic Response of Binders

As shown in the experimental investigation work in Chapter 4, bituminous binders exhibit nonlinear response at high shear stress levels. To take into account the nonlinear behaviour of the binders in mechanistic calculations, first relevant nonlinear theories need to be selected. Based on the literature review on nonlinear viscoelastic theories, the Schapery nonlinear theory has been selected. As discussed in the literature review section, this theory has many advantages over other nonlinear theories. The first advantage includes the practical number of laboratory tests required to obtain the nonlinear parameters in the theory. Another important advantage of the theory is its fundamentally strong theoretical background. Because of these reasons the theory is widely used for nonlinear viscoelastic analyses. In this chapter, the one dimensional representation of the theory and the model parameter determination technique are discussed. For all the binders, the nonlinear model parameters are given. For FE use, a suitable numerical formulation technique is also selected.

6.1 Schapery's Nonlinear Theory

The basic derivation of the Schapery nonlinear theory requires knowledge of thermodynamics; this is not presented here. Rather the final form of the theory for the uni-axial case is presented. For uni-axial deformation under isothermal conditions, the Schapery nonlinear theory for viscoelastic materials takes the following form [7]:

$$\varepsilon(t) = g_0 D_0 \sigma + g_1 \int_0^t \Delta D [\psi(t) - \psi(\tau)] \frac{d(g_2 \sigma)}{d\tau} d\tau \quad 6-1$$

where:

D_0 = instantaneous component of creep compliance at linear viscoelasticity

$\Delta D(\psi)$ = $D(\psi) - D_0$ is the transient component of creep compliance at linear viscoelasticity

$\psi(t)$ = reduced time

g_0 = nonlinear factor explaining stress dependency of the glassy compliance

g_1 = nonlinear factor explaining stress dependency of the transient part of the compliance

g_2 = nonlinear factor explaining the effect the stress rate on the transient part of the compliance

The reduced time $\psi(t)$ is given by:

$$\psi(t) = \int_0^t \frac{ds}{a_T \cdot a_\sigma} \quad 6-2$$

In the reduced time equation, the parameter a_T is the time-temperature shift factor that is used for thermorheological simple materials, the parameter a_σ is a stress shift factor, and s is integration variable. When all the nonlinear parameters: g_0, g_1, g_2 and a_σ are all set to 1, Equation 6-1 reduces to the classical theory of linear viscoelasticity. The creep compliance term in the integral can be represented by any relevant response model. In relation to suitability in formulation and computational efficiency in numerical environments, the most suitable method widely used in literature is to model the creep compliance with series of Kelvin-Voigt elements. If the laboratory characterization of the materials is conducted at different strain levels (strain controlled mode), the equivalent suitable model for implementation is the generalized Maxwell model. Further discussion on the suitability of response models for implementation in the nonlinear theory will be given in Chapter 7. First the method of model parameter determination is discussed below.

6.2 Methods of Parameter Determination

The nonlinear parameters in the Schapery's theory, given in Equation 6-1, need to be determined from creep tests. To elucidate the parameter determination procedures, first Equation 6-1 is used to obtain the strain response of a material for a step stress input $\sigma(t) = \sigma_0 H(t)$. The function $H(t)$ represents a unit step function and σ_0 is the magnitude of the applied stress. The resulting strain response is given as:

$$\varepsilon(t, \sigma_0) = g_0(\sigma_0)D_0\sigma_0 + g_1(\sigma_0)g_2(\sigma_0)\sigma_0\Delta D \left[\frac{t}{a_\sigma(\sigma_0)} \right] \quad 6-3$$

Dividing both sides by σ_0 the nonlinear creep compliance, denoted as $D_n(t, \sigma_0)$, can be obtained as:

$$\begin{aligned} D_n(t, \sigma_0) &= \frac{\varepsilon(t, \sigma_0)}{\sigma_0} = g_0(\sigma_0)D_0 + g_1(\sigma_0)g_2(\sigma_0)\Delta D \left[\frac{t}{a_\sigma(\sigma_0)} \right] \\ &= D_0(\sigma_0) + \Delta D_n(t, \sigma_0) \end{aligned} \quad 6-4$$

where:

$D_n(t, \sigma_0)$ = nonlinear creep compliance

$D_0(\sigma_0)$ = instantaneous value of the nonlinear creep compliance

$\Delta D_n(t, \sigma_0)$ = transient component of the nonlinear creep compliance

By considering the time independent and time dependent components of the creep compliance separately, the following relation can be derived:

$$g_0(\sigma_0) = \frac{D_0(\sigma_0)}{D_0} \quad \text{and} \quad g_1(\sigma_0)g_2(\sigma_0) = \frac{\Delta D_n(t, \sigma_0)}{\Delta D \left(\frac{t}{a_\sigma(\sigma_0)} \right)} \quad 6-5$$

The first relation given in Equation 6-5 implies that for a given stress σ_0 , the nonlinear parameter g_0 is obtained by dividing the nonlinear instantaneous creep compliance $D_0(\sigma_0)$ by the corresponding value D_0 in the linear range. Similarly the second relation in Equation 6-5 implies that for a given stress σ_0 the product of the nonlinear parameters $g_1(\sigma_0)$ and $g_2(\sigma_0)$ is obtained by dividing the transient component of the nonlinear creep compliance $\Delta D_n(t, \sigma_0)$ by the transient component of the linear creep compliance $\Delta D(t_r)$ with a stress reduced time. The stress reduced time is obtained as:

$$t_r = \frac{t}{a_\sigma(\sigma_0)} \quad 6-6$$

The above discussion on the parameter determination can alternatively be explained using the log-log plot of the creep compliance data versus time (see Figure 6-1). If vertical and horizontal shifting is required for the transient component of the nonlinear compliance curve to coincide with the transient

component of the linear compliance curve, $\log g_1 g_2$ and $\log a_\sigma$ represent the required amounts of the vertical and horizontal shifting respectively.

The parameter $g_0(\sigma)$ can also be obtained by shifting the horizontal part of the nonlinear creep compliance curve to the linear creep compliance curve. This section of the curve is seen at very low loading times and denotes the instantaneous creep response. Graphical illustration on the nonlinear model parameters determination is shown in Figure 6-1.

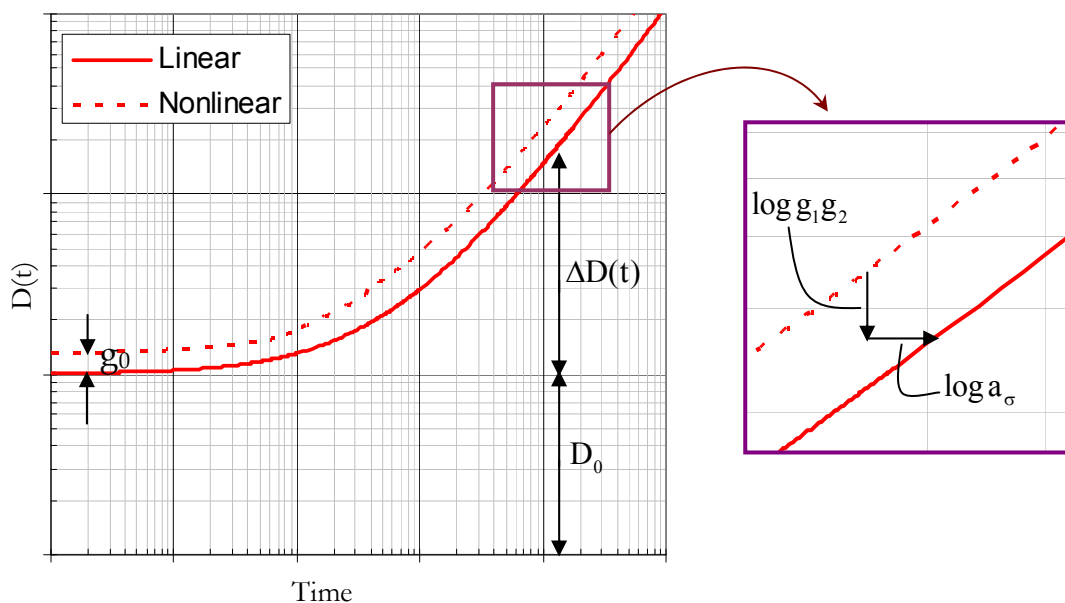


Figure 6-1 Graphical illustration for obtaining Schapery nonlinear parameters from the transient component of creep compliance curve

Figure 6-1 graphically illustrates the vertical and horizontal shifting of the creep curve to obtain the nonlinear parameters $a_\sigma(\sigma)$, $g_0(\sigma)$ and $g_1(\sigma)g_2(\sigma)$. In a nut shell, with a series of single step creep tests at different stress levels, the nonlinear parameters $g_0(\sigma)$, $a_\sigma(\sigma)$ and the product of g_1 and g_2 can be determined. To determine the nonlinear parameters g_1 and g_2 separately additional two steps creep tests are required (Figure 6-2).

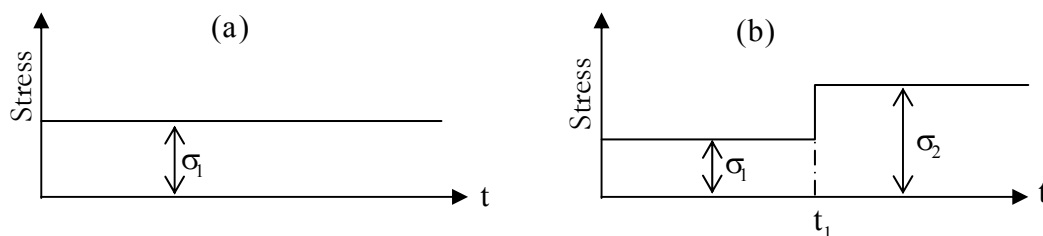


Figure 6-2 Tests required to obtain Schapery's nonlinear model parameters; (a) single step creep test, (b) two step creep test

The stress signal in a two step creep test is given by:

$$\sigma(t) = \sigma_1 H(t) + (\sigma_2 - \sigma_1)H(t - t_1) \quad 6-7$$

Substituting Equation 6-7 into Equation 6-1 the strain response for $t > t_1$ is given by:

$$\varepsilon(t) = g_0(\sigma_2)D_0\sigma_2 + g_1(\sigma_2) \left[g_2(\sigma_1)\sigma_1\Delta D \left[\frac{t_1}{a_\sigma(\sigma_1)} + \frac{t-t_1}{a_\sigma(\sigma_2)} \right] + \{g_2(\sigma_2)\sigma_2 - g_2(\sigma_1)\sigma_1\} \Delta D \left[\frac{t-t_1}{a_\sigma(\sigma_2)} \right] \right] \quad 6-8$$

If σ_2 is set to zero, which is equivalent to allowing the material to recover, the nonlinear parameters corresponding to the zero stress would equal unity; $g_1(\sigma_2) = g_2(\sigma_2) = a_\sigma(\sigma_2) = 1$. Equation 6-8 then reduces to:

$$\varepsilon(t) = g_2(\sigma_1)\sigma_1 \left[\Delta D \left[\frac{t_1}{a_\sigma(\sigma_1)} + t - t_1 \right] - \Delta D[t - t_1] \right] \quad 6-9$$

From Equation 6-9, with a known a_σ from the single step creep test data, the function $g_2(\sigma_1)$ can be determined. The second function, $g_1(\sigma_1)$, can then be determined with a known $g_2(\sigma_1)$ and the known product $g_1(\sigma_1)g_2(\sigma_1)$, which is determined previously in Equation 6-5. Here it becomes evident that the separation of the nonlinear parameters $g_1(\sigma_1)g_2(\sigma_1)$ necessitates response data from the recovery phase of a creep test.

6.2.1 Parameters From Frequency Domain Response Data

From the discussion in the previous section it is understood that the nonlinear parameter determination requires data from time domain creep experiments. However, the major part of the experimental investigation in this research is carried out in the frequency domain. To obtain the relevant nonlinear parameters, the time domain creep compliance curves of the materials need to be determined first. In order to obtain the time domain compliance curves the approach adopted in this research utilizes the frequency-time domain inter conversion methods. Similar approaches were also used in literature [3]. In performing the inter conversion process, the generalized Burgers' model was utilized. After the creep compliance curves in time domain were obtained, the nonlinear parameters were determined using the procedure outlined in the previous sections. The following steps explain the procedure involved in obtaining the nonlinear parameters at various temperatures:

- From frequency domain data, loss and storage compliance information at various shear stress levels is obtained.
- The loss and storage compliance data for each shear stress level are described using the Generalized Burgers' model. The model fitting procedure explained in Section 5.4.1 can be used.
- Step two is repeated for all temperatures.
- For each shear stress level at the various temperatures, the corresponding generalized Burgers' parameters, which are determined in step two, are used to generate the time domain creep compliance curve. For this purpose the relation given in Section 5.4.2 is used.
- The creep compliance curves are then used to determine the nonlinear model parameters following the method discussed in the previous section.

It should be noted that the creep compliance curves that are determined from the frequency domain data provide only information on the loading part of compliance curve. As discussed in Section 6.2, this material information can be used to determine the product of the nonlinear parameters $g_1(\sigma)g_2(\sigma)$. To separate the nonlinear parameters, data from the creep recovery phase is required, which cannot be obtained from the frequency domain data. Additional creep-recovery tests to separate the nonlinear parameters were not performed in this work. This will in turn dictate the choice of the numerical implementation technique that is to be adopted for this study. Details for the selected numerical approach will be dealt with later in the numerical formulation section. First the nonlinear parameter determination for the binders is presented.

6.3 Model Parameters for the Binders

In this section the nonlinear parameters for the binders are presented. To illustrate the parameter determination procedures, the mortar creep compliance curves at various temperatures have been used. Figure 6-3 presents the mortar's creep compliance curves for various shear stress levels at 0°C.

Considering the transient component of the compliance curves, the nonlinear parameters a_0 and the product g_1g_2 for various shear stress levels can be determined based on Equation 6-5. Spread sheet programs such as Excel can be used to perform the shifting procedure. In this program the values of g_1g_2 and a_0 can continuously be adjusted manually in the spread sheet program until the creep curves from the higher shear stress level coincides with the linear viscoelastic creep curve. After reasonable fit is obtained, the solver function can be employed for further optimization. Figure 6-4 shows the coinciding creep compliance curves after vertical and horizontal shifting is performed.

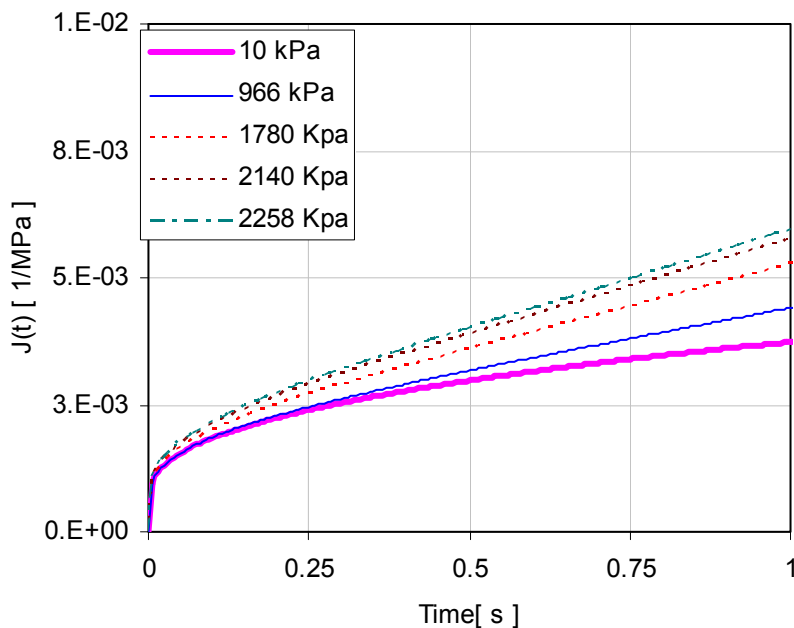


Figure 6-3 Creep compliance curves for various shear stress levels for the mortar at 0°C

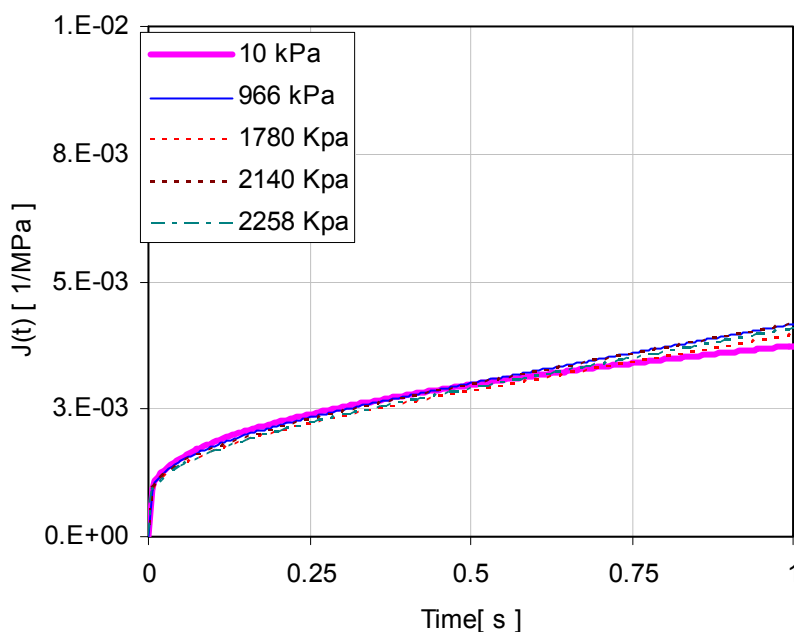


Figure 6-4 Coinciding creep compliance curves after vertical and horizontal shifting, mortar at 0°C

For the mortar data Figure 6-5 to Figure 6-10 present the creep compliance curves before and after shifting is performed at various temperatures. The values of the nonlinear parameters at all temperatures are given in Table 6-1.

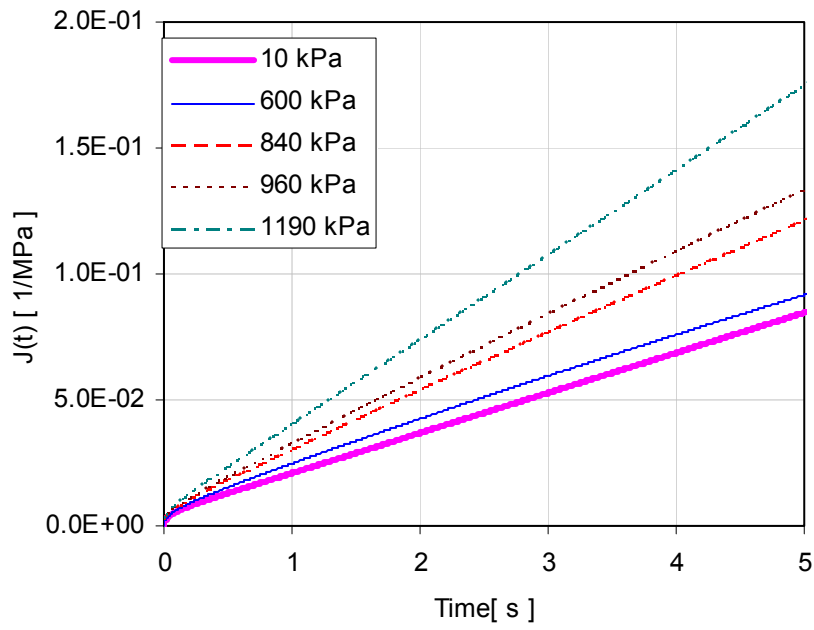


Figure 6-5 Creep compliance curves at different shear stress levels for the mortar at 10°C

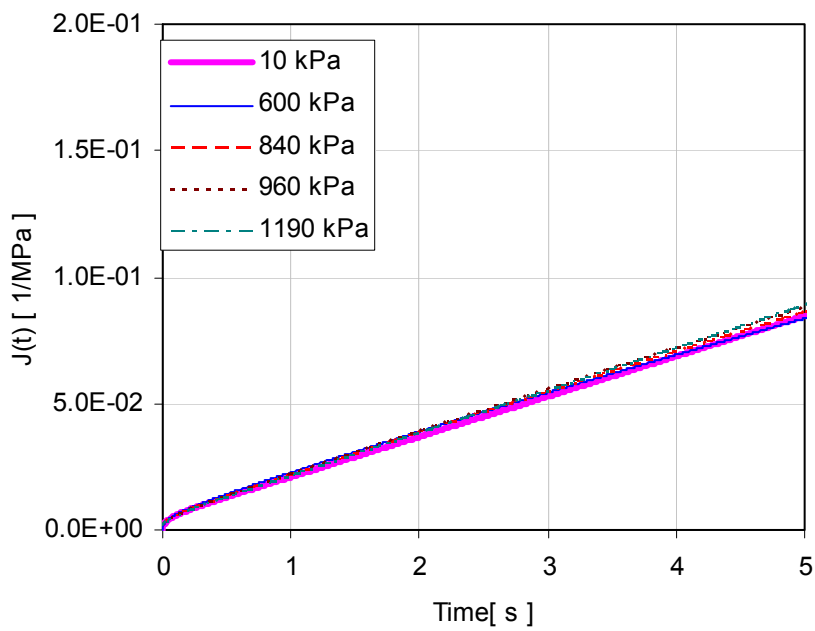


Figure 6-6 Coinciding creep compliance curves after vertical and horizontal shifting, mortar at 10°C

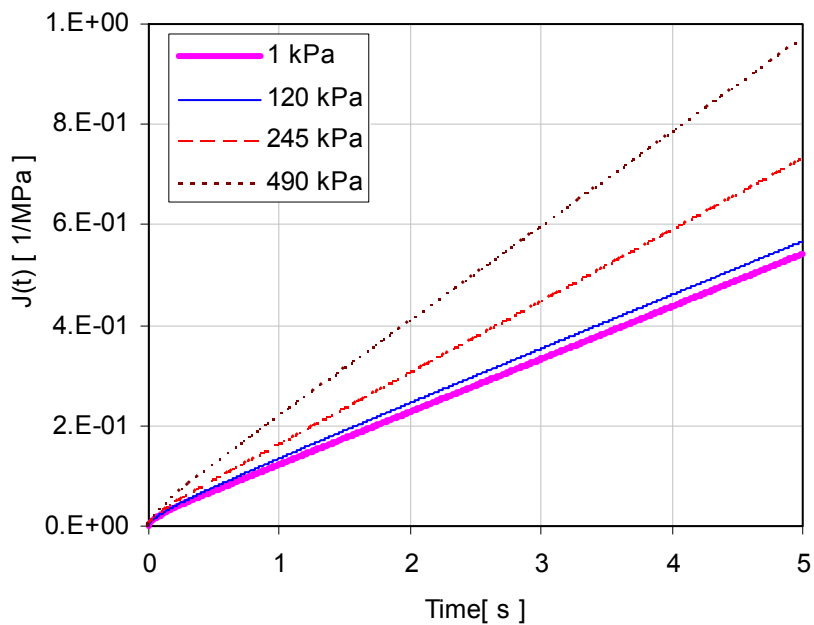


Figure 6-7 Creep compliance curves at different shear stress levels for the mortar at 20°C

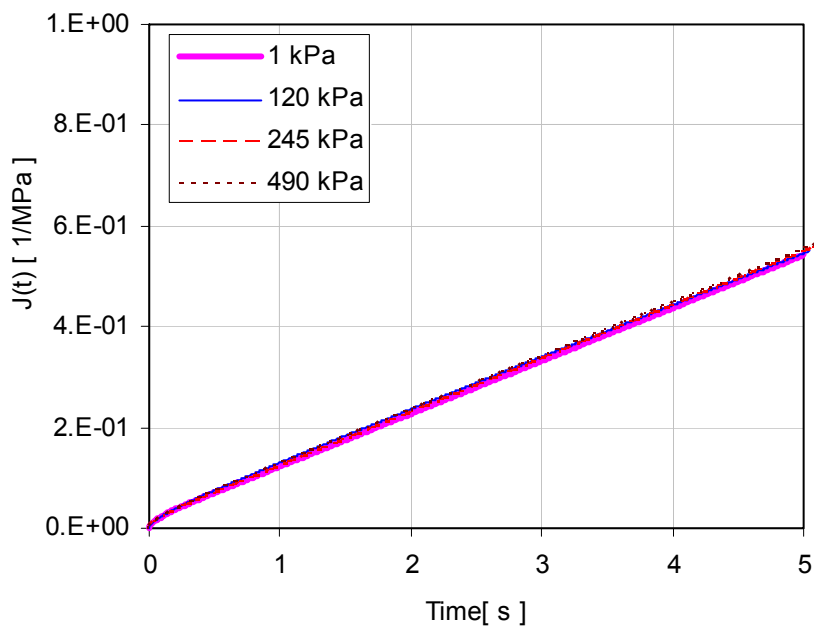


Figure 6-8 Coinciding creep compliance curves after vertical and horizontal shifting, mortar at 20°C

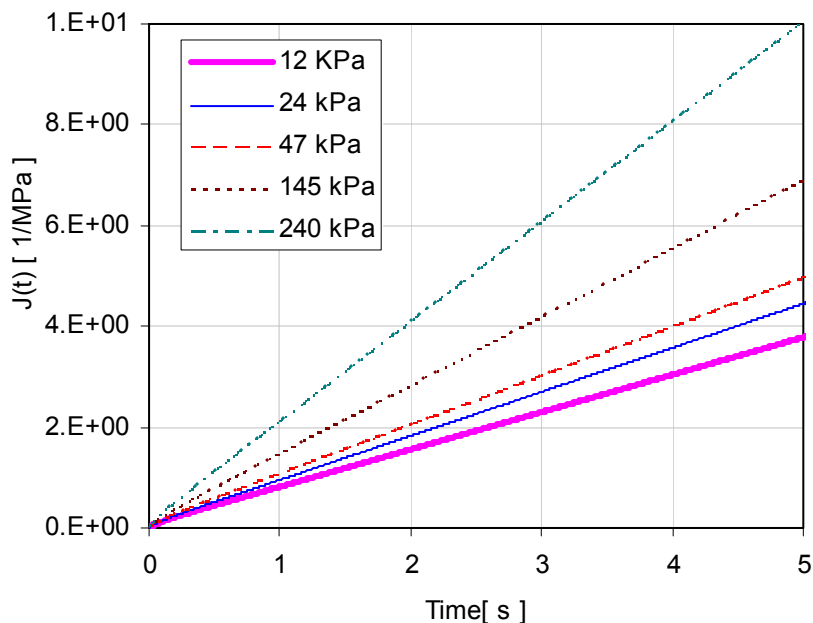


Figure 6-9 Creep compliance curves at different shear stress levels for the mortar at 30°C

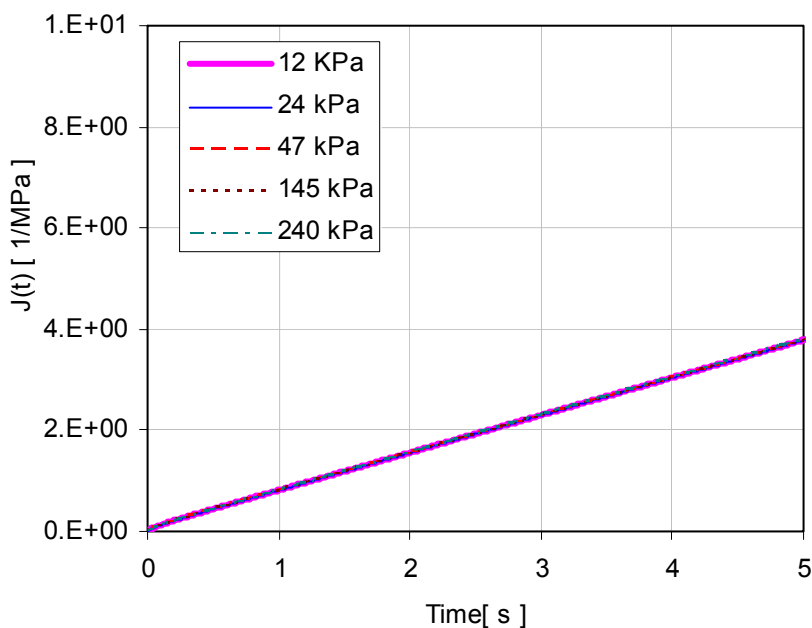


Figure 6-10 Coinciding creep compliance curves after vertical and horizontal shifting, mortar at 30°C

The above figures illustrate the parameter determination process for the nonlinear parameters a_σ and g_2 . The nonlinear parameter g_0 , which corresponds to the time independent (elastic) response component, need to be determined using similar procedure as shown in Figure 6-1. However, this has not been performed for two main reasons. First, accurate response data for the time independent response is obtained from very low temperatures, where the shear modulus approaches to the glassy modulus. As presented in Section 4.3.5

and Appendix C, good quality response data for the mortar was obtained only for -10°C and above. Hence, low temperatures response data is not available to accurately determine the nonlinear parameter g_0 . The second reason is because the nonlinear parameter g_0 is not of practical importance for mortar response modelling. This can be explained based on Figure 4-55 in Chapter 4. From that figure it can be seen that at low temperatures the shear stress level where nonlinear behaviour is observed for the mortar is very high (larger than 1 MPa). This implies that the value of the nonlinear parameter g_0 would remain unity at least for all shear stress levels less than 1 MPa. Since the maximum stress level at all higher temperatures is less than 1 MPa, the parameter g_0 can therefore be considered unity in modelling the response for all temperatures above -10°C .

6.3.1 Results and Discussions

The mortar data presented in Figure 6-4 to Figure 6-10 illustrate the process of nonlinear parameter determination. From the literature review in Chapter 2, it is known that frequency domain measurements provide material response information for short loading times. In Chapter 5, it has been shown using the time-temperature superposition principle that measurements conducted over a limited frequency window at various temperatures can be combined to form a master curve. For the selected reference temperature, the resulting master curve covers a wide range of frequencies. The time domain simulations that were performed in Chapter 5 also showed that for loading times of up to 10 ~ 15 seconds the frequency domain master curves can be used to simulate the time domain response. These discussions imply that in order to generate a time domain creep compliance curve covering a wide range of loading times, the frequency domain data need to cover a wide frequency window.

As explained in Chapter 4, for the measurements conducted at high shear stress levels, it was not possible to cover same shear stress ranges at the various temperatures. Because of this reason it was not possible to obtain a stress dependent master curve covering a wide range of frequencies/temperatures. Since a limited range of frequencies are covered at each temperature, the generated time domain creep compliance data would lack accurate material response information for long loading times. Hence, in the nonlinear model parameter determination at various temperatures, more attention was given to obtain best fits at short loading times. For the binders used in this research, analysis of the creep curve to loading times up to 5 seconds was chosen for temperatures above 10°C (see Figure 6-5 to Figure 6-10).

For the data at 0°C , as illustrated in Figure 6-3 and Figure 6-4, creep compliance curves with 1-second-long loading times were analyzed. When long loading times were considered, problems were encountered in obtaining coinciding creep curves by performing horizontal and vertical shifting. Since frequency domain data represents the short loading time response of a material, the creep

compliance data would be more accurate for short loading times and less accurate for high loading times. Based on this consideration the nonlinear parameter determination at 0°C was based on creep compliance curves with short loading times. The same procedure was followed for all other temperatures. For temperatures above 10°C, inclusion of the creep compliance data (with loading times of up to 5 seconds) in the nonlinear parameter determination did not affect the results. The nonlinear parameters were therefore determined based on the creep compliance data with loading times of 5 seconds.

To avoid repetition, the individual plots showing the parameter determination process for other binders are not presented. However, the nonlinear parameters at the various temperatures for all the binders are given in Table 6-1, Table 6-2 and Table 6-3. As discussed in the previous paragraph, the nonlinear parameter g_0 takes a value of unity for all the binders. Hence, only the values of a_σ and g_1g_2 are given in the tables.

Table 6-1 Schapery's nonlinear parameters for mastic

		0°C			
Stress [kPa]	50	668	1068	1268	
g_1g_2 [-]	1	1.06	1.1	1.15	
a_σ [-]	1	0.95	0.9	0.85	
		10°C			
Stress [kPa]	10	268	535	802	1070
g_1g_2 [-]	1	1.06	1.1	1.3	1.35
a_σ [-]	1	0.98	0.98	0.92	0.85
		20°C			
Stress [kPa]	2	200	334	400	
g_1g_2 [-]	1	1.18	1.3	1.36	
a_σ [-]	1	0.94	0.86	0.82	
		30°C			
Stress [kPa]	1	20	24	40	
g_1g_2 [-]	1	1.18	1.25	1.30	
a_σ [-]	1	0.96	0.95	0.92	

Table 6-2 Schapery's nonlinear parameters for mortar

0°C					
Stress [kPa]	10	965	1780	2140	2258
$g_1 g_2$ [-]	1	1.05	1.1	1.12	1.2
a_σ [-]	1	0.98	0.72	0.70	0.72
10°C					
Stress [kPa]	10	600	840	960	1190
$g_1 g_2$ [-]	1	1.05	1.22	1.27	1.5
a_σ [-]	1	0.95	0.85	0.82	0.75
20°C					
Stress [kPa]	1	120	245	490	
$g_1 g_2$ [-]	1	1.03	1.22	1.47	
a_σ [-]	1	0.99	0.91	0.83	
30°C					
Stress [kPa]	1	24	47	145	240
$g_1 g_2$ [-]	1	1.12	1.21	1.52	1.6
a_σ [-]	1	0.95	0.92	0.83	0.6

Table 6-3 Schapery's nonlinear parameters for B70/100 binder

0°C					
Stress [kPa]	10	200	400	450	500
$g_1 g_2$ [-]	1	1.03	1.04	1.1	1.2
a_σ [-]	1	0.99	0.98	0.95	0.9
10°C					
Stress [kPa]	10	200	350	452	503
$g_1 g_2$ [-]	1	1.04	1.2	1.26	1.28
a_σ [-]	1	0.98	0.94	0.8	0.75
20°C					
Stress [kPa]	10	135	185	203	
$g_1 g_2$ [-]	1	1.15	1.25	1.31	
a_σ [-]	1	0.96	0.88	0.84	
40°C					
Stress [kPa]	2	22	30		
$g_1 g_2$ [-]	1	1.06	1.2		
a_σ [-]	1	0.98	0.95		

6.4 Numerical Formulation

To apply the Schapery nonlinear theory in numerical environments, the uniaxial form of the theory given in Equation 6-1 need to be incrementally formulated. In literature different numerical approaches are used to solve the nonlinear viscoelastic integral equations [1, 4-6]. The formulation given by Lai and Baker [4] is based on the assumption that the nonlinear stress-based parameters are constant over the time increment. A recent formulation [1, 3] incorporates the possible variation of the nonlinear stress-based parameters over the time increment. It has been reported that the latter approach allows larger time steps to be taken in performing simulations. Hence, a better convergence rate can be obtained.

Application of the recent numerical formulation requires the nonlinear parameters $g_1(\sigma)$ and $g_2(\sigma)$ to be known. As illustrated in the previous section, the experimental data in this research provide only the product of these two nonlinear parameters. The formulation given by Lai and Baker [4], with the assumption of constant nonlinear stress-based parameters over a time increment, require only the product of nonlinear parameters $g_1(\sigma)$ and $g_2(\sigma)$ to be known. It is therefore suitable for the data available in this research. As mentioned elsewhere [3], the difficulty with this approach is that convergence problems might occur when large time steps are taken. However, with small time steps the approach is expected to provide similar results.

For the reasons discussed above, the numerical formulation [4] with the assumption of constant nonlinear parameters over a time increment has been selected for this research. To provide better convergence in simulations, the iterative procedure at the material gauss points suggested elsewhere [1] has been incorporated. The details of the iterative procedure will be presented in the implementation work in Chapter 7. Here the one dimensional incremental formulation is presented.

6.4.1 One Dimensional Formulation

In the convolution integral given in Equation 6-1, the creep compliance behaviour of the material needs to be represented with suitable mathematical functions for numerical formulation. Application of MHS model in the integral formulation is complex. Furthermore, in performing computations with small time steps, which are essential in nonlinear runs, the use of MHS model would lead to a huge computational memory requirement. On the contrary linear spring-dashpot combination models are computationally efficient and they are widely used in nonlinear formulations [2].

Following the chosen numerical approach for this study, the transient component of the creep compliance $\Delta D(\psi)$ in the Schapery theory can be given by [4]:

$$\Delta D(\psi) = \sum_{n=1}^N D_n \left[1 - \exp\left(\frac{-\psi}{\tau_n}\right) \right] \quad 6-10$$

The parameters D_n and τ_n are obtained from experimental data. It is important to note that these values correspond to the various Kelvin-Voigt parameters in the generalized Burgers' model. Consistent with this approach, the nonlinear parameter determination work presented in Section 6.2.1 also utilized the generalized Burgers' model.

Since measurements in this work are all conducted in shear mode, the parameters obtained from the shear compliance curve correspond to the material parameters in shear mode (J_n and τ_n). Using the corresponding shear compliance notations, the shear strain $\gamma(t)$ for an applied shear stress, σ^S , can be obtained using Equation 6-1 as:

$$\gamma(t) = g_0 J_0 \sigma^S + g_1 \int_0^t \Delta J[\psi(t) - \psi(\tau)] \frac{d(g_2 \sigma^S)}{d\tau} d\tau \quad 6-11$$

$$\Delta J(\psi) = \sum_{n=1}^N J_n \left[1 - \exp\left(\frac{-\psi}{\tau_n}\right) \right]$$

Substituting the exponential form of the transient creep compliance into the integral form in Equation 6-11, the shear strain can be given as:

$$\gamma(t) = g_0 J_0 \sigma^S + \sum_{n=1}^N g_1 \int_0^t J_n \left[1 - \exp\left(\frac{-(\psi(t) - \psi(\tau))}{\tau_n}\right) \right] \frac{d(g_2 \sigma^S)}{d\tau} d\tau \quad 6-12$$

Which can be rewritten as:

$$\gamma(t) = \gamma^0(t) + \sum_{n=1}^N \gamma^n(t) \quad 6-13$$

where:

$$\gamma^0(t) = \sigma^S \left[g_0 J_0 + g_1 g_2 \sum_{n=1}^N J_n \right] \quad 6-14$$

$$\gamma^n(t) = -g_1 \int_0^t J_n \left[\exp\left(\frac{-(\psi(t) - \psi(\tau))}{\tau_n}\right) \right] \frac{d(g_2 \sigma^S)}{d\tau} d\tau$$

For an infinitesimal time step increment the integral in Equation 6-14 can be written as:

$$\begin{aligned} \gamma^n(t) = & -g_1 \int_0^{t-\Delta t} J_n \left[\exp\left(\frac{-(\psi(t) - \psi(\tau))}{\tau_n}\right) \right] \frac{d(g_2 \sigma^S)}{d\tau} d\tau \\ & - g_1 \int_{t-\Delta t}^t J_n \left[\exp\left(\frac{-(\psi(t) - \psi(\tau))}{\tau_n}\right) \right] \frac{d(g_2 \sigma^S)}{d\tau} d\tau \end{aligned} \quad 6-15$$

Since,

$$\exp\left(\frac{-(\psi(t) - \psi(\tau))}{\tau_n}\right) = \exp\left(\frac{-\Delta\psi}{\tau_n}\right) \exp\left(\frac{-(\psi(t) - \Delta\psi - \psi(\tau))}{\tau_n}\right)$$

the first integral in 6-15 can be rewritten as:

$$\begin{aligned} & g_1 \int_0^{t-\Delta t} J_n \left[\exp\left(\frac{-(\psi(t) - \psi(\tau))}{\tau_n}\right) \right] \frac{d(g_2 \sigma^S)}{d\tau} d\tau \\ = & g_1 \exp\left(\frac{-\Delta\psi}{\tau_n}\right) \int_0^{t-\Delta t} J_n \left[\exp\left(\frac{-(\psi(t) - \Delta\psi - \psi(\tau))}{\tau_n}\right) \right] \frac{d(g_2 \sigma^S)}{d\tau} d\tau \\ = & -\exp\left(\frac{-\Delta\psi}{\tau_n}\right) \gamma^n(t - \Delta t) \end{aligned} \quad 6-16$$

If for an infinitesimal time increment Δt the nonlinear functions; g_1 , g_2 and a_σ are assumed constant and σ^S is assumed to vary linearly [4], the second integral in Equation 6-15 can be evaluated as:

$$g_1 \int_{t-\Delta t}^t J_n \left[\exp\left(\frac{-(\psi(t) - \psi(\tau))}{\tau_n}\right) \right] \frac{d(g_2 \sigma^S)}{d\tau} d\tau = J_n g_1 g_2 \frac{\Delta \sigma^S \tau_n}{\Delta \psi} \left[1 - \exp\left(\frac{-\Delta\psi}{\tau_n}\right) \right] \quad 6-17$$

where $\Delta\psi = \Delta\psi(t) - \Delta\psi(t - \Delta t)$. Substituting Equation 6-16 and Equation 6-17 into Equation 6-15 one obtains:

$$\gamma^n(t) = \exp\left(\frac{-\Delta\psi}{\tau_n}\right) \gamma^n(t - \Delta t) - J_n g_1 g_2 \frac{\Delta \sigma^S \tau_n}{\Delta \psi} \left[1 - \exp\left(\frac{-\Delta\psi}{\tau_n}\right) \right] \quad 6-18$$

From Equation 6-13 the incremental shear strain can be obtained as:

$$\Delta\gamma(t) = \left[\Delta\gamma^0(t) + \sum_{n=1}^N \Delta\gamma^n(t) \right] \quad 6-19$$

Using the expressions given in Equation 6-18 and Equation 6-14 into Equation 6-19 the incremental formulation for the shear strain becomes:

$$\Delta\gamma(t) = \left[J^* \Delta\sigma^S + \sum_{n=1}^N \alpha_n \gamma^n(t - \Delta t) \right] \quad 6-20$$

where J^* and α_n are given by:

$$J^* = g_0 J_0 + g_1 g_2 \sum_{n=1}^N J_n \left[1 + \frac{\tau_n}{\Delta\psi} \left[\exp\left(\frac{-\Delta\psi}{\tau_n}\right) - 1 \right] \right]$$

$$\alpha_n = \exp\left(\frac{-\Delta\psi}{\tau_n}\right) - 1$$
6-21

The above numerical formulations, adopted from [4], allow computation of the incremental strain (Equation 6-20) for an applied incremental stress. In numerical computations, using Equation 6-18 the viscoelastic strain component $\gamma^n(t)$ needs to be updated at the end of each time increment.

In strain controlled FE environments, like ABAQUS, the incremental strain is forwarded to the numerical routine and the corresponding stress is computed. This implies that at the beginning of the time step, the current stress and the current nonlinear parameters cannot be directly obtained because the nonlinear parameters are functions of the current stress and vice versa. This demands a procedure where trial stress values are first taken and the correct stress is computed in an iterative procedure. Such algorithms have been incorporated in other applications of the nonlinear theory in recent works [1, 3]. In this work, a similar procedure has also been incorporated to obtain a correct stress state in an iterative way. The details of the iterative procedure and the 3D generalization of the numerical formulation will be presented in Chapter 7.

6.5 Summary of Findings

The main findings and remarks that can be drawn from the material presented in this chapter are summarized below.

- Schapery's nonlinear theory has successfully been used to describe the observed nonlinear behaviour of the binders.
- The nonlinear theory requires time domain creep compliance data for parameter determination.
- For parameter determination purposes, the creep compliance curves at various shear stress levels have been determined from frequency domain experimental data.
- Schapery's nonlinear parameters were determined from the creep compliance curves at various shear stress levels. The parameters were obtained by performing vertical and horizontal shifting of the transient component of the creep compliance curves using spread sheet program.
- From literature a suitable numerical formulation was adopted. In the formulation assumption of constant nonlinear parameters over an incremental time steps was made.

References

- [1]. Haj-Ali, R.M. and Muliana, A.H., *Numerical finite element formulation of the Schapery non-linear viscoelastic material model*. International Journal for Numerical Methods in Engineering, 2004. **59**(1): p. 25-45.
- [2]. Henriksen, M., *Nonlinear viscoelastic stress analysis--a finite element approach*. Computers & Structures, 1984. **18**(1): p. 133-139.
- [3]. Huang, C.-W., Masad, E., Muliana, A., and Bahia, H., *Nonlinearly viscoelastic analysis of asphalt mixes subjected to shear loading*. Mechanics of Time-Dependent Materials, 2007. **11**(2): p. 91-110.
- [4]. Lai, J. and Bakker, A., *3-D schapery representation for non-linear viscoelasticity and finite element implementation*. Computational Mechanics, 1996. **18**(3): p. 182-191.
- [5]. Masad, E. and Somadevan, N., *Microstructural Finite-Element Analysis of Influence of Localized Strain Distribution on Asphalt Mix Properties*. Journal of Engineering Mechanics, 2002. **128**(10): p. 1105-1114.
- [6]. Poon, H. and Ahmad, M.F., *A finite element constitutive update scheme for anisotropic, viscoelastic solids exhibiting non-linearity of the Schapery type*. International Journal for Numerical Methods in Engineering, 1999. **46**(12): p. 2027-2041.
- [7]. Schapery, R.A., *On the characterization of nonlinear viscoelastic materials*. Polymer Engineering & Science, 1969. **9**(4): p. 295-310.

7

Implementation into ABAQUS

In Chapter 5, the MHS and the generalized Burgers' models were used to describe the time and temperature dependent behaviour of bituminous binders within the region of the linear viscoelastic response. For time domain applications, the one dimensional numerical formulations for the models were also given. In this chapter, the one dimensional formulations that were obtained for the two response models will be generalized into 3D form and implemented in the commercially available FE package, ABAQUS. Various runs that were made for code validation purposes are presented. Application of the response models for the meso-mechanistic PA design tool has also been presented. The last sections of the chapter present the implementation of the Schapery nonlinear viscoelastic model into ABAQUS. The one dimensional numerical formulation of this theory was given in Chapter 6. Code verification runs and application in the 2D idealized PA design tool are presented. Effects of linear viscoelastic assumption on the PA design tool results are evaluated. Discussions and summary of the results are given at the end of the chapter.

7.1 Constitutive Law in 3D

7.1.1 General

The stress and strain at any point within a loaded body can be decomposed into its deviatoric (shear) and hydrostatic (volumetric) components. The deviatoric stress, σ_{ij}^d , and the deviatoric strain tensor, ϵ_{ij}^d , are defined as:

$$\sigma_{ij}^d = \sigma_{ij} - \frac{1}{3} \delta_{ij} \sigma_{kk}$$

$$\epsilon_{ij}^d = \epsilon_{ij} - \frac{1}{3} \delta_{ij} \epsilon_{kk}$$
7-1

where:

σ_{ij}^d = deviatoric stress

σ_{ij} = stress

$\sigma_{kk} = \sigma_{11} + \sigma_{22} + \sigma_{33}$

ε_{ij}^d = deviatoric strain

ε_{ij} = strain

$\varepsilon_{kk} = \text{volumetric strain } (\varepsilon_{11} + \varepsilon_{22} + \varepsilon_{33})$

δ_{ij} = kronecker delta (1 for $i=j$ and 0 for $i \neq j$)

For an isotropic linear elastic material with shear modulus G and bulk modulus K , the stress-strain relation can be expressed as:

$$\sigma_{ij}^d = 2G \cdot \varepsilon_{ij}^d \quad 7-2$$

$$\sigma_{ij}^v = \frac{\sigma_{kk}}{3} \cdot \delta_{ij} = K \cdot \varepsilon_{kk} \cdot \delta_{ij}$$

In the above notation the term σ_{ij}^v denotes the volumetric stress. Since the total stress is the sum of the deviatoric stress and the volumetric stress, the stress for an isotropic material can be generalized as:

$$\sigma_{ij} = \sigma_{ij}^d + \sigma_{ij}^v$$

$$\sigma_{ij} = 2G \cdot \left[\varepsilon_{ij} - \frac{1}{3} \varepsilon_{kk} \cdot \delta_{ij} \right] + K \cdot \varepsilon_{kk} \cdot \delta_{ij} \quad 7-3$$

$$\underline{\sigma} = G \cdot [M_G] \underline{\varepsilon} + K \cdot [M_K] \underline{\varepsilon}$$

where the stress vector $\underline{\sigma}$ and the strain vector $\underline{\varepsilon}$ are given by:

$$\underline{\varepsilon} = \{ \varepsilon_{11}, \varepsilon_{22}, \varepsilon_{33}, 2\varepsilon_{12}, 2\varepsilon_{23}, 2\varepsilon_{31} \}$$

$$\underline{\sigma} = \{ \sigma_{11}, \sigma_{22}, \sigma_{33}, \sigma_{12}, \sigma_{23}, \sigma_{31} \}$$

The matrices $[M_G]$ and $[M_K]$ in Equation 7-3 are six by six in size and are given by:

$$[M_G] = \begin{pmatrix} 4/3 & -2/3 & -2/3 & 0 & 0 & 0 \\ -2/3 & 4/3 & -2/3 & 0 & 0 & 0 \\ -2/3 & -2/3 & 4/3 & 0 & 0 & 0 \\ 0 & 0 & 0 & 1 & 0 & 0 \\ 0 & 0 & 0 & 0 & 1 & 0 \\ 0 & 0 & 0 & 0 & 0 & 1 \end{pmatrix} \quad \text{and} \quad [M_K] = \begin{pmatrix} 1 & 1 & 1 & 0 & 0 & 0 \\ 1 & 1 & 1 & 0 & 0 & 0 \\ 1 & 1 & 1 & 0 & 0 & 0 \\ 0 & 0 & 0 & 0 & 0 & 0 \\ 0 & 0 & 0 & 0 & 0 & 0 \\ 0 & 0 & 0 & 0 & 0 & 0 \end{pmatrix}$$

7.1.2 Shear and Volumetric Deformation Characteristics of Asphaltic Materials

The three dimensional formulation given in Equation 7-3 for elastic materials is also valid for viscoelastic materials. The formulation can therefore be used to generalize the one dimensional formulations obtained in the previous chapter to a three dimensional form. In relation to the material properties, two approaches are generally used for modelling viscoelastic materials:

- The first approach is to model both the shear and the volumetric deformation components as time dependent. In this approach a constant Poisson's ratio for the material is taken [1].
- The second approach is to model the shear deformation component of the material as time dependent while the volumetric deformation component is modelled time independent. In this case the Poisson's ratio of the material becomes time dependent [16].

For asphalt mixture materials literature has shown that for hydrostatic pressure in the range applied by the usual tire contact stresses, the time dependent deformation behaviour of the material is highly pronounced in shear than in volumetric component [3, 17]. Because of this, the second approach, with elastic bulk modulus and viscoelastic shear modulus, is usually used for modelling the response of asphalt concrete materials [16, 18]. Since bituminous binders are highly incompressible, the approach becomes more realistic for modelling the mortar behaviour. Hence in the 3D formulation presented in Equation 7-3, the time dependent behaviour will be applied only on the shear modulus, G ; the Bulk modulus, K , will be modelled as time independent (elastic).

7.2 MHS Model in 3D

The one dimensional form of the numerical formulation that was obtained in Chapter 5 can be generalized into three dimensional form using Equation 7-3. The commercially available FE package, ABAQUS, is developed for strain controlled environment, which means that for a forwarded incremental strain in the computation the resulting incremental stress is computed. The constitutive forms for the MHS model given in Equation 5-22 to Equation 5-25 in Chapter 5 are formulated to suit this purpose. The one dimensional formulations given in Equation 5-22 to Equation 5-25 can now be generalized into three dimensional forms as:

$$\begin{aligned}
\bar{\sigma}_{t+1} = & \left(\frac{\chi_G}{1+G_0 \cdot \chi_G} + \frac{\Delta t}{\eta_{3G}} \right)^{-1} \cdot ([M_G] \bar{\epsilon}_{t+1} - [M_G] \bar{\epsilon}_t^3) \\
& + \left(\frac{\chi_G}{1+G_0 \cdot \chi_G} + \frac{\Delta t}{\eta_{3G}} \right)^{-1} \cdot \left(\frac{1}{1+G_0 \cdot \chi_G} \left([M_G] \sum_{j=1}^N b_j(m_1) \bar{\epsilon}_{t+1-j}^1 + [M_G] \sum_{j=1}^N b_j(m_2) \bar{\epsilon}_{t+1-j}^2 \right) \right) \\
& + \left(\frac{\chi_K}{1+K_0 \cdot \chi_K} + \frac{\Delta t}{\eta_{3K}} \right)^{-1} \cdot ([M_K] \bar{\epsilon}_{t+1} - [M_K] \bar{\epsilon}_t^3) \\
& + \left(\frac{\chi_K}{1+K_0 \cdot \chi_K} + \frac{\Delta t}{\eta_{3K}} \right)^{-1} \cdot \left(\frac{1}{1+K_0 \cdot \chi_K} \left([M_K] \sum_{j=1}^N b_j(m_1) \bar{\epsilon}_{t+1-j}^1 + [M_K] \sum_{j=1}^N b_j(m_2) \bar{\epsilon}_{t+1-j}^2 \right) \right)
\end{aligned} \tag{7-4}$$

For the notations used to represent the strains in the parabolic and linear dashpots, reference can be made to Figure 5-3 in Chapter 5. In Equation 7-4 the terms $\bar{\sigma}_{t+1}$ and $\bar{\epsilon}_{t+1}$ refer to the stress and strain vector at the current time step. The term $\bar{\epsilon}_t^3$ refers to the strain vector in the previous time step for the linear dashpot element. The subscripts K and G are used for differentiating model parameters for volumetric and shear components. It is important to note that the formulation given in Equation 7-4 is for a general case where the shear and volumetric components of the material are considered to be time dependent. As discussed in the previous section, for modelling the response of bituminous mortars, the volumetric component can be considered elastic. Hence the time dependent components of the volumetric deformation from Equation 7-4 need to be taken out. This will be done at a later stage.

The three dimensional formulation shown in Equation 7-4 requires an update of the current strain in the linear dashpot. This can be performed using the current stress, $\bar{\sigma}_{t+1}$, and the linear dashpot strain in the previous time step, $\bar{\epsilon}_t^3$, as follows:

$$\bar{\epsilon}_{t+1}^3 = \frac{\Delta t^m}{\eta_{3G}} [C_J] \bar{\sigma}_{t+1} + \frac{\Delta t^m}{\eta_{3K}} [C_B] \bar{\sigma}_{t+1} + \bar{\epsilon}_t^3 \tag{7-5}$$

In addition, the strains in the parabolic dashpots ($\bar{\epsilon}_{t+1}^1$ and $\bar{\epsilon}_{t+1}^2$) need to be computed for storage. This would require the stress in the parabolic dashpots ($\bar{\sigma}_{t+1}^1$) to be known. The stress and the strain values in the parabolic dashpots at the current time step can be computed using the following expressions:

$$\begin{aligned}
\bar{\sigma}_{t+1}^1 &= \bar{\sigma}_{t+1} - G_0 [M_G] \cdot \bar{\epsilon}_{t+1}^1 - K_0 [M_K] \cdot \bar{\epsilon}_{t+1}^1 \\
\bar{\epsilon}_{t+1}^1 &= \frac{\Delta t^m}{\eta_{1G} \tau_{1G}^{m-1}} [C_J] \bar{\sigma}_{t+1}^1 + \frac{\Delta t^m}{\eta_{1K} \tau_{1K}^{m-1}} [C_B] \bar{\sigma}_{t+1}^1 - \sum_{j=1}^N b_j(m_1) \bar{\epsilon}_{t+1-j}^1 \\
\bar{\epsilon}_{t+1}^2 &= \frac{\Delta t^n}{\eta_{2G} \tau_{2G}^{n-1}} [C_J] \bar{\sigma}_{t+1}^1 + \frac{\Delta t^n}{\eta_{2K} \tau_{2K}^{n-1}} [C_B] \bar{\sigma}_{t+1}^1 - \sum_{j=1}^N b_j(m_2) \bar{\epsilon}_{t+1-j}^2
\end{aligned} \tag{7-6}$$

The matrices $[C_J]$ and $[C_B]$ are the shear compliance matrix and the bulk compliance matrix respectively and are given by:

$$[C_J] = \begin{pmatrix} 1/3 & -1/6 & -1/6 & 0 & 0 & 0 \\ -1/6 & 1/3 & -1/6 & 0 & 0 & 0 \\ -1/6 & -1/6 & 1/3 & 0 & 0 & 0 \\ 0 & 0 & 0 & 1 & 0 & 0 \\ 0 & 0 & 0 & 0 & 1 & 0 \\ 0 & 0 & 0 & 0 & 0 & 1 \end{pmatrix} \text{ and } [C_B] = \begin{pmatrix} 1/9 & 1/9 & 1/9 & 0 & 0 & 0 \\ 1/9 & 1/9 & 1/9 & 0 & 0 & 0 \\ 1/9 & 1/9 & 1/9 & 0 & 0 & 0 \\ 0 & 0 & 0 & 0 & 0 & 0 \\ 0 & 0 & 0 & 0 & 0 & 0 \\ 0 & 0 & 0 & 0 & 0 & 0 \end{pmatrix}$$

In the above formulations a general approach with viscoelastic K and viscoelastic G is presented. Since for the mortar the volumetric deformation is modelled elastic, the time dependent volumetric deformation components in Equation 7-5 and Equation 7-6 need to be taken out, and as a result it can all be set to nil. This is equivalent to assigning a very high value to the model parameters corresponding to the time dependent volumetric response (η_{1K} , η_{2K} and η_{3K}). For elastic K and viscoelastic G , the above formulations given in Equation 7-4 to Equation 7-6 simplifies to:

$$\begin{aligned} \underline{\sigma}_{t+1} &= \left(\frac{\chi_G}{1 + G_0 \cdot \chi_G} + \frac{\Delta t}{\eta_{3G}} \right)^{-1} \cdot ([M_G] \underline{\varepsilon}_{t+1} - [M_G] \underline{\varepsilon}_t^3) \\ &+ \left(\frac{\chi_G}{1 + G_0 \cdot \chi_G} + \frac{\Delta t}{\eta_{3G}} \right)^{-1} \cdot \left(\frac{1}{1 + G_0 \cdot \chi_G} \left([M_G] \sum_{j=1}^N b_j(m_1) \underline{\varepsilon}_{t+1-j}^1 + [M_G] \sum_{j=1}^N b_j(m_2) \underline{\varepsilon}_{t+1-j}^2 \right) \right) \\ &+ K \cdot ([M_K] \underline{\varepsilon}_{t+1}) \end{aligned} \quad 7-7$$

$$\underline{\varepsilon}_{t+1}^3 = \frac{\Delta t^m}{\eta_{3G}} [C_J] \underline{\sigma}_{t+1} + \underline{\varepsilon}_t^3 \quad 7-8$$

$$\begin{aligned} \underline{\sigma}_{t+1}^1 &= \underline{\sigma}_{t+1} - G_0 [M_G] \cdot \underline{\varepsilon}_{t+1}^1 - K_0 [M_K] \cdot \underline{\varepsilon}_{t+1}^1 \\ \underline{\varepsilon}_{t+1}^1 &= \frac{\Delta t^m}{\eta_{1G} \tau_{1G}^{m-1}} [C_J] \underline{\sigma}_{t+1}^1 - \sum_{j=1}^N b_j(m_1) \underline{\varepsilon}_{t+1-j}^1 \\ \underline{\varepsilon}_{t+1}^2 &= \frac{\Delta t^n}{\eta_{2G} \tau_{2G}^{n-1}} [C_J] \underline{\sigma}_{t+1}^1 - \sum_{j=1}^N b_j(m_2) \underline{\varepsilon}_{t+1-j}^2 \end{aligned} \quad 7-9$$

These relations define the constitutive relation for the MHS model in 3D. Hereafter the process of FE implementation is discussed. Results from ABAQUS runs are also presented.

7.2.1 FE Implementation

In analyzing mechanical problems using continuum mechanics, three sets of equations (governing physical laws) are generally used. These are:

- Equations of motion
- Kinematic equations
- Constitutive equations

The kinematic equations are essential to describe motion and deformation of a body. The equation of motion determines the behaviour of the system; motions, balance of forces, moments etc. These two equations are common to all continuum materials, whether elastic or viscoelastic, linear or nonlinear. For details on these laws reference is made to various literature in solid mechanics [4, 19]. The third law, constitutive laws, which reflect the stress-strain relation for materials, are required to distinguish between different materials. It constitutes the mechanical properties, which are considered as the finger prints of the material. Since the equations of motion and kinematic equations are common to all materials, new constitutive laws can, therefore, be implemented in existing FE programs.

In this regard the commercially available FE package ABAQUS allows implementation of user defined material subroutines (UMAT). This subroutine is used to define the mechanical constitutive behaviour of the material. The FE implementation work in this thesis therefore involves scripting the UMAT code for the mechanical models.

7.2.2 Requirement for the UMAT

The requirements in writing the UMAT code are specified in Abaqus User Subroutines Reference Manual [2]. The UMAT subroutine is used to define the constitutive behaviour of a material. During simulation this subroutine will be called at all material calculation points (gauss points) of elements for which the material definition includes a user-defined material behaviour. The subroutine must provide the following:

- It must provide the material Jacobian matrix, $\partial\sigma_{ij}/\partial\varepsilon_{kl}$, for the constitutive model.
- It must also update the stresses and user state variables to their values at the end of the increment for which it is called.

For the MHS model, the relevant constitutive relations are given in Equation 7-4 to Equation 7-9. For these relations user subroutine code has been scripted using FORTRAN language. The subroutine for the MHS model performs the following functions;

- Updates the stress at the end of each time step increment using Equation 7-7.
- Updates strains for the linear dashpot using Equation 7-8.
- Computes and stores strain values for parabolic dashpots as state variables. Equation 7-9 is used for this purpose.
- Provides a material Jacobian matrix, called DDSDDDE.

Following the constitutive relation given in Equation 7-7 the following Jacobian, is specified in the UMAT:

$$\text{DDSDDDE} = \left[\frac{\chi_G}{1 + G_0 \cdot \chi_G} + \frac{\Delta t}{\eta_{3G}} \right]^{-1} \cdot [M_G] + K \cdot [M_K] \quad 7-10$$

In Equation 7-10, the coefficient K represents the bulk modulus of the material.

Various simulations were performed to validate the UMAT code. One method of validation was through analysis of problems with known analytical solutions. The other method utilized consists of performing simulation using the 2D PA design tool and comparing the UMAT simulation results with simulations obtained using the built-in material model in ABAQUS. For the later equivalent mechanical properties of the material for the built-in material model need to be determined. Details on the verification runs performed are presented in the next section.

7.2.3 UMAT Verification Runs

7.2.3.1 Parabolic Dashpot Response

In Chapter 5 the analytical solution to the parabolic dashpot response, with a block pulse load were used to illustrate the applicability of the numerical approach in one dimension. As part of the UMAT code validation in ABAQUS, the same problem is reproduced here using 3D models. For this purpose a simple 8 element cubical FE model was used (Figure 7-1). The boundary conditions are prescribed in such a way that a uniform stress is obtained throughout the element. For this purpose all the nodes in the bottom face of the cube are restrained for vertical displacement. In addition node number 1 (Figure 7-1) is restrained for movement in the two orthogonal direction in the horizontal plane. Node number 2 is also restrained in the horizontal plane in one direction. The applied load is a uni-axial block pulse load in the vertical direction.

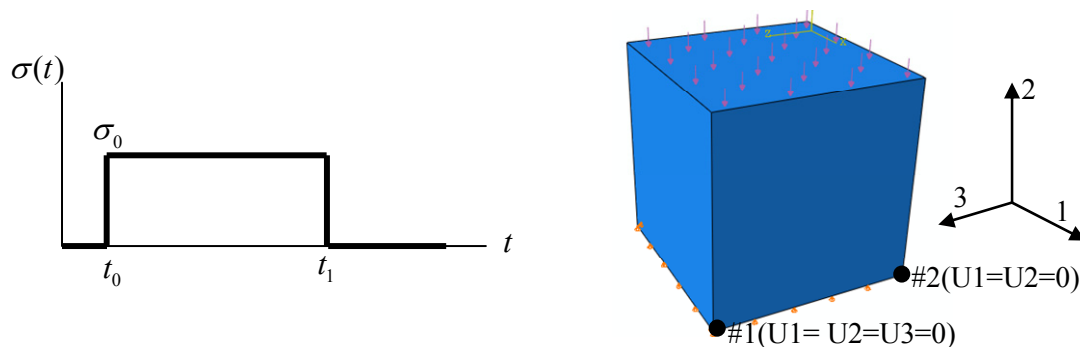


Figure 7-1 Block pulse load (left) and test FE model in ABAQUS (right)

In the UMAT the shear and the bulk modulus properties need to be specified. A bulk modulus value of 1000 MPa is arbitrarily assumed. To obtain the response of a single parabolic dashpot, the model parameters for the two springs, the linear dashpot and the second parabolic dashpot in the MHS model need to be assigned very high values. The equivalent MHS model parameters (in shear mode) representing a single parabolic dashpot response (with uni-axial properties $\eta=1$ MPa.s and $\tau=1$ s) are given in Table 7-1.

Table 7-1 MHS model parameters (equivalent to a single parabolic dashpot)

G_0	G_∞	τ_1	η_1	m	τ_2	η_2	n	η_3
[MPa]	[MPa]	[s]	[MPa]	[-]	[s]	[MPa]	[-]	[MPa]
0	1E10	1	1/3	0 to 1	1	1E10	0	1E10

The simulation results for the strain response of each parabolic dashpot, for various values of fractional coefficients m , were investigated. Similar to the one dimensional simulations performed in Chapter 5, the UMAT results are in good agreement with the analytical solutions. Figure 7-2 shows the analytical results plotted against the UMAT computed results for various parabolic dashpot coefficients.

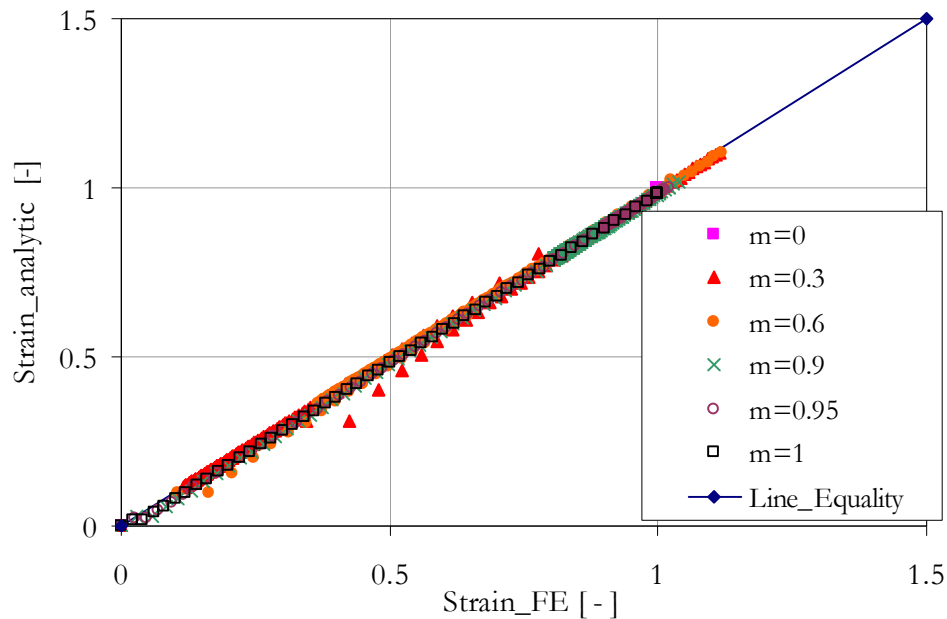


Figure 7-2 Parabolic dashpot responses (solid; analytical [14], dashed; UMAT)

To test further the accuracy of the UMAT code, with all response elements being active, back calculation of a known asphalt mixture response data were performed. Results are given in the next section.

7.2.3.2 AC Mixture Response

The back calculation procedure for AC mixture response involves simulating the frequency domain response data. In order to obtain the MHS model parameters, first the analytical form of the model was used to describe the frequency domain response data of the AC mixture. The model parameters were then used to back calculate the material stiffness and phase angle data by simulating a uni-axial displacement controlled test at selected frequencies. The simulations were performed using the cubical test block shown in Figure 7-1. The procedures used in model parameter determination and numerical back calculation are presented below.

A) Numerical Back Calculation

From frequency domain response data, the MHS model parameters for two AC mixtures were determined in Chapter 5 (Table 5-1). For the numerical back calculation performed in this chapter, the MHS model parameters corresponding to the RAP mixture were used. Back calculation was performed at various frequencies. Since the numerical code is developed in deviatoric and volumetric terms, the equivalent material properties for shear had to be determined from the mixture stiffness data. However, the Poisson's ratio of the material was not exactly known, and the bulk modulus K had to be assumed. In order to perform the back calculation with realistic values; based on literature, a reasonable assumption for the bulk modulus was made in such a way that the

Poisson's ratio receives a value between 0.3 and 0.4 in the frequency range of 1 to 10 Hz at a temperature of 10°C [16]. Consequently, a bulk modulus value of 15,000 MPa was used. For the other parameters, Equation 7-11 was used to convert the model parameters obtained from the (E^*) master curve to the shear equivalents for use in the UMAT code.

$$G = \frac{3EK}{9K - E} \quad \& \quad \eta_{iG} = \frac{\eta_i}{3} \quad 7-11$$

In Equation 7-11 the first expression is used to convert E_∞ and E_0 to G_∞ and G_0 respectively. The second expression is used to convert the η_i values for the parabolic and linear dashpot to the respective shear equivalents η_{iG} . Using the cubical FE model in ABAQUS, a sinusoidal varying displacement signal was applied. At each frequency a total of seven to eight load cycles were applied. In each load cycle 40 time steps were taken. The resulting stress signal was analyzed to back calculate the values of the modulus and the phase angle. These values were then compared with the analytical results. Figure 7-3 illustrates the quality of fit between the numerically back calculated and analytical values. Figure 7-4 also illustrates the variation of the dynamic Poisson's ratio corresponding to the estimated elastic bulk modulus value of 15,000 for the RAP mixture. Similar trends for the dynamic Poisson's ratio are also reported in literature [11].

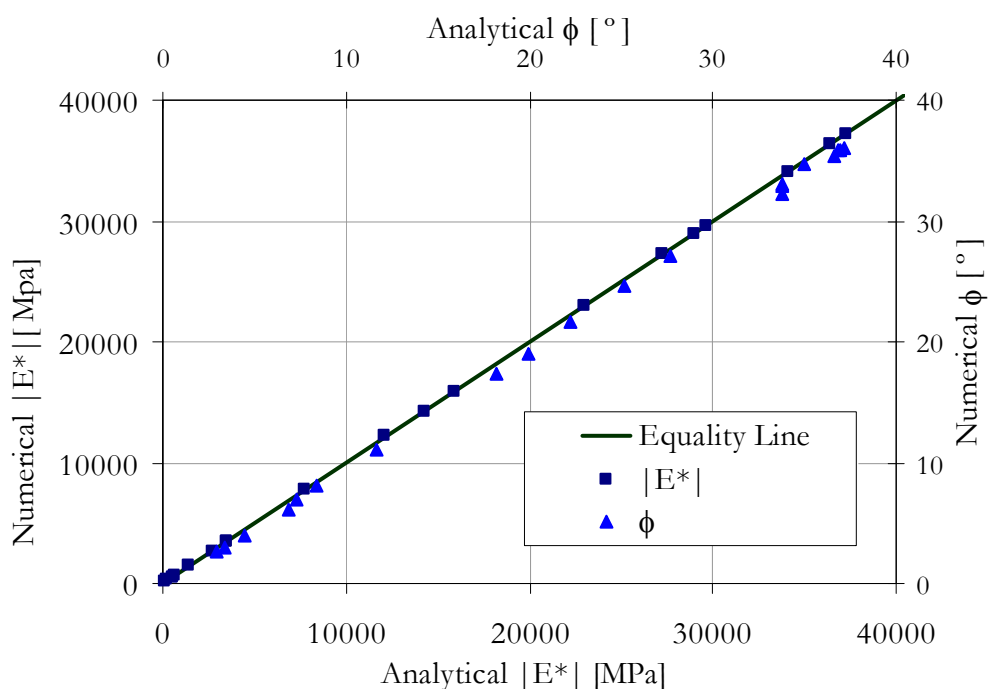


Figure 7-3 Results from numerical back calculation (RAP mixture data)

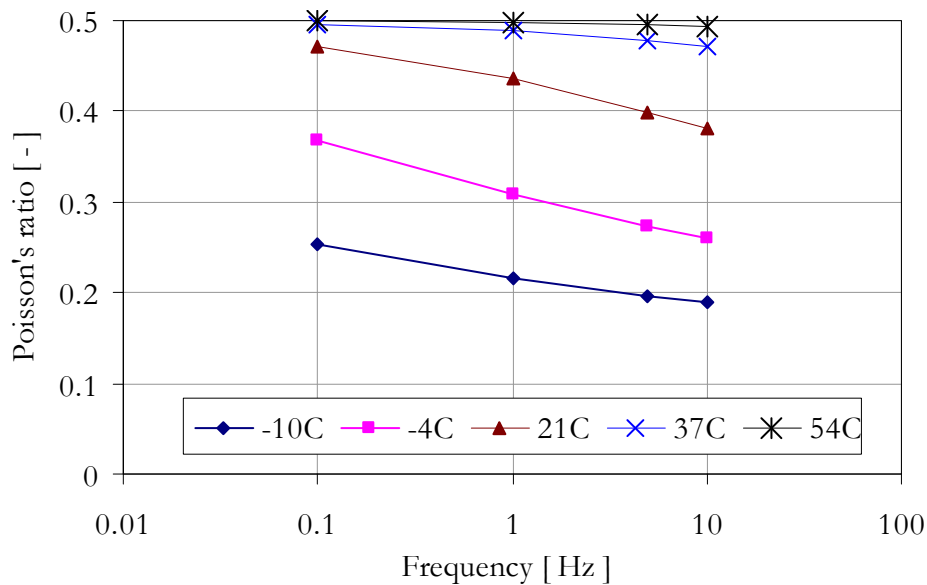


Figure 7-4 Indications on the variation of the Poisson's ratio (RAP mixture)

Figure 7-3 shows very good agreement between the numerically back calculated and the analytically obtained response data. In the next section the model application to a meso mechanics PA design tool is presented.

7.2.4 Application in Meso Mechanistic PA Design Tool

The MHS model was applied in the FE based meso mechanics design tool for PA. This tool, developed at Delft University of Technology [10, 12], provides insight into stresses and strains developed in bituminous mortar and interface layers within a PA mixture. The tool requires the geometry of the PA mixture, the surface loading and the behaviour of the component materials in the PA mixture to be specified. The structural model used in the design tool derives the geometry from the mixture volumetric composition, the surface loading from the contact stress distribution under a wheel and the material behaviour from laboratory tests. Details about the design tool are discussed elsewhere [9, 10, 12, 13]. The main purpose here is to illustrate the application of the MHS response model for modelling the mortar behaviour in the design tool. For this purpose the 2D-idealized PA model, illustrated in Figure 7-5, is utilized.

7.2.4.1 Geometry

The geometry of the PA structure is influenced by the material composition. For the size of the stone particles, the default equivalent size of 3.4 mm was taken. The mortar composition was determined based on a default mortar content of 4.5% by weight. A 20% void content in the mixture was also assumed. These values are within the practical range of the normal PA mixture composition used on the Dutch motorways.

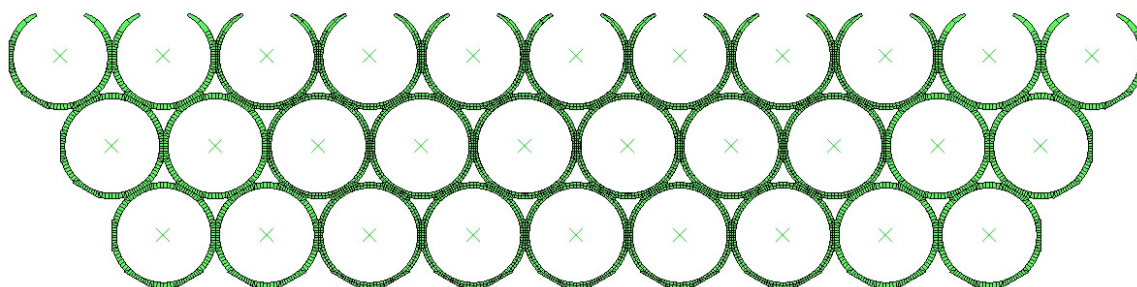


Figure 7-5 The 2D idealised PA model

7.2.4.2 Component Material behaviour

The tool requires the behaviour of the different components of the mixture to be specified. These include the stones, the thin interfacial zone (adhesive zone) and the bituminous mortar. The stones are modelled as rigid bodies. The interfacial zones are assigned a normal and a shear stiffness value. The mortar bridge between stone-stone areas is modelled as behaving viscoelastic. For modelling the mortar response, the only available material model in ABAQUS is the Prony series. Now that the MHS model is implemented in ABAQUS, the mortar response can be modelled with the MHS model. The MHS model parameters for a mortar at a reference temperature of 10°C have been given in Chapter 5 (Table 5-1). For comparison purposes, computations using the built-in material model have also been made. For this purpose the Prony series parameters were determined from the mortar master curve. The Prony series model fit to the mortar master curve data at 10°C is shown in Figure 7-6. Table 7-2 presents the Prony series model parameters at 10°C.

Table 7-2 Prony series model parameters for a mortar at 10°C (12 terms)

G_0 [MPa]	1749.2					
τ_i [s]	4.12E-5	1.7E-4	7.0E-4	2.9E-3	1.2E-2	4.9E-2
α_i [-]	3.66E-1	5.0E-2	2.13E-1	1.07E-1	1.1E-1	7.3E-2
τ_i [s]	2.0E-1	8.4E-1	3.5	14.3	58.8	242.4
α_i [-]	4.9E-2	2.1E-2	6.3E-3	2.0E-3	4E-4	2.2E-4

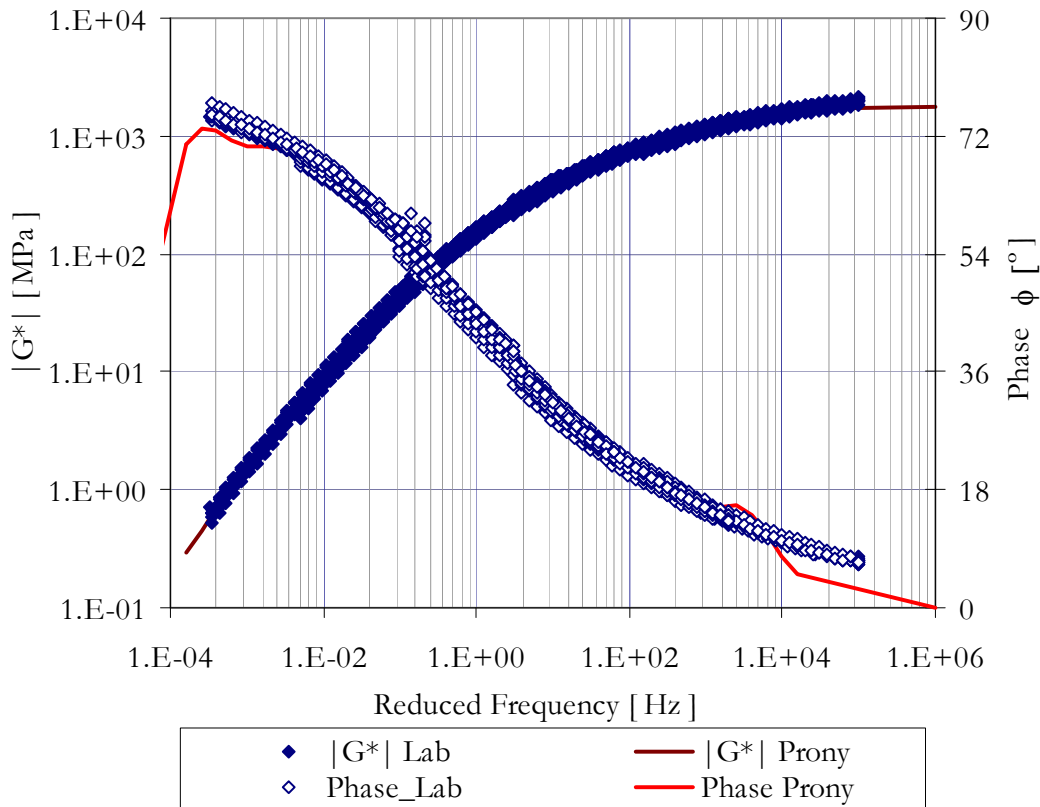


Figure 7-6 Prony series fit (12 terms) to a mortar master curve ($T_{ref} = 10^{\circ}\text{C}$)

For the simulation made using the Prony series, a Poisson's ratio of 0.49 was used. A G_0 value of 1749 (see Table 7-2) was taken; this corresponds to a bulk modulus value of about 195,000 MPa. To allow time independent volumetric response in ABAQUS, all the time dependent Prony series parameters of the bulk modulus have been set to nil. For the adhesive zone default normal and shear stiffness values of 10,000 MPa/mm and 3000 MPa/mm were taken.

7.2.4.3 Surface Loading

In the PA model, surface loadings on individual stones are applied. This surface loading model is available to derive the loading in the vertical, longitudinal and transversal directions [11]. This model was derived from the contact pressure measurement data reported elsewhere [5]. Detailed information on the surface loading model can be found in literature [9, 10, 12, 13]. For this simulation input a contact pressure of 0.8 MPa was used.

7.2.4.4 Simulation Results

A 50 kN wheel load applied by a Good Year 425R65 super single tyre is used [9]. The width of the wheel patch for this commercial tyre equals 330 mm. For the assumed contact pressure of 0.8 MPa, the calculated length of the wheel patch becomes 190 mm. With these parameters, the wheel loads travelling at a speed of 80 km/h were simulated on the PA model. The built-in material model in ABAQUS (Prony series) and the UMAT code for the MHS were used to

perform the simulations. Results from the two material models were compared. Figure 7-7 shows selected nodes for analysis and impressions of the von Mises stress at the central area of the 2D idealised models.

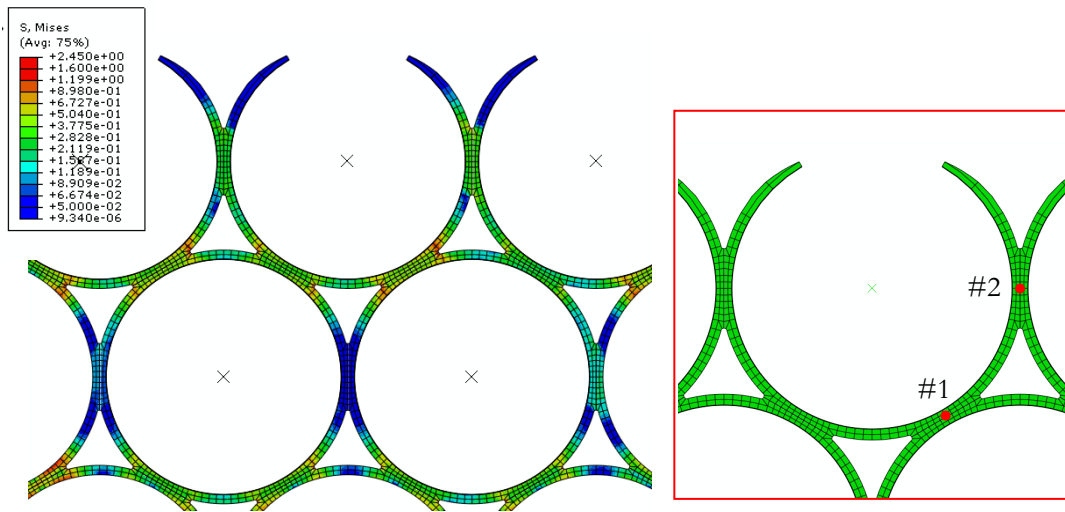


Figure 7-7 Impressions of the simulation result (left; the central part of the 2D idealised model, right; contact points used for analysis)

For the two mortar response models, i.e. the MHS and the Prony series models, Figure 7-8 and Figure 7-9 give impressions of the hysteresis loop that develops within the mortar in the PA mixture. The data corresponds to the stress-strain values computed in the vertical and horizontal direction at location 1 (see Figure 7-7). Similarly for location 2, the shear stresses and strains computed as a function of time using the two response models are presented in Figure 7-10 and Figure 7-11.

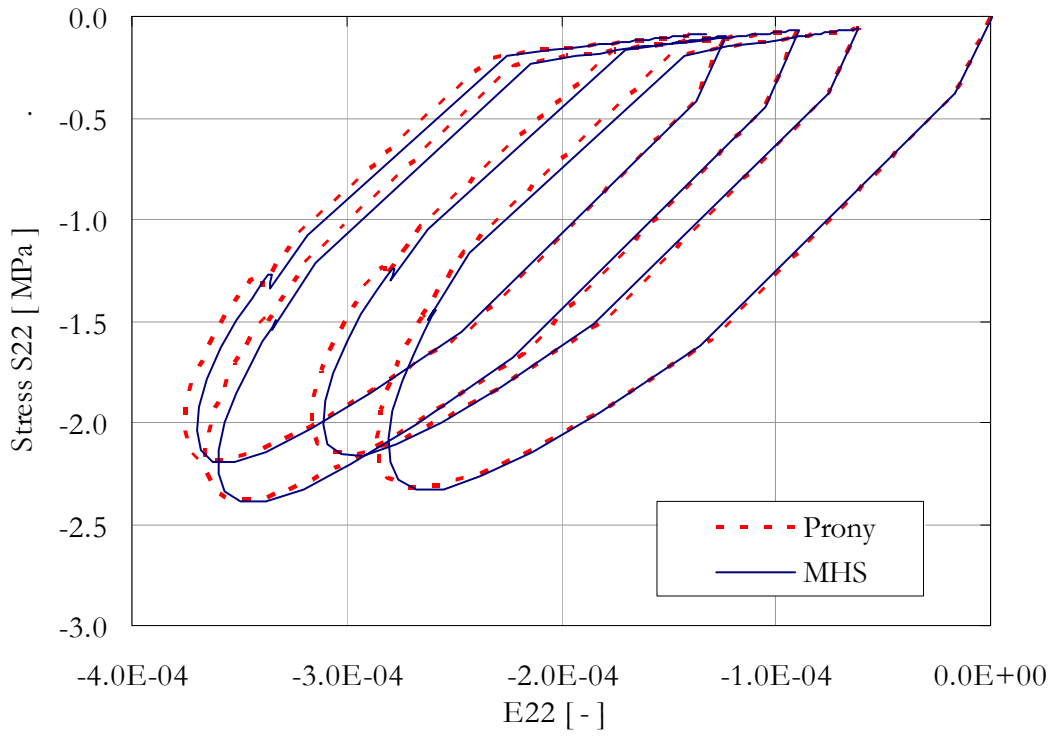


Figure 7-8 Hysteresis loop at contact number 1(S22-E22)

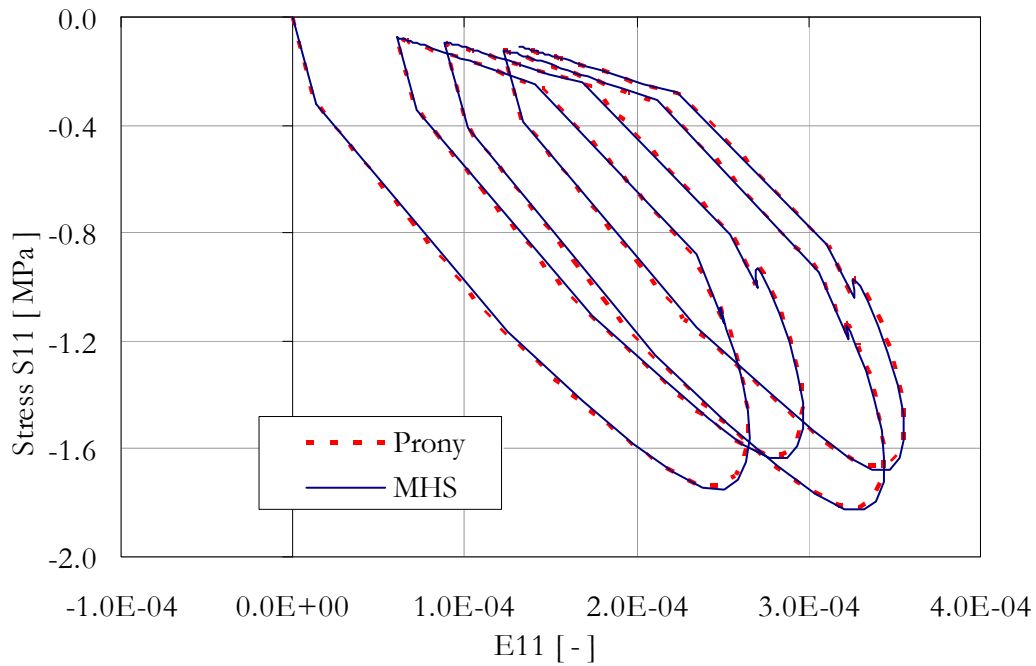


Figure 7-9 Hysteresis loop at contact number 1 (S11-E11)

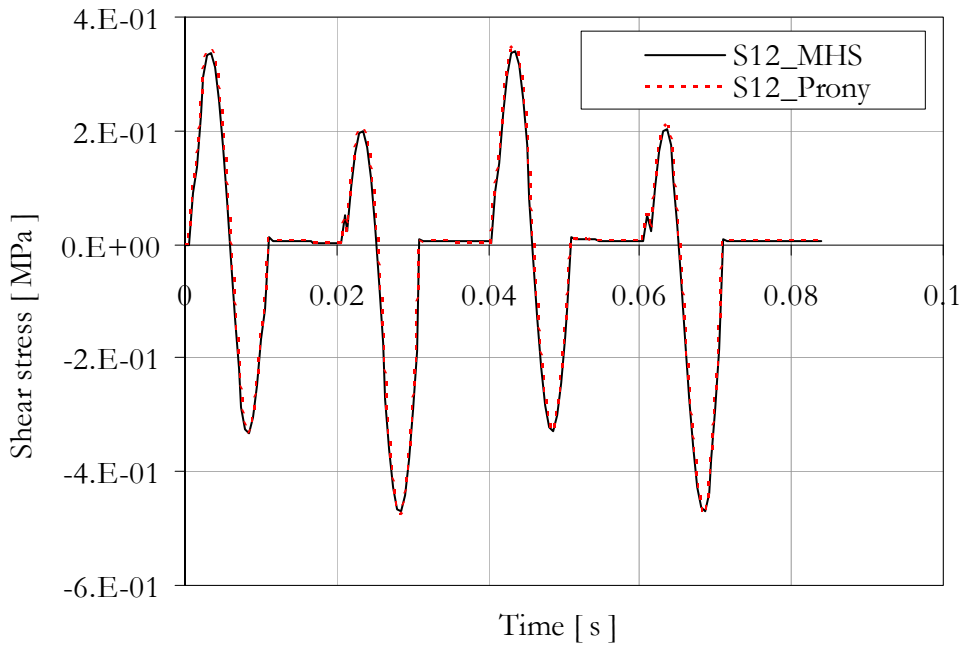


Figure 7-10 Comparison of shear stress (E12) for contact number 2

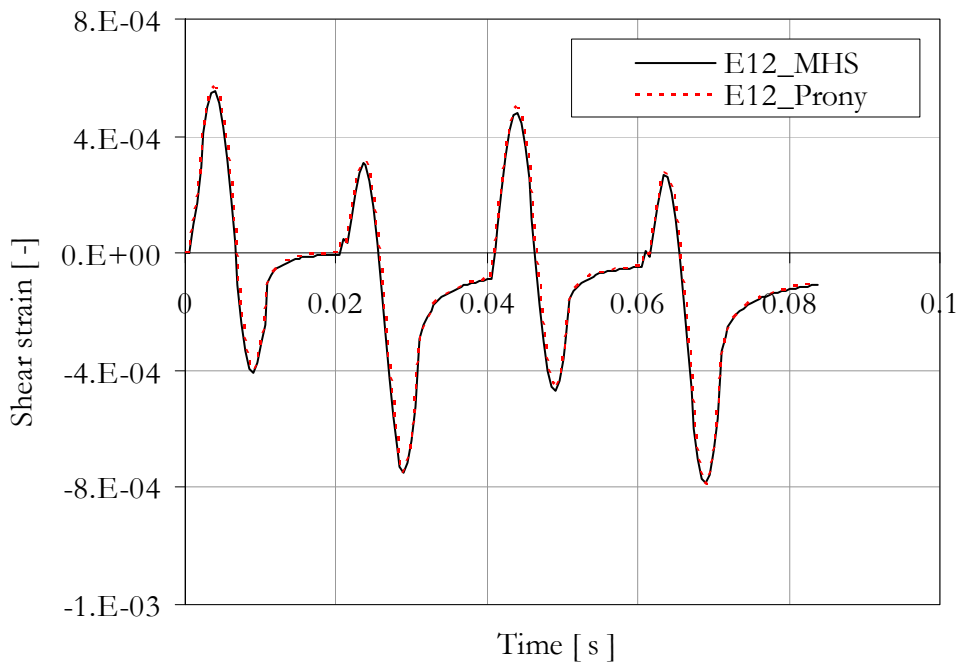


Figure 7-11 Comparison of shear strains (E12) for contact number 2

The above results show the applicability of the MHS model in numerical environments. The figures show that the results obtained from the MHS and Prony series model are very similar. In reference to Figure 7-6, it can be seen that the Prony series description of the master curve data in the intermediate frequency range is very good. However, poor fits are observed at the extreme low and high frequencies. On the other hand, an excellent description of the master curve over the complete frequency window has been obtained for the MHS model (Chapter 5). Nevertheless, the effect of the poor phase angle fit that

was observed for the Prony series model was not reflected in the numerical results. This can be explained in relation to the loading speed. The frequency of loading for a truck with a speed of 80 km/hr is in the range of 10 to 100 Hz. For this frequency range, both models have shown an excellent description of the master curve data (see Figure 7-6 above, and Figure 5-5 in Chapter 5). As a result, both response models are expected to provide very similar results.

Discussion

In Chapter 5, the MHS model demonstrated an excellent performance in describing the response of various materials over a wide frequency window. The model has also been considered very attractive for practical use due to the few number of model parameters. The expected serious limitation of the model was its computational memory requirement when used in a numerical environment.

Using the meso mechanistic PA design tool, the computational memory and time requirement of the model was evaluated. The finite element mesh consisted of 1261 nodes and 492 elements. In a single simulation 168 time steps were considered, and it was performed using a 2 GB RAM computer. In terms of computational time, it was observed that the MHS model requires 2.5 to 3 times as much computational time as the Prony series model. Memory problems were not encountered in the simulation. Taking into consideration the model accuracy in describing the material response over a wide range of frequency with only few model parameters, the model can, therefore, be considered very practical for modelling mortar response. Its performance in comparison to the generalized Burgers' model will further be assessed in the later sections.

7.3 Generalized Burgers' model in 3D

Following a similar approach as was used for the MHS model, the 2D constitutive form of the generalized Burgers' model given in Chapter 5 was generalized into 3D form using Equation 7-3. The incremental stress for the generalized Burgers' model can be obtained using:

$$\begin{aligned} \Delta \underline{\sigma}(t) = & \frac{1}{J^*} \left[[M_G] \Delta \underline{\varepsilon}(t) - [M_I] \frac{\Delta t}{\eta_0} (\underline{\sigma}(t - \Delta t)) + [M_G] \sum_{n=1}^N \underline{\varepsilon}^n(t - \Delta t) \left(\exp\left(\frac{-\Delta t}{\tau_n}\right) - 1 \right) \right] \\ & + K [M_K] \Delta \underline{\varepsilon}(t) \end{aligned} \quad 7-12$$

$$J^* = \left[J_0 + \frac{\Delta t}{2\eta_0} + \sum_{n=1}^N J_n - \sum_{n=1}^N \frac{J_n}{\Delta t} \tau_n \left[1 - \exp\left(\frac{-\Delta t}{\tau_n}\right) \right] \right]$$

In Equation 7-12 the terms $\Delta \underline{\sigma}$ and $\Delta \underline{\varepsilon}$ refer to the incremental stress and incremental strain vector for the current time step. The strain term $\underline{\varepsilon}^n$ is also a vector and it refers to the component of the incremental viscoelastic strain. The

parameters J_0 and η_0 are model parameters for the elastic spring and linear dashpot respectively in the generalized Burgers' model. The spring and dashpot parameters for the various Kelvin-Voigt elements are referred with J_n and η_n where $\tau_n = \eta_n J_n$.

Equation 7-12 requires that at each time increment the strain term $\underline{\varepsilon}^n$ for each Kelvin-Voigt element need to be updated. The incremental value for this strain term can be obtained using:

$$\Delta \underline{\varepsilon}^n(t) = [C_1] \underline{\varepsilon}^n(t - \Delta t) \left(\exp\left(\frac{-\Delta t}{\tau_n}\right) - 1 \right) + [C_J] J_n \frac{\Delta \underline{\sigma}}{\Delta t} \tau_n \left[1 - \exp\left(\frac{-\Delta t}{\tau_n}\right) \right] \quad 7-13$$

The matrices appearing in Equation 7-12 and Equation 7-13 are all six by six in size. The matrices $[M_G]$, $[M_K]$ and $[C_J]$ have been defined in the previous sections. The matrix $[C_1]$ is given as:

$$[C_1] = \begin{pmatrix} 2/3 & -1/3 & -1/3 & 0 & 0 & 0 \\ -1/3 & 2/3 & -1/3 & 0 & 0 & 0 \\ -1/3 & -1/3 & 2/3 & 0 & 0 & 0 \\ 0 & 0 & 0 & 1 & 0 & 0 \\ 0 & 0 & 0 & 0 & 1 & 0 \\ 0 & 0 & 0 & 0 & 0 & 1 \end{pmatrix}$$

Knowing the incremental stress values at each time increment, the total stress is updated with:

$$\underline{\sigma}(t) = \underline{\sigma}(t - \Delta t) + \Delta \underline{\sigma}(t) \quad 7-14$$

Similarly the value of the viscoelastic strain component, $\varepsilon^n(t)$, is updated as:

$$\underline{\varepsilon}^n(t) = \underline{\varepsilon}^n(t - \Delta t) + \Delta \underline{\varepsilon}^n(t) \quad 7-15$$

The constitutive relations given in Equation 7-12 to Equation 7-15 allow computation of the stress for an incrementally applied strain. These relations have been used to write the UMAT code for use in ABAQUS.

7.3.1 Requirement for the UMAT

In the case of the generalized Burgers' model, the UMAT code performs the following functions;

- The stress at the end of each time step increment is updated using Equation 7-14

- The strain terms for each Kelvin-Voigt element are updated using Equation 7-15
- A material Jacobian is provided (Equation 7-16).

Following the constitutive relation given in Equation 7-12 the following Jacobian, is specified in the UMAT. The Coefficient K represents the bulk modulus of the materials. The coefficient matrices $[M_G]$ and $[M_K]$ have been given in Section 7.1.1.

$$DDSDDE = \frac{1}{J^*} \cdot [M_G] + K \cdot [M_K] \quad 7-16$$

7.3.2 UMAT Verification Runs

Analogous to the approach used for the MHS model, routine simulations were performed to check the accuracy of the UMAT code. For brevity the routine back calculations performed using the master curve data are not presented. Results that are obtained from the application of the UMAT code to the meso mechanics model for PA is illustrated in the next section.

7.3.3 Application in Meso Mechanistic PA Design Tool

Application of the generalized Burgers' model to a meso mechanics PA design tool is illustrated. Similar to the simulations that were made using the MHS model; truck loads travelling at 80 km/hr were simulated. The model parameters for the generalized Burgers' model and MHS model at 10°C have been given in Chapter 5 (Table 5-6 and Table 5-1). Considering the stone particle located at the centre of the 2D idealized model, the resulting stress and strain signals in the mortar were analyzed. These results were compared with the stress/strain signals obtained in the previous section using the MHS model.

As discussed in Chapter 5, the two models can describe the master curve data for wide frequency window. For loading rates corresponding to a speed of 80 km/hr, both response models describe the experimental data very well. One can, therefore, reasonably expect close results from the finite element simulation. Figure 7-12 to Figure 7-16 illustrate the excellent agreement between the generalized Burgers' and MHS model simulation results. The contact locations 1 and 2 were illustrated in Figure 7-7.

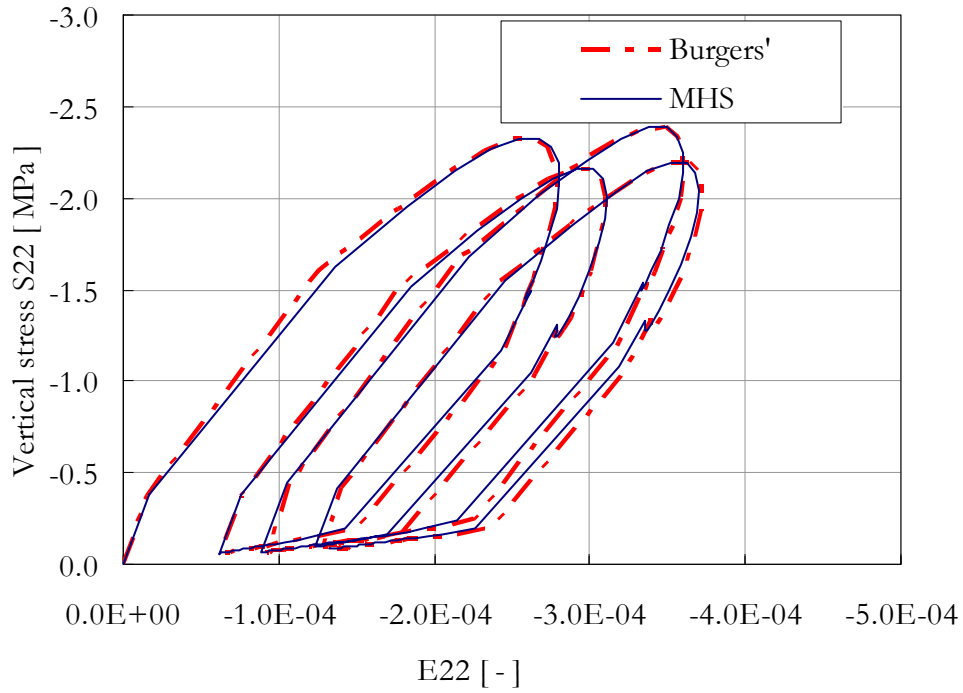


Figure 7-12 A Hysteresis loop for contact number 1(MHS and generalized Burgers' model)

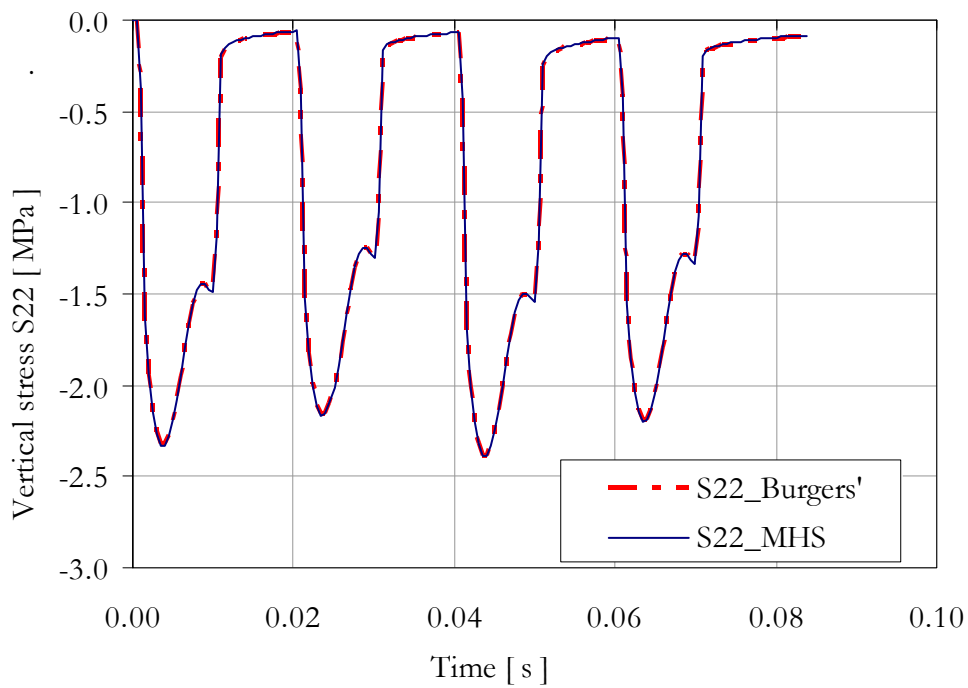


Figure 7-13 Comparison of vertical stress (S22) for contact number 1

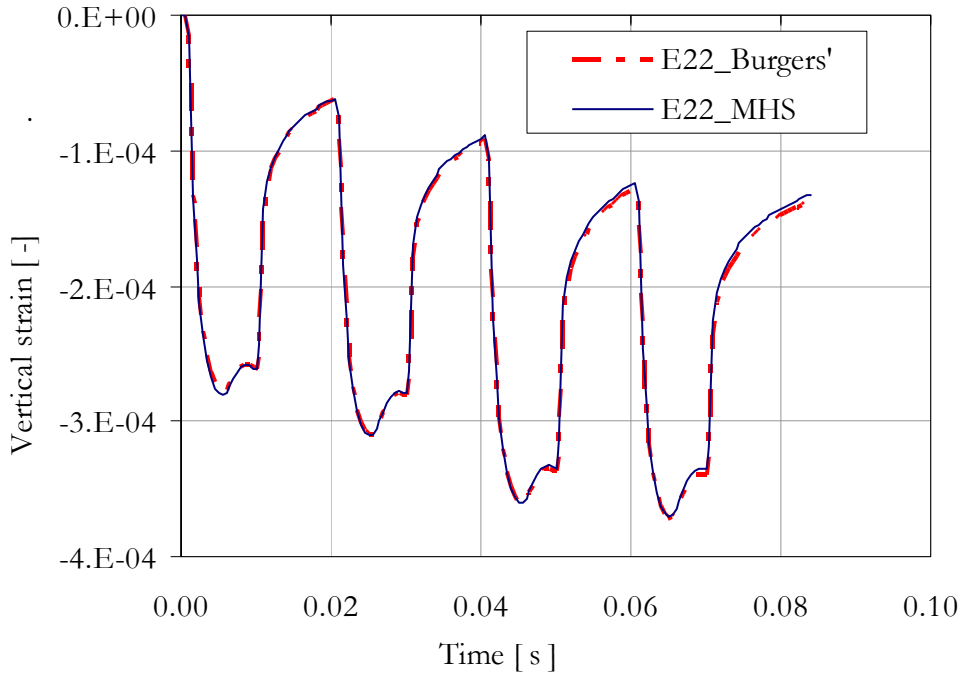


Figure 7-14 Comparison of vertical strains (E22) for contact number 1

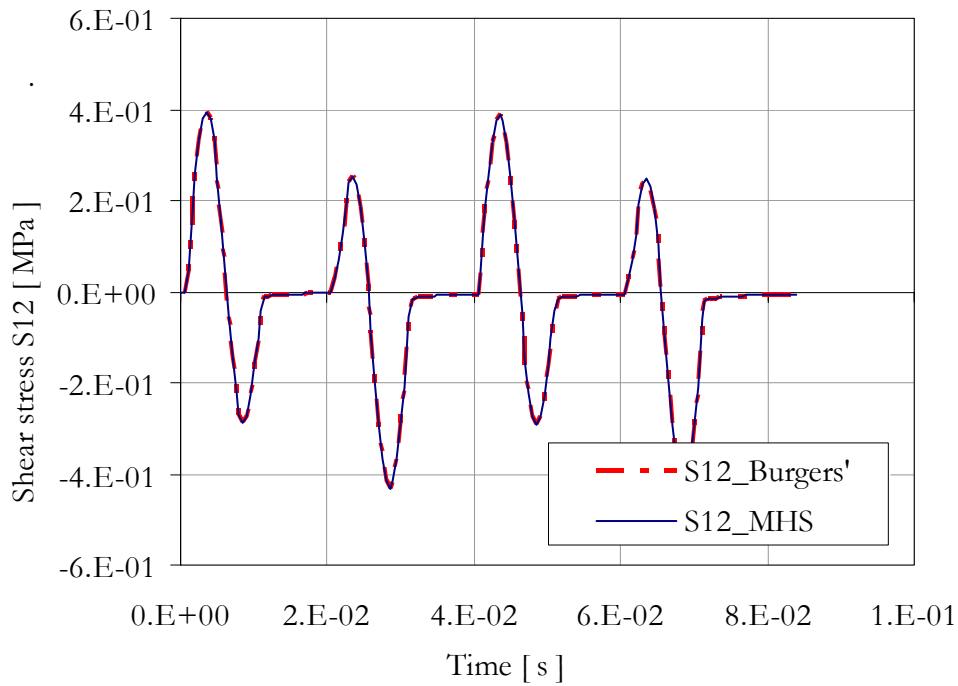


Figure 7-15 Comparison of shear stress (E12) for contact number 2

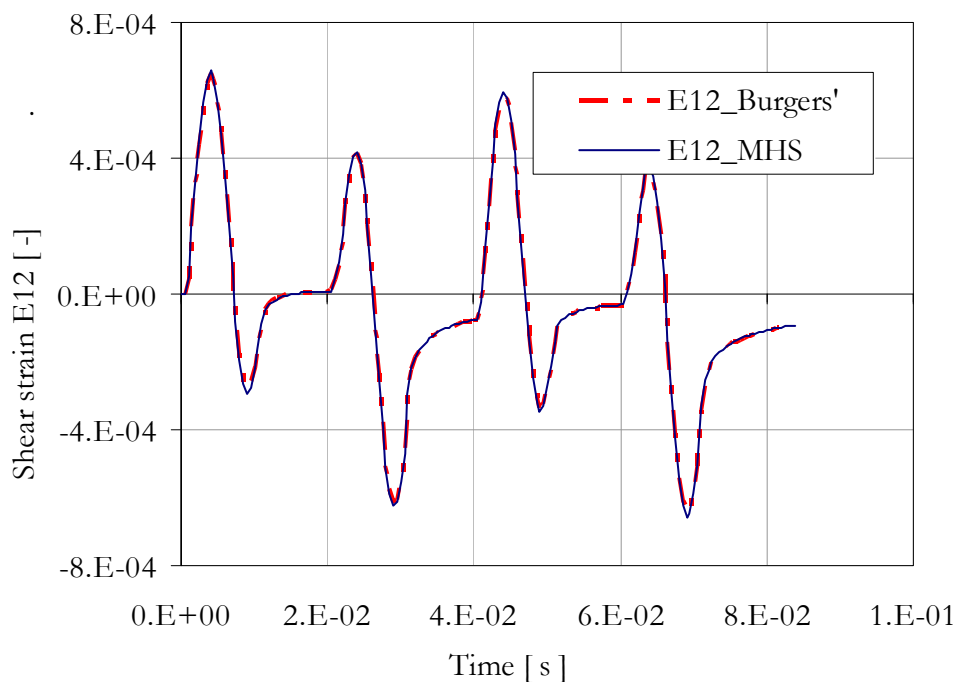


Figure 7-16 Comparison of shear strains (E12) for contact number 2

7.3.3.1 Remarks

The results presented in Figure 7-12 to Figure 7-16 show that the numerical outputs from the generalized Burgers and the MHS UMAT codes are very similar. As discussed in Chapter 5, comparably good fits to the mortar master curve data were obtained for both models (Figure 5-4 and Figure 5-26). The good quality of fit to the experimental data in the case of the generalized Burgers' model was achieved by using a number of Kelvin-Voigt elements (12 terms in this particular case). This has resulted in a total of 26 model parameters for the Burgers' model. A relatively poor fit was observed for the phase angle at the extreme low frequency regions. For the MHS model, a better quality of fit for the whole frequency range was obtained with only 7 model parameters.

In the case of the MHS model, the accuracy of the model and the few number of model parameters makes the model very attractive for practical use. In terms of computational time the generalized Burgers' model requires less time than the MHS model. Based on the simulations performed using the 2D idealized PA design tool, the advantage of the generalized Burgers' model in terms of computational time is about 1.5 times faster. As the model size grows, the computational memory and time required by the MHS model would further increase which makes the use of the generalized Burgers' model more efficient. For application in the PA design tool, even though the MHS model requires a little more computational time, it can still be considered very practical model for use due to its added advantage in accuracy and required number of model parameters.

7.4 Nonlinear Viscoelastic Model in 3D

In Chapter 6, the Schapery nonlinear theory was used for modelling the nonlinear viscoelastic behaviour of the binders. Due to the suitability and computational efficiency of the spring-dashpot combination models, the creep behaviour of the material in Schapery's nonlinear theory is usually represented with the generalized Burgers' model. Following this approach, the one dimensional numerical formulation of the theory was given in Chapter 6. In the formulation, if all the nonlinear parameters are set to unity, the formulation reduces to the case of the generalized Burgers' model in the linear viscoelastic mode. For the case of the MHS model, implementation of the model in the Schapery nonlinear theory is complex. Furthermore, due to its memory storage requirement the model application in nonlinear viscoelastic problems would require a very high computational memory. Therefore, the scope of the MHS model application in this thesis is limited to problems in the linear viscoelastic range. The 3D generalization of the Schapery nonlinear theory is presented in the next section.

7.4.1 Schapery Theory in 3D

7.4.1.1 Stress Indicator

The nonlinear parameters obtained in the previous chapter are based on one dimensional formulation. In this thesis, laboratory tests performed for parameter determination are in shear mode; as a result the nonlinear parameters were obtained as a function of shear stress. For three dimensional generalizations a stress level indicator needs to be chosen. An effective stress invariant called effective stress, $\hat{\sigma}$, also called von Mises stress, is used to account for the stress dependence behaviour of materials in 3D formulations [7, 14]. The effective stress $\hat{\sigma}$ is defined as:

$$\hat{\sigma} = \sqrt{\frac{3}{2} s_{ij} s_{ij}} \quad 7-17$$

where s_{ij} denotes the components of the deviatoric stress tensor:

$$s_{ij} = \sigma_{ij} - \frac{1}{3} \sigma_{kk} \delta_{ij} \quad 7-18$$

The indices denote directions ($i, j = 1..3$) and repeated indices denote summation.

It is important to note that the response data from the laboratory is obtained in pure shear. For pure shear, τ , the effective stress $\hat{\sigma}$ is equal to $\sqrt{3} \tau$. This relation is useful in incorporating the stress dependent behaviour of the material in the 3D formulation.

7.4.1.2 3D Formulation

Similar to the formulation used in the linear viscoelastic case, the total deformation within an isotropic body is decomposed into deviatoric and

volumetric components. The deviatoric and volumetric strains are denoted by $\varepsilon_{ij}^d(t)$ and $\varepsilon_{kk}(t)$ respectively. From the one dimensional formulation given in Chapter 6, the incremental shear strain, $\Delta\gamma(t) = 2\varepsilon_{ij}^d(t)$, corresponding to an incremental shear stress, $\Delta\sigma^S$, is given by:

$$\Delta\gamma(t) = 2\varepsilon_{ij}^d(t) = \left[J^* \Delta\sigma^S + \sum_{n=1}^N \alpha_n \gamma^n(t - \Delta t) \right] \quad 7-19$$

where J^* , α_n and $\gamma^n(t)$ are given by:

$$\begin{aligned} J^* &= g_0 J_0 + g_1 g_2 \sum_{n=1}^N J_n \left[1 + \frac{\tau_n}{\Delta\Psi} \left[\exp\left(\frac{-\Delta\Psi}{\tau_n}\right) - 1 \right] \right] \\ \alpha_n &= \exp\left(\frac{-\Delta\Psi}{\tau_n}\right) - 1 \\ \gamma^n(t) &= 2\varepsilon_{ij}^n(t) = g_1 \exp\left(\frac{-\Delta\Psi}{\tau_n}\right) \gamma^n(t - \Delta t) - J_n g_1 g_2 \frac{\Delta\sigma^S \tau_n}{\Delta\Psi} \left[1 - \exp\left(\frac{-\Delta\Psi}{\tau_n}\right) \right] \end{aligned} \quad 7-20$$

For time independent (elastic) volumetric response, the change in volumetric strain is given by:

$$\Delta\varepsilon_{kk}(t) = g_0 B_0 \frac{\Delta\sigma_{kk}}{3} \quad 7-21$$

Using Equation 7-1, the deviatoric and volumetric deformation components can be combined to obtain the following 3D formulation.

$$\Delta\varepsilon_{ij}(t) = J^* [C_J] \Delta\sigma_{ij} + \sum_{n=1}^N \alpha_n [C_I] \varepsilon_{ij}^n(t - \Delta t) + B g_0 [C_B] \Delta\sigma_{ij} \quad 7-22$$

The compliance matrices $[C_J]$, $[C_I]$ and $[C_B]$ have been given in section 7-2 and section 7-3. Using the 3D equivalent of the relation given in Equation 7-20, the strain component, $\varepsilon_{ij}^n(t)$, needs to be updated at the end of each time increment using the following equation:

$$\varepsilon_{ij}^n(t) = \exp\left(\frac{-\Delta\Psi}{\tau_n}\right) [C_I] \varepsilon_{ij}^n(t - \Delta t) - J_n g_1 g_2 \frac{\tau_n}{\Delta\Psi} \left[1 - \exp\left(\frac{-\Delta\Psi}{\tau_n}\right) \right] [C_J] \Delta\sigma_{ij} \quad 7-23$$

The above formulations allow computation of the incremental strain for a known incremental stress. However, the current stress and the current nonlinear parameters cannot be directly obtained because the nonlinear parameters are functions of the current stress and vice versa. This implies an

iterative procedure is required to obtain the correct stress and nonlinear parameters. For this purpose an iterative procedure at the material level is included. This procedure allows larger time steps to be taken and provided better convergence in numerical simulations [6, 8].

Iterative Procedure

In ABAQUS, strains are UMAT inputs and stresses need to be computed. The iterative procedure given below allows computation of the incremental strains (using Equation 7-22) based on the nonlinear parameters that are obtained using a trial stress value. Then, the error between the computed strain and the input strain is calculated. The error is minimized in an iterative way by adjusting the incremental stress until the computed strain and the input strain are within a specified error margin. The iterative method used to obtain the correct state of stress from a trial value is presented below.

To begin the iteration at a given time step, all the nonlinear parameters are assumed to be equal to the corresponding values from the previous time step. This implies at the beginning of each time increment; $\mathbf{g}_0^t = \mathbf{g}_0^{t-\Delta t}$, $\mathbf{g}_1^t \mathbf{g}_2^t = \mathbf{g}_1^{t-\Delta t} \mathbf{g}_2^{t-\Delta t}$ and $\mathbf{a}_\sigma^t = \mathbf{a}_\sigma^{t-\Delta t}$. Then using the stress equivalent relation of Equation 7-22, the trial stress can be obtained as:

$$\Delta\sigma_{ij}(\text{trial}) = \frac{1}{J^*} \left[[\mathbf{M}_G] \Delta\varepsilon_{ij}(t) - \sum_{n=1}^N \alpha_n [\mathbf{M}_G] \Delta\varepsilon_{ij}^n(t - \Delta t) \right] + \frac{1}{B \mathbf{g}_0} \cdot [\mathbf{M}_K] \Delta\varepsilon_{ij}(t) \quad 7-24$$

The parameter B denotes the bulk compliance of the material. All the coefficient matrices have been given in Section 7-2. Using the trial stress value for the current time step (Equation 7-24), new nonlinear parameters are determined. By using the newly computed nonlinear parameters and the trial incremental stress, the incremental strain ($\Delta\varepsilon_{ij}(t) = \Delta\underline{\varepsilon}(t)$) is computed using Equation 7-22. The difference between the computed strain and the input strain from ABAQUS yields a residual strain vector. The residual strain vector, $\underline{\mathbf{R}}$, can then be obtained as:

$$\underline{\mathbf{R}} = \Delta\underline{\varepsilon}(t) - \Delta\underline{\varepsilon}(t)_{\text{ABAQUS}} \quad 7-25$$

The strain residual is then minimized using the Newton-Raphson iterative method. The residual strain at iteration cycle m+1 is calculated from:

$$\underline{\mathbf{R}}^{m+1}(t) = \underline{\mathbf{R}}^m(t) + \frac{d\underline{\mathbf{R}}}{d\sigma^m(t)} d\sigma^m(t) \quad 7-26$$

When convergence is achieved the residual reduces to a tolerable low value. By setting $\underline{\mathbf{R}}^{m+1}(t)$ to zero, the stress correction for the next iteration can be obtained as:

$$d\underline{\sigma}^m(t) = -\underline{R}^m(t) \left[\frac{d\underline{R}}{d\underline{\sigma}^m(t)} \right]^{-1} \quad 7-27$$

The corrected stress increment at the next iteration cycle $m+1$ for the current time step increment is then given by:

$$\Delta\underline{\sigma}^{m+1}(t) = \Delta\underline{\sigma}^m(t) + d\underline{\sigma}^m(t) \quad 7-28$$

In a nut shell, the numerical process to obtain the correct stress state at the material level is summarized as follows:

- At the beginning of the time increment, start with trial nonlinear parameters taken from the previous converged state (from the previous time step).
- Using the incremental strain value obtained from ABAQUS, calculate the trial stress based on Equation 7-24.
- Calculate the updated nonlinear parameters using the new state of stress.
- Calculate the incremental strain using Equation 7-22.
- Calculate the residual strain using Equation 7-25 and iterate through Equation 7-25 to Equation 7-28 until the following tolerance is met, i.e.

$$\frac{|d\underline{\sigma}^{m+1}(t)|}{|\Delta\underline{\sigma}^{m+1}(t)|} < \text{Limit} \quad 7-29$$

where Limit is a specified tolerance level.

A user subroutine code was scripted using the formulations given in Equation 7-19 to Equation 7-29. The subroutine is required to update the final value of the stress (obtained from Equation 7-28). The subroutine also needs to provide the Jacobian (referred in ABAQUS as DDSDDDE). For this purpose the relation given in Equation 7-30 is used.

$$\text{DDSDDDE} = \frac{1}{J^*} [M_G] + \frac{1}{B.g_0} [M_K] \quad 7-30$$

7.4.2 UMAT Runs

The UMAT code has been thoroughly checked by performing various routine calculations. Some results using the mortar response data are presented in this section. Figure 7-17 graphically illustrates the nonlinear parameters obtained from the mortar data collected at 20°C. For other temperatures, the nonlinear parameters have been given in a tabular form in Chapter 6.

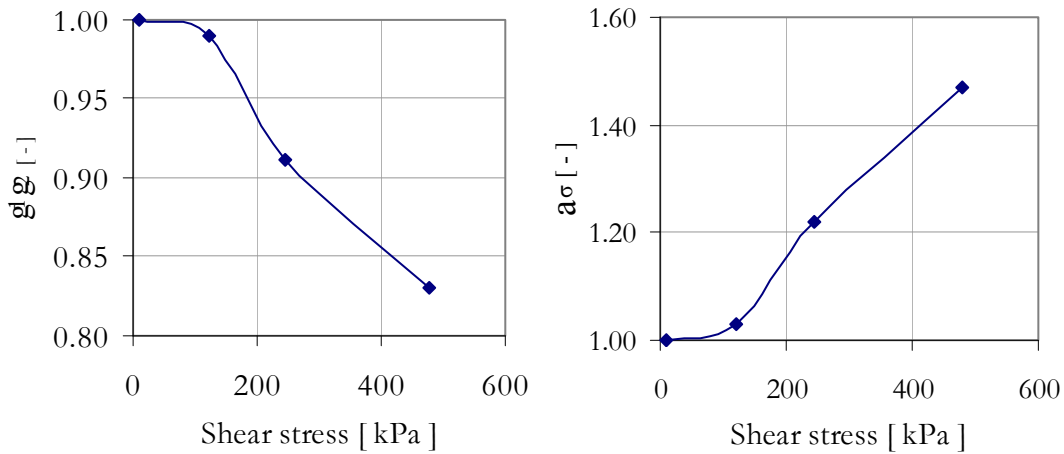


Figure 7-17 Schapery nonlinear parameters for the mortar at 20°C

The creep curves that were used to obtain the nonlinear parameters in Chapter 6 were numerically back calculated. This is performed to check the accuracy of the numerical code. For the data shown in Figure 6-7 in Chapter 6, the numerically back calculated results are illustrated in Figure 7-18.

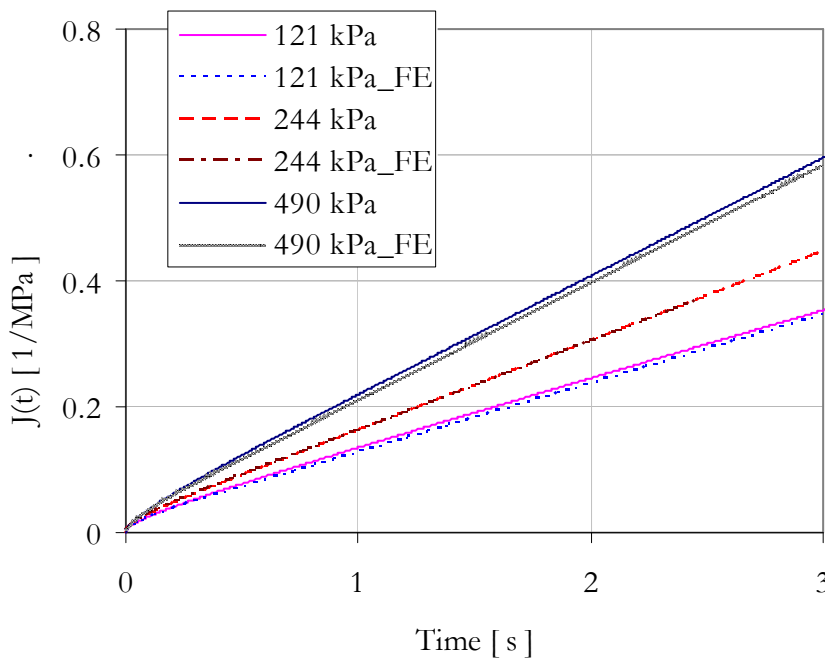


Figure 7-18 Back calculated creep curves for the mortar at 20°C

Other computations performed include back calculation of the frequency sweep data for various stress levels. The back calculated frequency sweep data at three different stress levels for the mortar at 20°C is presented in Figure 7-19 and Figure 7-20. These figures compare FE simulation results with the experimental data. In these simulations, the complex modulus and phase angle results presented were based on an analysis of load signal series of 10 cycles long.

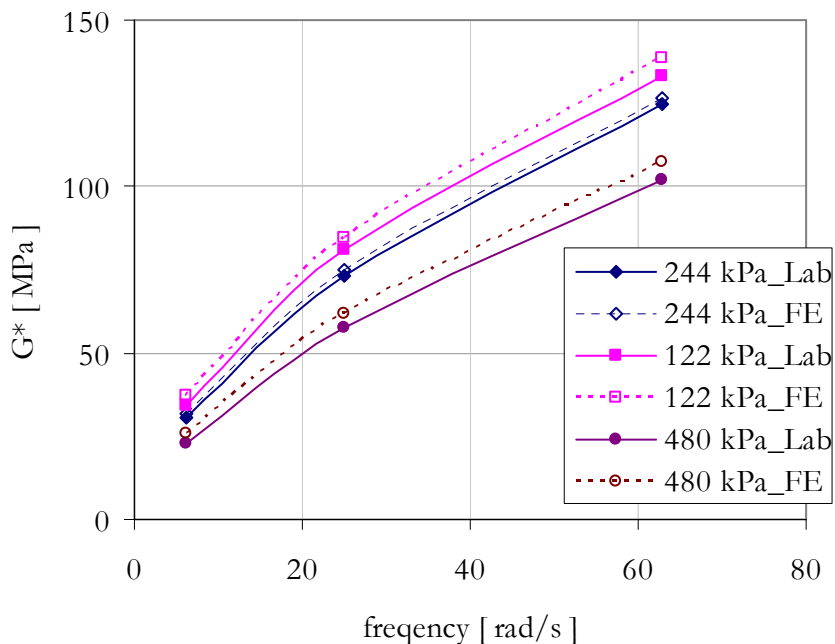


Figure 7-19 Back calculated and measured results for complex modulus, G^*

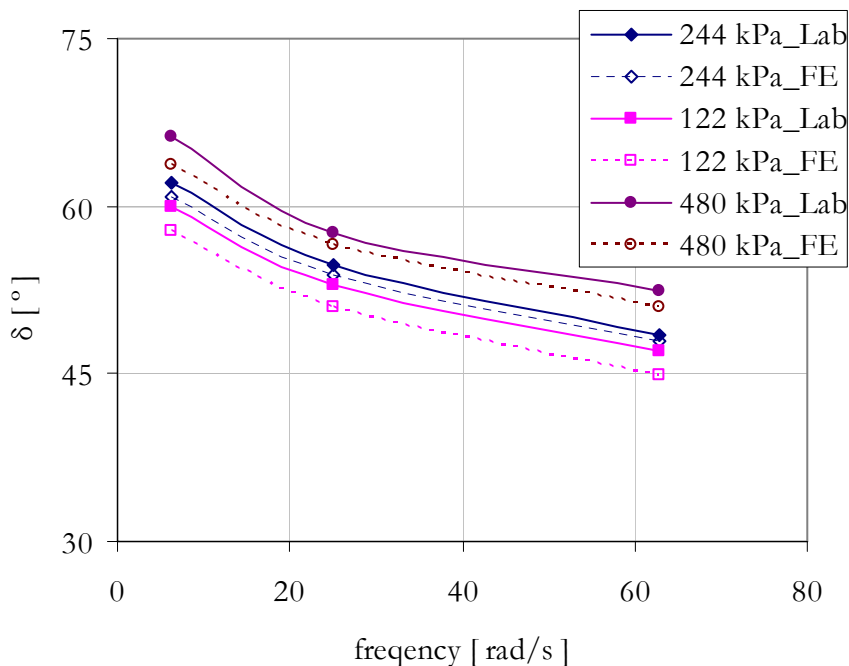


Figure 7-20 Back calculated and measured results for phase angle, δ

Figure 7-19 and Figure 7-20 show that the numerical back calculations are in a reasonable agreement with the experimental data. The maximum discrepancy observed for the G^* amounts to 4%. For back calculations that were performed at the lower stress levels the discrepancy is limited to about 2%. In addition to the possible numerical inaccuracies, these discrepancies can also be attributed to the approximate function that is used to describe the nonlinear parameters. As shown in Figure 7-17 accurate description of the nonlinear parameters as a function of shear stress level would require more data points. Polynomial

function was used to describe the variation of the nonlinear parameters as a function of stress. When more data points are obtained, better agreement between the measured and back calculated values can be obtained.

7.4.3 Effect of Nonlinearity on Data Interpretation Techniques

In this section the data interpretation technique that was used for the mortar testing in Chapter 4 is re-evaluated. It has been mentioned that unlike a uniaxial test setup, where a relatively uniform stress is obtained across the diameter of the test specimen, the shear stress distribution across the diameter of a cylindrical mortar sample is not uniform. For the data interpretation, an assumption was made such that the distribution of the shear stress across the diameter of the mortar sample remains linear. Now that the nonlinear behaviour of the mortar is known, evaluation of this assumption can be made.

Using the mortar response data at 20°C, a sinusoidal varying torque with amplitude 10.3 N-mm has been applied on the mortar sample. On the assumption of linearly-varying stress distribution across the diameter of the mortar specimen, this is equivalent to a maximum shear stress of 244 kPa at the outer periphery of the sample. This value can also be verified using a linear viscoelastic simulation. The data interpretation technique that was used for translating the measured torque in the sample to the shear stress was performed based on this assumption.

Based on the nonlinear viscoelastic run, the actual shear stress distribution across the diameter of the mortar columns was analyzed. Figure 7-21 shows the von Mises stress distribution corresponding to the applied torque value of 10.3 N-mm. The figure on the right also shows the variation of the nonlinear parameter g_1g_2 across the diameter of the mortar. This parameter was stored during the simulation as a solution dependent variable (SDV). As discussed in previous section a value of 1 indicates linear viscoelastic behaviour. While values greater than 1 imply that a nonlinear behaviour of the mortar is observed. From this figure it can be seen that the material on the outer periphery of the sample exhibited a nonlinear behaviour, whereas, the material in the centre of the sample remained in the linear range.

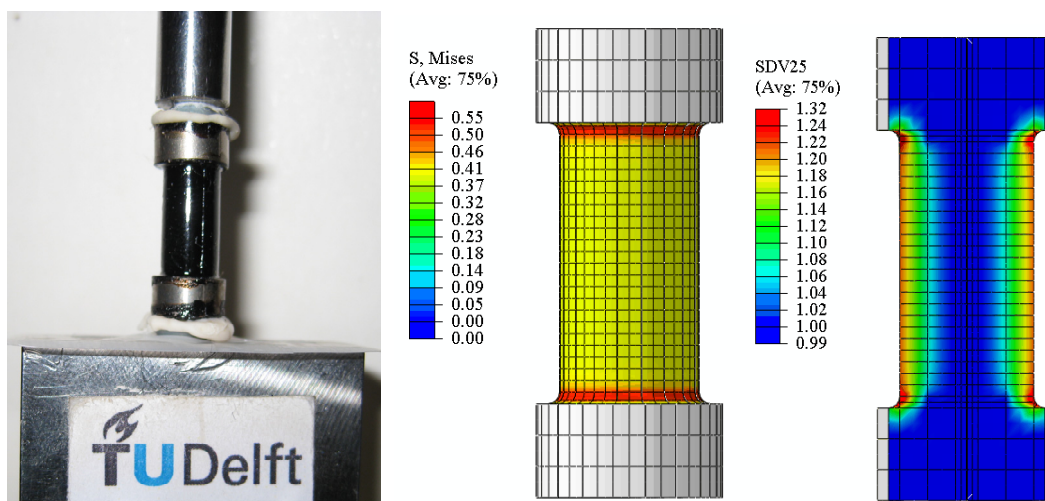


Figure 7-21 Mortar test setup(left), FE model showing von Mises stress distribution (middle), and distribution of the nonlinear parameter $g1g2$ (right) Considering the material at mid height of the specimen, the shear stress distribution across the diameter of the specimen is plotted for both the linear and nonlinear viscoelastic case. Figure 7-22 shows the stress distribution obtained from the two cases.

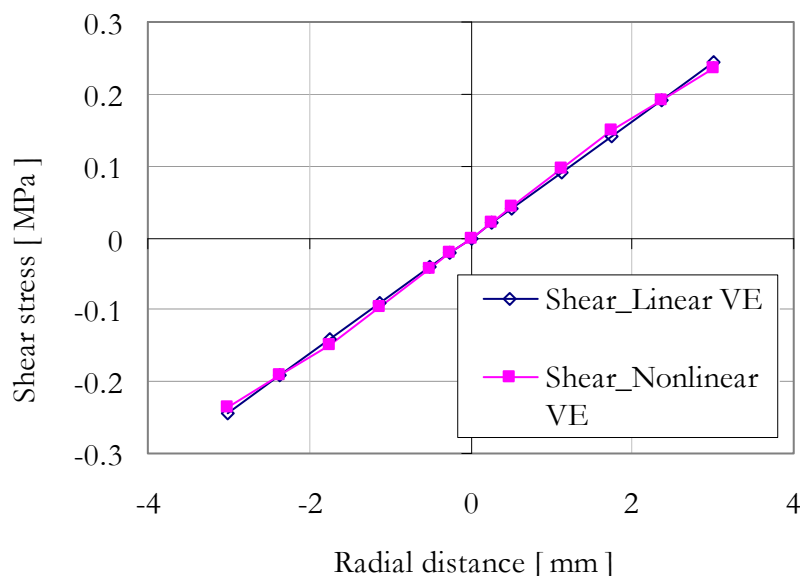


Figure 7-22 Shear stress distribution across the diameter of the mortar sample for linear and nonlinear viscoelastic simulations

A maximum shear stress of 243.7 kPa and 237.0 kPa has been found at the outer periphery of the mortar sample for the linear and nonlinear viscoelastic simulations respectively. This implies that the assumed maximum shear stress at the outer periphery is larger than the actual value (2.8% higher). In comparison to the data scatter observed in the frequency sweep data, which is about 5%, this difference can be considered to be marginal.

For the deformation measurement maximum tangential displacement of 0.01226 mm and shear strain of 0.00193 were obtained from the nonlinear simulation. For the linear simulation the tangential displacement 0.01122 mm and a shear strain of 0.00176 were obtained. This corresponds to an effective specimen height of 12.746 mm and 12.733 mm for the linear and nonlinear simulations respectively. This has also shown a difference of less than 1% and hence, the transfer function that was used to translate the rotational deformation into shear stress in Chapter 4 remains valid. Therefore, it has been concluded that the effects of the non uniform shear stress distribution on the mortar test results are minimal. This conclusion is meant for the test geometry used in this research. Different test geometries would require further investigation.

7.4.4 Nonlinear Simulations with the PA Design Tool

7.4.4.1 Nonlinear Effects at Low Temperatures

To evaluate the effects of nonlinear behaviour on the PA mixture response at low temperatures, simulations using the PA design tool were performed at 10°C. Both linear viscoelastic and nonlinear viscoelastic cases were considered. The loading is kept the same as that used in the MHS and the generalized Burgers' model simulations. The stress and strain signals obtained from the linear and nonlinear viscoelastic analysis were analyzed. For comparison, two locations in the mortar zone (node number 1 and node number 2), at the centre of the stone-stone contact area, were selected (Figure 7-23).

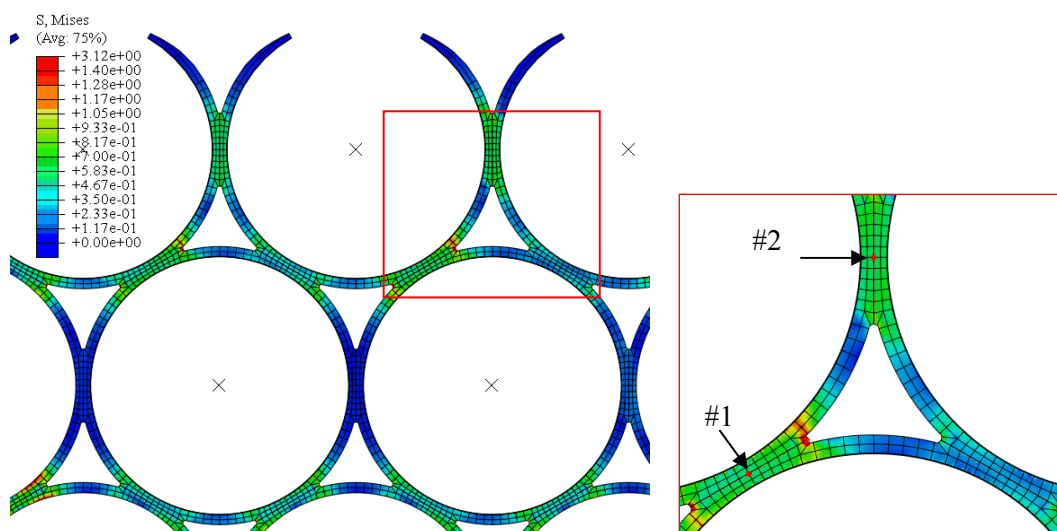


Figure 7-23 von Mises stress distribution (left) and nodal locations used for analysis (right)

Figure 7-24 to Figure 7-26 illustrate the stress and strain computed within the mortar bridge at two different locations. The solid lines represent the results obtained from the linear viscoelastic simulations using the generalized Burgers' model. The nonlinear viscoelastic simulation results are represented with the dashed lines.

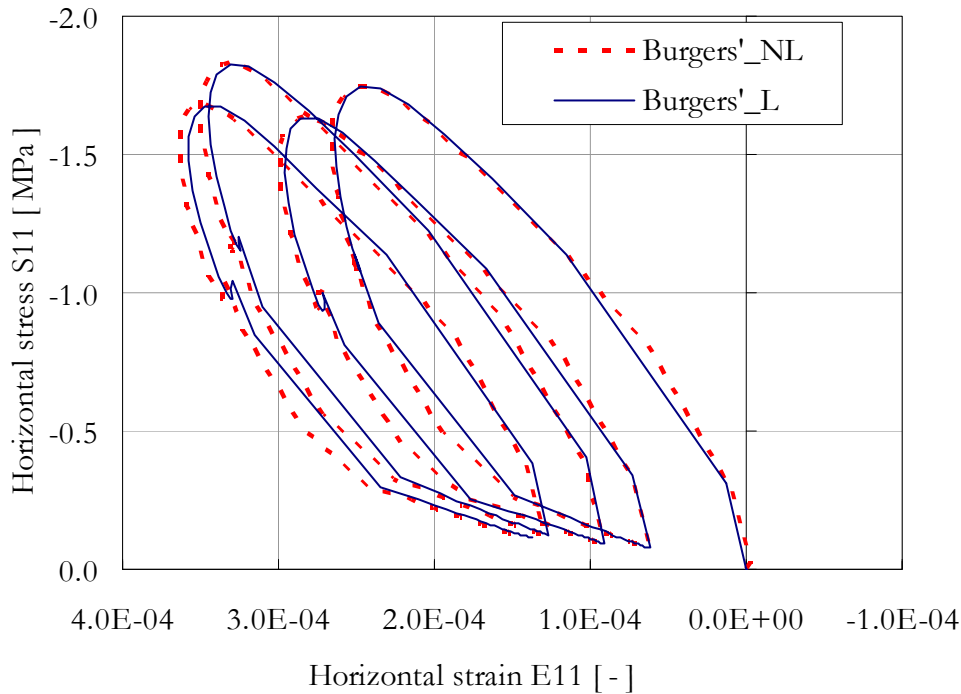


Figure 7-24 Comparison of Hysteresis loop at 10°C; location 1, horizontal direction

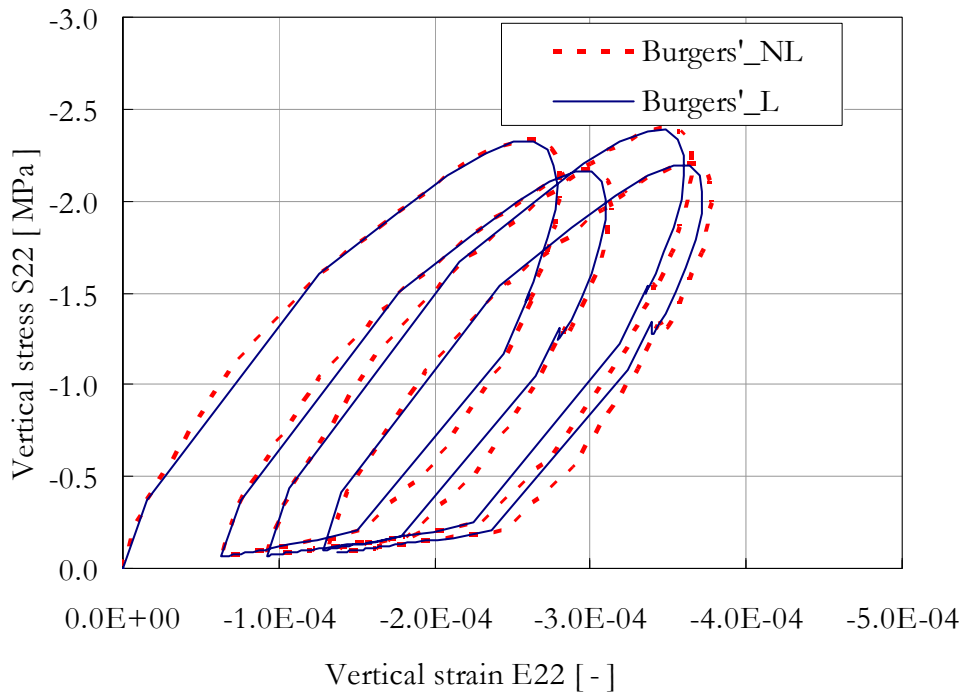


Figure 7-25 Comparison of Hysteresis loop at 10°C; location 1, vertical direction

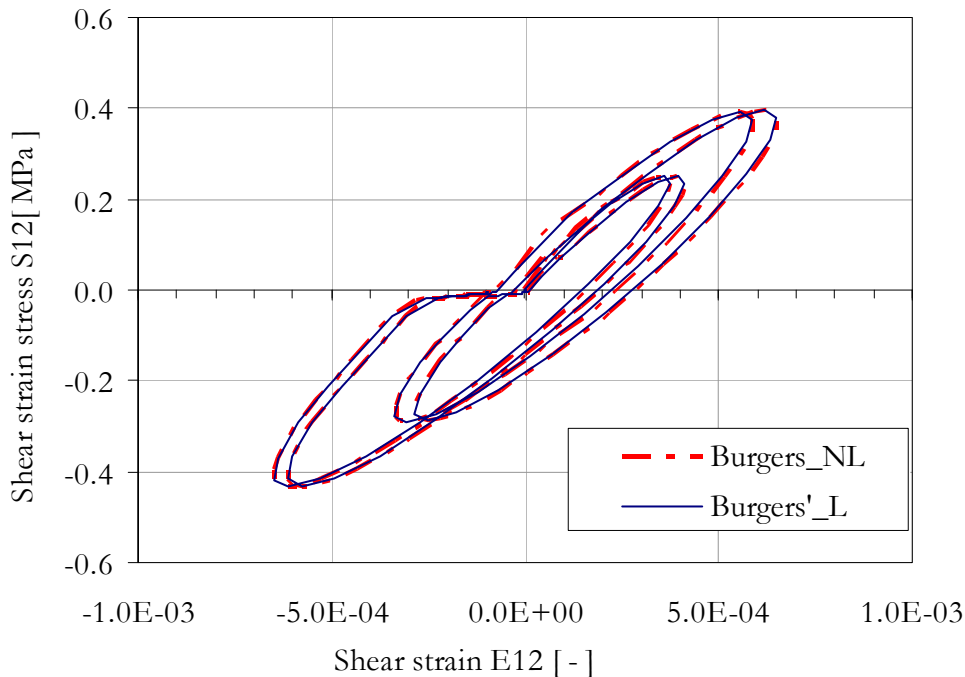


Figure 7-26 Comparison of Hysteresis loop at 10°C; location 2, shear

The above figures show that there is no visible difference between the linear and nonlinear viscoelastic simulations. This implies, for the wheel loading considered in this simulation (contact stress of 0.8 MPa) the mortar behaviour does not exhibit any nonlinear behaviour at 10°C. For temperatures lower than 10°C, the stress level where nonlinearity is observed is at a much higher level. This can be seen from the experimental investigation results discussed in Chapter 4. Consequently, for similar wheel loading conditions at low temperatures, the linear and nonlinear viscoelastic computations will not show difference in results. Based on this, it can be concluded that the effect of the nonlinear response on the PA design tool results is insignificant at low temperature ranges. This conclusion will also remain valid for mixtures with similar binder content but lower void content, such as dense asphalt concrete mixtures.

7.4.4.2 Nonlinear Effects at Intermediate Temperatures

To further evaluate the effects of nonlinear behaviour at intermediate temperatures on the meso mechanistic performance computations, similar simulations were made at 20°C. Unlike the results obtained at low temperature, the mortar behaviour at 20°C was observed to exhibit highly nonlinear behaviour. As a result much higher deformations were obtained from the nonlinear viscoelastic computations. Figure 7-27 illustrates the difference in the vertical strains computed at location 2 for the linear and nonlinear viscoelastic simulations.

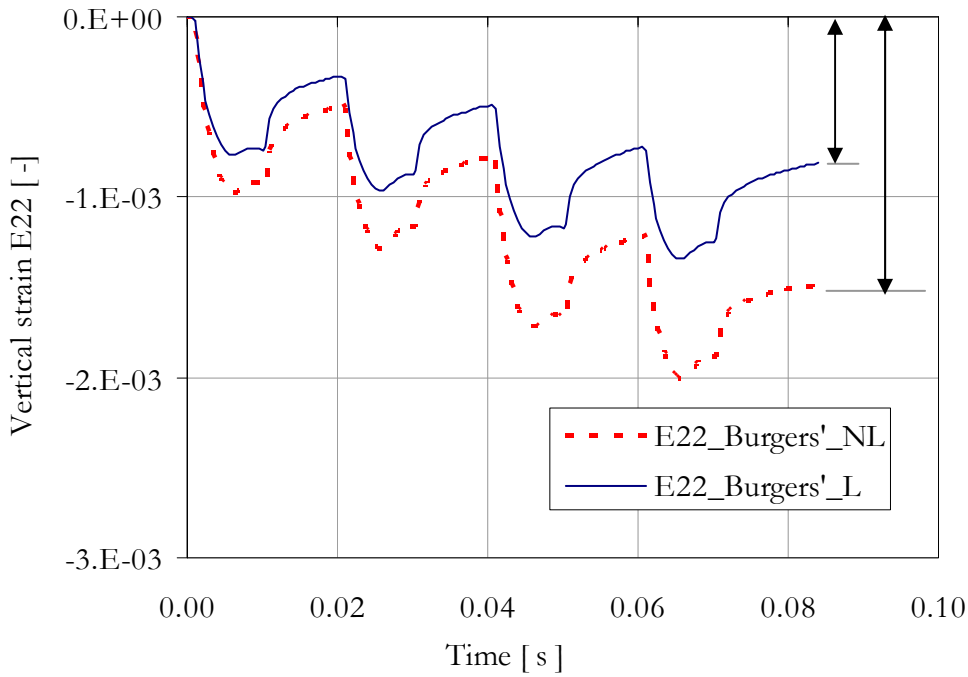


Figure 7-27 Vertical strains at location 2; linear and nonlinear viscoelastic runs
 The deformation in the horizontal direction (E11) and shear direction (E12) also show considerable differences. For node locations 1 and 2, the hysteresis loop presented in Figure 7-28 to Figure 7-30 illustrate the difference in results for the linear and nonlinear viscoelastic runs. It can also be seen from these figures that the value of the stress remains relatively the same for both linear and nonlinear viscoelastic cases.

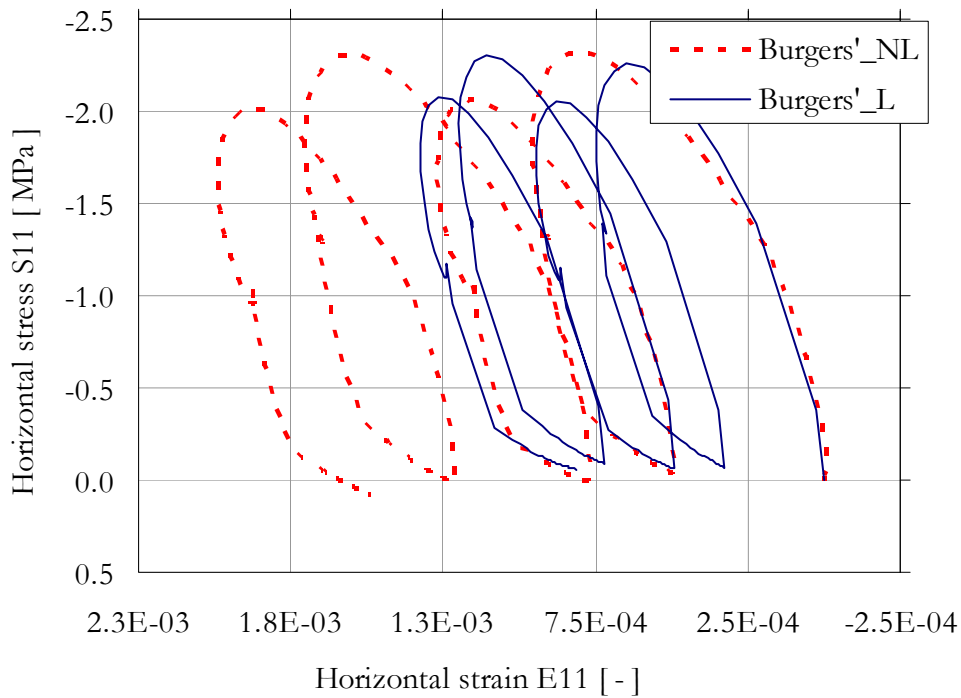


Figure 7-28 Comparison of Hysteresis loop at 20°C; location 1, horizontal direction

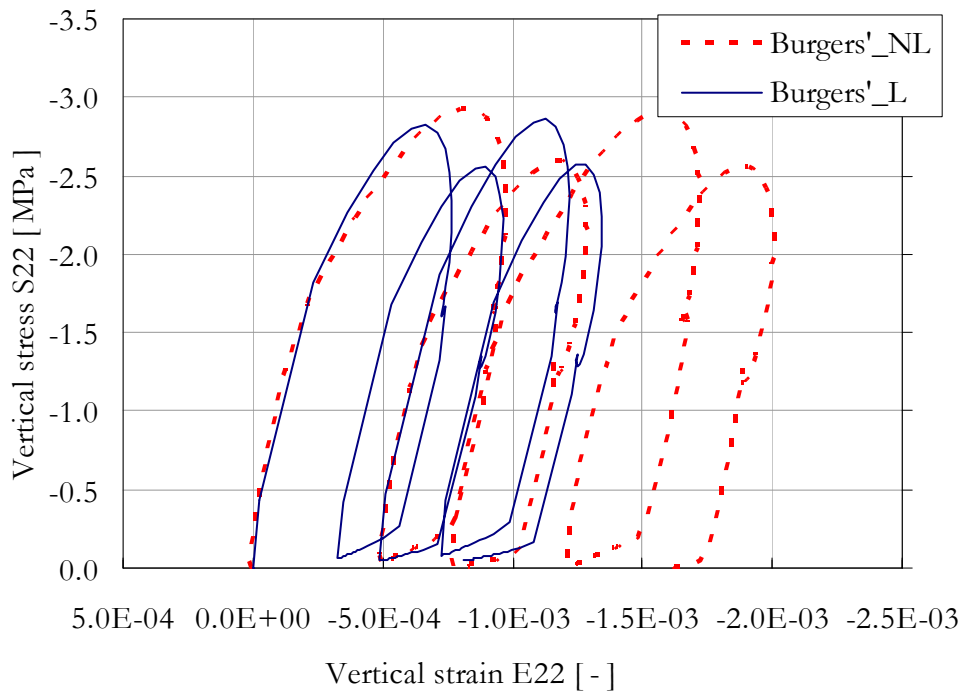


Figure 7-29 Comparison of Hysteresis loop at 20°C; location 1, vertical direction

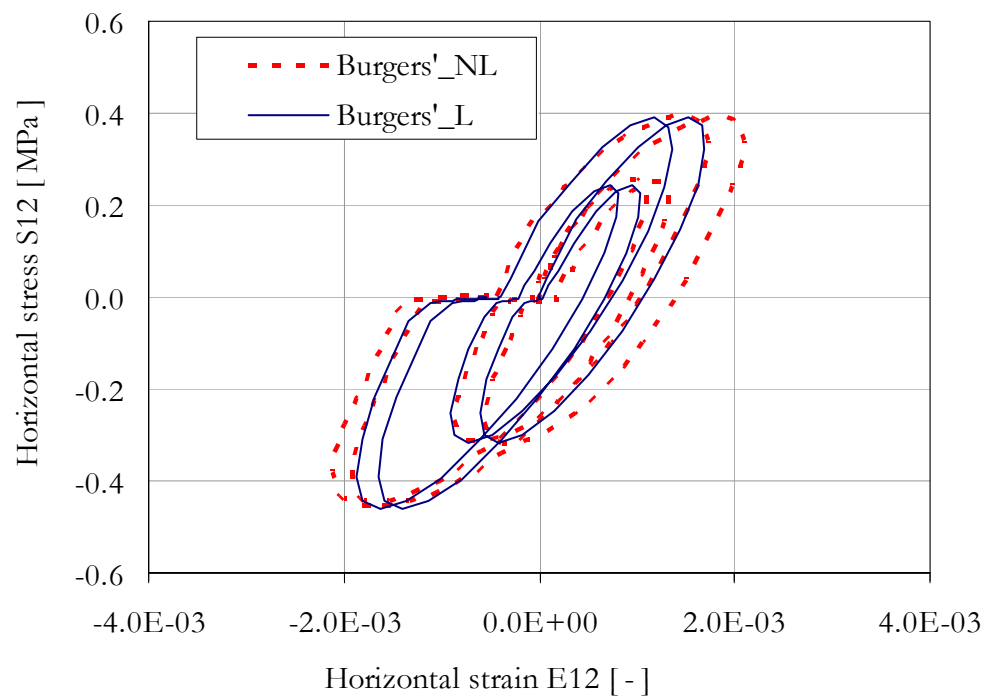


Figure 7-30 Comparison of Hysteresis loop at 20°C; location 2, shear

7.4.4.3 Discussions

The simulations performed in this research showed that the nonlinear viscoelastic behaviour of the mortar at lower temperatures is not of importance for performance computations. This conclusion, however, is based on the mortar type considered in this research, and for an assumed contact stress of 0.8 MPa for the wheel load.

The simulations performed at 20°C show a highly nonlinear behaviour. In terms of vertical deformation at location 1, maximum vertical strains of 8.12E-4 and 14.9E-4 were obtained for the linear and nonlinear viscoelastic runs respectively (see Figure 7-27). The maximum vertical strain obtained using the nonlinear run is 1.83 times higher than the value obtained for the linear case.

The meso mechanics PA design tool uses a dissipated energy based fatigue relation and Figure 7-28 to Figure 7-30 show that a large amount of dissipated energy is calculated for the nonlinear case. The dissipated energy computed e.g. at location 1 at 20°C has been found to be 1.42E-3 MPa and 2.19E-3 MPa for the linear and nonlinear viscoelastic runs respectively. To illustrate the difference in the predicted life expectancy (N_f), the damage model given in Equation 7-31 can be used. This damage model is used for estimation of life expectancy in the PA design tool [15].

$$N_f = \left(\frac{W_{\text{initial_cycle}}}{W_0} \right)^{-b} \quad 7-31$$

The parameter W_0 denotes the energy limit that will lead to failure within one cycle and b is the model parameter. Relevant damage parameters for the mortar at 20°C are not available. Damage parameters for 0°C and 10°C for a different kind of mortar are available in literature [15]. Using approximate values of $W_0 = 0.5$ MPa and $b = 2.7$ for the mortar at 20°C, the linear and nonlinear viscoelastic runs leads to a fatigue life expectancy of 7.38 million and 2.33 million load cycles respectively. This computation shows that due to the linear viscoelastic assumption, the predicted fatigue life cycle is overestimated by a factor of 3. Here, it is important to note that the life estimation is only indicative, and as such the exact factor could be higher or lower. Accurate interpretation of the dissipated energy to life cycle estimation requires determination of relevant damage parameter for the mortar at 20°C. One should also be cautioned not to extrapolate this finding to explain the ravelling performance of a PA mixture without taking into account the high healing capacity of the mortar at intermediate to higher temperatures.

However, the above results have a direct implication in evaluating the permanent deformation characteristics of asphalt mixtures. The simulation results have shown that the assumption of linear viscoelasticity at intermediate to higher temperature significantly underestimates computed deformations. This implies that proper mechanistic computations for evaluating the rutting resistance of asphalt mixtures need to incorporate the nonlinear behaviour of the mortar.

7.5 Summary of Findings and Remarks

The main findings and remarks that can be drawn from the material presented in this chapter are summarized below.

7.5.1 The MHS Model

- The one dimensional numerical formulation of the model was generalized into 3D form. Deformations were decoupled into volumetric and deviatoric components. The volumetric and deviatoric deformations were modelled as elastic and viscoelastic respectively.
- The model was successfully implemented in ABAQUS. Application of the MHS model to the 2D idealised PA design tool was illustrated.
- It was shown that computational memory problems cannot be considered as an impediment for the model application in the 2D PA design tool. The model can also be used in FE simulations performed to interpret laboratory results.

7.5.2 The Generalized Burgers' Model

- Similar to the MHS model, the volumetric and deviatoric properties were modelled as elastic and viscoelastic respectively.
- The model was successfully implemented in ABAQUS.
- Application of the model to the 2D idealised PA design tool was illustrated.
- For the generalized Burgers' model and the MHS model, the outputs obtained from the 2D PA tool showed excellent agreement.
- In terms of computational efficiency on the simulation made on the 2D PA design tool, the use of the generalized Burges' model resulted in two times shorter computational time than the MHS model.

7.5.3 The Schapery Nonlinear Theory

- The Schapery theory was successfully used for modelling the nonlinear response of binders. The nonlinear model was implemented into ABAQUS.
- Application on the 2D PA design tool has been illustrated.
- Effects of nonlinear behaviour on PA design tool results were investigated. For temperatures of 10°C and below, effects were found to be minimal. However, for 20°C and above, it was concluded that linear viscoelastic assumptions highly underestimate computed deformations.

References

- [1]. ABAQUS inc, *ABAQUS User's Manual, Version 6.6*. 2006, Pawtucket, RI.
- [2]. ABAQUS inc, *ABAQUS User Subroutines Reference Manual Vol. Version 6.6*. 2006, Pawtucket, RI.
- [3]. Benedetto, H.D., Mondher, N., Sauzèat, C., and Olard, F., *Three-dimensional Thermo-viscoplastic Behaviour of Bituminous Materials. The DBN Model*. Road Materials and Pavement Design, 2007. **8**(2): p. 285-315.
- [4]. Blaauwendraad, J., *Theory of Elasticity CT 5141, Energy Principles and Variational Methods*. 2002, Delft: TU Delft.
- [5]. De Beer, M., Fisher, C., and Jooste, F.J. *Determination of Pneumatic/Pavement Interface Contact Stresses Under Moving Loads and Some Effects on Pavement with Thin Asphalt Surfacing Layers*. in *Proceedings of the Eighth International Conference Structural Design of Asphalt Pavements*. 1997. USA.
- [6]. Haj-Ali, R.M. and Muliana, A.H., *Numerical finite element formulation of the Schapery non-linear viscoelastic material model*. International Journal for Numerical Methods in Engineering, 2004. **59**(1): p. 25-45.
- [7]. Henriksen, M., *Nonlinear viscoelastic stress analysis--a finite element approach*. Computers & Structures, 1984. **18**(1): p. 133-139.
- [8]. Huang, C.-W., Masad, E., Muliana, A., and Bahia, H., *Nonlinearly viscoelastic analysis of asphalt mixes subjected to shear loading*. Mechanics of Time-Dependent Materials, 2007. **11**(2): p. 91-110.
- [9]. Hurman, M., *Lifetime Optimisation Tool, LOT, Main Report*. 2008: Delft.
- [10]. Hurman, M., Mo, L.T., and Woldekidan, M.F., *Unravelling Porous Asphalt Concrete, Towards a Mechanistic Material Design Tool*. Road Materials and Pavement Design, 2009. **10**: p. 233-262.
- [11]. Hurman, M., Scarpas, T., Kasbergen, C., and T, M. *Development of a structural FEM for Road Surfaceing Seals*. in *International Conference on Computational & Experimental Engineering & Sciences (ICCES' 03)*. 2003. Greece.
- [12]. Hurman, M., Mo, L., Woldekidan, M.F., Khedoe, R.N., and Moraal, J., *Overview of the LOT meso mechanical research into porous asphalt raveling*. Advanced Testing and Characterisation of Bituminous Materials, Vols 1 and 2, 2009: p. 507-518.
- [13]. Hurman, M., Mo, L., Woldekidan, M.F., Khedoe, R.N., and Moraal, J. *Overview of the LOT meso mechanical research into porous asphalt raveling*. in *Proceedings of the 7th Int. RILEM Symposium Advanced Testing and Characterization of Bituminous Materials*. 2009. Rhodes, Greece.
- [14]. Lai, J. and Bakker, A., *3-D schapery representation for non-linear viscoelasticity and finite element implementation*. Computational Mechanics, 1996. **18**(3): p. 182-191.
- [15]. Mo, L., *Damage Development In The Adhesive Zone and Mortar of Porous Asphalt Concrete*. 2010, Delft.
- [16]. Nilsson, R., Oost, I., and Hopman, P., *Viscoelastic Analysis of Full-Scale Pavements: Validation of VEROAD*. Transportation Research Record: Journal of the Transportation Research Board, 1996. **1539**(-1): p. 81-87.
- [17]. Weissmann, S., Harvey, J.T., Sackman, J.L., and Long, F. *Selection of Laboratory Test Specimen Dimension for Permanent Deformation of Asphalt Concrete Pavements*. in *Transportation Research Record 1681*. 1997. Washington D.C.
- [18]. Zhang, W., Drescher, A., and Newcomb, D.E., *Viscoelastic Analysis of Diametral Compression of Asphalt Concrete*. Journal of Engineering Mechanics, 1997. **123**(6): p. 596-603.
- [19]. Zienkiewicz, O.C. and Taylor, R.L., *The Finite Element Method*. 6 ed. 2005.

8

Conclusions and Recommendations

The main goal of this research was to find appropriate mortar response model. The model is meant for use in FE based meso mechanics design tools. As discussed in Chapter 2, these tools intrinsically allow a more realistic examination of stresses and strains in the mortar with in a mixture. This information can be used as input in performance models to get insight on the mixture long term performance characteristics such as ravelling and rutting. To realise this objective two major tasks were set; i.e. laboratory investigation on mortar response characteristics and constitutive modelling. Chapter 4 to Chapter 7 discussed the details of the work involved in this research. Each of these chapters concluded with a summary of the most important findings.

In this chapter, the most important findings and conclusions are presented. Section 8.1 first presents the general conclusions and recommendations from a broad perspective. In Section 8.2, the conclusions and recommendations specific to the various topics that are covered in this study are summarized. For more details the reader is invited to read the relevant chapters.

8.1 General Conclusions and Recommendations

8.1.1 General Conclusions

To fully explore the potential of meso mechanics for modelling asphalt mixture response, it is important that the mixture geometry, the loading and the component material behaviour are represented as accurately as possible. In relation to the component material behaviour, the work presented in this research show that good understanding of the response requires an elaborate experimental program. Furthermore, accurate response models capable in

describing the experimental data over a wide range of loading conditions (temperatures, frequencies and stress levels) are required. In meso mechanical computations these response models allow a realistic representation of the material response for a given loading condition, hence providing a more reliable input for performance models.

The response investigation work that was carried out on bitumen, mastic and mortar showed that linear viscoelastic limits for the binders vary with temperature. For the mortar and mastic, shear stresses as low as 10 kPa can cause nonlinear behaviour at temperatures of 30°C and above, high shear stresses in the range of 1 MPa are required to observe nonlinear behaviour at 0°C. Appropriate response models for the binders should therefore be capable of describing the response characteristics as a function of temperature, frequency and stress level.

In analyzing the response data within the linear viscoelastic range, it was found necessary to include a number of Kelvin-Voigt elements to the Burger's model, so as to describe the response data over a wide frequency window. With the Huet-Sayegh model, an excellent description of the response was obtained. However, addition of a linear dashpot was found necessary to allow the model to simulate viscous deformations. For time domain applications the numerical formulations for the models were obtained. By simulating the creep/relaxation response of the mortar, it was shown that both the time and frequency domain response of the binder can be described accurately with one set of model parameters.

Both the generalized Burgers' model and the modified Huet-Sayegh model were implemented in ABAQUS. In formulating the 3D generalization, an elastic bulk modulus and a viscoelastic shear modulus was assumed. Application of both models in the available meso mechanical PA design tool indicated that the models lead to results that hardly differ. For practical use, however, the models have different implications. The MHS requires the fewest parameters to accurately describe mortar response but results in significant demands in terms of computational power limiting its applicability for large numerical models. On the other hand the generalized Burgers' model has much more parameters, but its computational efficiency in numerical environments makes it more broadly applicable.

For modelling the nonlinear response of binders, the Schapery nonlinear theory has been selected. For this theory, the numerical formulations given by Lai and Baker allow incorporation of the generalized Burgers' model for modelling the creep compliance of the material at various stress levels. This formulation was adopted in this research and implementation into ABAQUS was made. Application into the 2D idealized PA design tool showed that assumption of linear viscoelastic behaviour for the mortar at temperatures of 20°C and above significantly underestimated the computed deformations. Computations made

at 10°C showed that nonlinear effects for the selected wheel loading conditions were negligible. These findings underline the importance of the binder's nonlinear behaviour in performance computations at high temperatures (such as rutting). Since ravelling is detrimental at low temperatures, the results imply that assumption of linear viscoelastic behaviour in ravelling performance computation of PA is acceptable.

8.1.2 General Recommendations

For linear viscoelastic computations, depending on the size of the meso mechanics model, it is possible that computational memory requirements may hinder the use of the MHS model. In order to allow utilization of the model for various scales of problems, it is important to develop appropriate history truncation methods to optimize computational memory requirements. This also paves a way for the model application in nonlinear computations.

The effects of environmental loading on the material behaviour have not been investigated in this thesis. Even though nonlinear behaviour was observed to show negligible effects for computations made at low temperatures, it is important to further investigate the change in the material behaviour as a result of aging and moisture effects. By incorporating the environmental loading factors to the nonlinear model, a more comprehensive mixture performance evaluation can be made.

8.2 Specific Conclusions and Recommendations

8.2.1 Related to Experimental Work

8.2.1.1 Conclusions

- Use of the cone and plate setup in a DSR shear test provides a uniform shear stress distribution in the test sample. The setup delivers good results for pure bitumen. For mastic, the setup with the lower cone angle results in inconsistent measurement data. This is believed to be a result of particle jamming in the vicinity of the tip of the cone.
- For mortar testing, the cylindrical specimen can be used to obtain good quality response data. Ensuring good clamping results in better repeatability in test results. The use of the specimen geometry for testing at higher temperatures was problematic due to excessive creep.

8.2.1.2 Recommendations

- For the mastic testing, to avoid the observed inconsistency in test results, a higher cone angle and larger gap is suggested. This can avoid the possible jamming of particulate matters in the vicinity of the cone tip. In general, the

uses of the CP setup for testing materials containing particulate matter need careful consideration.

- For mortar testing at high temperatures a different type of mortar column specimen with a lower height needs to be developed.
- For mortar specimen size used in this thesis, frequencies close to 300 rad/s to 400 rad/s need to be avoided due to the resonance frequency effect on test results.

8.2.2 Related to Modelling Linear Viscoelastic Response of Binders

8.2.2.1 Conclusions

- The MHS and the generalized Burgers' models accurately described the response of various binders and asphalt mixtures over a wide frequency range. Generally the MHS provides a better description of the response data as compared to the generalized Burgers' model.
- The MHS model was successfully applied for time domain use in numerical environments. The numerical formulation for the MHS model requires the entire strain history of the parabolic dashpots to be stored.
- Using both models, it was shown that the time and frequency domain response of the binders can be simulated with one set of model parameters.

8.2.2.2 Recommendations

- Both the MHS and the generalized Burgers' model can be used for modelling the response of binders. For cases where computational memory is of importance, utilization of the generalized Burges' model is efficient.

8.2.3 Related to Modelling Nonlinear Viscoelastic Response of Binders

8.2.3.1 Conclusions

- The Schapery nonlinear theory has been selected for modelling the nonlinear behaviour of the binders. Unlike other nonlinear theories, Schapery's theory requires a practical number of laboratory tests for parameter determination.
- The nonlinear model parameters can be determined from response data obtained from time domain creep tests. The approach used in this thesis utilized the frequency domain response data to obtain the time domain creep response for various shear stress levels.

- Due to the difference in the linear viscoelastic range at various temperatures, the Schapery nonlinear parameters were determined for each temperature of interest.

8.2.3.2 Recommendations

- In this work stress induced nonlinear effects were considered. Literature has reported the suitability of the nonlinear theory to incorporate other environmental factors such as aging and moisture effects. Incorporating these factors into the nonlinear model will allow coupling of the mechanical and environmental loading effects. This, together with meso mechanics approach, will provide better insight into asphalt mixture performance characteristics.

8.2.4 Related to FE Implementation

8.2.4.1 Conclusions

- In the linear viscoelastic mode, the MHS and the generalized Burgers' model were implemented into ABAQUS. For this purposes user material subroutines codes were scripted.
- Various numerical simulations were performed to check the code accuracy. The material models were then used in the 2D idealized PA model. Results obtained for the two material models were compared. In terms of accuracy, comparable results have been obtained. The computational time requirement for the MHS model was found to be higher.
- The one dimensional numerical formulation for the Schapery nonlinear theory was generalized into 3D form. For implementation into ABAQUS, a UMAT code was scripted. Code accuracy was thoroughly checked by performing various routine calculations.
- The effect of nonlinear behaviour on PA mixture response was evaluated. It was found that – for the considered load case, i.e. a commercial truck tyre (50 kN wheel load) travelling at 80 km/h – significant effects were observed at temperatures of 20°C and above. At temperatures of 10°C and below the effects of nonlinear behaviour remain negligible.

Appendixes

Appendix A

B70/100 Response at Various Shear Stress Levels

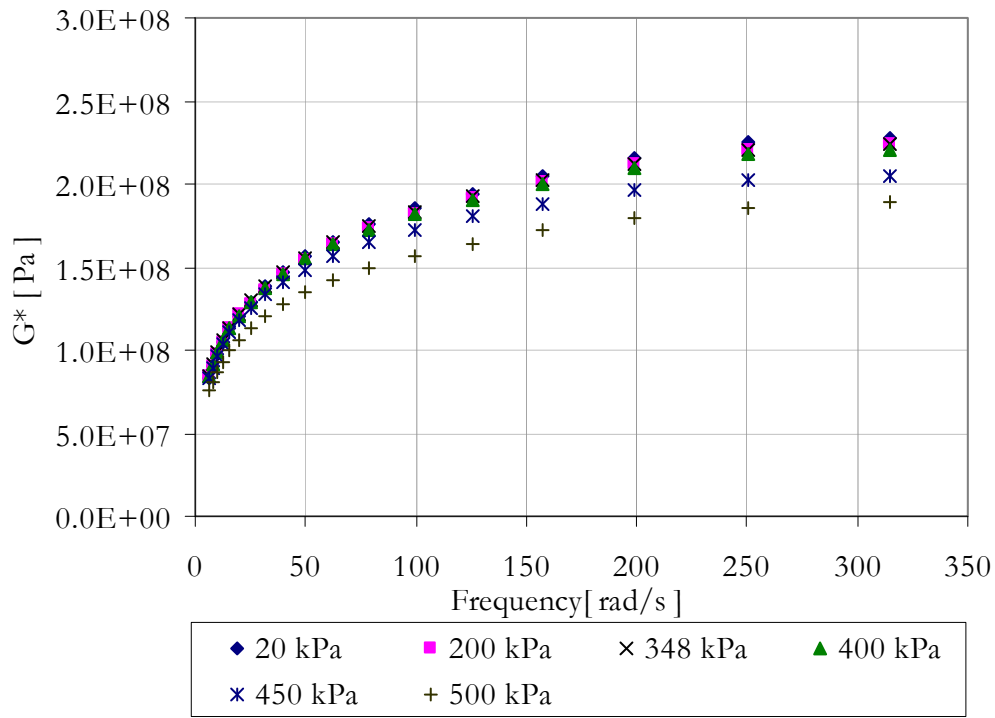


Figure A-1 Frequency sweep results at 0°C; complex modulus

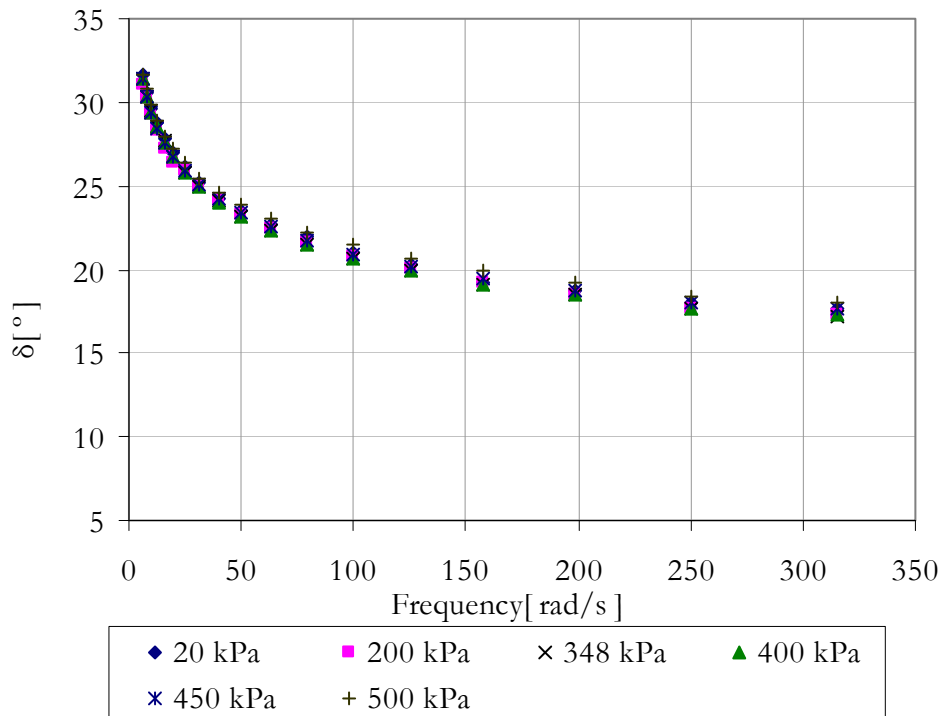


Figure A-2 Frequency sweep results at 0°C; phase angle

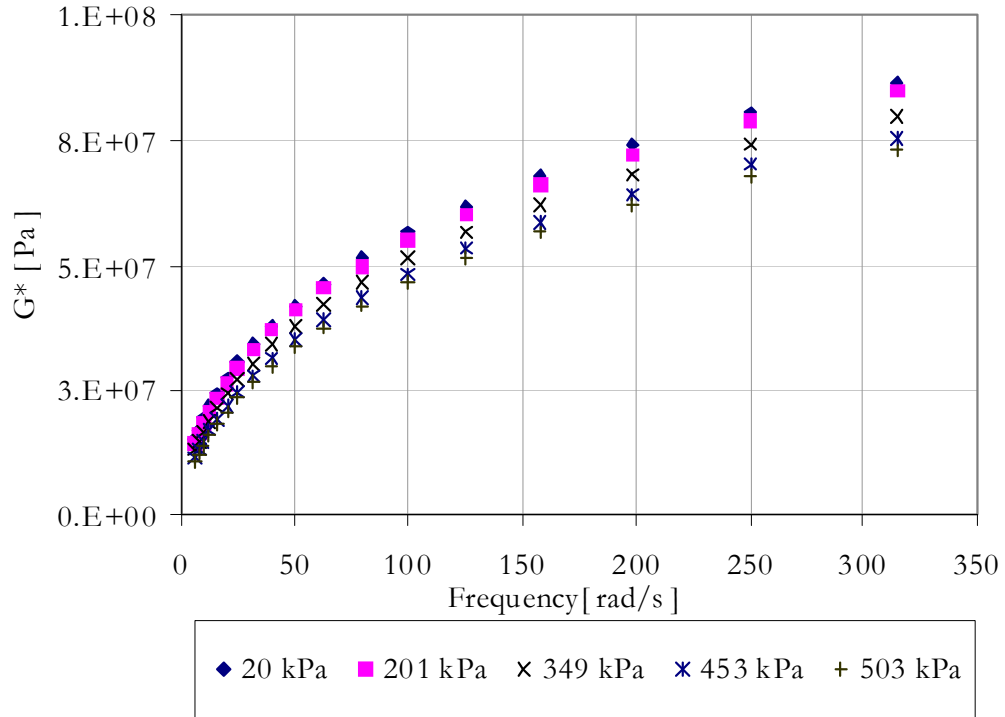


Figure A-3 Frequency sweep results at 10°C; complex modulus

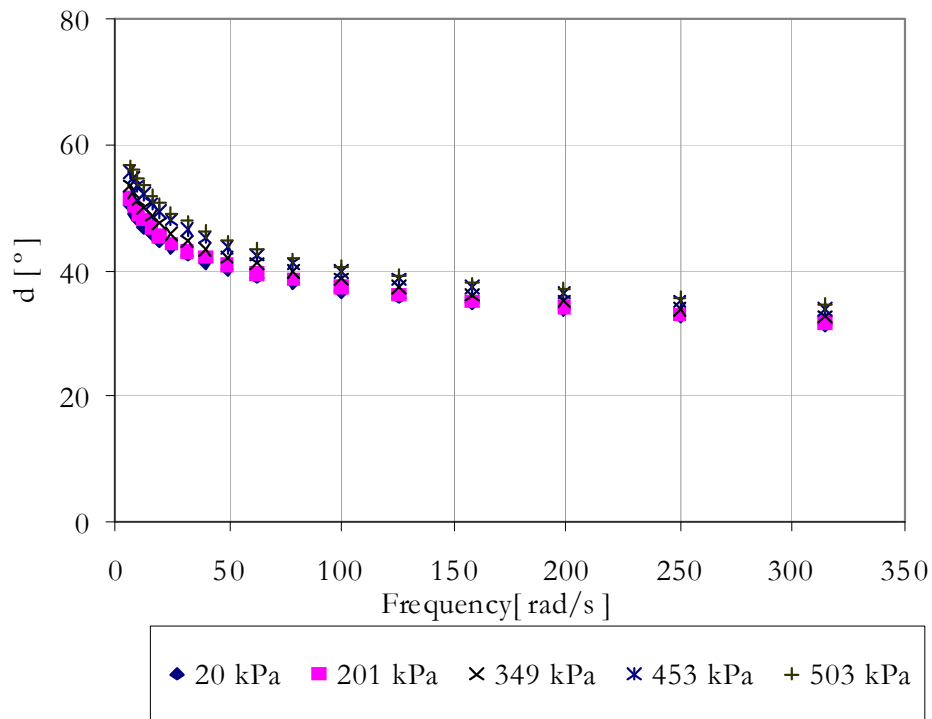


Figure A-4 Frequency sweep results at 10°C; phase angle

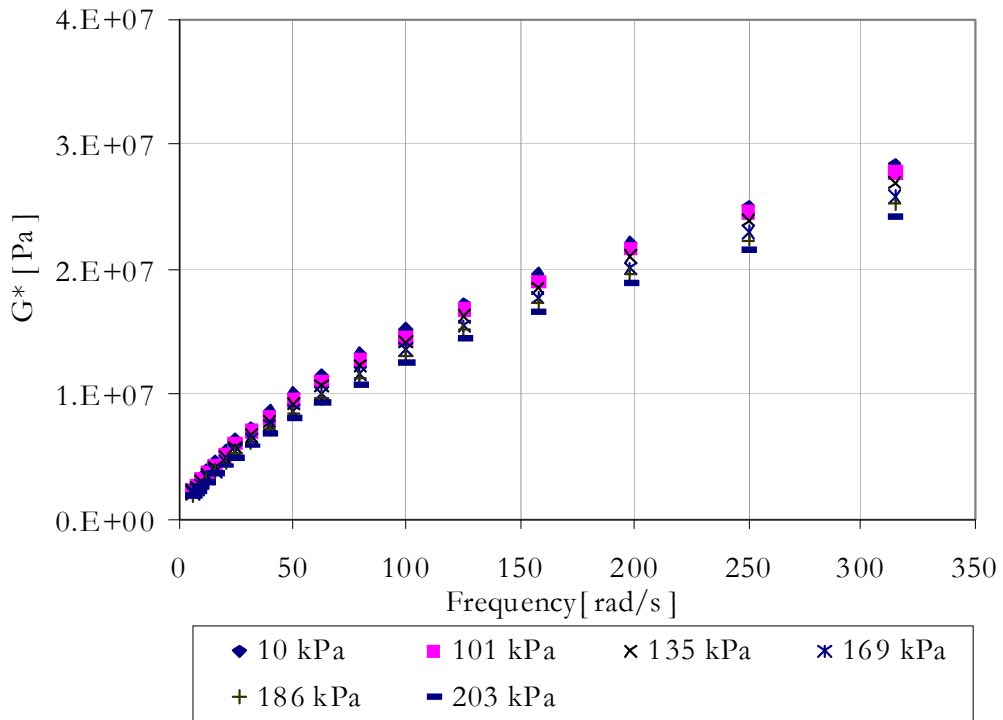


Figure A-5 Frequency sweep results at 20°C; complex modulus

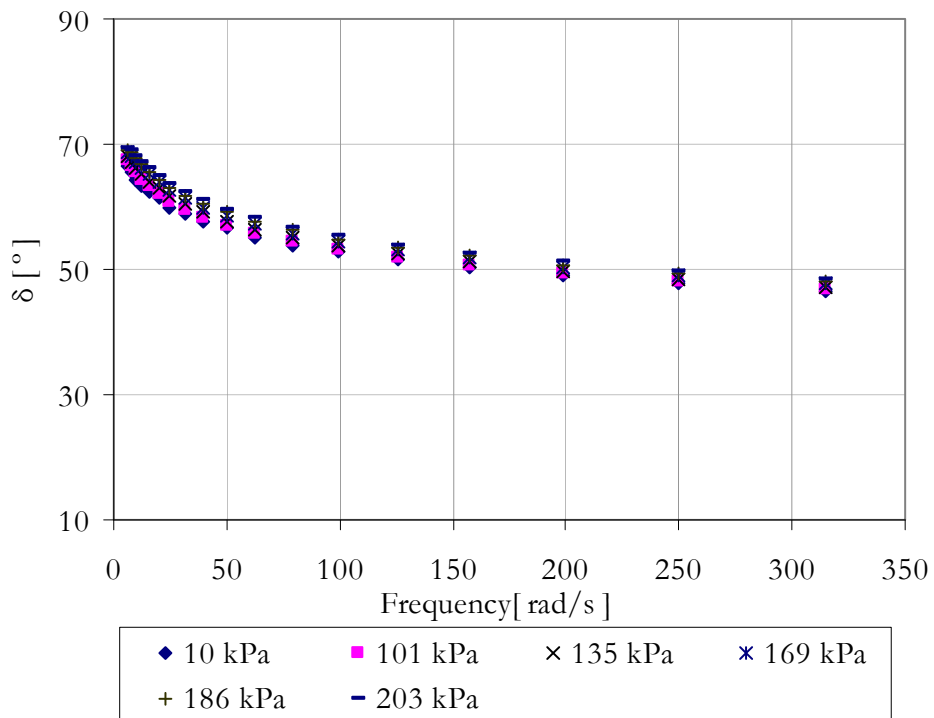


Figure A-6 Frequency sweep results at 20°C; phase angle

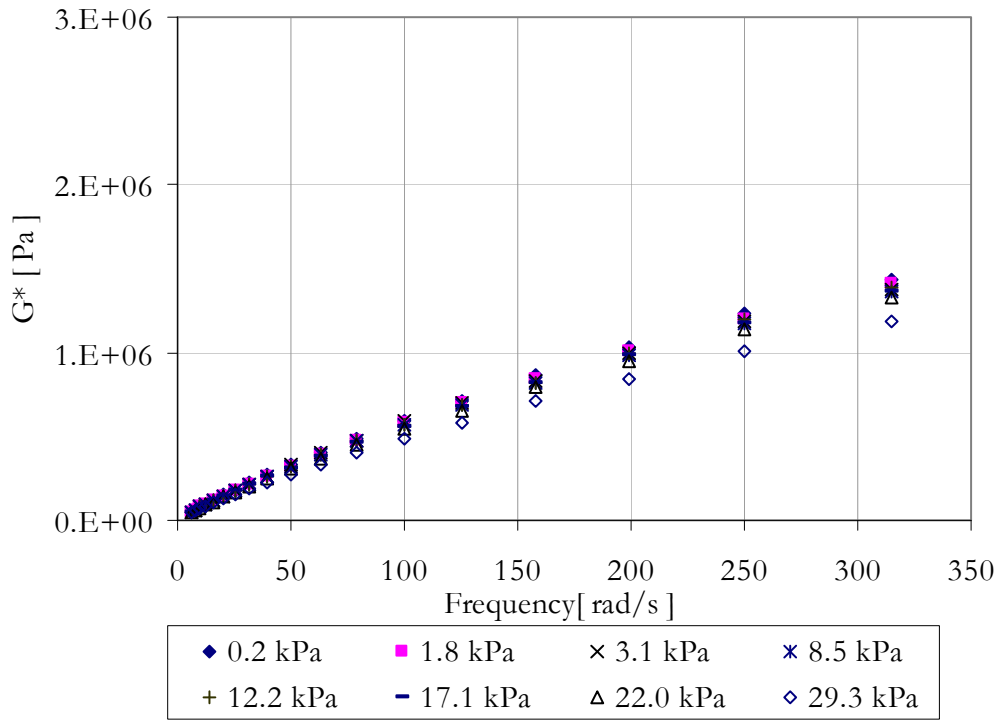


Figure A-7 Frequency sweep results at 40°C; complex modulus

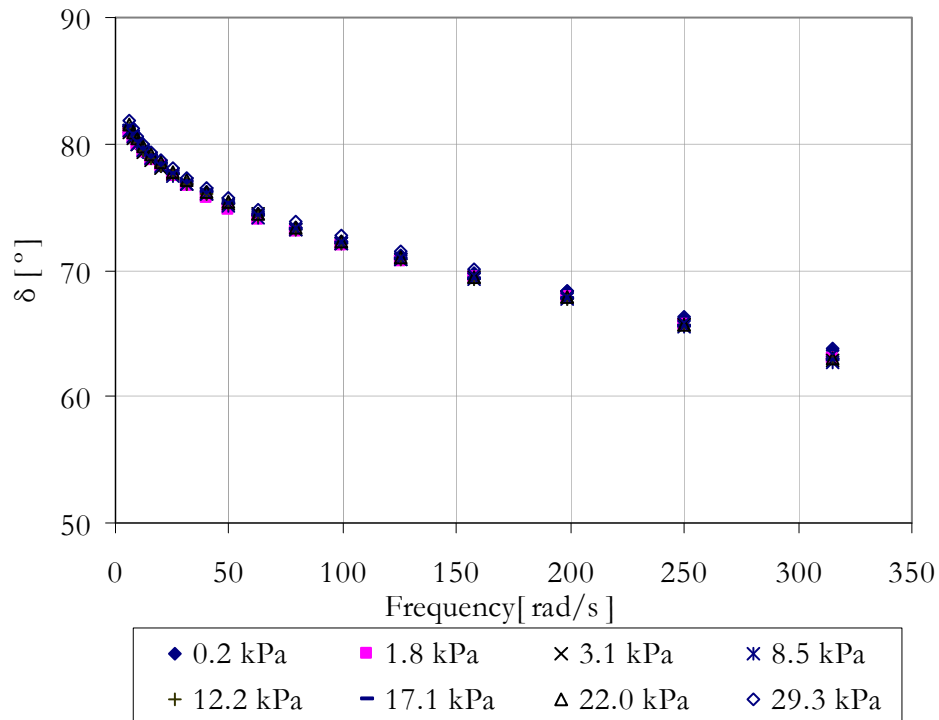


Figure A-9 Frequency sweep results at 40°C; phase angle

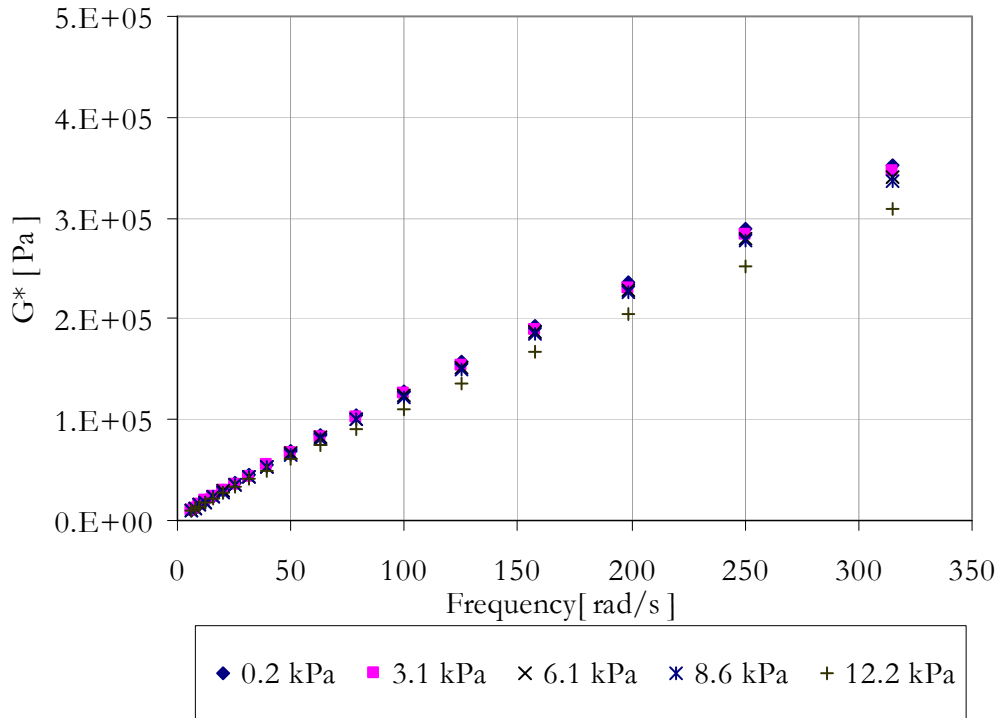


Figure A-10 Frequency sweep results at 50°C; complex modulus

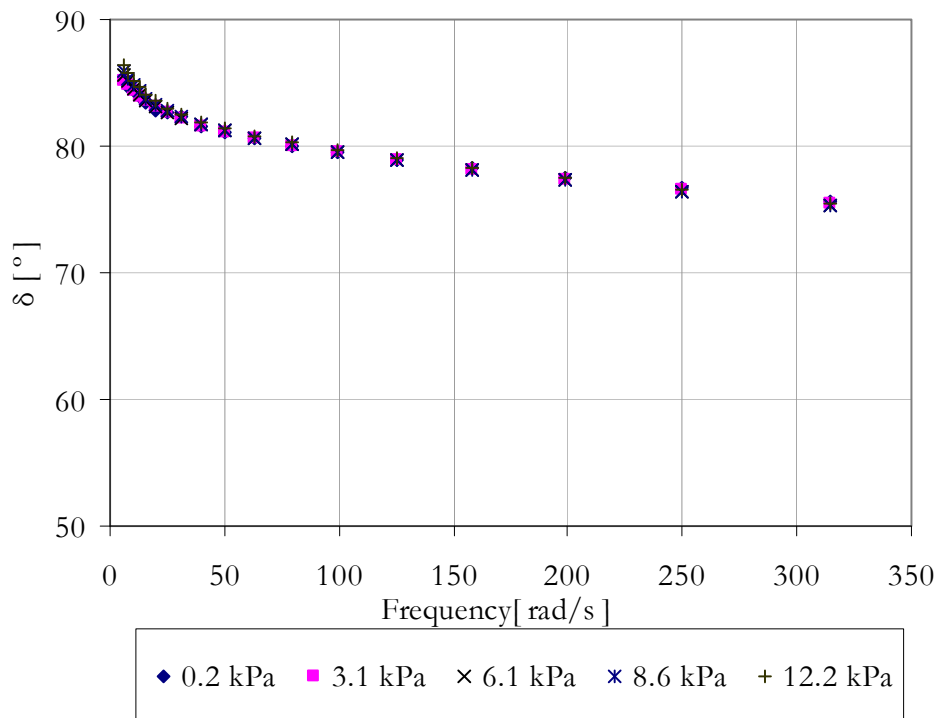


Figure A-11 Frequency sweep results at 50°C, phase angle

Appendix B

B70/100 Mastic Response at Various Shear Stress Levels

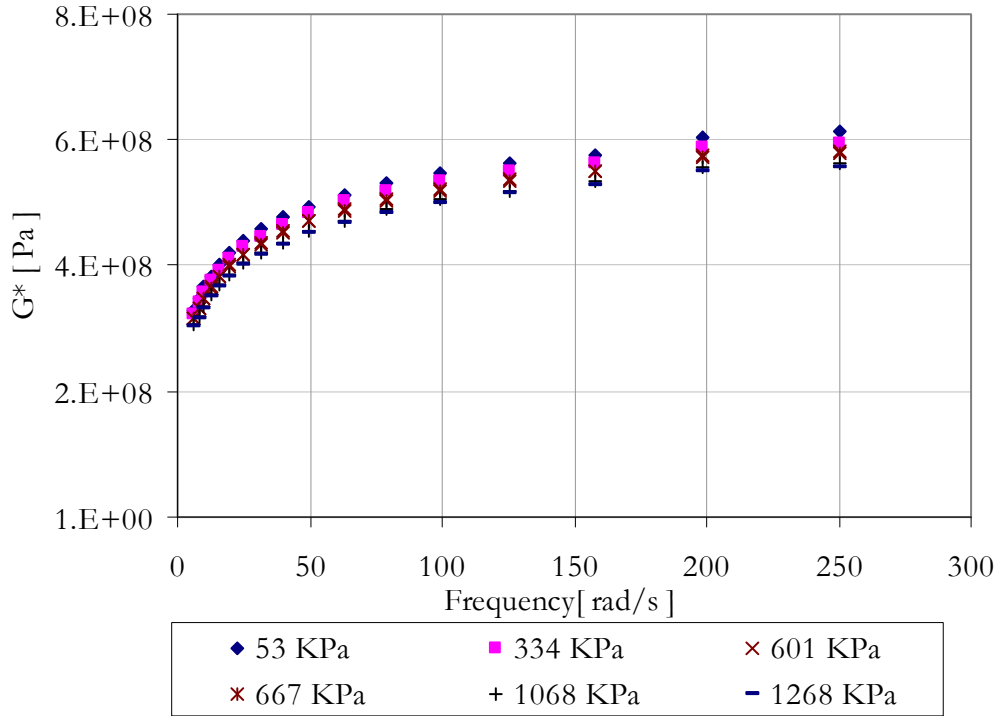


Figure B-1 Frequency sweep results at 0°C; complex modulus for B70/100 Mastic

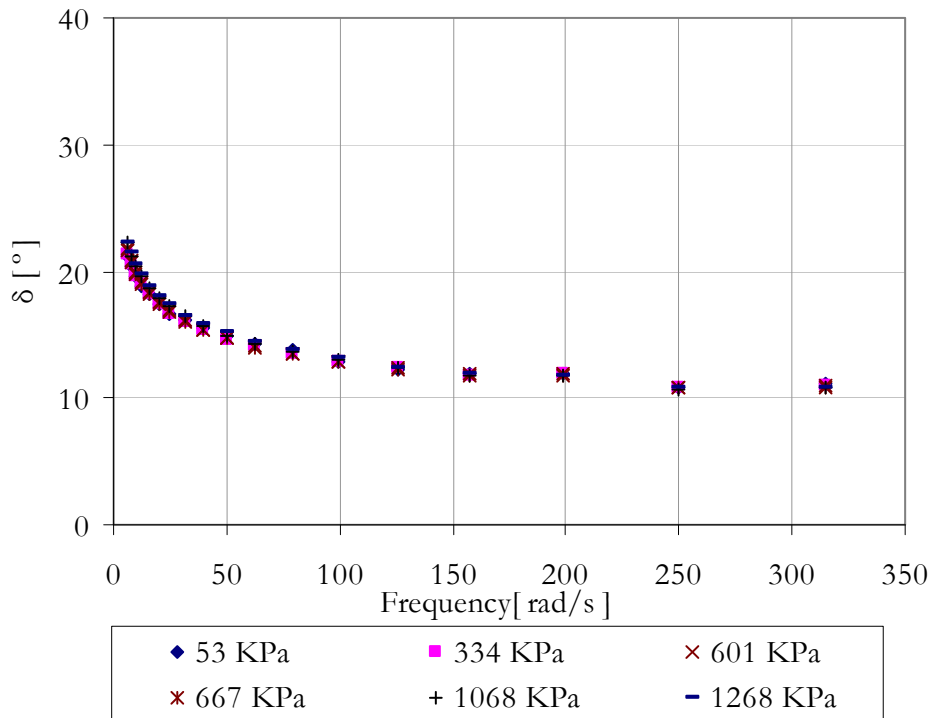


Figure B-2 Frequency sweep results at 0°C; Phase angle for B70/100 Mastic

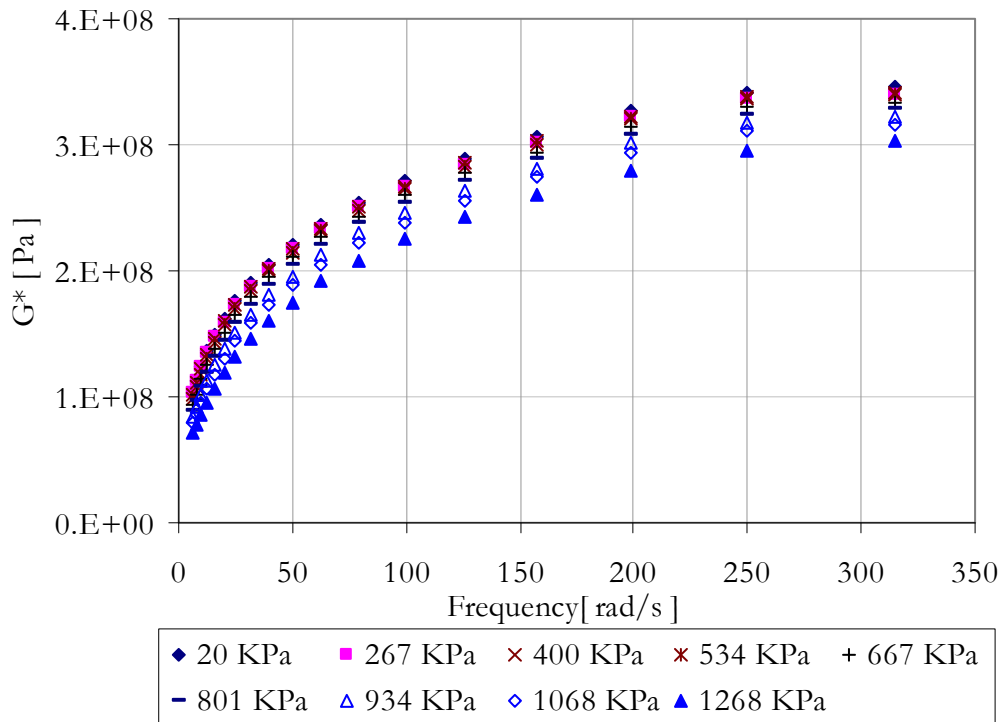


Figure B-3 Frequency sweep results at 10°C; complex modulus for B70/100 Mastic

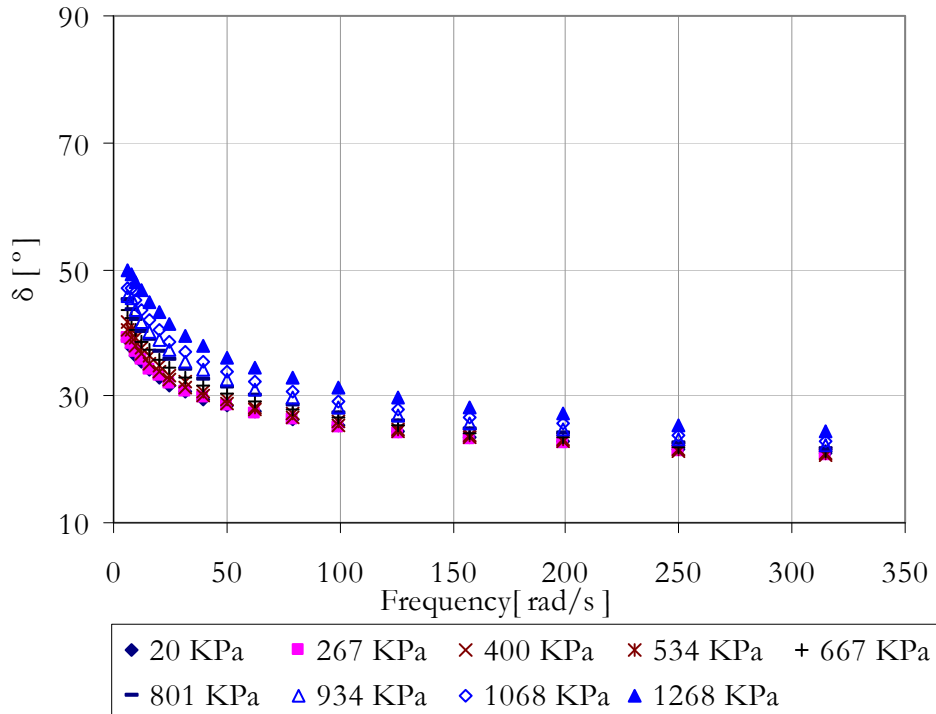


Figure B-4 Frequency sweep results at 10°C; Phase angle for B70/100 Mastic

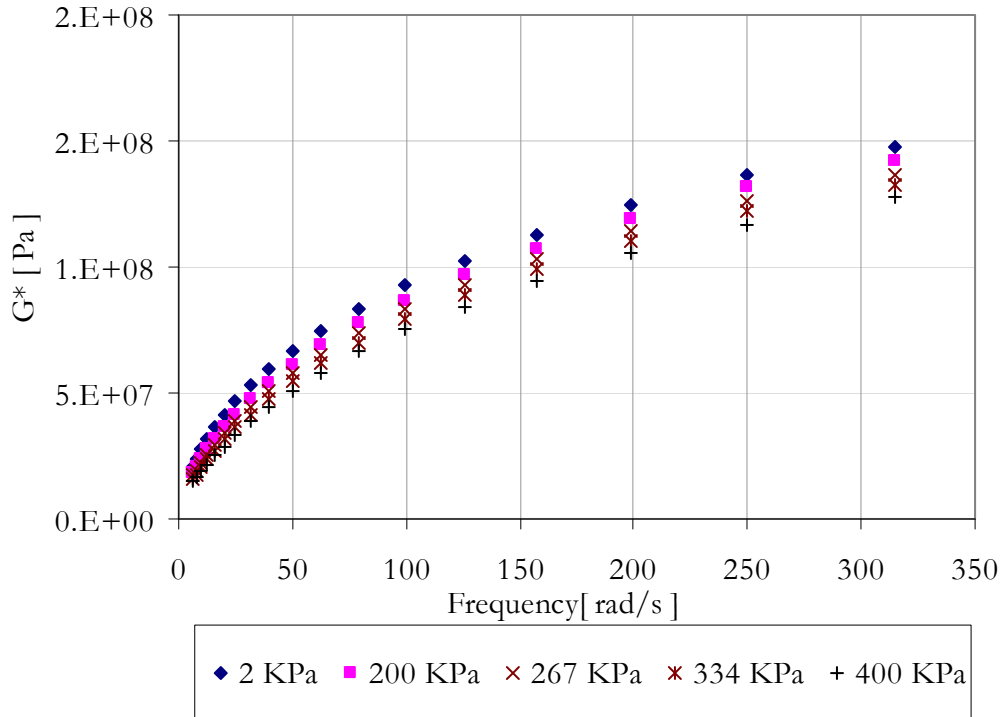


Figure B-5 Frequency sweep results at 20°C; complex modulus for B70/100 Mastic

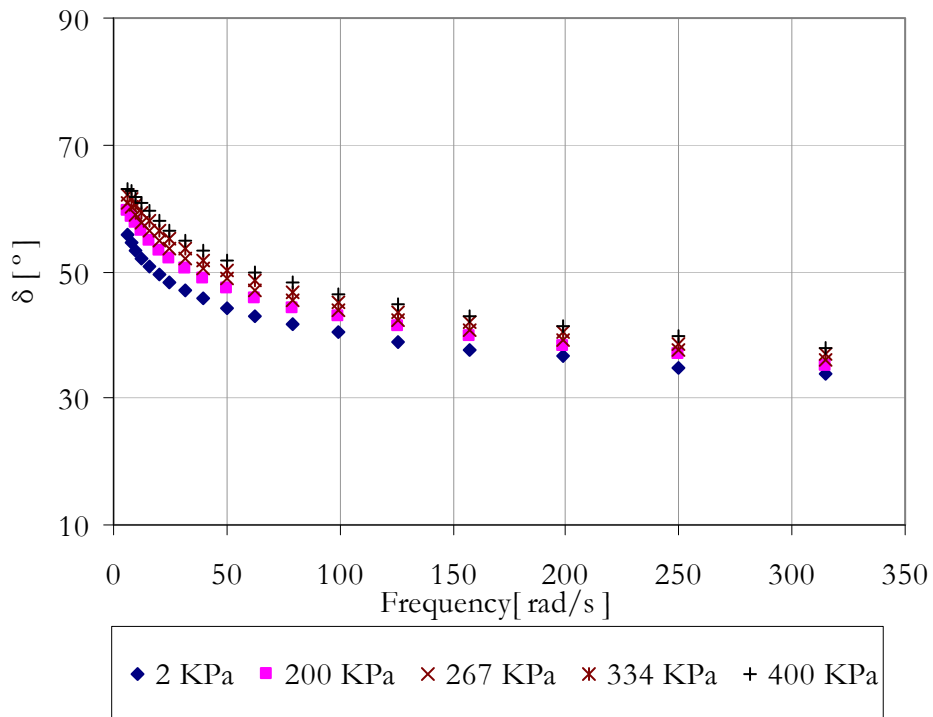


Figure B-6 Frequency sweep results at 20°C; Phase angle for B70/100 Mastic

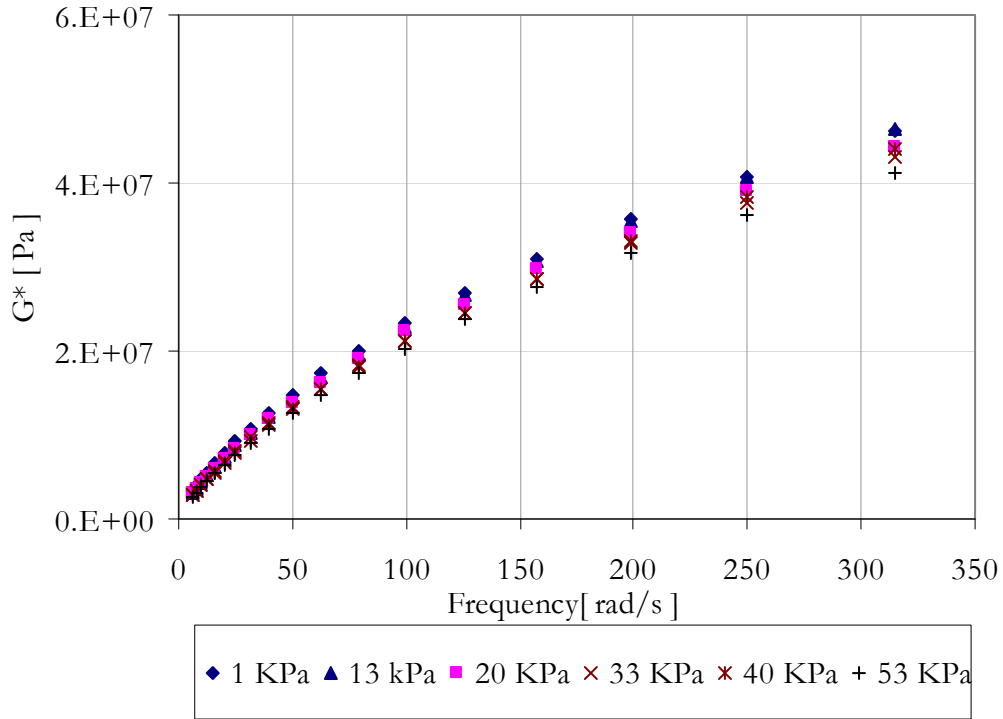


Figure B-7 Frequency sweep results at 30°C; complex modulus for B70/100 Mastic

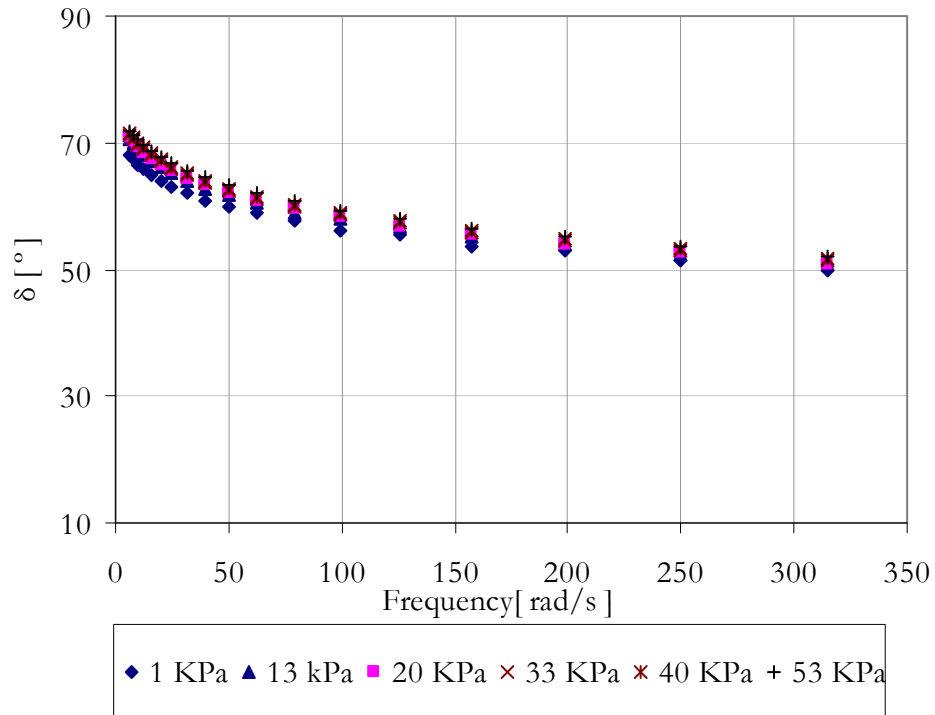


Figure B-8 Frequency sweep results at 30°C; Phase angle for B70/100 Mastic

Appendix C

Mortar Response at Various Shear Stress Levels

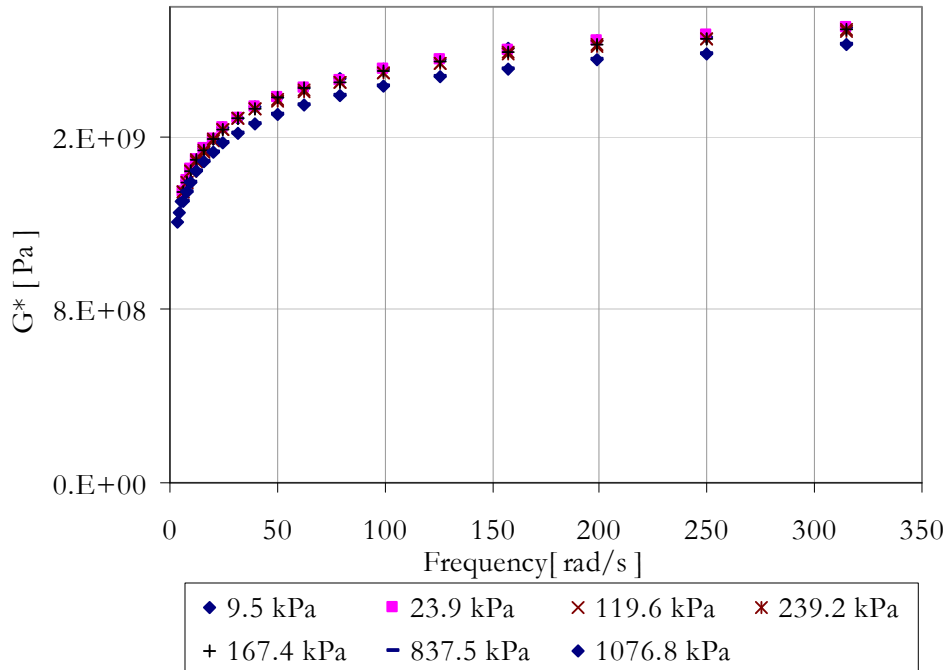


Figure C-1 Frequency sweep results at -10°C; complex modulus for mortar

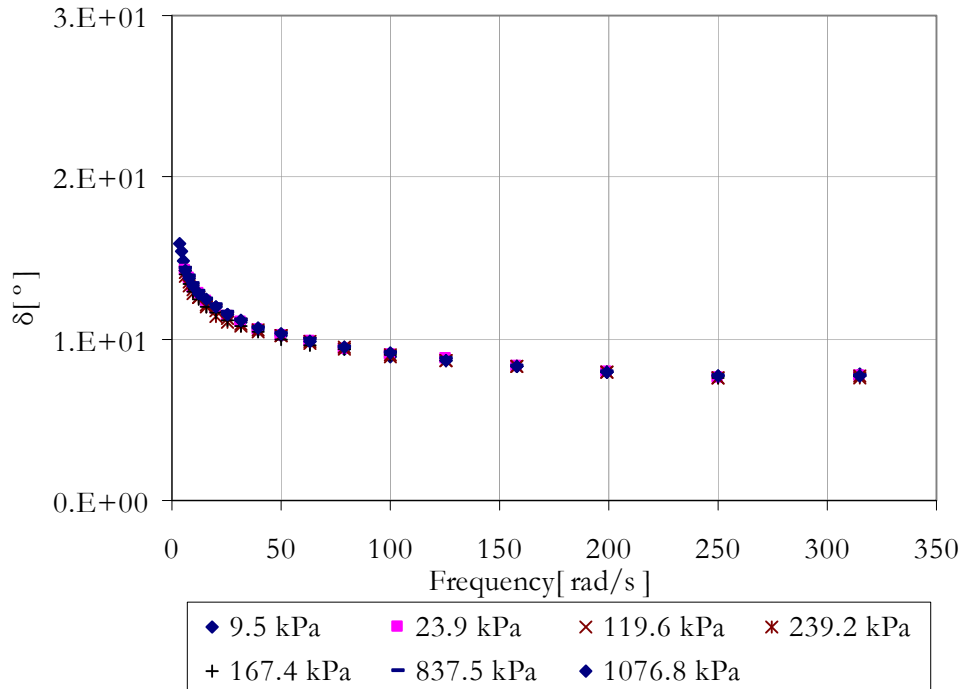


Figure C-2 Frequency sweep results at -10°C; Phase angle for mortar

In this test, a temperature fluctuation was observed at the later stages of the test procedure, i.e. at higher shear stress values. Hence data corresponding to shear stress values between 1100 kPa to 2375 kPa are not included.

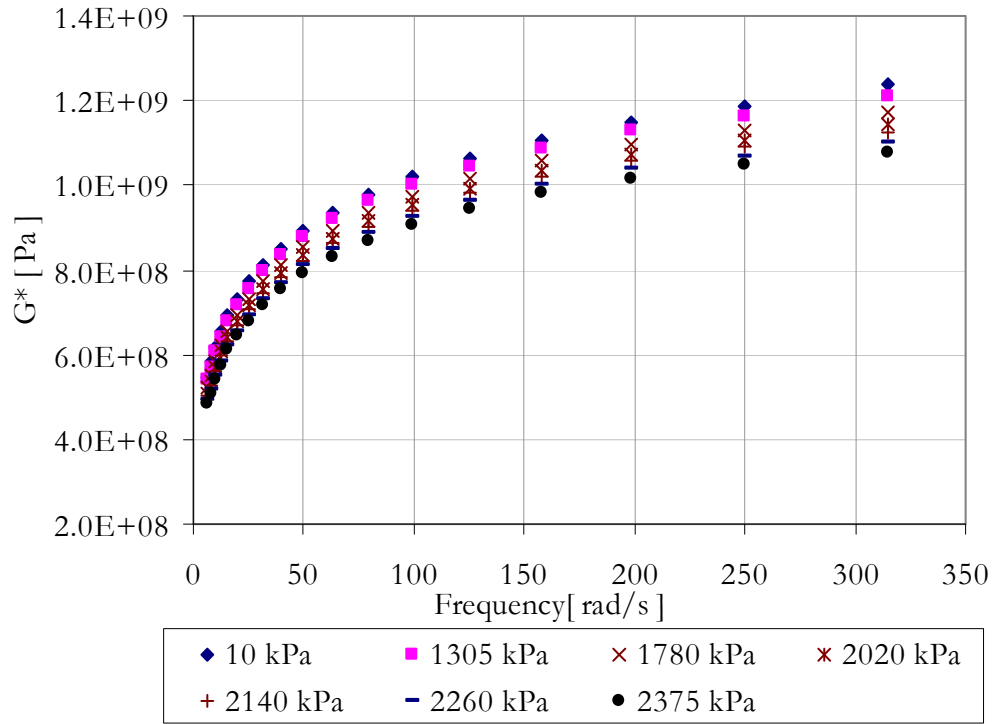


Figure C-3 Frequency sweep results at 0°C; complex modulus for mortar

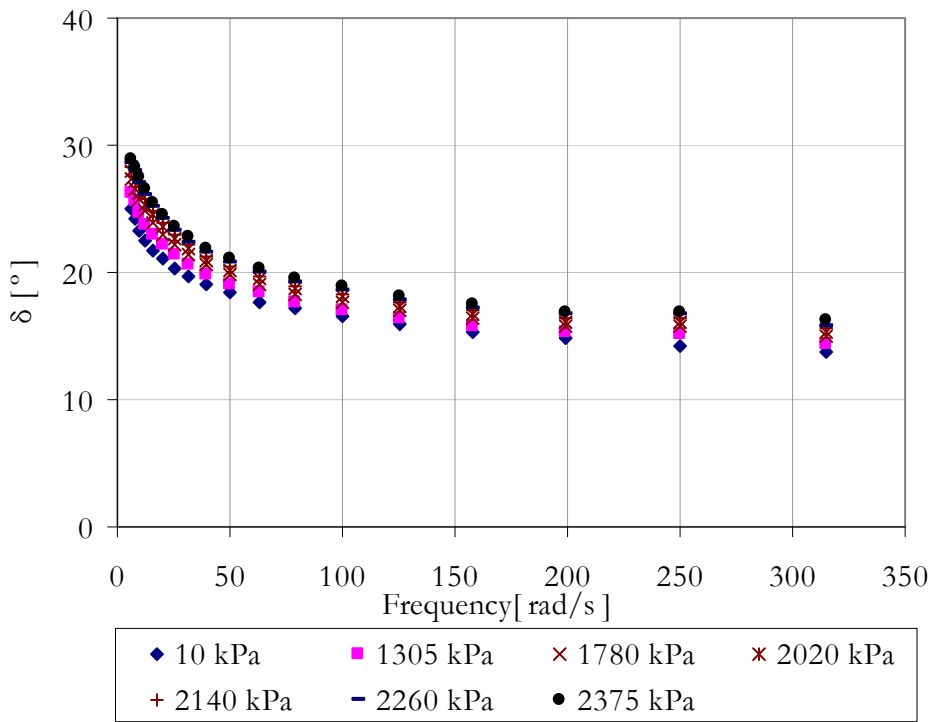


Figure C-4 Frequency sweep results at 0°C; Phase angle for mortar

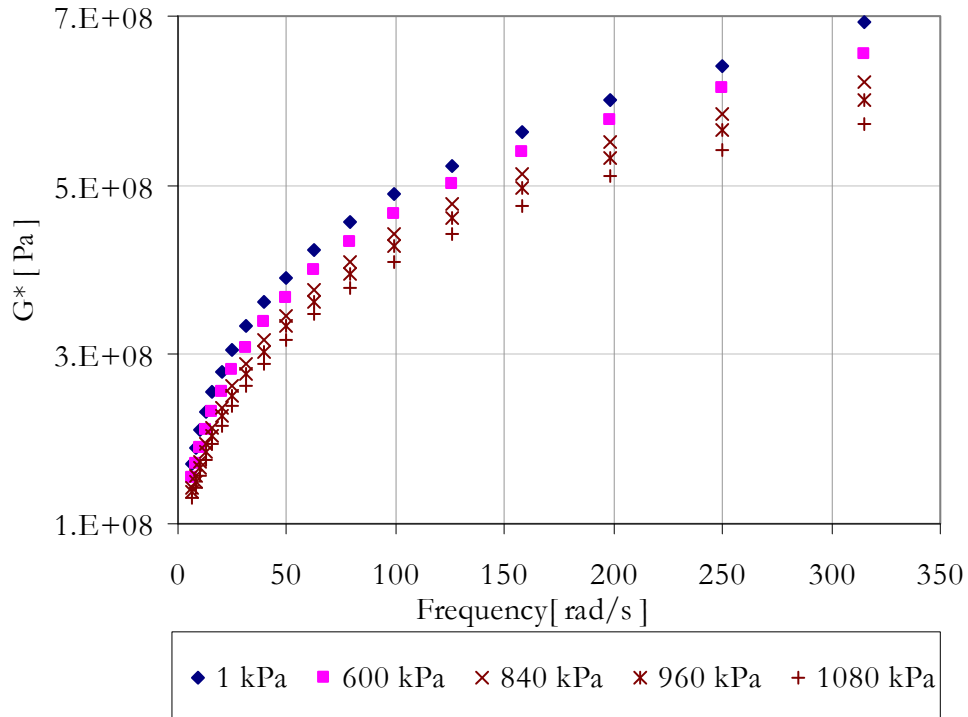


Figure C-5 Frequency sweep results at 10°C; complex modulus for mortar

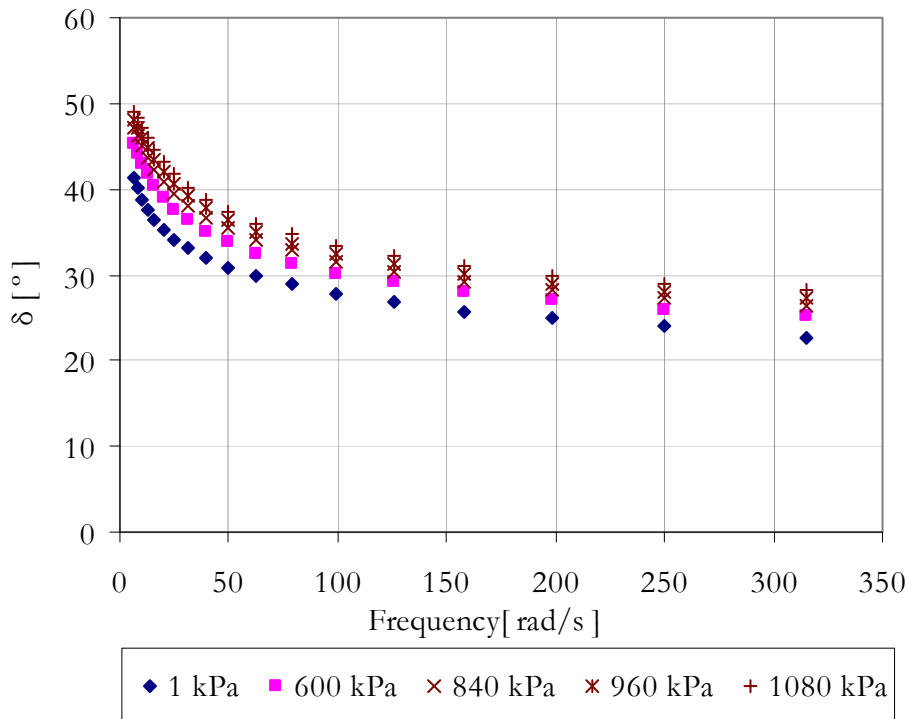


Figure C-6 Frequency sweep results at 10°C; Phase angle for mortar

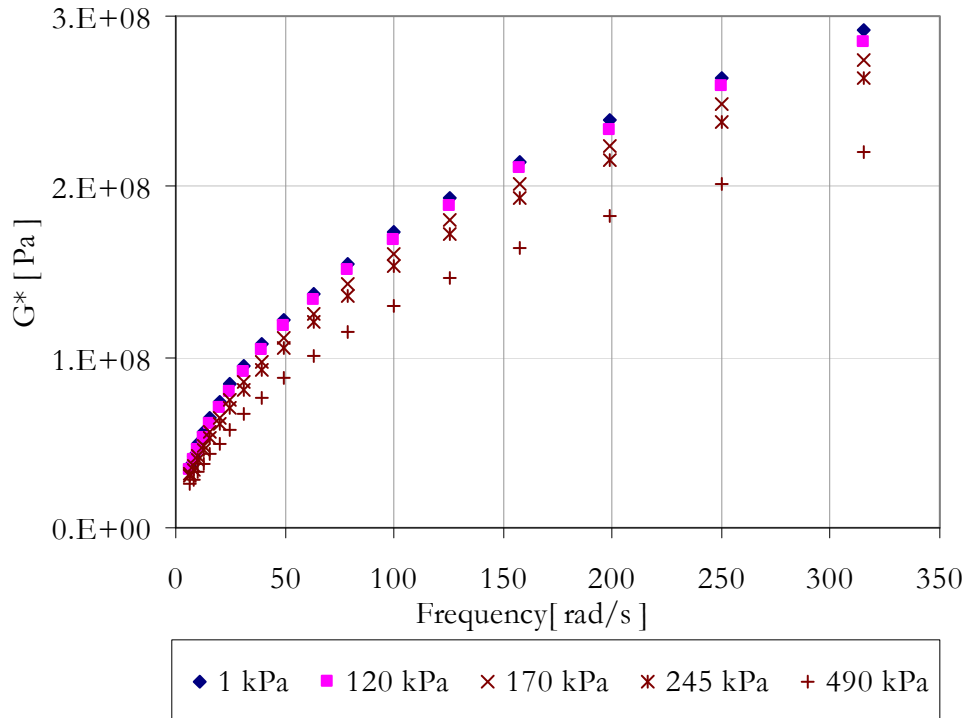


Figure C-7 Frequency sweep results at 20°C; complex modulus for mortar

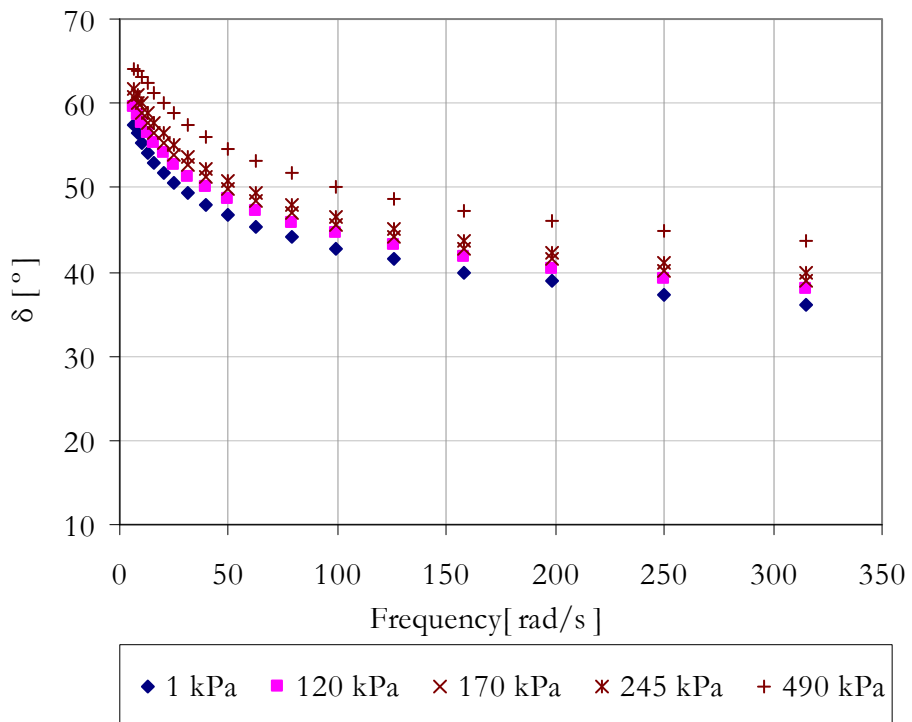


Figure C-8 Frequency sweep results at 20°C; Phase angle for mortar

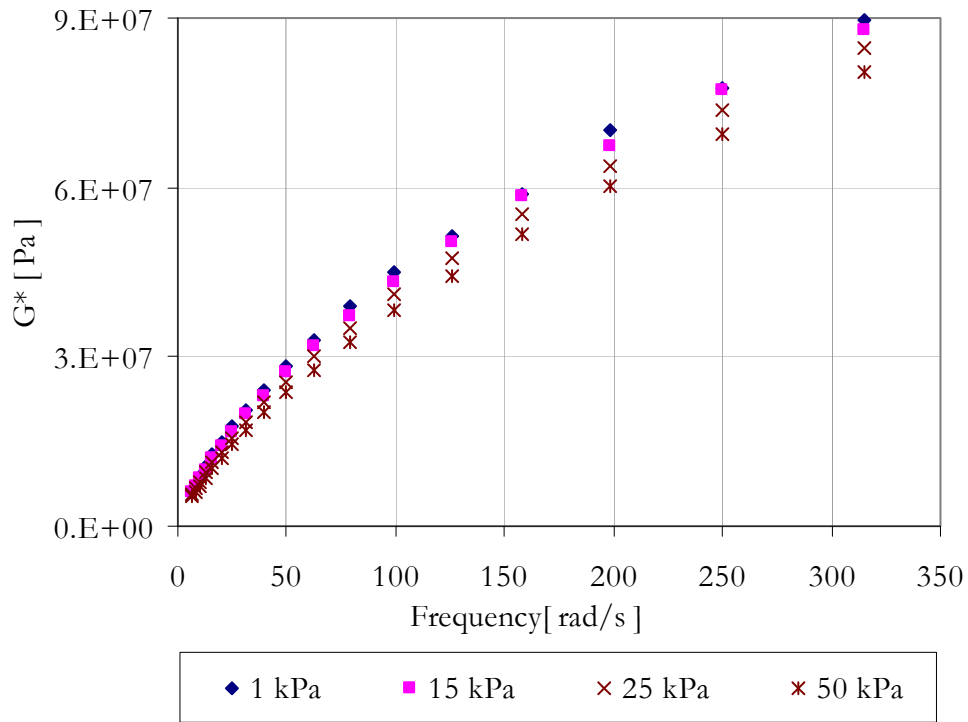


Figure C-9 Frequency sweep results at 30°C; complex modulus for mortar

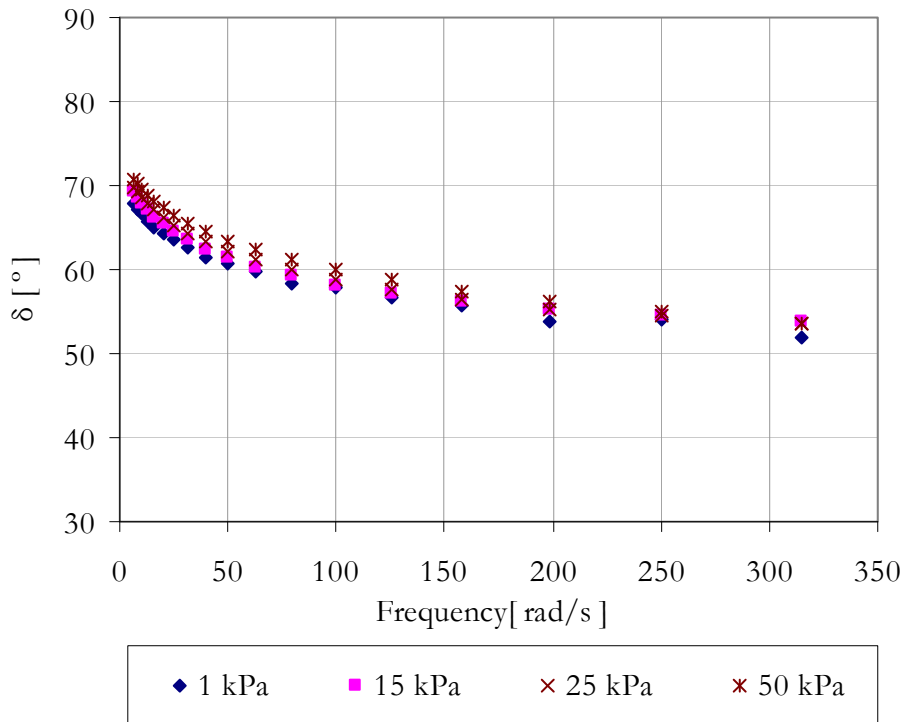


Figure C-10 Frequency sweep results at 30°C; Phase angle for mortar

Appendix D

Relaxation Test Simulations for Mortar at 20°C

The following plots illustrate the relaxation test simulations for the mortar at 20°C. The strain loading rates have been given in Chapter 5.

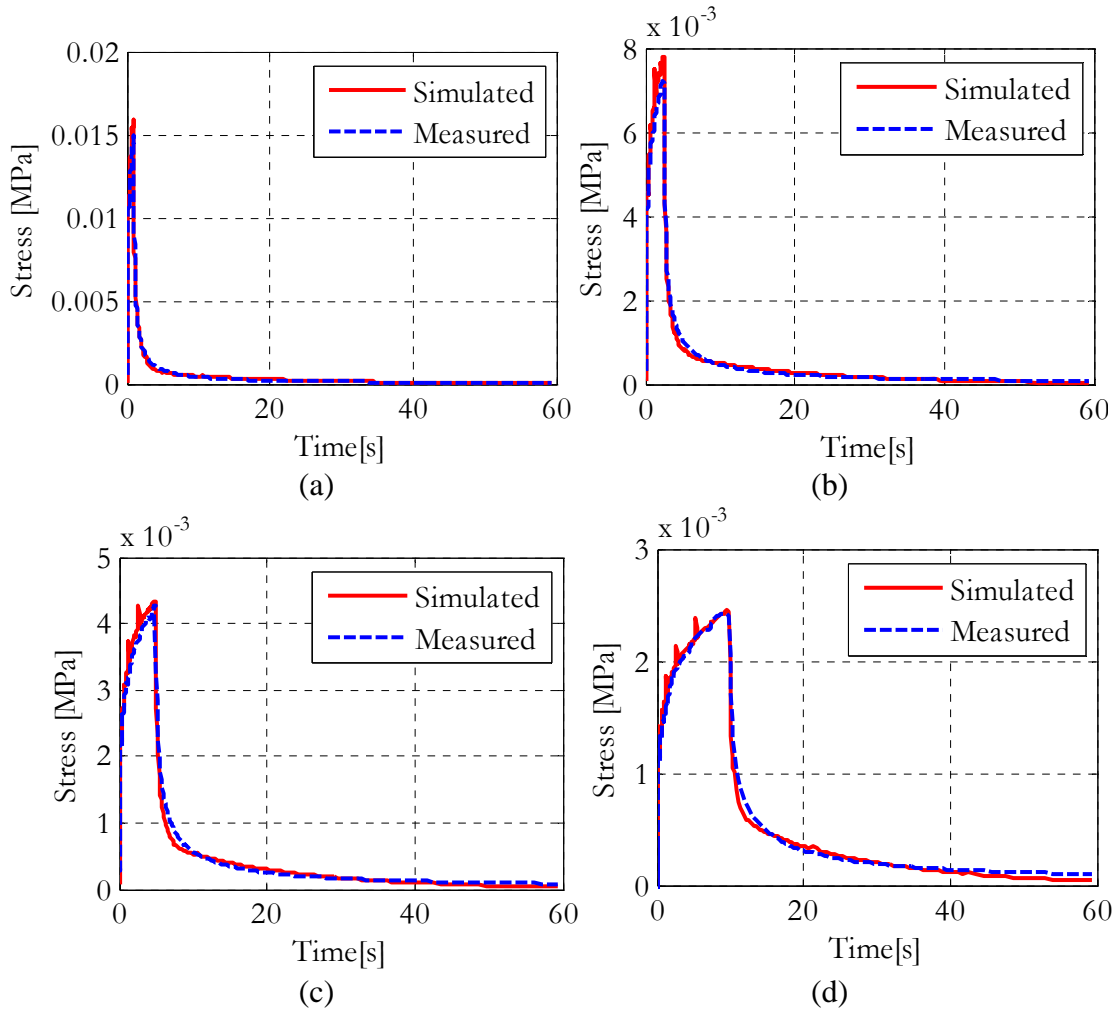


Figure D-1 Generalized Burgers' model, measured and simulated relaxation curves for the mortar at 20°C, Sample no 2. (time step 1s (a), 2.5s (b), 5s (c) and 10s (d))

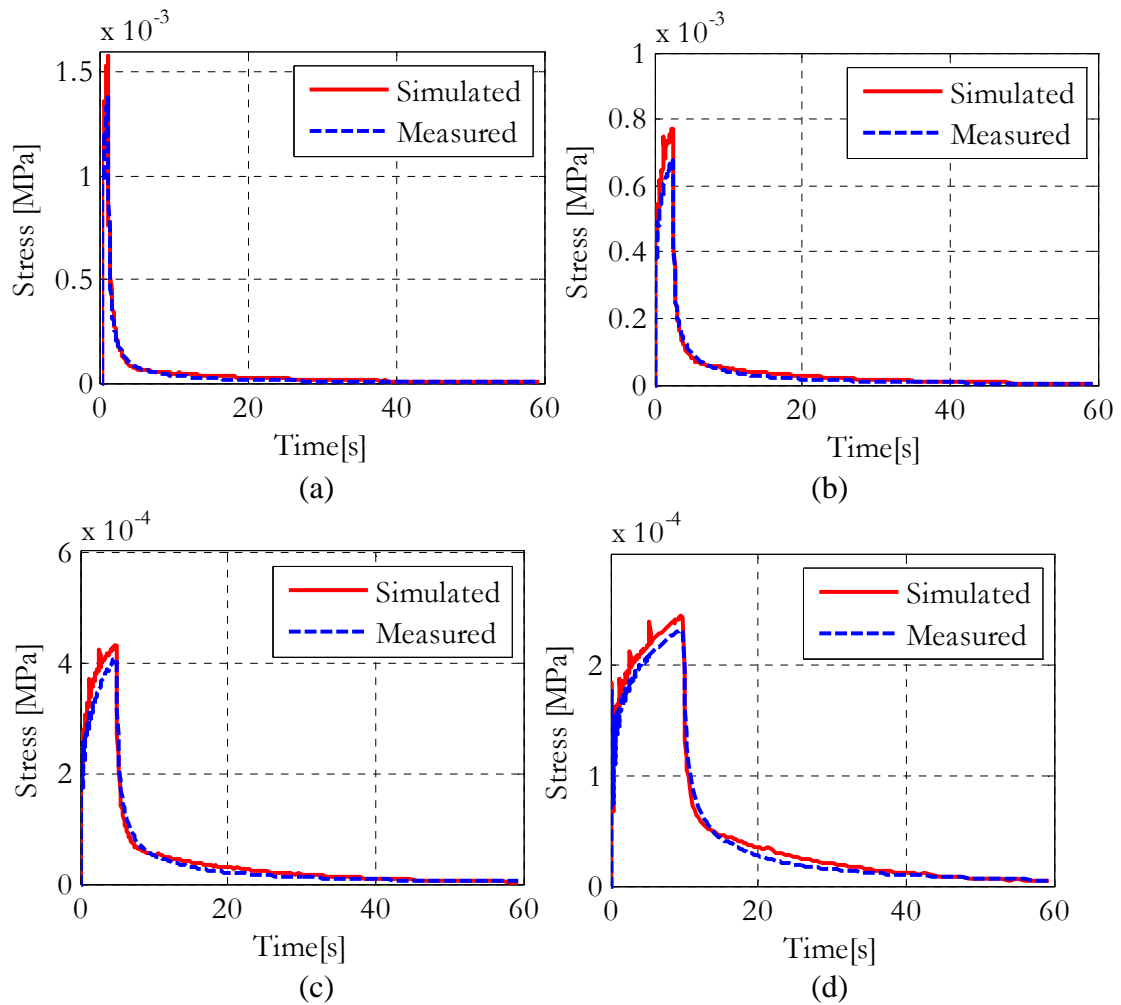


Figure D-2 Generalized Burgers' model, measured and simulated relaxation curves for the mortar at 20°C , Sample no 3. (time step 1s (a), 2.5s (b), 5s(c) and 10s (c))

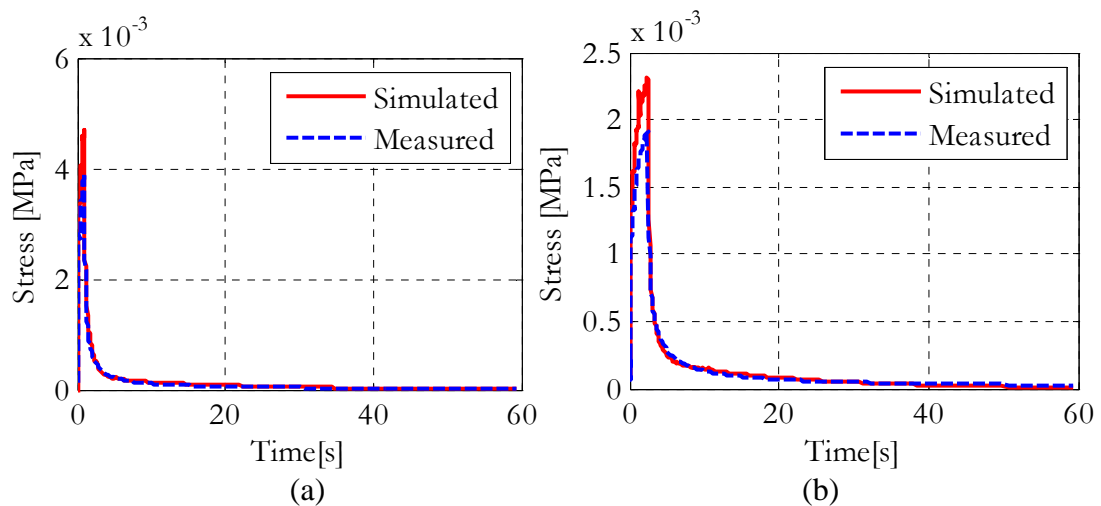


Figure D-3 Generalized Burgers' model, measured and simulated relaxation curves for the mortar at 20°C , Sample no 4. (time step 1s (a), 2.5s (b))

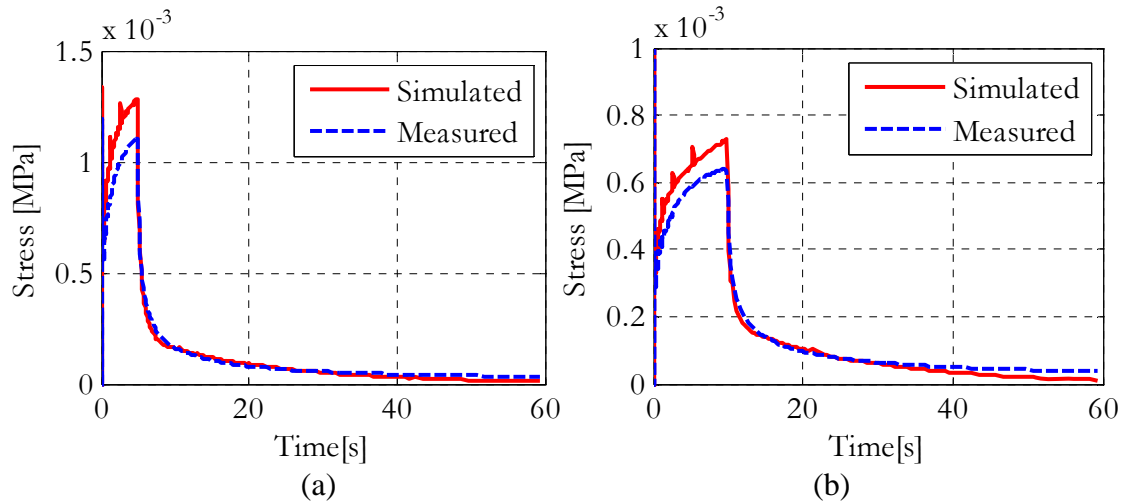


Figure D-4 Generalized Burgers' model, measured and simulated relaxation curves for the mortar at 20°C , Sample no 4. (time step 5s(a) and 10s (b))

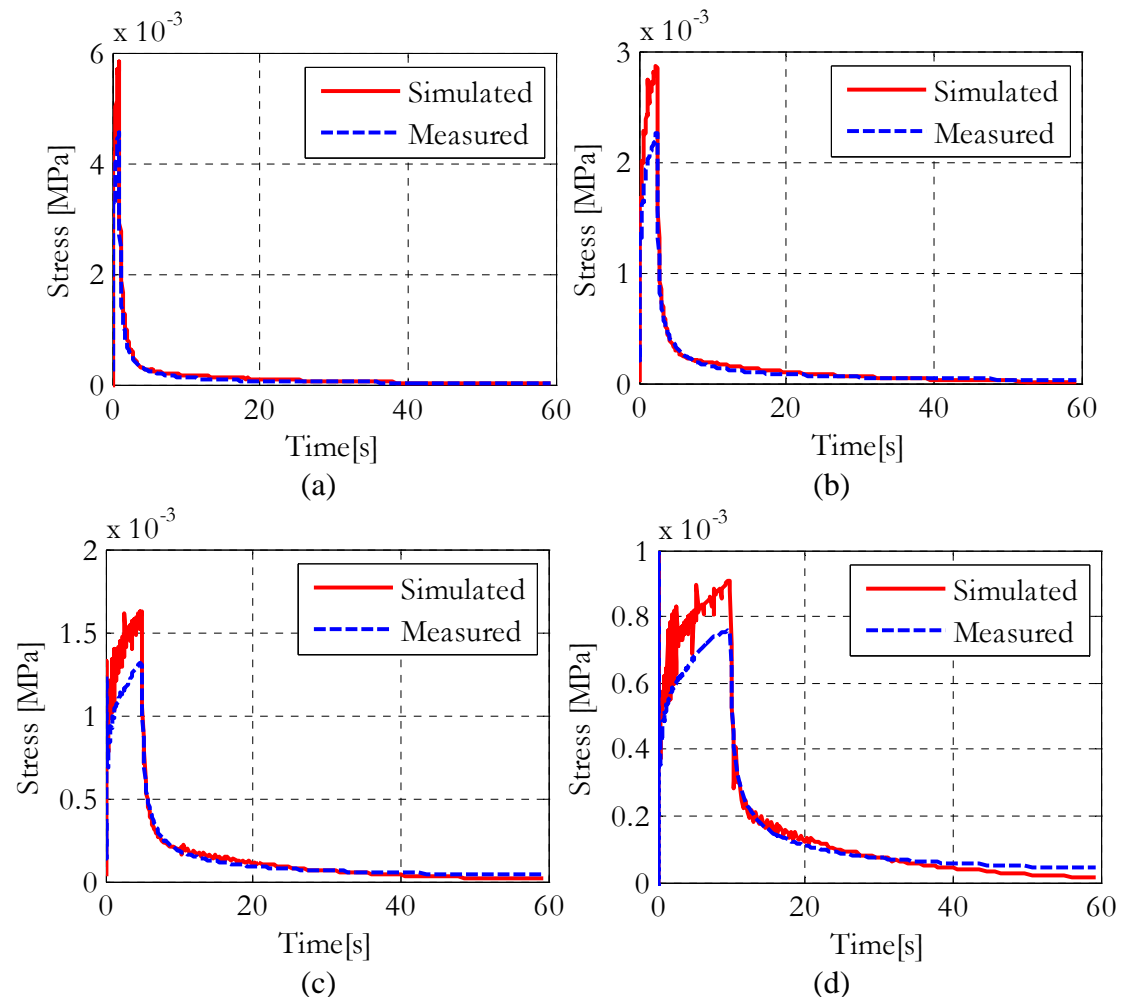


Figure D-5 Generalized Burgers' model, measured and simulated relaxation curves for the mortar at 20°C , Sample no 5. (time step 1s (a), 2.5s (b), 5s(c) and 10s (c))

Appendix E

Brief Overview of the PA Design Tool

Here a brief overview of the meso mechanical PA design tool (Life Optimization Tool, LOT) is presented. The tool basically translates moving wheel loads on the surface of a pavement into stress and strain signals in the bituminous mortar and adhesive zones. These signals are used as an input to a relevant damage model, which provides fatigue life performance prediction. The design tool relies on the component materials behaviour, the geometry of the mixture and the loading. Details on the three basic components are given below. More details about the design tool can be found elsewhere [2-9]

I. Component Material Behaviour

The response of the PA structure is dependent on the response of the individual component materials. The following assumptions are made in defining component material behaviour.

- Stone: Stone are modelled as rigid bodies or by application of boundary conditions. Given the stiffness of a solid stone (in the order of 50,000 MPa) compared to that of mortar (in the order of 100 to 5,000 MPa) it becomes clear that the largest part of in-mixture deformation will occur within the mortar. This supports the assumption to model the stones purely rigid. Furthermore insight into stress and strain in individual stones is not required. Within LOT ravelling is caused by cohesive or adhesive failure. Failure through fracture of the aggregates is not considered.
- Voids: The voids are considered to have no resistance to any deformation.
- Adhesive zone: The adhesive zone is assigned a thickness of 0.01 mm. This thickness is very limited when compared to the diameter of the stones and the width of the mortar bridges. This has led to the conclusion that the response behaviour of the adhesive zone is of secondary importance. Due to the limited thickness of the adhesive zone, only limited deformations over the zone will occur due to the lack of deformable volume. The adhesive zone is therefore simply modelled linear elastically; the assigned stiffness is high and based on the stiffness of surrounding mortar.
- Mortar: From the above it is clear that all efforts should go to defining the response behaviour of the mortar. Currently

the mortar is modelled as being linear viscoelastic. The viscoelastic properties are to be determined via various response measurements on actual PA mortar so that the response of the modelled mixture structure be as close as possible to that of the real PA mixture.

II. Load

In the design tool, the load of a tyre to the pavement surface is applied via forces acting on individual stones. First of all insight into the contact stresses between tyre and pavement structure is obtained via interpretation of measurement data reported in literature [1]. The interpretation of the measurement data led to the definition of the following stress time signals.

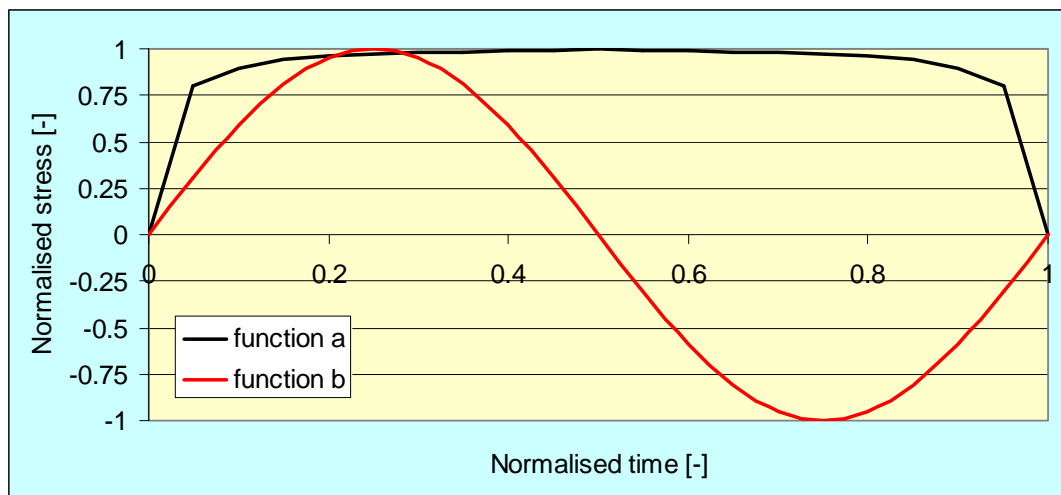


Figure E-1 Defined basic signals for surface load.

Translation of the basic signals into the load signal that is applied to the FE-model starts by multiplication of the normalised time with the time it requires a tyre to pass over a certain point. The next step is to compose the 3D stress signals by combining the defined functions. This is performed on the basis of multipliers that allow the definition of all required signals on the basis of the local contact pressure. The applied equations and multipliers are listed in table E-1.

	Function a	Function b
Vertical bulk stress	σ_{contact}	
Transversal bulk stress	$0.15 * \sigma_{\text{contact}}$	
Longitudinal bulk stress free wheel	$0.025 * \sigma_{\text{contact}}$	$0.3 * \sigma_{\text{contact}}$
Longitudinal bulk stress driven wheel	$-F_a/F_d * \sigma_{\text{contact}}$	$0.3 * \sigma_{\text{contact}}$

Table E-1 Parameters for translation of basic functions into bulk stress signal.

Where σ_{contact} : Local vertical contact stress [MPa]; F_a : axle load [kN]; F_d : driving force [kN]. The driving force is determined via the following equation.

$$F_d = \frac{P * tp * (1 - loss)}{v} \tag{E-1}$$

Where P: engine power [kW]; tp: throttle position, e.g. 0.8 [-]; loss: losses in drive shafts and gear boxes etc [-]; v: speed [m/s]. Then the foot print in which each individual stone is sitting is determined. On the basis of this foot print the bulk stresses are translated into stone forces, see Figure E-2.

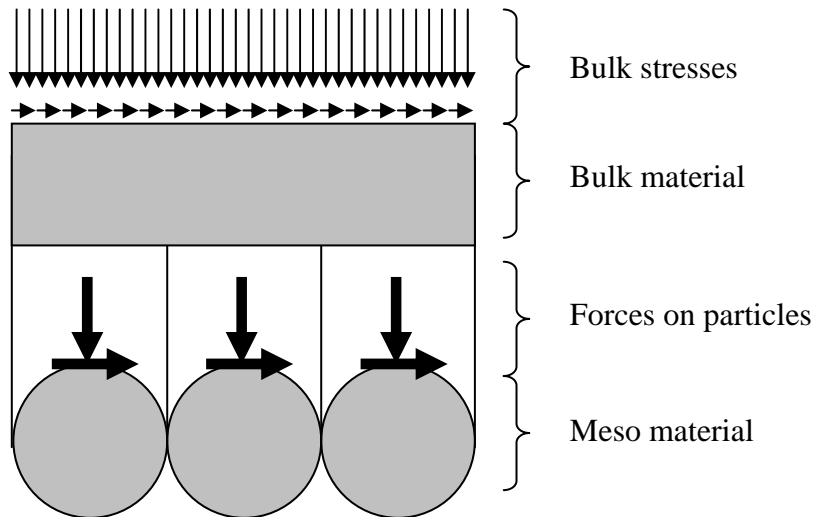


Figure E-2 2D schematics of the principle of translating bulks stress into particle forces on the basis of footprint area.

With the above described functions force signals for individual stones at the pavement surface are determined. Figure E-3 gives an example of these signals.

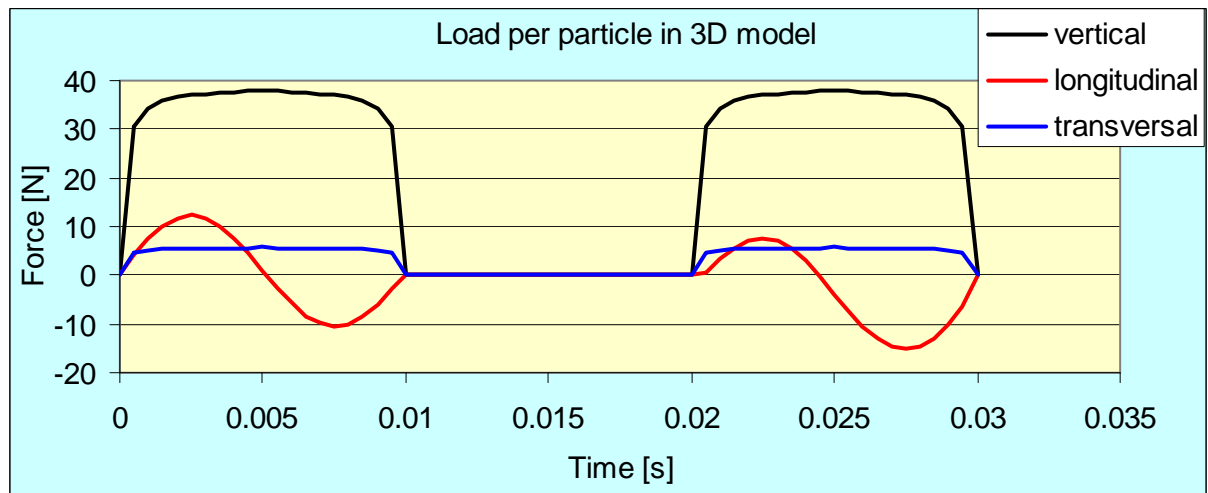


Figure E-3 Example of applied load signals.

III. Geometry

The design tool contains three geometric models for the PA mixture. These are the 2D idealised, 3D idealised and the 2D photo/scan. By combination of the three models insight into the stress-strain-time signals in real 3D PA

structures is obtained. Short description of the three geometries is given below.

A) Idealised models

The idealised models consider perfectly round and rigid spheres bond together via mortar bridges. Figure E-4 gives an overview of the 2D idealised model. The particles themselves are not visible and formed by implementation of restraints. In this case the crosses that mark the centre of the various particles have the freedom to rotate and translate. All nodes at edge of the particle are rigidly connected to the master nodes indicated by the crosses; this effectively creates rigid body stone particles.

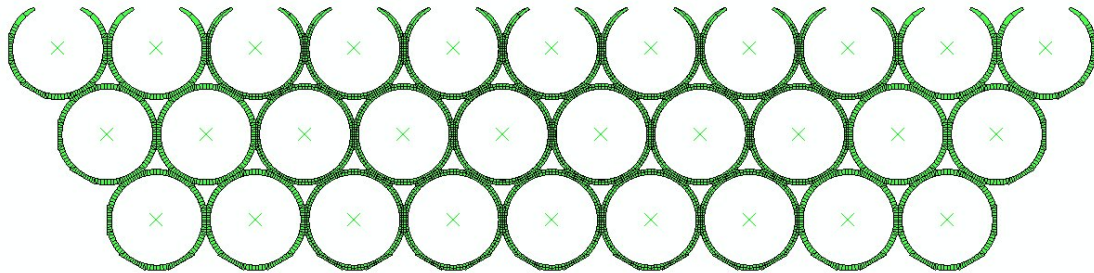


Figure E-4 Overview of the 2D idealised model.

The model consists of three layers of stone particles. In each layer the outer two particles are enclosed in a mortar film modelled by a single layer of elements. The mortar films closer to the middle of the model are modelled by two layers of elements. Figure E-5 is an enlargement of the transition area where the mesh is refined.

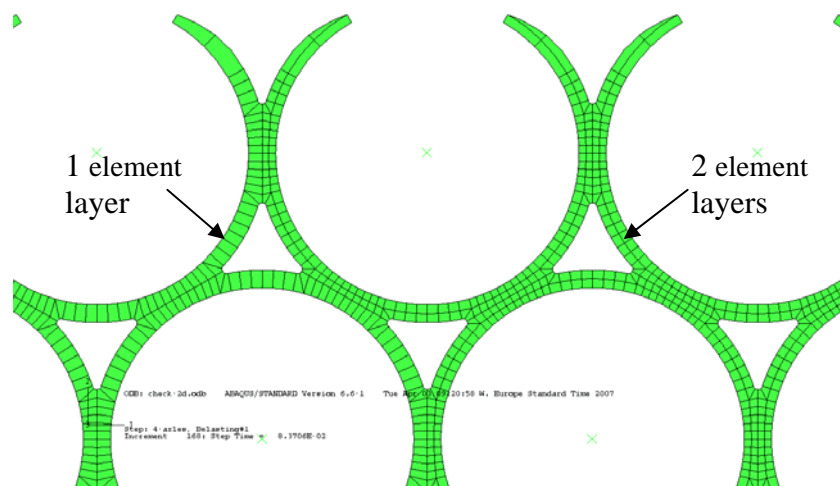


Figure E-5 The mesh is finer in the middle part of the model.

Particles closest to the centre of the model are fitted with a layer of thin elements that represent the adhesive zone, see figure E-6 for an enlargement. Figure E-6 also gives an impression of the fineness of the mesh in the central area. The adhesive zone has a thickness of 0.01 mm.

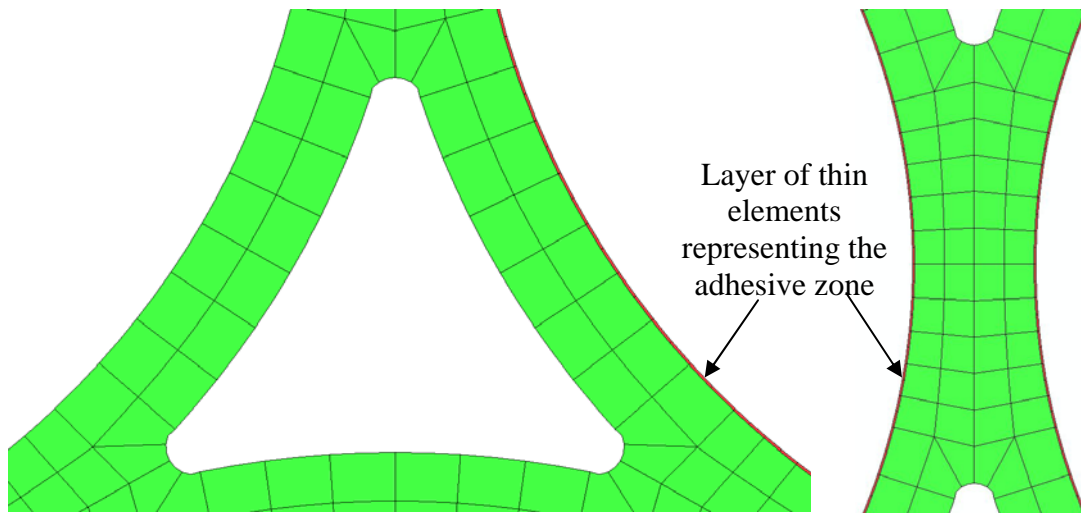


Figure E-6 Left: the central particles only are equipped with a layer of elements representing the adhesive zone. Right: detail of contact area.

The size of 3D models tends to explode quite easily. To prevent this, the 3D model needs to be physically smaller than the 2D model. Also the elements need to be larger. Figure E-7 gives an overview of the 3D idealised model.

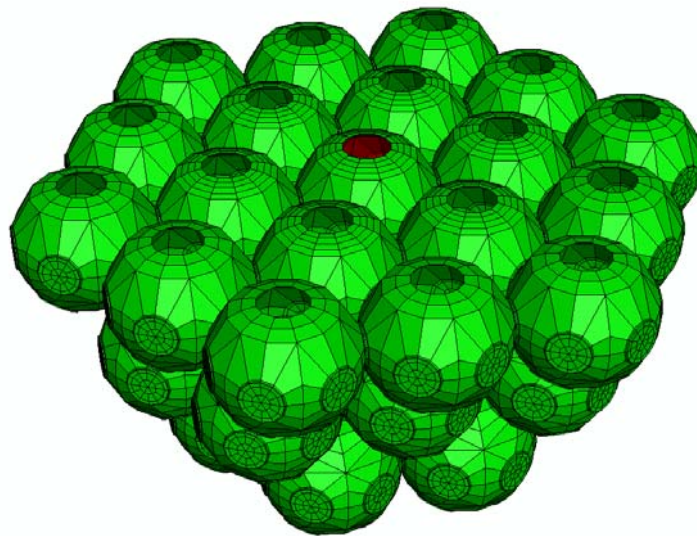


Figure E-7 Overview of the 3D idealised model.

As is shown by figure E-7 the 3D model contains 40 modelled stones. Three layers of stones are present over the height. Also in the 3D model the stones are modelled by rigid bodies.

The meshes of the idealised models are generated by the LOT input generator on the basis of seven parameters, see Figure E-8.

Figure E-8 Inputs that control the geometry of the idealised models.

The equivalent grain radius, R , governs the diameter of the modelled stone particles. This diameter is derived on the basis of the mixture grading curve.

$$D = \frac{\sum_{i=1}^n D_i \cdot fr_i}{\sum_{i=1}^n fr_i} \quad \text{and} \quad R = \frac{D}{2} \quad (\text{E-2})$$

Where D : Equivalent grain diameter [mm]; R : Equivalent grain radius, i.e. radius of modelled stone particles [mm]; n : number of fractions in the stone particle grading, i.e. $D > 2$ mm [-]; i : fraction counter [-]; D_i : Diameter of stones particles in the i^{th} fraction [mm]; fr_i : size of the i^{th} fraction [m/m].

The mortar film thickness which controls the modelled mortar film thickness in the areas where there is no stone-stone contact is determined using:

$$Ft = \left(\frac{V_m + V_s}{V_s} \right)^{1/3} \cdot \frac{D}{2} - \frac{D}{2} \quad \text{with} \quad V_m = V_b + V_{sf} \quad (\text{E-3})$$

Where D is the equivalent grain diameter, i.e. modelled grain diameter [mm]; V_m : relative volume of mortar [m³/kg]; V_s : relative volume of stone [m³/kg]; V_b : relative volume of bitumen [m³/kg]; V_{sf} : relative volume of sand and filler [m³/kg]. the parameters V_b , V_{sf} and V_s are determined as follows.

$$V_b = \frac{f_b}{\gamma_b}, \quad V_{sf} = \frac{f_{sf}}{\gamma_{sf}}, \quad V_s = \frac{f_s}{\gamma_s} \quad (\text{E-4})$$

Where f_b : bitumen content (m/m in 100%) [-]; γ_b : specific mass of binder [kg/m³]; f_{sf} : sand and filler (< 2 mm) content (m/m in 100%) [-]; γ_{sf} : specific mass of sand/filler [kg/m³]; f_s : stone (> 2mm) content (m/m in 100%) [-]; γ_s : specific mass of stone [kg/m³]. The various mass contents, f_b , f_{sf} , and f_s follow from a calculation on the basis of the input of the percentage of stone in mineral and the input of the amount of bitumen on mineral.

The final basic parameter that is required to generate the mesh is the distance between stones, d_s . This parameter follows from the void percentage in the compacted mixture.

$$V_c = 1.63 \cdot d_s^3 \cdot \sin\left(\frac{2}{3}\pi\right); V_m = \frac{8}{3}\pi \cdot \left(F_t + \frac{D}{2}\right)^3 \text{ and } V = \left(1 - \frac{V_m}{V_c}\right) \quad (\text{E-5})$$

Where V_c : volume of the considered cell [mm³]; d_s : distance between stones [mm]; F_t : film thickness [mm]; D : stone diameter [mm]; V_m : volume of material in the considered cell [mm³]; V : void ratio [-]. The parameter d_s is then obtained as:

$$d_s = \sqrt[3]{\frac{V_m}{(1-V) \cdot 1.63 \cdot \sin\left(\frac{2}{3}\pi\right)}} \quad (\text{E-8})$$

The void content is direct input for the LOT input generator. The other parameter that is required is the thickness of the interface. In the tool it is arbitrarily set to a value of 0.01 mm. The interface is considered to be part of the mortar film. When an interface is present the mortar film thickness is thus reduced with 0.01 mm to allow for implementation of the interface.

B) Scan/Photo models

The geometry of the scan or photo models is obtained from real PA images. These images are translated into a 2D element mesh. Figures E-9 gives an illustration of the models. In this model adhesive zones are also present in the meshes that are derived from photographs. These adhesive zones have a thickness of 0.01 mm. The Adhesive zones are present in the central upper part of the models.

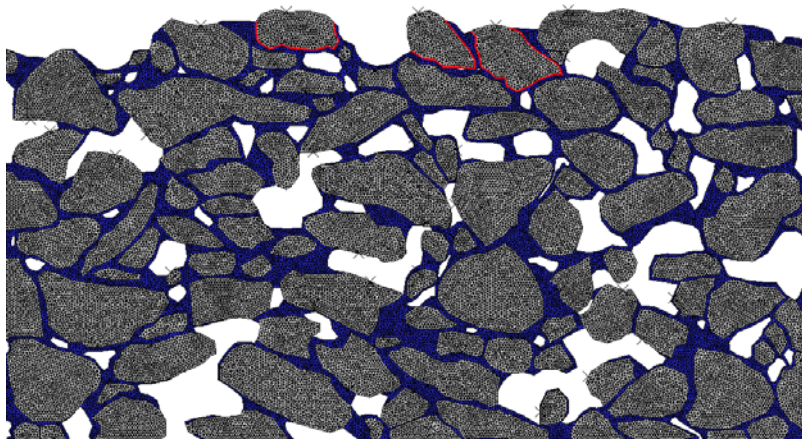


Figure E - 9 Indication of adhesive zones in photo-model.

For more information on the details of the design tool the reader is suggested to read literature [1-9].

References

- [1]. De Beer, M., Fisher, C., and Jooste, F.J. *Determination of Pneumatic/Pavement Interface Contact Stresses Under Moving Loads and Some Effects on Pavement with Thick Asphalt Surfacing Layers*. in *Proceedings of the Eighth International Conference Structural Design of Asphalt Pavements*. 1997. USA.
- [2]. Huurman, M., *Lifetime Optimisation Tool, LOT, Main Report*. 2008: Delft.
- [3]. Huurman, M., Milne, T.I., and Van de Ven, M.F.C., *Development of a structural FEM for road surfacing seals*, in ICCES. 2003: Curfu, Greece.
- [4]. Huurman, M., Mo, L., and Woldekidan, M.F., *Unravelling Porous Asphalt Concrete, Towards a Mechanistic Material Design Tool*. *Int. Journal Road Materials and Pavement Design*, 2009. **10**(Special Issue).
- [5]. Huurman, M., Mo, L., and Woldekidan, M.F., *Porous asphalt ravelling in cold weather conditions*, in *ENVIROAD 2009, 2nd International Conference on Environmentally Friendly Roads*. 2009: Warsaw, Poland.
- [6]. Huurman, M., Mo, L.T., and Woldekidan, M.F., *Unravelling Porous Asphalt Concrete, Towards a Mechanistic Material Design Tool*. *Road Materials and Pavement Design*, 2009. **10**: p. 233-262.
- [7]. Huurman, M., Mo, L., and Woldekidan, M., *Mechanistic Design of Silent Asphalt Mixtures*. *International Journal of Pavement Research and Technology*, 2010. **3**(2): p. 56-64.
- [8]. Huurman, M., Scarpas, T., Kasbergen, C., and T, M. *Development of a structural FEM for Road Surfacing Seals*. in *International Conference on Computational & Experimental Engineering & Sciences (ICCES' 03)*. 2003. Greece.
- [9]. Huurman, M., Mo, L., Woldekidan, M.F., Khedoe, R.N., and Moraal, J., *Overview of the LOT meso mechanical research into porous asphalt raveling*. *Advanced Testing and Characterisation of Bituminous Materials, Vols 1 and 2*, 2009: p. 507-518.

CURRICULUM VITAE

Name Milliyon Fekade Woldekidan
Date and Place of Birth 4th February, 1977, Showa, Ethiopia

Educational Background

2004-2006 Master of Science degree (MSc.) in Structural Engineering, Road and Railway specialization, at Delft University of Technology, The Netherlands.

2003-2004 Master of Engineering degree (MEng.) in Municipal Water and Infrastructure, Integrated Urban Engineering specialization, at UNESCO-IHE, The Netherlands.

1994-1999 Bachelor of Science degree (BSc.), in Civil Engineering at Addis Ababa University, Faculty of Technology, Ethiopia.

Work Experience

2006-2011 PhD Researcher at the Road and Railway Engineering section of Delft University of Technology, Delft, The Netherlands.

2001–2003 Road Engineer at MH Engineering plc. & DHV Consultants B.V.; Addis – Awassa Trunk Road Rehabilitation Project, Ethiopia.

2000- 2001 Road and Assistant Bridge Engineer at MH Engineering plc. & China Wanbao Engineering Corporation; Woldia - Alamata Trunk Road construction project, Ethiopia.

1999 – 2000 Junior Civil Engineer at Kajimma Corporation; Addis-Gohatsion Trunk Road construction project, Ethiopia.

